# Geochemical ‘Scouts’ for Processes in Earth’s Lithospheric Mantle

**Marina Veter**

Principal Supervisor: Prof. Stephen F. Foley
Associate Supervisor: Dr. Olivier Alard

A Thesis submitted for the degree of
Doctor of Philosophy,
Department of Earth and Environmental Sciences
Macquarie University

September 2020

*to my grandparents, Valdemar and Maria and my dad, Viktor*

# ACKNOWLEDGEMENTS

One of the best parts of finishing a thesis is writing the acknowledgements – when you take the time to sit down and reflect on the past few years of your life and just realize how many people accompanied you on this way. It is overwhelming and I am grateful to each and every one of them.

Nevertheless, I feel most indebted to my primary supervisor Prof. Stephen Foley, who first introduced me to LA-ICP-MS analysis and its magic and later sparked my fascination for trace elements in olivines. I ended up following Steve from Germany to Australia for my PhD studies, which turned out to be one of my biggest adventures so far. Especially during these last years, I came to know that Steve's knowledge is bottomless, his modesty and patience I consider supernatural, and his enthusiasm and dedication are admirable. I am really grateful for you giving me this opportunity and always providing your advice, help and guidance, and sharing your wisdom in challenging moments of life.

I would like to express my gratitude to my associate supervisor A./Prof. Olivier Alard, the main drive force in LA-ICP-MS refinement. Thank you for sharing your analytical finesse, for pushing the limits of LA-ICP-MS and letting me in on this adventure, for sharing your expertise and knowledge beyond analytical questions, and especially for your unlimited and contagious positivity.

Thank you to the staff in the Macquarie GeoAnalytical (MQGA) including Yi-Jen Lai, Yoann Greau, Tim Murphy, Peter Wieland, Manal Bebbington, as well as Stephan Buhre and Nora Groschopf from Johannes Gutenberg-University in Mainz, Germany. I appreciate your guidance and expertise in sample preparation and high-quality data acquisition, which is the essence of this thesis. Thank you to Sally-Ann Hodgekiss for your Creative Cloud expertise.

The biggest win on this journey is the people I met and friendships I made. I am grateful to each and every one for creating happy and unforgettable memories with me, be it on the beaches or in the mountains, exploring the city or national parks, joining for yoga and teaching me badminton, watching a ridiculous number of movies, sharing your laughter and sorrow, but especially sharing your food and your drink with me. Special thanks to Laura Otter, Michael Förster, Rosa Didonna, and Thusitha Nimalsiri. for your enormous help and support on the last meters of my PhD journey, for your continuous friendship, motivational speeches, coffee sessions and so much more. Thank you to the Macquarie cohort (past and present) including Alex Wellhäuser, Anthony Lanati, Ben Demmert, Chunfei Chen, Chutian Shu, Francesca Mirolo, Halimulati "Alanur" Ananuer, Hindol Ghatak, Ilya Fomin, Isra Ezad, Josh Shea, Jon Munnikhuis, Kim Jessop, Kui Han, Lauren Gorojovsky, Maria "Coti" Manassero, Milena Schönhofen, Mingdi Gao, Olga Ortega, Robyn Gardner, Sarath Kumara, Sinan Özaydin, Vili Grigorova and Zairong Liu. I'd like to thank my personal motivation crew from Germany Elisa Hartmann, Julia Intemann, Katha Schmitt, and Marianne Richter for knowing how to cheer me up and make me believe in myself. You are all very dear to me.

Finally, my deepest thanks to my family, especially my mom, for your unconditional love, unwavering support, motivation and confidence. Ohne eure Unterstützung, Motivation und Liebe wäre ich nie so weit gekommen und meine Dankbarkeit lässt sich schwer in Worte fassen.

*"If I have seen further than others, it is by standing upon the shoulders of giants"*
*– Isaac Newton*

# AUTHOR'S STATEMENT OF ORIGINALITY

I, Marina Veter, declare that this work has not previously been submitted for a degree or diploma in any university. To the best of my knowledge and belief, the thesis contains no material previously published or written by another person except where due reference is made in the thesis itself.

| | |
|---|---|
| Marina Veter | 30.09.2020 |
| | Date |

# ABSTRACT

Investigation of the geochemical composition of the Earth's subcontinental lithospheric mantle provides insights into the Earth's evolution, including early magmatic and metasomatic processes. Samples of the lithospheric mantle are exposed on the Earth's surface predominantly in orogenic peridotite massifs or entrained as mantle xenoliths in volcanic rocks, such as kimberlites and alkali basalts. The silicate phases olivine, orthopyroxene, clinopyroxene and garnet are the main constituents of the mantle peridotites and thus their trace element composition records petrogenetic processes through time. The Earth's oldest subcontinental lithospheric mantle rocks are highly depleted peridotites that experienced up to 40% partial melting, thus completely consuming clinopyroxene and garnet, leaving behind a residue composed almost exclusively of olivine and orthopyroxene. Therefore, these minerals bear great potential to record depletion and re-enrichment events in the mantle and promise to be useful petrogenetic indicators for our understanding of geochemical construction of lithospheric profiles. However, trace element concentrations in olivine and orthopyroxene are very low, and often close to analytical detection limits, complicating the acquisition of low-level abundances elements.

This study focused on the optimisation of a conventional and widely used *in situ* LA-ICP-MS procedure to enable the acquisition of low-level trace elements in olivine and orthopyroxene. The analytical limitations were addressed by the addition of molecular hydrogen gas (5 mL $min^{-1}$) to the carrier gas flow and tested on the reference material glasses NIST 612, BCR-2G as well as a natural olivine. The measured elements were extended to a palette of 72 masses, including rare earth elements and the rarely analysed volatile chalcophile and siderophile group of elements. The improved method resulted in slightly enhanced sensitivities (1.5-fold), highly improved precision (e.g., on Ga from 68 to 34 RSD%) and slightly improved limits of detection ranges (e.g., Cu from 6–10 to 4–6 ng $g^{-1}$), which enable acquisition of a complete rare earth element pattern in natural olivines.

The enhanced LA-ICP-MS method was then applied on natural mantle peridotite xenoliths from Mt Gambier, southeastern Australia. Mt Gambier is a well-studied locality in Australia and represents relatively unmetasomatised continental mantle. New trace element analyses of olivine, orthopyroxene and clinopyroxene and the extended element palette to REE (especially in olivine and orthopyroxene) and the volatile chalcophile and siderophile elements (e.g., Mo, Ag, Cd, In, and Sb) allow us to estimate a more complete composition of the lithosphere, which makes it a potential keystone for composition of continental lithospheric mantle.

The improved method was also used to collect new trace and ultra-trace element data for minerals in cratonic mantle xenoliths from the Kaapvaal craton (southern Africa) and North Atlantic craton (West Greenland). The compositions are compared and contrasted with each other and with the off-craton continental mantle xenoliths from Mt Gambier. Both cratons experienced a high degree of partial melting,

yet their mineralogical and geochemical compositions show differences, which are related to different later re-enrichment processes. The addition of Si-rich melt resulted in higher modal orthopyroxenes in the Kaapvaal peridotites (28 ±10 %) compared to West Greenland (11 ±12 %), whereas carbonate-rich melt addition produces olivine and clinopyroxene whilst orthopyroxene is consumed, resulting in higher olivine/orthopyroxene. Later metasomatic enrichment processes introduced secondary clinopyroxene and garnet, which are recorded in increased LREE and MREE in orthopyroxenes from West Greenland and Kaapvaal peridotite xenoliths.

# TABLE OF CONTENTS

# LIST OF FIGURES

# LIST OF TABLES

# CHAPTER 1

# INTRODUCTION

## 1.1 Aims and Structure of the Thesis

Determining the chemical composition of the Earth's subcontinental lithospheric mantle (SCLM) and the distribution of elements within it and its host phases is of significant value for the reconstruction, and our understanding, of the Earth's evolution and composition. After accretion of the primitive Earth and subsequent segregation of core, mantle and crust, the geochemical composition of the mantle has been modified by multiple depletion and metasomatic re-enrichment processes. Peridotite xenoliths, predominantly entrained in kimberlitic or alkali basaltic rocks, are direct samples of the upper mantle brought to the Earth's surface by volcanic activity and offer great opportunities to reconstruct the composition and geochemical processes that have governed Earth's mantle evolution. However, most xenoliths experienced variable degrees of alteration in geochemical and mineralogical composition by passing re-fertilizing melts and/or fluids. In order to estimate the Earth's primitive mantle composition, these infiltrating metasomatic events need to be characterised and "stripped" away to uncover the original composition.

Numerous geochemical studies have thoroughly investigated the isotopic, major element and lithophile trace element composition of peridotite xenoliths from different geotectonic settings and localities and have characterised geochemical fingerprints for various types of mantle metasomatism. Furthermore, investigations of element partitioning between mantle peridotite phases have established that clinopyroxene and garnet are the major hosts for the majority of incompatible elements. Even though olivine and orthopyroxene are modally the most abundant silicate phases in the mantle, their geochemical incompatible trace element contribution to the upper mantle has been largely neglected due to insignificantly low or unmeasurable concentrations. Relative to lithophile elements, the investigation of volatile chalcophile and siderophile elements (VCSE) and their distribution and behaviour in the Earth's mantle is underrepresented and still poorly understood. It is assumed that sulphide phases are the major hosts for VCSE, however silicate phases do incorporate some amounts (ng $g^{-1}$) of these elements as well and given the fact that silicate phases are the major constituents of the mantle, their low VCSE concentrations should be taken into account. The problematics of analytical limitations combined with low element concentrations close to or below the detection limit explain the lack of data for (ultra-) trace element and 'non-traditional' element (e.g., VCSE) in the dominant mantle phases olivine and orthopyroxene, and to a lesser degree in clinopyroxene and garnet. Acquiring this additional information, we can better estimate the Earth's bulk composition.

### 1.1.1 Aims

The main objectives of this thesis are:

1) Overcome the analytical limitations by refining *in-situ* LA-ICP-MS measurement for analysis of low-level concentration elements, e.g., incompatible REE in olivines and orthopyroxenes, and VCSE in silicates;

2) Apply the improved method on natural mantle peridotite xenoliths and determine the distribution and behaviour of VSCE in mantle silicate phases. For this purpose, mantle spinel-peridotite xenoliths from Mt Gambier, southeastern Australia were chosen, which represent unusually fresh samples of the upper mantle relatively unaffected by enriching metasomatic processes;

3) Apply the method to samples of the cratonic lithosphere mantle and compare previous observations with more "complex" samples that experienced several different depletion and re-enrichment events. For this part, kimberlite-hosted xenoliths from two different cratons, the Kaapvaal craton, south Africa and the North Atlantic craton, West Greenland were chosen for investigation.

### 1.1.2 Thesis structure

This thesis is prepared as a "thesis by publication" and comprises five chapters: this introductory chapter (Chapter 1), three related manuscripts (Chapter 2–4) and a concluding chapter (Chapter 5).

Chapter 1 gives an overview of the aims and motivations for this study as well as a literature review with relevant background information.

Chapter 2 is a method development contribution and focusses on the improvement of LA-ICP-MS measurement protocols with the aim to increase sensitivity and decrease detection limits, thus allowing acquisition of ultra-trace elements and VCSE. This method is tested on certified reference materials and natural olivines and is applied on natural samples in the subsequent chapters.

Chapter 3 presents new ultra-trace element data for silicate phases from spinel lherzolite xenoliths from Mt Gambier, chosen to represent relatively unmetasomatized sub-continental lithospheric mantle. With the improved method I acquired the most complete set of elements yet measured and determined partition coefficients for rarely analysed elements between mantle silicate phases.

Chapter 4 applies the same method on more complex samples, kimberlite xenoliths from the Kaapvaal craton in south Africa and North Atlantic craton in West Greenland. Both localities have a rich but distinct history in depletion and enrichment events.

Chapter 5 summarises findings from the preceding chapters and puts them into context of the thesis aims.

The chapters are formatted according to manuscript preparation requirements resulting in slight overlap and unavoidable repetition of background information and method description as a matter of necessity for the individual manuscripts.

### 1.1.3 Contribution of authors

The initial ideas for each manuscript were suggested by the two supervisors Stephen Foley (SF) and Olivier Alard (OA) and further developed by the candidate, SF and OA during discussion of results and preparation of the manuscripts. Mt Gambier samples were collected and provided by OA; Kaapvaal and West Greenland samples were provided by SF, Dorrit Jacob and Graham Pearson. All data acquisition, analysis, interpretation and manuscript preparation were done by the candidate unless explicitly stated otherwise.

Whole rock major element oxides in Chapter 3 were acquired in a previous study by OA (Alard, 2000), the rest of the data was collected by the candidate as part of this thesis. Some olivine and orthopyroxene major and trace element concentrations for Kaapvaal samples were acquired by Tatjana Rehfeldt (as indicated in the chapter) and completed by the candidate to have a full set of elements and minerals.

## 1.2 Subcontinental Lithospheric Mantle

The subcontinental lithospheric mantle (SCLM) is a rigid, chemically distinct region of predominantly depleted ultramafic rocks including dunite, harzburgite and lherzolite. The robust, cool and buoyant lithospheric keels underlie the continental crust and overlie the more ductile asthenosphere and represent a mechanical, thermal and/or chemical boundary layer (e.g. Boyd and Gurney, 1986; Pearson *et al.*, 1995; Griffin *et al.*, 1999a). The thickness of the SCLM was long debated, with initial seismological studies estimating the thickness up to 400 km in cratonic areas (e.g. Jordan, 1975) contrary to recent geophysical studies that agree on a maximum thickness of 250 km beneath Archaean cratons (e.g. Doin *et al.*, 1996; Doin *et al.*, 1997; Jaupart and Mareschal, 1999; Rudnick and Nyblade, 1999; Forte and Perry, 2000; Pearson and Nowell, 2002) and a shallower lithosphere-asthenosphere boundary (LAB) depth of few tens of kilometres beneath Proterozoic and Phanerozoic crust and active rift zones. Extensive thermobarometry studies around the Kaapvaal craton on kimberlite-entrained xenoliths indicate equilibration pressures equivalent to maximum depths up to 250 km, whereas xenoliths in kimberlites erupted through the circum-cratonic Proterozoic crust suggest significantly thinner lithosphere (Pearson and Nowell, 2002).

The petrography and geochemical composition of the lithospheric mantle can be estimated by examining mantle rocks available at the Earth's surface that occur in diverse geological settings. Two main direct sources for mantle rocks are (1) xenoliths entrained in volcanic rocks and (2) orogenic peridotite

massifs tectonically emplaced into the crust. The massif peridotites sample the shallow lithosphere (<100 km) and are characterised by large spatial exposures (up to 120 $km^2$) allowing the study of *in-situ* field relations in the SCLM. However, extensive petrogenetic processes, such as serpentinization, interaction with migrating crustal fluids and deformation during emplacement, are superimposed on the original geochemistry (e.g. Pearson and Nowell, 2002; Lorand and Luguet, 2016; Griffin and O'Reilly, 2019). Xenoliths represent mantle fragments transported by volcanic rocks during eruption and range in size up to about 80 centimetres in diameter. In contrast to orogenic peridotites, mantle xenoliths sample a larger vertical section of the lithosphere, reaching depths down to the diamond stability field and thus provide deeper insights into the SCLM than massif peridotites. However, the rapid ascent and sampling disrupts the spatial relationships between rocks and thus may be less representative. Kimberlite and alkali basalt hosted xenoliths may experience contamination and metasomatic alteration by interaction with the host magma (e.g. Frey and Green, 1974; Menzies and Murthy, 1980; Pearson and Nowell, 2002; Lorand and Luguet, 2016; Griffin and O'Reilly, 2019).

## 1.3 Age of the SCLM

Determining the age and composition of the SCLM is fundamental to our understanding of the evolution and stabilisation processes of the continental roots. During the last few decades, numerous approaches were established providing invaluable insights. Pioneering isotopic studies of SCLM from cratonic regions for example, established that these deep roots remained isolated from homogenizing effects of convective mantle for billions of years and thus preserved their isotopic heterogeneity (e.g. Kramers, 1977; Menzies and Murthy, 1980). Further detailed incompatible-element isotopic studies (e.g., Nd and Sr) on kimberlite and alkali-basalt xenoliths reveal the complex history of enrichment processes within the lithospheric mantle post-dating the depletion events that formed the lithospheric mantle (e.g. Pearson, 1999a, b). However, these particular isotopic systems provide information on enrichment ages and not on the formation ages of the SCLM. A more reliable approach for estimating the segregation of the lithospheric mantle was shown to be achieved with the Re–Os isotope system, due to more compatible behaviour of Os and its greater resistance to host–rock interaction in contrast to incompatible element isotope systems (e.g. Pearson, 1999a; Pearson and Nowell, 2002). The application of Re–Os isotope systems was successfully extended to the analysis of sulphide inclusions in primary minerals (Alard *et al.*, 2000), chromites (Chesley *et al.*, 1999) or in combination with platinum group elements (PGE) (Pearson *et al.*, 2002) supporting a more robust estimate of Re–Os ages.

Numerous studies on mantle peridotite xenoliths from different cratonic regions (Kaapvaal, Siberia, Wyoming, North Atlantic, Tanzania and Slave) all demonstrate Archaean Re–Os formation ages of the lithospheric roots, mostly ranging between 2.7–3.2 Ga (Pearson and Nowell, 2002, and reference therein). Re-depletion-model ages for kimberlite and alkali-basalt hosted peridotite xenoliths from areas adjacent to the Archaean cratons (e.g., southern Africa, Siberia) produce Proterozoic ages ranging between ~2.0–

2.2 Ga, consistent with Proterozoic ages of the overlying crust. The agreement of crustal basement and lithospheric mantle ages from cratonic and circum-cratonic regions indicates a persistent coupling of the crust and lithospheric keel over long time periods (e.g. Griffin *et al.*, 1999a; Pearson, 1999a; Pearson and Nowell, 2002). Alkali-basalt hosted mantle xenoliths or massif peridotites often characterise areas of mostly Phanerozoic tectonic activity and produce Re–Os-model ages younger than cratonic and circum-cratonic ages. However, some localities demonstrate remnants of older ages in the underlying lithospheric mantle (e.g., in SE Australia, 1.9 Ga; Handler *et al.* (1997)) that are inconsistent with the overlying Phanerozoic crust. This discrepancy in ages in such regions is attributed to the resistance of the shallower Proterozoic mantle, which survives re-working events such as rifting and differentiation (Pearson and Nowell, 2002).

# CHAPTER 2

# LA-ICP-MS SIGNAL ENHANCEMENT BY HYDROGEN GAS ADDITION TO CARRIER GAS

Marina **Veter**[1]*, Olivier **Alard**[1,2,3], Stephen F. **Foley**[1,2]

[1] Department of Earth and Environmental Sciences, Macquarie University, NSW 2109, Australia

[2] ARC Centre of Excellence for Core to Crust Fluid Systems, Department of Earth and Environmental Sciences, Macquarie University, NSW 2109, Australia

[3] Géosciences Montpellier, UMR 5243, CNRS & Université Montpellier, 34095 Montpellier, France

* Corresponding author: marina.veter@mq.edu.au

## ABSTRACT

Laser ablation-ICP-MS is a powerful and widely used *in situ* method that requires minimal sample preparation and acquires rapid multi-element data with high spatial resolution – features that contribute to its growing popularity. The increasing demand for analysing samples with low-level compositions close or below detection limit necessitates the continuous improvement of this analytical technique. The motivation for this study is the acquisition of the underrepresented low-concentrated trace and ultra-trace elements, such as the rare earth and chalcophile elements in the major mantle forming silicate mineral olivine.

We test the influence of molecular hydrogen gas added to the LA-ICP-MS and compare it with the standard method (He-Ar carrier gas). The hydrogen gas is set to a constant flow of 5 mL $min^{-1}$ and is admixed to the He-sample aerosol mixture before entering the torch. Our results show a clear improvement in sensitivity on certified reference material (CRM) glasses NIST 612 and BCR-2G. It is shown that the sensitivity enhancement in Zn, As and Cd is coupled to the higher first ionisation energy in these elements, indicating a temperature increase in the plasma when using LA-ICP-MS in hydrogen mode. The enhanced method considerably enhances the precision of measurements, expressed as RSD%, improving from 3–16 to 2–6 % on CRM. Analyses on natural olivine demonstrate improvements in precision (e.g., RSD% enhancing for Ga from 68 to 34 %) and the limit of detection (improved LOD ranges for e.g., Cu from 6–10 to 4–6 ng $g^{-1}$, Nd from 1–2 to 0.6–1.0 ng $g^{-1}$). These advances facilitate the acquisition of a complete REE pattern on natural olivines, filling the gaps in predominantly missing MREE. Furthermore, the volatile chalcophile and siderophile group of elements (e.g., Mo, Cd, In) are now accessible with more precision.

**Keywords:** LA-ICP-MS; hydrogen; sensitivity; limit of detection; olivine.

## 2.1 Introduction

Over the last thirty years, laser ablation-inductively coupled plasma-mass spectrometry (LA-ICP-MS) has become a widely used technique for the *in situ* analysis of major, minor and trace element analyses in solid samples. The advantages of minimal sample preparation and high spatial resolution with rapid multi-element acquisition make LA-ICP-MS unequivocally a powerful analytical method with multiple fields of applications and has become the predominant technique for trace element analysis of geological samples. Since its introduction, considerable advances have been achieved in the improvement of ablation and sampling behaviour, transportation of ablated aerosols to the ICP-MS, as well as vaporization, atomization and ionization of aerosols in the plasma leading to always improving detection limit, better accuracy and improved reproducibility.

Yet, trace element fingerprints of many key minerals remain out of reach because of their very low-level concentration (few ng $g^{-1}$ or less). For instance, the two major mineral phases in common peridotites are olivine and orthopyroxene (opx): these minerals make up 80–95 % of most mantle peridotites and yet contain many trace elements in concentrations of just a few µg $g^{-1}$ to ng $g^{-1}$. This has led to an over-emphasis on analyses of clinopyroxene and garnet. An example is the initial conclusion of widespread Ti-depleted mantle (Salters and Shimizu, 1988), which was later explained by Ti being sequestered in opx (Rampone *et al.*, 1991b). The low concentrations of many trace elements in olivine and opx mean that complete rare earth element (REE) patterns are a rarity in the literature, and many elements, including chalcophile elements, have been largely ignored. Gathering information on the concentrations of a wide range of trace elements including the 'non-traditional' volatile chalcophile and siderophile elements in olivine and opx has not received much attention so far and yet promises to yield new insights into magmatic and metasomatic processes in the mantle. However, currently used laser ablation ICP-MS techniques require some adjustments to improve sensitivities and detection limits, since a wide range of elements of interest in olivines and opx are below detection limit.

The ablation of colourless and pale coloured minerals such as quartz, calcite, and feldspar was initially problematical because they are transparent to visible and near-IR light. This was addressed with the introduction of UV wavelength laser systems coupled to ICP-mass spectrometers because these minerals absorb ultraviolet light (<300 nm) more effectively (Chenery and Cook, 1993). Furthermore, the introduction of the now prevalent shorter UV wavelength lasers has successfully demonstrated enhancement in ablation behaviour and an increase in the fraction of smaller particles in the aerosol (Jeffries *et al.*, 1995; Günther *et al.*, 1997; Guillong and Günther, 2002; Günther and Hattendorf, 2005). Other limitations of LA-ICP-MS systems are elemental fractionation and matrix effects (Fryer *et al.*, 1995; Jeffries *et al.*, 1996), which have been shown to be reduced by switching to shorter UV wavelength lasers such as ArF 193 nm excimer laser systems (Günther *et al.*, 1997), applying lower repetition rates, and intermediate energy densities.

While significant advances have been made in the last 30 years regarding laser wavelength, cell geometry, and ICP-MS, the composition of the atmosphere in the sample chamber and aerosol carrier gases has always been a key aspect of LA-ICP-MS techniques. Eggins *et al.* (1998a) demonstrated that ablation in an argon atmosphere has a higher impact on particle re-deposition and aerosol transport, whereas helium as a carrier gas improves the aerosol uptake and transport to the ICP and enhances the ICP-MS sensitivity, thus is much more efficient than Ar. However, the main limitation for the analysis of natural samples continues to be the desire for higher spatial resolution, which correlates with a decrease in sensitivity and an increase in the limits of detection (LOD): a reduction in ablation crater diameter by a factor of two results in four times less sensitivity and four times higher LODs (Guillong and Heinrich, 2007). These challenges are being addressed in a number of approaches, including the addition of molecular gases (e.g., $O_2$, $N_2$, $H_2$) to argon ICP-MS systems, which has been shown to increase the ionization potential and plasma temperature and thus successfully tackles the above-mentioned limitations (Louie and Soo, 1992; Durrant, 1993; Guillong and Heinrich, 2007). Given the many factors that affect the instrumentation, the experimental set-up, as well as measurement parameters and sample diversity, a key problem is the reproducibility of results that usually carries a significant uncertainty.

The motivation for this study was the acquisition of low-level concentration elements in silicate minerals in rocks of the Earth's mantle, with a focus on olivine and opx. The low concentrations of many trace elements in olivine and opx mean that complete rare earth element (REE) patterns in literature, including chalcophile elements, are widely underrepresented. However, currently used laser ablation ICP-MS techniques require some adjustments to improve sensitivities and detection limits, since a wide range of elements of interest in olivines and opx are not detectable. A little-tested method that may improve sensitivities is the addition of hydrogen to the carrier gas (Guillong and Heinrich, 2007), which we refer to in the following as "hydrogen mode" or "$H_2$-mode". This study compares the standard He-Ar carrier gas routine, referred to as "normal mode", and hydrogen mode LA-ICP-MS measurements on certified reference glasses and addresses the advantages and drawbacks of $H_2$ addition to He–Ar plasma. Furthermore, we apply and test the method on a natural and fresh olivine from a mantle peridotite xenolith from Mt Gambier (SE Australia). We chose a flow rate of 5 ml $min^{-1}$ hydrogen gas, following the study by Guillong and Heinrich (2007), who successfully demonstrated sensitivity enhancement in laser ablation-ICP-MS measurements by adding small amounts of hydrogen gas (0–14 ml $min^{-1}$) to the carrier gas.

## 2.2 Analytical set-up

### 2.2.1 Samples

For this study we used three certified reference materials (CRMs) with known concentrations (preferred values GeoReM database; http://georem.mpch-mainz.gwdg.de); two synthetic glasses NIST SRM 610 and 612, and the synthetic glass with a natural basaltic composition USGS BCR-2G. These CRMs

are homogeneous in composition and cover a wide range of element concentrations, making them ideal materials for our method development and testing. In addition, we measured natural silicate phases (olivine, opx and cpx) in thin sections from Mt Gambier in the Newer Volcanic Province, SE Australia, which is known to have particularly fresh, unaltered silicate minerals. In this study, we present the results for olivine, since these are the most abundant phases in Earth's mantle and show by far the lowest trace element concentrations. Olivines from Mt Gambier are found in mantle-derived peridotite xenoliths entrained in an alkali basaltic host rock; these xenoliths contain relatively fresh and large grains. Testing the method on natural phases like olivine is essential to demonstrate the applicability of the method for natural samples, since the matrix effects between natural mineral phases and CRM glasses have been shown to be significant.

### 2.2.2 Instrumentation set-up LA-ICP-MS + $H_2$

Instrumentation, laser setting, cell geometry and tubing are kept constant between the "normal mode" and the $H_2$-mode. The analytical data acquisition was performed in the laboratories of Macquarie Geoanalytical (MQGA) at Macquarie University in Sydney (Australia). Our standard LA-ICP-MS set-up (Figure 1) comprise an Agilent 7700cs quadrupole ICP mass spectrometer, coupled with a Photon Analyte G2 193 nm ArF Excimer laser system equipped with a HelEx II Active 2-Volume Cell which features a large primary cell allowing to fit numerous (or large) samples and a nested microcell with a volume of ~2.5 $cm^3$ in which ablation occurs (Eggins *et al.*, 2005). Helium rather than Ar is used as the ablation medium

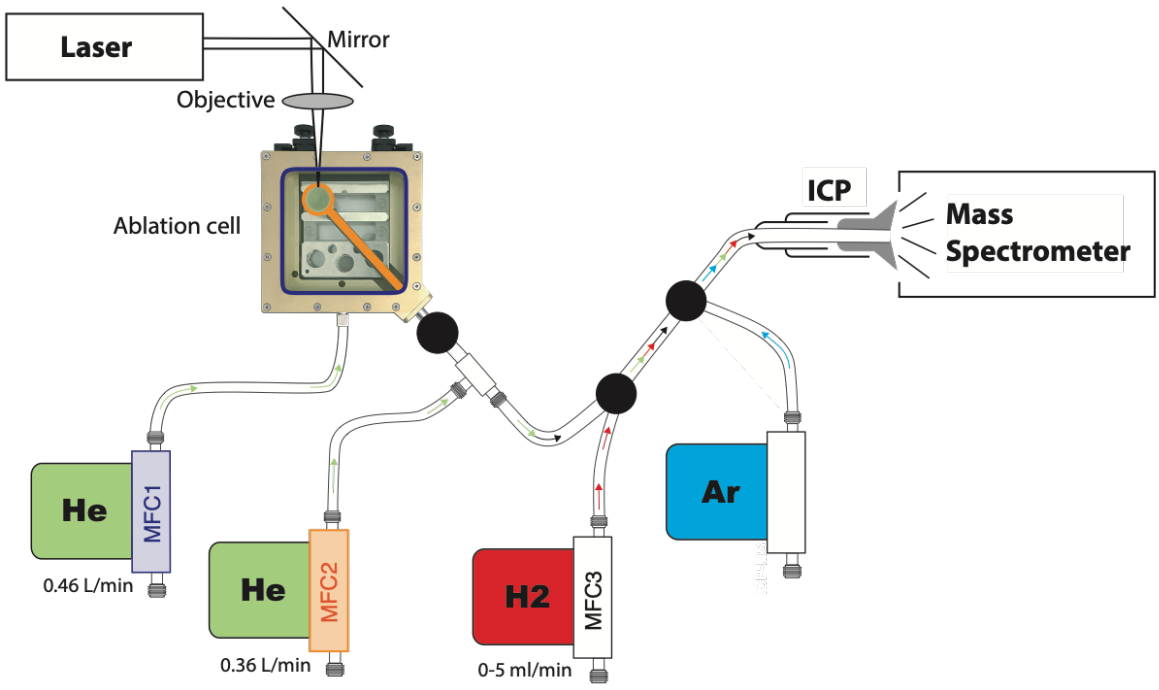


Figure 1 Schematic set-up of the modified LA-ICP-MS system with molecular hydrogen gas (red) added as additional gas after the ablation. Green boxes (He) represent the two mass flow controllers with gas flows for the primary cell (MFC1, purple) and for the nested microcell (MFC2, orange). Argon gas (blue) is added as the last gas, before entering the torch.

to reduce deposition of surface condensate around the ablation site and to produce a complementary increase in sample yield to the ICP-MS (Eggins *et al.*, 1998a; Horn *et al.*, 2003). Helium gas flow rates were set at 0.46 L $min^{-1}$ and 0.36 L $min^{-1}$ (Table 1) for the primary and the nested microcell, respectively, and remained unchanged for normal- and hydrogen-mode.

In normal mode the He plus ablated material is then mixed with an Ar flow at 0.90 ±0.04 L $min^{-1}$, before entering the torch via a 30 ml savilex container. In $H_2$-mode, high purity $H_2$ is added at the exit of the ablation cell via a Y connector, i.e., no $H_2$ is going through the ablation cells (Figure 1). Hydrogen is delivered through a dedicated mass flow controller calibrated for low flow 0–20 mL $min^{-1}$.

After positioning the torch, automatic tuning in laser mode was carried out on NIST SRM 610, focusing on maximum counts rates while keeping oxide production (ThO/Th) below 1 % and minimising element fractionation. The laser was operated at 5 Hz pulse repetition rate with a laser energy density between 3.0–3.6 J $cm^{-2}$ (2.4 mJ) using a constant spot diameter of 65 µm on CRMs and 110 µm on olivine grains. Each measurement started with 170 s background acquisition followed by 60 s ablation and 70 s wash out time. Extended gas blank (i.e., background) was preferred in order to lower as much as possible the variability of the background signal and thus improve the limit of detection.

Table 1 Summary of LA-ICP-MS instrumentation and the operating parameters applied for the test runs in 'normal' and 'hydrogen' mode.

| *Laser ablation system* | *Photon Analyte G2 ArF Excimer Laser HelEx II Active 2-Volume Cell* |
|---|---|
| Wavelength | 193 nm |
| Pulse width | 5 ns |
| Energy density | 3.0–3.6 J $cm^{-2}$ |
| Repetition rate | 5 Hz |
| Laser spot sizes | 65–110 µm |
| Background | 170 s |
| Ablation time | 60 s |
| Wash-out | 70 s |
| *ICP-mass spectrometer* | *Agilent 7700cs* |
| RF power | 1350 W |
| MFC 1 (He) | 0.46 L $min^{-1}$ |
| MFC 2 (He) | 0.36 L $min^{-1}$ |
| MFC 3 ($H_2$) optional | 0 or 5 mL $min^{-1}$ |
| Nebulizer gas flow (Ar) | 0.86–0.94 L $min^{-1}$ |

### 2.2.3 Methods and data processing

In this study, the effects of admixed hydrogen gas to a standard laser ablation-ICP-MS set-up are investigated on a wide range of mass fractions for a total of 72 trace element isotopes to be able to thoroughly document any improvements (e.g., elimination of polyatomic interferences, increase in sensitivity, decrease in limit of detections etc.) and drawbacks (e.g., newly formed polyatomic

interferences). However, measuring 72 masses in one run is not recommended, as it consequently requires the following adjustments, either decreasing the dwell time on each mass to allow all m/z being recorded, or if dwell times are kept constant increase the sweeping mass time to unreasonable duration, i.e., ≫1 s. Both options are disadvantageous, in the first case decreasing the dwell time allows to sweep through all masses, but to significantly decrease counts means going against our primary analytical target to increase the sensitivity. In the second case, long sweep time yield low vertical resolution during ablation by increasing dephasing between volume ablated and measured material, which lead to enhanced down-hole fractionation (e.g., Eggins *et al.*, 1998a). Thus, the best solution was found to be splitting the element list into two separate methods, (1) 'standard' silicate elements including all REEs and lithophile elements ($^{7}$Li, $^{25}$Mg, $^{27}$Al, $^{29}$Si, $^{43}$Ca, $^{44}$Ca, $^{45}$Sc, $^{47}$Ti, $^{51}$V, $^{53}$Cr, $^{55}$Mn, $^{57}$Fe, $^{59}$Co, $^{60}$Ni, $^{62}$Ni, $^{63}$Cu, $^{66}$Zn, $^{69}$Ga, $^{71}$Ga, $^{85}$Rb, $^{86}$Sr, $^{88}$Sr, $^{89}$Y, $^{90}$Zr, $^{93}$Nb, $^{95}$Mo, $^{98}$Mo, $^{133}$Cs, $^{137}$Ba, $^{138}$Ba, $^{139}$La, $^{140}$Ce, $^{141}$Pr, $^{146}$Nd, $^{147}$Sm, $^{153}$Eu, $^{157}$Gd, $^{159}$Tb, $^{163}$Dy, $^{165}$Ho, $^{166}$Er, $^{169}$Tm, $^{172}$Yb, $^{175}$Lu, $^{178}$Hf, $^{181}$Ta, $^{208}$Pb, $^{209}$Bi, $^{232}$Th, $^{238}$U) and (2) 'transition' elements with focus on volatile chalcophile and siderophile elements ($^{25}$Mg, $^{29}$Si, $^{43}$Ca, $^{44}$Ca, $^{45}$Sc, $^{51}$V, $^{63}$Cu, $^{66}$Zn, $^{69}$Ga, $^{71}$Ga, $^{72}$Ge, $^{73}$Ge, $^{74}$Ge, $^{75}$As, $^{86}$Sr, $^{88}$Sr, $^{89}$Y, $^{90}$Zr, $^{93}$Nb, $^{95}$Mo, $^{97}$Mo, $^{98}$Mo, $^{100}$Mo, $^{107}$Ag, $^{109}$Ag, $^{111}$Cd, $^{112}$Cd, $^{114}$Cd, $^{115}$In, $^{121}$Sb, $^{123}$Sb, $^{139}$La, $^{140}$Ce, $^{153}$Eu, $^{166}$Er, $^{172}$Yb, $^{178}$Hf, $^{182}$W, $^{183}$W, $^{184}$W, $^{185}$Re, $^{187}$Re, $^{205}$Tl, $^{208}$Pb, $^{209}$Bi, $^{232}$Th, $^{238}$U). Major elements and a selection of trace elements were measured in both element palettes to allow quality control of each measurement. Each block of natural olivines was bracketed by 3 spots on each of the CRMs in order to correct for instrument drift and monitor the accuracy.

Data reduction was carried out using the GLITTER software (Macquarie University, Sydney), which automates data processing of time-resolved LA-ICP-MS trace element and isotope raw data. In order to achieve quantitative concentrations NIST SRM 610 was used as the external standard using the values from GeoReM database (Jochum *et al.*, 2005) for calibration of measurements. In this study, the reference glasses NIST SRM 612 and BCR-2G were measured as quality control samples along with natural olivine samples, where $SiO_2$ wt% concentrations from previously acquired electron microprobe analyses were applied for internal standardisation ($^{29}$Si) (Perkins and Pearce, 1995; Longerich *et al.*, 1996). The GLITTER software enables a careful inspection of the time-resolved analyses to check for lack of homogeneity in the analyzed volume, and thus to screen and filter for outliers that, especially in natural samples, might result from inclusions or mixed analyses. Local backgrounds were used instead of the more advantageous but less realistic interpolated or averaged session background.

## 2.3 Results and Discussion

### 2.3.1 Background and limits of detection

The addition of an extra gas has potential drawbacks, such as the formation of hydrides which may interfere with the analysis of other elements. The hydrogen mode measurements demonstrate a considerable increase (factor >4) in background intensities on, e.g., $^{47}$Ti, $^{85}$Rb, $^{133}$Cs and $^{137}$Ba (Figure 2). The gas blank

increase may be related to formation of polyatomic interferences, e.g. on mass $^{47}Ti^{+}$ from $^{40}Ar^{4}He^{1}H_3$ or $^{29}Si^{16}O^{1}H_2^{+}$, on $^{85}Rb^{+}$ from $^{40}Ar_2{}^{4}He^{1}H$ and on $^{133}Cs^{+}$ from $^{40}Ar_3{}^{4}He_3{}^{1}H$ and/or $Ar_3CH$. Arsenic and antimony show a significant increase in background intensities as well, factor ~ 5 and 2.5, respectively, but both elements display a simultaneous increase in sensitivity by a similar factor to that seen in the gas blank, which is most probably not the result of overlapping interferences. Smaller increases, by factor <2 were observed on masses $^{45}Sc$, $^{53}Cr$, $^{55}Mn$, and $^{115}In$, and the remaining masses have either a similar or decreased gas blank intensity for hydrogen mode analyses. Yet, overall, the addition of hydrogen resulted in slightly better values for the limits of detection (LOD). The minimum detection limit at 99% confidence level (MDL) is determined by Poisson counting statistics.

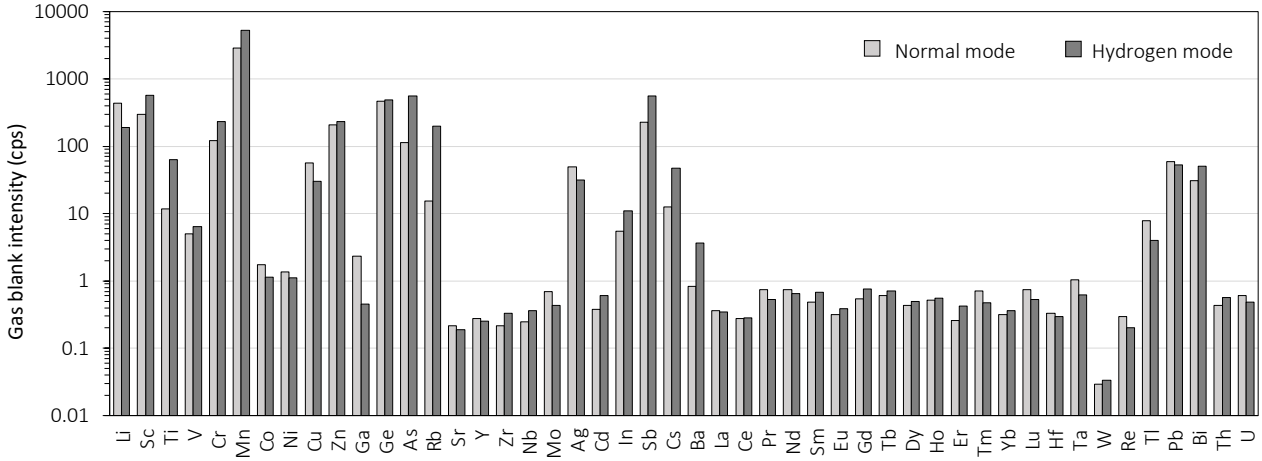


Figure 2 Gas blank intensities (cps) for normal mode (light grey) and hydrogen mode (dark grey).

Figure 3 shows the ratio between the LOD in normal and hydrogen mode plotted for the recommended isotopes for trace elements. Elements with ratios below 1 imply an increased detection limit in hydrogen mode, consistent with higher gas blanks on Sc, Ti, Rb, In and Cs, which is indicative of hydrogen-based interferences. These were also confirmed by monitoring background counts on mass 45, 47, 85, 115 and 133 while varying $H_2$ (±He) flow from 0 to 10 mL $min^{-1}$. These observations suggest that formation of complex poly atomic $H^{+}$ species are occurring and should be monitored. However, these polyatomic interferences are plasma gas related and thus remain constant and are subtracted during the background correction procedure. Elements with LOD ratios above 1.5 in Figure 3, except Zn and Cd, also show an improved gas blank signal that enhances the detection capabilities. Values between 1 and 1.5 have a minimal detection improvement because the enhanced sensitivity is being partly compensated by increased gas blanks. The LOD ranges for the analysed silicate reference glasses NIST 612 and BCR-2G, and the natural Mt Gambier olivine are shown in Table 4, Table 5 and Table 6, respectively.

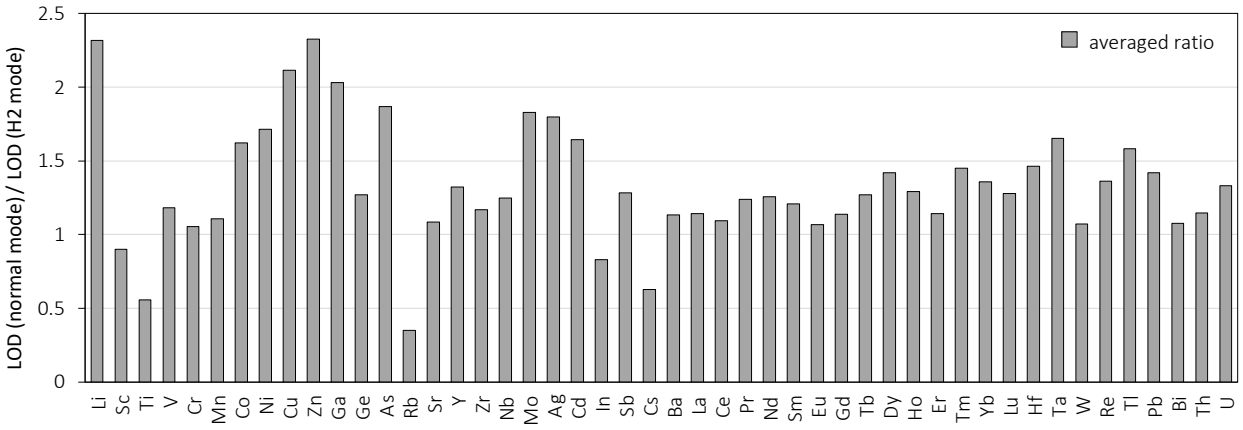


Figure 3 Ratios of limits of detection (LOD) expressed as LOD in normal mode divided by LOD in hydrogen mode. The mean values were calculated on the basis of all acquired measurements including silicate glass reference materials and the measured natural olivine.

### 2.3.2 Sensitivity and background intensities

To investigate the sensitivity enhancement for LA-ICP-MS multi-element analysis with hydrogen addition, we measured 72 masses on certified silicate glasses and natural silicate phases both in normal mode and hydrogen mode to facilitate direct comparison. Figure 4 shows the isotopic abundance-corrected sensitivity (in cps/µg $g^{-1}$) for NIST 612 (blue squares) and BCR-2G (red circles) silicate glasses for all minor and trace elements analysed. The results for analyses in hydrogen mode are shown as dark symbols and display consistently higher sensitivities for all elements in both materials compared to measurements in normal mode (light symbols). A few elements with noticeably lower abundance-corrected sensitivities ($^{66}$Zn, $^{75}$As, $^{111,112,113}$Cd and $^{121,123}$Sb) are those with higher first ionization energy (Guillong and Heinrich, 2007). The troughs in the pattern in hydrogen mode are considerably reduced for As and Cd, and almost removed for Zn and Sb. This improvement is ascribed to the higher thermal conductivity of added hydrogen gas that consequently increases electron temperature in the plasma (Murillo and Mermet, 1989; Guillong and Heinrich, 2007). Lithium shows low abundance-corrected sensitivities in both modes; however, this

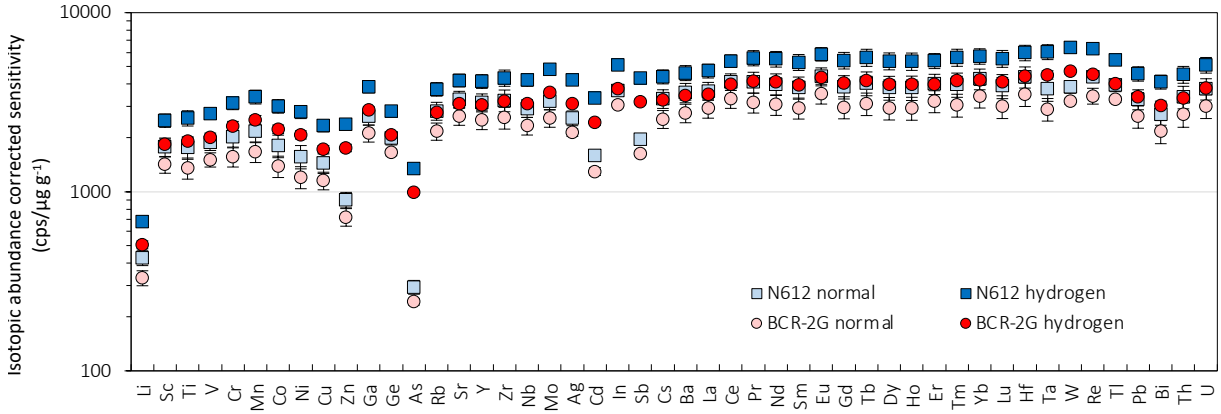


Figure 4 Isotopic abundance corrected sensitivity (cps/µg $g^{-1}$) for NIST 612 and BCR-2G. Light symbols are normal mode, and dark symbols are results for hydrogen mode showing a consistent improvement in sensitivity for all elements in both reference materials. Error bars represent 1 standard deviation, and in hydrogen mode are predominantly smaller than the symbol.

effect of a trough is due to mass bias, which is seen in a general increase in sensitivity with increasing mass. In our study, we achieved a 1.5-fold improvement in sensitivity for almost all elements, which is lower than that demonstrated by Guillong and Heinrich (2007) who showed a 2–3-fold improvement.

Figure 5 illustrates the sensitivity enhancement factor in hydrogen mode analysis as a function of the 1st ionisation potential and supports the observation above that Zn and As sensitivities are significantly improved due to higher 1st ionisation potentials. Any observed deviation from this trend is indicating possible interferences that were further investigated below.

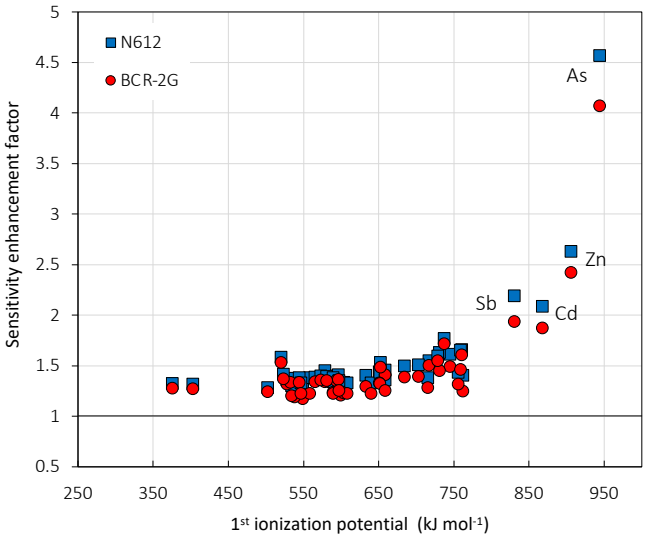


Figure 5 Sensitivity enhancement factor as a function of 1st ionisation potential demonstrating that the significant sensitivity gain for Zn and As (shown in Figure 4) is a result of the high 1st ionisation potential.

Table 2 summarises the sensitivity data on NIST 612, BCR-2G and a representative Mt Gambier olivine for both normal and hydrogen modes. The values clearly show that all sensitivities (cps/µg $g^{-1}$) improve in the hydrogen mode. Another important observation is the accompanying improvement in the calculated standard deviation (SD) for $H_2$ mode measurements, which indicates an improvement of measurement precision. The reproducibility (relative standard deviation in per cent, RSD %) for normal (solid dashes) and hydrogen modes (open squares) on RMs is displayed in Figure 6, and demonstrates a significant, mostly 3–4-fold, improvement of hydrogen mode measurements. Not only are the RSD % values in $H_2$ mode much lower, but they also span a more confined range between 2–6 %, compared to 3–16 % in normal mode analyses. The reproducibility difference in per cent between the modes shows an improvement for NIST 612 on average by 67%, for BCR-2G by 50% and for Mt Gambier olivine by 39% (Table 2).

### 2.3.3 Preferred isotopes

The investigation of the gas blank has already demonstrated that new polyatomic species involving atmospheric (O, N, C) and plasma gas elements (Ar, He, Kr) is possible and can be significant. However, as pointed out, their formation remains constant throughout the session and therefore their effect is automatically corrected through the background routine correction procedure embedded in GLITTER.

Table 2 Average abundance corrected sensitivity (cps/µg $g^{-1}$) comparison between normal (no H2) and hydrogen modes in NIST 612, BCR-2G and natural Mt Gambier olivine.

| | | NIST 612 | | | | | | | | | BCR-2G | | | | | | | | | GamTR1 olivine | | | | | | | | |
|---|---|---|---|---|---|---|---|---|---|---|---|---|---|---|---|---|---|---|---|---|---|---|---|---|---|---|---|---|
| | | no $H_2$ | | | | with $H_2$ | | | | | no $H_2$ | | | | with $H_2$ | | | | | no $H_2$ | | | | with $H_2$ | | | | |
| ***isotope*** | | Avrg | SD | RSD % | n | Avrg | SD | RSD % | n | *diff%* | Avrg | SD | RSD % | n | Avrg | SD | RSD % | n | *diff%* | Avrg | SD | RSD % | n | Avrg | SD | RSD % | n | *diff%* |
| 7 | **Li** | 429 | 42.4 | 9.87 | 6 | 683 | 16.2 | 2.37 | 6 | *-76.0* | 330 | 31.7 | 9.6 | 6 | 508 | 24.1 | 4.74 | 6 | *-50.7* | 842 | 190 | 22.6 | 3 | 1152 | 83.0 | 7.21 | 3 | *-68.1* |
| 45 | **Sc** | 1779 | 216 | 12.1 | 12 | 2505 | 140 | 5.58 | 11 | *-54.0* | 1422 | 153 | 10.8 | 12 | 1845 | 126 | 6.84 | 12 | *-36.4* | 3474 | 516 | 14.8 | 6 | 4044 | 442 | 10.9 | 6 | *-26.3* |
| 47 | **Ti** | 1770 | 252 | 14.2 | 6 | 2581 | 75.1 | 2.91 | 6 | *-79.6* | 1360 | 184 | 13.5 | 6 | 1920 | 100 | 5.23 | 6 | *-61.3* | 3521 | 793 | 22.5 | 3 | 4368 | 317 | 7.25 | 3 | *-67.8* |
| 51 | **V** | 1891 | 191 | 10.1 | 12 | 2729 | 114 | 4.18 | 11 | *-58.6* | 1512 | 138 | 9.12 | 12 | 2018 | 109 | 5.40 | 12 | *-40.8* | 3662 | 541 | 14.8 | 6 | 4474 | 377 | 8.43 | 6 | *-42.9* |
| 53 | **Cr** | 2039 | 262 | 12.9 | 6 | 3136 | 118 | 3.75 | 6 | *-70.8* | 1567 | 192 | 12.3 | 6 | 2332 | 139 | 5.94 | 6 | *-51.6* | 4039 | 914 | 22.6 | 3 | 5349 | 382 | 7 | 3 | *-68.4* |
| 55 | **Mn** | 2182 | 302 | 13.8 | 6 | 3393 | 116 | 3.43 | 6 | *-75.2* | 1677 | 220 | 13.1 | 6 | 2524 | 143 | 5.66 | 6 | *-56.9* | 4338 | 976 | 22.5 | 3 | 5771 | 413 | 7 | 3 | *-68.2* |
| 59 | **Co** | 1810 | 260 | 14.4 | 6 | 3008 | 95.8 | 3.19 | 6 | *-77.9* | 1391 | 190 | 13.6 | 6 | 2238 | 123 | 5.48 | 6 | *-59.8* | 3605 | 810 | 22.5 | 3 | 5107 | 366 | 7 | 3 | *-68.1* |
| 62 | **Ni** | 1577 | 235 | 14.9 | 6 | 2797 | 83.1 | 2.97 | 6 | *-80.0* | 1210 | 170 | 14.1 | 6 | 2080 | 110 | 5.28 | 6 | *-62.5* | 3147 | 706 | 22.4 | 3 | 4742 | 341 | 7 | 3 | *-68.0* |
| 63 | **Cu** | 1446 | 180 | 12.5 | 12 | 2339 | 79.4 | 3.40 | 11 | *-72.8* | 1156 | 130 | 11.3 | 12 | 1731 | 81.0 | 4.68 | 12 | *-58.5* | 2834 | 407 | 14.4 | 6 | 3828 | 283 | 7 | 6 | *-48.5* |
| 66 | **Zn** | 903 | 89.6 | 9.93 | 12 | 2376 | 84.7 | 3.56 | 11 | *-64.1* | 724 | 81.5 | 11.3 | 12 | 1758 | 83.9 | 4.77 | 12 | *-57.6* | 1733 | 251 | 14.5 | 6 | 3881 | 285 | 7 | 6 | *-49.2* |
| 71 | **Ga** | 2655 | 295 | 11.1 | 12 | 3860 | 122 | 3.17 | 11 | *-71.5* | 2124 | 230 | 10.8 | 12 | 2859 | 125 | 4.38 | 12 | *-59.5* | 5091 | 729 | 14.3 | 6 | 6158 | 377 | 6 | 6 | *-57.3* |
| 74 | **Ge** | 1996 | 171 | 8.56 | 6 | 2815 | 86.0 | 3.05 | 5 | *-64.3* | 1657 | 67.3 | 4.06 | 6 | 2079 | 59.8 | 2.88 | 6 | *-29.2* | 3774 | 103 | 2.74 | 3 | 4467 | 110 | 2 | 3 | *-10.5* |
| 75 | **As** | 294 | 26.0 | 8.85 | 6 | 1344 | 43.1 | 3.21 | 5 | *-63.8* | 243 | 10.1 | 4.13 | 6 | 992 | 29.8 | 3.01 | 6 | *-27.2* | 551 | 16.4 | 2.97 | 3 | 2123 | 56.4 | 3 | 3 | *-10.7* |
| 85 | **Rb** | 2834 | 325 | 11.5 | 6 | 3744 | 120 | 3.21 | 6 | *-72.0* | 2179 | 240 | 11.0 | 6 | 2785 | 153 | 5.49 | 6 | *-50.2* | 6852 | – | – | 1 | 6034 | – | – | 1 | – |
| 88 | **Sr** | 3294 | 344 | 10.4 | 12 | 4196 | 161 | 3.85 | 11 | *-63.2* | 2639 | 288 | 10.9 | 12 | 3101 | 150 | 4.85 | 12 | *-55.6* | 6586 | 1303 | 19.8 | 3 | 7657 | – | – | 1 | – |
| 89 | **Y** | 3155 | 363 | 11.5 | 12 | 4141 | 180 | 4.35 | 11 | *-62.3* | 2527 | 304 | 12.0 | 12 | 3056 | 162 | 5.30 | 12 | *-56.0* | 5966 | 1147 | 19.2 | 5 | 6554 | 852 | 13.0 | 4 | *-32.4* |
| 90 | **Zr** | 3248 | 450 | 13.9 | 12 | 4332 | 184 | 4.25 | 11 | *-69.4* | 2599 | 361 | 13.9 | 12 | 3197 | 167 | 5.22 | 12 | *-62.4* | 6479 | 1002 | 15.5 | 5 | 6748 | 722 | 10.7 | 4 | *-30.9* |
| 93 | **Nb** | 2921 | 323 | 11.0 | 12 | 4207 | 163 | 3.88 | 11 | *-64.8* | 2339 | 265 | 11.3 | 12 | 3108 | 153 | 4.92 | 12 | *-56.6* | 6382 | 944 | 14.8 | 2 | 7346 | 490 | 6.66 | 2 | *-54.9* |
| 95 | **Mo** | 3218 | 342 | 10.6 | 12 | 4833 | 156 | 3.23 | 11 | *-69.5* | 2578 | 286 | 11.1 | 12 | 3582 | 152 | 4.24 | 12 | *-61.7* | 5962 | 911 | 15.3 | 6 | 7574 | 543 | 7.17 | 6 | *-53.1* |
| 109 | **Ag** | 2583 | 244 | 9.44 | 6 | 4215 | 134 | 3.19 | 5 | *-66.3* | 2140 | 102 | 4.76 | 6 | 3111 | 92.2 | 2.96 | 6 | *-37.7* | 4990 | – | – | 1 | 6389 | – | – | 1 | – |
| 111 | **Cd** | 1593 | 112 | 7.04 | 6 | 3328 | 123 | 3.69 | 5 | *-47.6* | 1299 | 65.6 | 5.05 | 6 | 2437 | 89.5 | 3.67 | 6 | *-27.3* | 2624 | 267 | 10.2 | 3 | 5119 | 257 | 5.03 | 2 | *-50.5* |
| 115 | **In** | 3691 | 262 | 7.10 | 6 | 5109 | 169 | 3.31 | 5 | *-53.4* | 3064 | 92.7 | 3.02 | 6 | 3766 | 117 | 3.11 | 6 | *2.83* | 6840 | 191 | 2.79 | 3 | 7996 | 168 | 2.11 | 3 | *-24.6* |
| 121 | **Sb** | 1970 | 143 | 7.25 | 6 | 4319 | 160 | 3.71 | 5 | *-48.8* | 1637 | 52.8 | 3.22 | 6 | 3179 | 113 | 3.55 | 6 | *10.1* | 3663 | 93.4 | 2.55 | 3 | 6665 | 101 | 1.51 | 2 | *-40.8* |
| 133 | **Cs** | 3316 | 396 | 11.9 | 6 | 4398 | 154 | 3.50 | 6 | *-70.7* | 2549 | 292 | 11.5 | 6 | 3272 | 188 | 5.74 | 6 | *-49.9* | 5663 | 214 | 3.77 | 2 | – | – | – | 0 | – |
| 138 | **Ba** | 3583 | 444 | 12.4 | 6 | 4620 | 149 | 3.23 | 6 | *-73.9* | 2755 | 326 | 11.8 | 6 | 3437 | 189 | 5.50 | 6 | *-53.6* | 6189 | 2342 | 37.8 | 3 | 7957 | 734 | – | 2 | – |
| 139 | **La** | 3660 | 420 | 11.5 | 12 | 4737 | 187 | 3.94 | 11 | *-65.7* | 2932 | 357 | 12.2 | 12 | 3501 | 168 | 4.81 | 12 | *-60.5* | 7764 | 708 | 9.12 | 2 | 7972 | – | – | 1 | – |
| 140 | **Ce** | 4119 | 435 | 10.6 | 12 | 5377 | 193 | 3.58 | 11 | *-66.1* | 3302 | 380 | 11.5 | 12 | 3980 | 179 | 4.49 | 12 | *-61.0* | 8111 | 1207 | 14.9 | 4 | 8586 | 1116 | 13.0 | 2 | *-12.7* |
| 141 | **Pr** | 4103 | 546 | 13.3 | 6 | 5593 | 165 | 2.94 | 6 | *-77.9* | 3151 | 400 | 12.7 | 6 | 4160 | 221 | 5.30 | 6 | *-58.2* | 3448 | – | – | 1 | 10127 | – | – | 1 | – |
| 146 | **Nd** | 4000 | 552 | 13.8 | 6 | 5520 | 157 | 2.84 | 6 | *-79.5* | 3073 | 403 | 13.1 | 6 | 4107 | 212 | 5.17 | 6 | *-60.6* | – | – | – | 0 | 7058 | 1577 | 22.3 | 3 | – |
| 147 | **Sm** | 3829 | 542 | 14.1 | 6 | 5297 | 150 | 2.84 | 6 | *-79.9* | 2940 | 394 | 13.4 | 6 | 3939 | 202 | 5.13 | 6 | *-61.8* | – | – | – | 0 | 7412 | – | – | 1 | – |
| 153 | **Eu** | 4409 | 507 | 11.5 | 12 | 5876 | 247 | 4.20 | 11 | *-63.5* | 3536 | 447 | 12.6 | 12 | 4346 | 211 | 4.86 | 12 | *-61.6* | 7096 | 1699 | 23.9 | 3 | 9743 | – | – | 1 | – |
| 157 | **Gd** | 3873 | 576 | 14.9 | 6 | 5424 | 156 | 2.88 | 6 | *-80.6* | 2974 | 419 | 14.1 | 6 | 4036 | 209 | 5.18 | 6 | *-63.3* | – | – | – | 0 | 7126 | 1218 | 17.1 | 2 | – |
| 159 | **Tb** | 4052 | 616 | 15.2 | 6 | 5631 | 175 | 3.12 | 6 | *-79.5* | 3110 | 447 | 14.4 | 6 | 4189 | 226 | 5.40 | 6 | *-62.4* | 10000 | – | – | 1 | 6452 | – | – | 1 | – |
| 163 | **Dy** | 3828 | 583 | 15.2 | 6 | 5377 | 166 | 3.10 | 6 | *-79.7* | 2939 | 422 | 14.4 | 6 | 4000 | 217 | 5.41 | 6 | *-62.3* | 7824 | – | – | 1 | – | – | – | 0 | – |
| 165 | **Ho** | 3828 | 595 | 15.5 | 6 | 5356 | 184 | 3.44 | 6 | *-77.8* | 2939 | 430 | 14.6 | 6 | 3984 | 226 | 5.67 | 6 | *-61.3* | 5114 | 4651 | 90.9 | 3 | 6897 | – | – | 1 | – |
| 166 | **Er** | 4009 | 519 | 12.9 | 12 | 5392 | 261 | 4.84 | 11 | *-62.6* | 3214 | 451 | 14.0 | 12 | 3985 | 212 | 5.32 | 12 | *-62.0* | 6845 | 1302 | 19.0 | 4 | 7494 | – | – | 1 | – |
| 169 | **Tm** | 3984 | 615 | 15.4 | 6 | 5634 | 173 | 3.08 | 6 | *-80.1* | 3057 | 446 | 14.6 | 6 | 4190 | 222 | 5.31 | 6 | *-63.6* | 6073 | 945 | 15.6 | 2 | 7692 | – | – | 1 | – |
| 172 | **Yb** | 4277 | 565 | 13.2 | 12 | 5721 | 280 | 4.89 | 11 | *-63.0* | 3430 | 495 | 14.4 | 12 | 4230 | 224 | 5.30 | 12 | *-63.3* | 7565 | 1211 | 16.0 | 5 | 7635 | 0.00 | 0.00 | 2 | *-100* |
| 175 | **Lu** | 3911 | 600 | 15.4 | 6 | 5553 | 168 | 3.02 | 6 | *-80.3* | 3000 | 437 | 14.6 | 6 | 4130 | 218 | 5.27 | 6 | *-63.8* | 7482 | 1982 | 26.5 | 3 | 8860 | 432 | 4.88 | 2 | *-81.6* |
| 178 | **Hf** | 4386 | 593 | 13.5 | 12 | 5980 | 324 | 5.41 | 11 | *-60.0* | 3517 | 523 | 14.9 | 12 | 4422 | 255 | 5.76 | 12 | *-61.3* | 8215 | 1065 | 13.0 | 4 | 7188 | – | – | 1 | – |
| 181 | **Ta** | 3776 | 577 | 15.3 | 6 | 6047 | 190 | 3.15 | 6 | *-79.4* | 2899 | 418 | 14.4 | 6 | 4498 | 243 | 5.40 | 6 | *-62.5* | 6913 | 2523 | 36.5 | 2 | 7501 | – | – | 1 | – |
| 182 | **W** | 3861 | 312 | 8.08 | 6 | 6393 | 234 | 3.66 | 5 | *-54.7* | 3204 | 119 | 3.73 | 6 | 4705 | 162 | 3.44 | 6 | *-7.75* | 6291 | 720 | 11.4 | 3 | 8985 | – | – | 1 | – |
| 187 | **Re** | 4390 | 309 | 7.03 | 6 | 6301 | 233 | 3.70 | 5 | *-47.5* | 3434 | 348 | 10.1 | 6 | 4539 | 199 | 4.39 | 6 | *-56.7* | 6567 | 1843 | 28.1 | 3 | 8875 | – | – | 1 | – |
| 205 | **Tl** | 3943 | 321 | 8.15 | 6 | 5456 | 178 | 3.25 | 5 | *-60.1* | 3276 | 122 | 3.72 | 6 | 4021 | 120 | 2.99 | 6 | *-19.8* | 7059 | – | – | 1 | 7094 | – | – | 1 | – |
| 208 | **Pb** | 3290 | 420 | 12.8 | 12 | 4567 | 224 | 4.91 | 11 | *-61.6* | 2639 | 375 | 14.2 | 12 | 3397 | 186 | 5.49 | 12 | *-61.3* | 6496 | 1024 | 15.8 | 4 | 7396 | 375 | 5.08 | 5 | *-67.8* |
| 209 | **Bi** | 2722 | 370 | 13.6 | 12 | 4113 | 200 | 4.86 | 11 | *-64.2* | 2177 | 321 | 14.8 | 12 | 3042 | 164 | 5.41 | 12 | *-63.3* | 5335 | 166 | 3.12 | 3 | 6844 | 486 | 7.10 | 2 | *128* |
| 232 | **Th** | 3392 | 488 | 14.4 | 12 | 4523 | 273 | 6.04 | 11 | *-58.0* | 2720 | 429 | 15.8 | 12 | 3351 | 208 | 6.22 | 12 | *-60.6* | 6274 | 1358 | 21.6 | 5 | 6243 | 972 | 15.6 | 2 | *-28.0* |
| 238 | **U** | 3765 | 512 | 13.6 | 12 | 5110 | 301 | 5.89 | 11 | *-56.7* | 3021 | 457 | 15.1 | 12 | 3796 | 233 | 6.14 | 12 | *-59.4* | 6872 | 1267 | 18.4 | 5 | – | – | – | 0 | – |

Avrg = average abundance corrected sensitivity in cps/µg $g^{-1}$; SD = standard deviation; n = number of analyses; RSD % = relative standard deviation in per cent
diff.% = difference of RSD% values between normal and hydrogen mode measurements

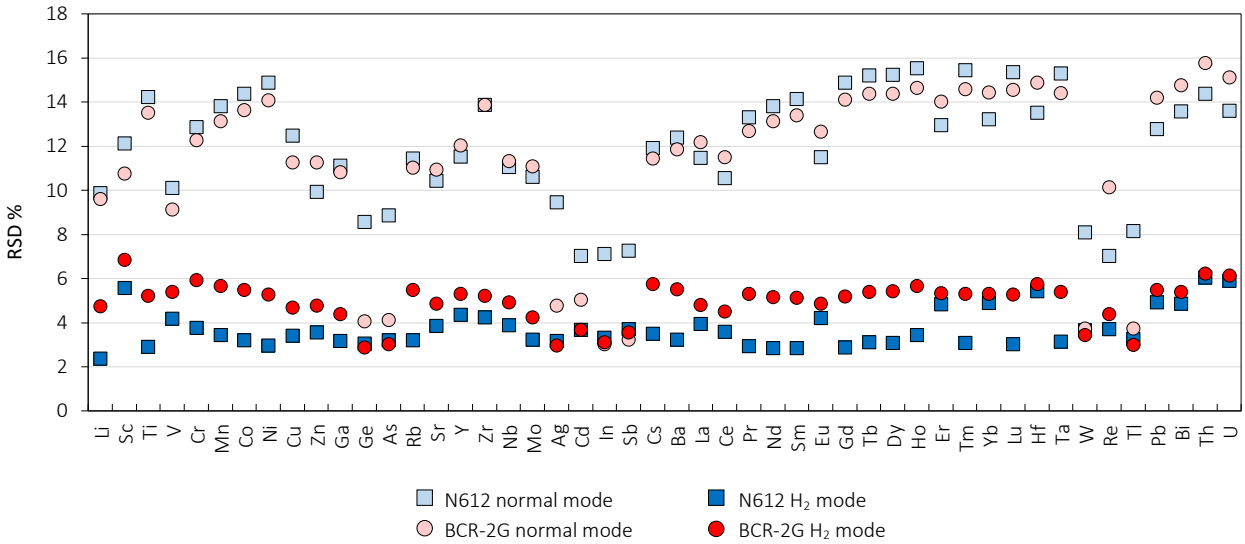


Figure 6 Sensitivity enhancement by the hydrogen mode, expressed as Relative Standard Deviation (RSD) in per cent vs. measured elements comparing both normal (dashes) and hydrogen mode (open squares) in certified reference material glasses NIST 612 and BCR-2G. Data points acquired in hydrogen mode display a significant improvement in RSD values with a much narrower range varying between 2–6 % compared to normal mode RSD varying between 3–16 %.

Multiple isotopes were measured for some elements in order to track reduction or elimination of polyatomic interferences or the new formation of new ones with the addition of hydrogen gas. Using the background corrected counts per second for each isotope we investigated if the isotopic ratio is in agreement (± 5%) with the natural abundances as reported by IUPAC (Meija *et al.*, 2016). In the case of high discrepancy, as a rule of thumb unless otherwise stated, the isotope yielding the least counts was chosen. The mass fractions were compared with certified values from the GeoReM database (http://georem.mpch-mainz.gwdg.de; Jochum *et al.*, 2005).

Table 3 shows the trace element concentrations for both methods on NIST 612, BCR-2G and the natural Mt Gambier olivine. On the basis of this data, the following isotopes are recommended for measurements using LA-ICP-MS with addition of hydrogen: $^{71}$Ga, $^{74}$Ge, $^{95}$Mo, $^{109}$Ag, $^{111}$Cd, $^{121}$Sb, $^{182}$W and $^{187}$Re. The criteria for these choices are a comparison of sensitivities between normal and hydrogen mode, as well as comparison of measured concentrations and preferred values from GeoReM database. For BCR-2G, the addition of $H_2$ considerably improves the precision (SD) and the accuracy (deviation from GeoReM preferred value), whereas NIST 612 shows a less notable improvement.

All isotope measurements on NIST 612 are very precise for both methods and were not affected by the creation of overlapping interferences. In hydrogen mode, isotope concentrations for Ga, Mo, Sb, W, and Re agree within 5 %, and for Ge, Ag and Cd within 10 % of the preferred GeoReM values. The natural basaltic rock BCR-2G shows higher variability in the concentration of multi-isotope elements than the synthetic NIST 612 reference material, which results in higher discrepancy between the methods as well as some higher deviations from literature values.

Table 3 Recommended isotopes (*) on the basis of measured certified RM concentrations and deviations from GeoReM preferred values, and occurrences of polyatomic interferences.

| | | NIST 612 | | | | | | | | | | | BCR-2G | | | | | | | | | | GamTR1 olivine | | | | | |
|---|---|---|---|---|---|---|---|---|---|---|---|---|---|---|---|---|---|---|---|---|---|---|---|---|---|---|---|---|
| | | no H2 | | | | | with H2 | | | | | | no H2 | | | | | with H2 | | | | | no H2 | | | with H2 | | |
| | *GeoReM* | Avrg | SD | n | RSD% | diff.% | Avrg | SD | n | RSD% | diff.% | *GeoReM* | Avrg | SD | n | RSD% | diff.% | Avrg | SD | n | RSD% | diff.% | Avrg | SD | n | Avrg | SD | n |
| **Ga69** | *36.9* | 36.4 | 0.586 | 12 | 1.61 | -1.47 | 36.4 | 0.537 | 11 | 1.47 | -1.31 | *23* | 43.0 | 4.87 | 12 | 11.3 | **87.0** | 87.8 | 3.33 | 12 | 3.79 | **282** | 0.0256 | 0.00578 | 6 | 0.0354 | 0.00360 | 6 |
| **Ga71*** | *36.9* | 36.8 | 0.695 | 12 | 1.89 | -0.233 | 36.5 | 0.468 | 11 | 1.28 | -1.19 | *23* | 21.7 | 0.575 | 12 | 2.65 | -5.57 | 21.9 | 0.380 | 12 | 1.73 | -4.71 | 0.0231 | 0.0158 | 6 | 0.00847 | 0.00287 | 6 |
| **Ge72** | *36.1* | 39.8 | 0.680 | 6 | 1.71 | **10.3** | 39.3 | 0.879 | 5 | 2.24 | 8.75 | *1.5* | 3.03 | 0.650 | 6 | 21.5 | **102** | 2.87 | 0.0967 | 6 | 3.36 | **91.6** | 1.62 | 0.219 | 3 | 1.63 | 0.0811 | 3 |
| **Ge73** | *36.1* | 40.3 | 0.785 | 6 | 1.95 | **11.7** | 38.4 | 0.953 | 5 | 2.48 | 6.37 | *1.5* | 2.96 | 1.03 | 6 | 35.0 | **97.3** | 3.06 | 0.118 | 6 | 3.84 | **104** | 1.03 | 0.0921 | 3 | 0.916 | 0.118 | 3 |
| **Ge74*** | *36.1* | 39.9 | 0.818 | 6 | 2.05 | **10.4** | 39.3 | 0.570 | 5 | 1.45 | 8.87 | *1.5* | 2.21 | 0.956 | 6 | 43.3 | **47.2** | 1.66 | 0.0844 | 6 | 5.10 | **10.4** | 0.876 | 0.0186 | 3 | 0.836 | 0.103 | 3 |
| **Mo95*** | *37.4* | 35.7 | 1.65 | 12 | 4.62 | -4.52 | 36.7 | 0.490 | 11 | 1.33 | -1.79 | *270* | 254 | 5.73 | 12 | 2.26 | -5.87 | 250 | 3.67 | 12 | 1.47 | -7.58 | 0.0143 | 0.00427 | 6 | 0.0115 | 0.00287 | 6 |
| **Mo97** | *37.4* | 36.9 | 0.904 | 6 | 2.45 | -1.36 | 36.7 | 0.849 | 5 | 2.31 | -1.80 | *270* | 258 | 4.10 | 6 | 1.59 | -4.50 | 251 | 3.88 | 6 | 1.54 | -6.95 | 0.0189 | 0.0147 | 3 | 0.0154 | 0.00985 | 3 |
| **Mo98** | *37.4* | 35.9 | 1.60 | 12 | 4.45 | -3.95 | 36.7 | 0.709 | 11 | 1.93 | -1.84 | *270* | 255 | 6.40 | 12 | 2.51 | -5.57 | 250 | 4.02 | 12 | 1.61 | -7.42 | 0.157 | 0.0242 | 6 | 0.175 | 0.0116 | 6 |
| **Mo100** | *37.4* | 36.8 | 0.853 | 6 | 2.32 | -1.57 | 36.5 | 0.927 | 5 | 2.54 | -2.49 | *270* | 259 | 5.60 | 6 | 2.16 | -3.97 | 251 | 2.10 | 6 | 0.837 | -7.14 | 0.197 | 0.0225 | 3 | 0.163 | 0.0200 | 3 |
| **Ag107** | *22* | 20.8 | 0.655 | 6 | 3.15 | -5.57 | 20.2 | 0.423 | 5 | 2.09 | -7.99 | *0.5* | 0.366 | 0.130 | 6 | 35.6 | **-26.8** | 1.03 | 0.124 | 6 | 12.0 | **107** | 0.0195 | | 1 | | | 0 |
| **Ag109*** | *22* | 20.9 | 0.617 | 6 | 2.96 | -5.14 | 20.4 | 0.508 | 5 | 2.50 | -7.42 | *0.5* | 0.337 | 0.0885 | 6 | 26.2 | **-32.5** | 1.02 | 0.132 | 6 | 12.9 | **104** | 0.0129 | | 1 | 0.00390 | | 1 |
| **Cd111*** | *28.1* | 27.5 | 1.22 | 6 | 4.44 | -2.24 | 25.2 | 1.88 | 5 | 7.44 | **-10.3** | *0.2* | 0.283 | 0.225 | 6 | 79.6 | **41.3** | 0.183 | 0.0317 | 6 | 17.4 | -8.67 | 0.0191 | 0.0112 | 3 | 0.0275 | 0.00078 | 2 |
| **Cd112** | *28.1* | 26.7 | 0.766 | 6 | 2.87 | -5.01 | 24.9 | 1.46 | 5 | 5.87 | **-11.3** | *0.2* | 0.490 | 0.0859 | 6 | 17.5 | **145** | 0.331 | 0.0324 | 6 | 9.79 | **65.6** | 0.159 | 0.0288 | 3 | 0.0801 | 0.0245 | 3 |
| **Cd114** | *28.1* | 26.8 | 1.06 | 6 | 3.97 | -4.58 | 25.3 | 1.68 | 5 | 6.67 | **-10.1** | *0.2* | 0.375 | 0.100 | 6 | 26.8 | **87.3** | 0.274 | 0.0402 | 6 | 14.6 | **37.2** | 0.0910 | 0.0132 | 3 | 0.0706 | 0.00917 | 3 |
| **Sb121*** | *34.7* | 33.6 | 0.851 | 6 | 2.54 | -3.30 | 33.3 | 0.737 | 5 | 2.22 | -4.13 | *0.35* | 0.467 | 0.193 | 6 | 41.3 | **33.5** | 0.301 | 0.0131 | 6 | 4.35 | **-14.0** | 0.0307 | 0.0137 | 3 | 0.0282 | 0.0163 | 2 |
| **Sb123** | *34.7* | 33.5 | 0.662 | 6 | 1.98 | -3.44 | 33.4 | 0.725 | 5 | 2.17 | -3.74 | *0.35* | 0.653 | 0.541 | 6 | 82.9 | **86.4** | 0.258 | 0.0362 | 6 | 14.0 | **-26.4** | 0.0395 | 0.0120 | 2 | 0.0308 | 0.00953 | 3 |
| **W182*** | *38* | 38.5 | 0.745 | 6 | 1.94 | 1.22 | 38.8 | 0.892 | 5 | 2.30 | 2.08 | *0.5* | 0.573 | 0.107 | 6 | 18.6 | **14.6** | 0.486 | 0.0333 | 6 | 6.86 | -2.80 | 0.00214 | 0.00099 | 3 | 0.00168 | | 1 |
| **W183** | *38* | 38.6 | 0.626 | 6 | 1.62 | 1.63 | 38.6 | 0.967 | 5 | 2.51 | 1.51 | *0.5* | 0.550 | 0.102 | 6 | 18.6 | 9.90 | 0.522 | 0.0365 | 6 | 6.98 | 4.40 | 0.0120 | | 1 | 0.00245 | 0.00021 | 2 |
| **W184** | *38* | 38.6 | 0.870 | 6 | 2.25 | 1.57 | 38.6 | 1.29 | 5 | 3.34 | 1.49 | *0.5* | 0.574 | 0.146 | 6 | 25.5 | **14.8** | 0.490 | 0.0265 | 6 | 5.41 | -2.07 | 0.0118 | | 1 | | | 0 |
| **Re185** | *6.63* | 6.72 | 0.116 | 6 | 1.72 | 1.31 | 6.66 | 0.282 | 5 | 4.23 | 0.513 | *0.01* | 0.00917 | 0.00734 | 6 | 80.1 | **47.8** | 0.00438 | 0.00165 | 4 | 37.6 | **-29.4** | 0.00205 | | 1 | 0.00058 | | 1 |
| **Re187*** | *6.63* | 6.73 | 0.174 | 6 | 2.58 | 1.53 | 6.72 | 0.243 | 5 | 3.61 | 1.33 | *0.01* | 0.0121 | 0.00917 | 6 | 75.8 | **95.2** | 0.00677 | 0.00273 | 6 | 40.3 | 9.17 | 0.00066 | 0.00045 | 3 | 0.00054 | | 1 |

Bold numbers are >10% difference between measured concentrations and GeoReM preferred reference values.

Avrg = average concentration in µg $g^{-1}$; SD = standard deviation; n = number of analyses; RSD % = relative standard deviation in per cent; diff.% = difference in per cent with GeoReM preferred values

Based on these variations, we recommend employing the isotopes marked with an asterisk in Table 3 when using hydrogen mode analysis. The two Ga isotopes measured on NIST 612 are in good agreement with reference values in both modes, normal and hydrogen. However, on BCR-2G the isotope $^{71}$Ga is in good agreement with reference values and is preferred over $^{69}$Ga. The concentration on the latter isotope increases from ~43 µg g$^{-1}$ in normal mode to ~88 µg g$^{-1}$ in hydrogen mode, thus being up to 2-fold and 4-fold higher, respectively, compared to GeoReM value of 23 µg g$^{-1}$ and measured $^{71}$Ga ~22 µg g$^{-1}$ in both modes.

Germanium shows no big difference between the three measured isotopes in both modes on NIST 612 with deviations from GeoReM preferred values being <8 % in hydrogen mode. However, BCR-2G values show an explicit improvement on mass $^{74}$Ge in hydrogen mode, with mass fraction decreasing from 2.2 µg g$^{-1}$ in normal mode to 1.6 µg g$^{-1}$ in hydrogen mode, thus decreasing the deviation from reference values from 32 % to 9 %, respectively. Measurements on olivines reinforce the choice of $^{74}$Ge with concentrations of 0.8 µg g$^{-1}$, compared to 1.6 µg g$^{-1}$ and 0.9 µg g$^{-1}$ on Ge 72 and 73, respectively.

The four measured Mo isotopes display comparable results for both RM glasses in both modes and show a deviation from reference values in hydrogen mode only by <2 % on NIST 612 and <8 % on BCR-2G. Olivine concentrations on the other hand, differ between the lighter $^{95,97}$Mo and the heavier $^{98,100}$Mo isotopes by factor 10 (0.011 and 0.015 µg g$^{-1}$, 0.175 and 0.163 µg g$^{-1}$, respectively) and the precision (SD) of 0.003 µg g$^{-1}$ is by far best on $^{95}$Mo, hence, it is the recommended isotope (Table 3).

The two silver isotopes 107 and 109 in NIST 612 are very homogeneous in both modes and are in good agreement with GeoReM values with a slight increase from ~5.6 % in normal mode to ~8.3 % in hydrogen mode. BCR-2G measurements show no big difference in concentration between both isotopes, however, the data acquired in normal mode (~0.35 µg g$^{-1}$) is in better agreement with the GeoReM literature data (0.5 µg g$^{-1}$), than in hydrogen mode (~1.0 µg g$^{-1}$). The olivine results in this case are underrepresented and don't show a clear result, however, we chose the isotope $^{109}$Ag to be a good recommendation.

Cadmium concentrations on NIST 612 show not much variation between the three measured isotopes (~27 µg g$^{-1}$) and are in good agreement with literature value (28.1 µg g$^{-1}$; <5 % deviation) in normal mode but concentrations in hydrogen mode are lower (~25 µg g$^{-1}$) and thus deviate by ~12 % from the literature. BCR- 2G on the other hand, show an explicit improvement on mass $^{111}$Cd, where the concentration decreases from 0.28 µg g$^{-1}$ in normal mode to 0.18 µg g$^{-1}$ in hydrogen mode, thus improves the deviation from 29 % to 9.5 %, respectively. Results in olivine support the recommendation of $^{111}$Cd by showing by far the lowest concentration and the best precision (0.0001 µg g$^{-1}$).

Antimony results in NIST 612 show no big difference between the two measured isotopes and deviate from preferred GeoReM values by <4 % in both modes. BCR-2G on the other hand, shows more variability in normal mode between $^{121}$Sb and $^{123}$Sb with concentrations of 0.47 and 0.65 µg g$^{-1}$, as well as higher deviations from literature values, 25 % and 46 %, respectively. Hydrogen mode analyses enhance the precision and accuracy, with concentrations dropping to 0.30 µg g$^{-1}$ for $^{121}$Sb and 0.26 µg g$^{-1}$ for $^{123}$Sb,

thus decreasing the difference with GeoReM data to 16 % and 36 %, respectively. Other criteria of choice for $^{121}$Sb as the recommended isotope is its notable higher sensitivity in hydrogen mode (1819 cps/µg g$^{-1}$, compared to $^{123}$Sb with 1416 cps/µg g$^{-1}$).

The three measured tungsten isotopes 182, 183 and 184 in NIST 612 are for both modes very consistent in their concentration (~38.6 µg g$^{-1}$) and in their agreement with GeoReM value (deviation <2 %). However, in BCR-2G $^{183}$W seems to have the most accurate measurement in the normal mode, but in hydrogen mode isotopes 182 and 184 are closer to the GeoReM preferred value and differ by 2.9 % and 2.1 %, respectively. Also, the sensitivities in $^{182}$W and $^{184}$W are much higher compared to $^{183}$W, with 1250, 1450 and 660 cps/µg g$^{-1}$, respectively. In this study, we recommend using $^{182}$W, which displays 6-fold lower concentrations on the natural olivine grain in normal mode compared to $^{183}$W and $^{184}$W (0.0021, 0.0120 and 0.0118 µg g$^{-1}$, respectively).

Rhenium isotopes 185 and 187 in NIST 612 show no significant variation nor improvement for both modes with mass fractions deviating by less than 1.5 % from published GeoReM value (6.63 µg g$^{-1}$). The natural basaltic BCR-2G glass on the other hand with a much lower GeoReM preferred value of 0.0062 µg g$^{-1}$ shows a clear hydrogen advantage for $^{187}$Re with a measured concentration of 0.0068 µg g$^{-1}$, with an improvement in both, precision (0.0121 µg g$^{-1}$ in normal mode and 0.0027 µg g$^{-1}$ in hydrogen mode) and accuracy (49 % in normal mode and 8.4 % deviation in hydrogen mode).

It is noteworthy, that in hydrogen mode the precision and reproducibility for all measured isotopes on BCR-2G shows a significant improvement, whereas NIST 612 shows an improvement only for half of the isotopes.

### 2.3.4 Accuracy and precision

The acquired concentrations for normal and hydrogen mode analyses for NIST 612 and BCR-2G are shown in Table 4 and Table 5, respectively. Even though we cannot report a great improvement in precision and accuracy on the synthetic NIST 612 glass in hydrogen mode, we can see no disadvantage compared to the analyses without hydrogen. All values agree within <5 % with reference values, with the exception of Sc, Ge, As, Ag, Cd, In and Bi that agree within 6–12 %, with only Tl deviating by 24 %. The results on the natural volcanic BCR-2G glass show a larger enhancement in both precision and accuracy in hydrogen mode, although, more values deviate by more than 10 % from GeoReM preferred values than with the more thoroughly studied NIST 612 glass. This high discrepancy may be due to differences in matrix effects between synthetic NIST 612 and basaltic BCR-2G glasses.

The greater improvements in hydrogen mode for BCR-2G than NIST 612 are particularly important for elements with low concentrations. The NIST 612 glass is uniformly doped with many trace elements in the concentration range of 35–40 µg g$^{-1}$, for which the improvements due to hydrogen addition are not noticeable. Examples for elements with lower (and different) concentrations for which the hydrogen mode is shown to be especially effective are [1] Ge, which returns 1.66 µg g$^{-1}$ in hydrogen mode compared to the

GeoReM value of 1.5 µg $g^{-1}$ and 2.2 µg $g^{-1}$ in normal mode, and [2] Re, for which the GeoReM value of 0.0062 µg $g^{-1}$ is matched much better in hydrogen mode (0.0068 µg $g^{-1}$), than in normal mode (0.0121 µg $g^{-1}$; Table 5).

The preliminary measurements in normal and hydrogen mode on the natural Mt Gambier olivine sample are shown in Table 6. The results are very insightful and elements with statistically relevant measurements show an improvement in hydrogen mode in the precision (SD), LOD and concentrations. An example for precision enhancement is displayed in Ga enhancing from 0.0158 to 0.0029 µg $g^{-1}$, in In

Table 4 NIST 612 concentrations (µg $g^{-1}$) acquired in normal and hydrogen mode. Measurement results are compared to published preferred GeoReM abundances.

| *NIST 612* | | normal mode | | | | | | hydrogen mode | | | | | |
|---|---|---|---|---|---|---|---|---|---|---|---|---|---|
| | *GeoReM* | Avrg | SD | n | RSD % | diff.% | LOD (range) | Avrg | SD | n | RSD % | diff.% | LOD (range) |
| **Li** | *40.2* | 40.2 | 0.868 | 6 | 2.16 | 0.00415 | 0.0916-0.119 | 40.6 | 0.680 | 6 | 1.68 | 0.908 | 0.0432-0.0504 |
| **Sc** | *39.9* | 43.1 | 3.87 | 12 | 8.98 | 8.02 | 0.0189-0.0376 | 44.7 | 1.59 | 11 | 3.57 | **12.0** | 0.0247-0.0378 |
| **Ti** | *44.0* | 43.7 | 1.84 | 6 | 4.22 | -0.742 | 0.0469-0.0918 | 43.4 | 2.23 | 6 | 5.12 | -1.27 | 0.11-0.135 |
| **V** | *38.8* | 38.7 | 0.786 | 12 | 2.03 | -0.226 | 0.00128-0.00731 | 38.7 | 0.603 | 11 | 1.56 | -0.159 | 0.00136-0.00376 |
| **Cr** | *36.4* | 33.8 | 1.22 | 6 | 3.61 | -7.22 | 0.149-0.171 | 35.7 | 0.775 | 6 | 2.17 | -1.89 | 0.145-0.163 |
| **Mn** | *38.7* | 37.9 | 0.584 | 6 | 1.54 | -1.95 | 0.0671-0.0786 | 38.1 | 0.367 | 6 | 0.963 | -1.43 | 0.0604-0.0656 |
| **Co** | *35.5* | 35.0 | 0.345 | 6 | 0.984 | -1.35 | 0.00153-0.00436 | 35.0 | 0.506 | 6 | 1.45 | -1.46 | 0.00122-0.00202 |
| **Cu** | *37.8* | 39.9 | 2.29 | 12 | 5.75 | 5.46 | 0.0144-0.0202 | 38.1 | 1.36 | 11 | 3.57 | 0.887 | 0.00638-0.0093 |
| **Zn** | *39.1* | 36.6 | 1.22 | 12 | 3.33 | -6.32 | 0.115-0.14 | 37.1 | 0.645 | 11 | 1.74 | -5.16 | 0.0417-0.062 |
| **Ga** | *36.9* | 36.8 | 0.695 | 12 | 1.89 | -0.233 | 0.00243-0.00503 | 36.5 | 0.468 | 11 | 1.28 | -1.19 | 0.00116-0.00237 |
| **Ge** | *36.1* | 39.9 | 0.818 | 6 | 2.05 | **10.4** | 0.0521-0.086 | 39.3 | 0.570 | 5 | 1.45 | 8.87 | 0.0361-0.064 |
| **As** | *35.7* | 32.8 | 1.20 | 6 | 3.68 | -8.24 | 0.0472-0.0956 | 31.7 | 0.630 | 5 | 1.99 | **-11.2** | 0.0234-0.0472 |
| **Rb** | *31.4* | 31.5 | 0.406 | 6 | 1.29 | 0.409 | 0.00318-0.00351 | 31.9 | 0.252 | 6 | 0.792 | 1.44 | 0.00845-0.00947 |
| **Sr** | *78.4* | 78.1 | 1.60 | 12 | 2.04 | -0.323 | 0.00074-0.00081 | 79.6 | 1.83 | 11 | 2.29 | 1.52 | 0.0005-0.00077 |
| **Y** | *38.3* | 38.7 | 0.950 | 12 | 2.46 | 0.964 | 0.00049-0.00076 | 39.1 | 1.31 | 11 | 3.36 | 1.97 | 0.00031-0.00044 |
| **Zr** | *37.9* | 37.7 | 1.09 | 12 | 2.88 | -0.587 | 0.00065-0.00115 | 39.1 | 1.17 | 11 | 3.00 | 3.19 | 0.00123-0.00123 |
| **Nb** | *38.9* | 38.3 | 0.730 | 12 | 1.90 | -1.46 | 0.00053-0.00091 | 39.0 | 0.880 | 11 | 2.26 | 0.243 | 0 |
| **Mo** | *37.4* | 35.7 | 1.65 | 12 | 4.62 | -4.52 | 0.00199-0.00502 | 36.7 | 0.490 | 11 | 1.33 | -1.79 | 0.00109-0.00167 |
| **Ag** | *22.0* | 20.9 | 0.617 | 6 | 2.96 | -5.14 | 0.0079-0.0125 | 20.4 | 0.508 | 5 | 2.50 | -7.42 | 0.00392-0.0066 |
| **Cd** | *28.1* | 27.5 | 1.22 | 6 | 4.44 | -2.24 | 0.00622-0.00798 | 25.2 | 1.88 | 5 | 7.44 | **-10.3** | 0.00401-0.00516 |
| **In** | *38.9* | 36.8 | 0.621 | 6 | 1.69 | -5.45 | 0.00051-0.00174 | 36.5 | 0.516 | 5 | 1.41 | -6.24 | 0.00083-0.00164 |
| **Sb** | *34.7* | 33.6 | 0.851 | 6 | 2.54 | -3.30 | 0.0192-0.0345 | 33.3 | 0.737 | 5 | 2.22 | -4.13 | 0.0133-0.0236 |
| **Cs** | *42.7* | 41.0 | 0.437 | 6 | 1.07 | -4.08 | 0.00128-0.00275 | 41.9 | 0.261 | 6 | 0.622 | -1.87 | 0.00265-0.003 |
| **Ba** | *39.3* | 39.1 | 0.872 | 6 | 2.23 | -0.577 | 0.00652-0.00689 | 39.7 | 0.771 | 6 | 1.94 | 0.988 | 0.00246-0.00538 |
| **La** | *36.0* | 36.1 | 0.666 | 12 | 1.85 | 0.329 | 0.00024-0.00059 | 36.7 | 1.15 | 11 | 3.14 | 1.93 | 0.00018-0.00025 |
| **Ce** | *38.4* | 38.4 | 0.587 | 12 | 1.53 | 0.117 | 0.00035-0.00072 | 38.9 | 0.795 | 11 | 2.04 | 1.28 | 0.00022-0.00051 |
| **Pr** | *37.9* | 37.6 | 0.414 | 6 | 1.10 | -0.871 | 0.00024-0.00038 | 38.1 | 0.355 | 6 | 0.931 | 0.554 | 0.00022-0.00023 |
| **Nd** | *35.5* | 35.1 | 0.537 | 6 | 1.53 | -1.16 | 0.00256-0.00262 | 35.7 | 0.287 | 6 | 0.805 | 0.446 | 0.00069-0.00189 |
| **Sm** | *37.7* | 37.6 | 0.646 | 6 | 1.72 | -0.195 | 0.0013-0.00221 | 37.8 | 0.396 | 6 | 1.05 | 0.371 | 0.00113-0.00165 |
| **Eu** | *35.6* | 35.7 | 0.615 | 12 | 1.72 | 0.220 | 0.00048-0.00075 | 36.2 | 0.968 | 11 | 2.67 | 1.75 | 0.0003-0.00048 |
| **Gd** | *37.3* | 37.7 | 0.606 | 6 | 1.61 | 1.15 | 0.00114-0.00208 | 38.1 | 0.576 | 6 | 1.51 | 2.04 | 0.00106-0.00144 |
| **Tb** | *37.6* | 36.7 | 0.636 | 6 | 1.73 | -2.45 | 0.00024-0.00045 | 37.1 | 0.636 | 6 | 1.71 | -1.24 | 0.00012-0.00023 |
| **Dy** | *35.5* | 35.6 | 0.519 | 6 | 1.46 | 0.244 | 0.00073-0.00134 | 35.8 | 0.588 | 6 | 1.64 | 0.850 | 0.00067-0.00103 |
| **Ho** | *38.3* | 37.7 | 0.650 | 6 | 1.72 | -1.62 | 0.00015-0.00038 | 37.9 | 0.774 | 6 | 2.04 | -1.03 | 0.00014-0.0002 |
| **Er** | *38.0* | 38.5 | 0.690 | 12 | 1.79 | 1.37 | 0.00066-0.00116 | 39.3 | 1.57 | 11 | 3.99 | 3.32 | 0.00041-0.00094 |
| **Tm** | *36.8* | 36.7 | 0.665 | 6 | 1.81 | -0.272 | 0.00033-0.00051 | 36.8 | 0.729 | 6 | 1.98 | -0.0679 | 0.00015-0.00015 |
| **Yb** | *39.2* | 38.5 | 0.851 | 12 | 2.21 | -1.74 | 0.00188-0.00318 | 39.2 | 1.47 | 11 | 3.74 | 0.107 | 0.00118-0.00189 |
| **Lu** | *37.0* | 36.5 | 0.580 | 6 | 1.59 | -1.31 | 0.00047-0.00058 | 36.8 | 0.797 | 6 | 2.17 | -0.505 | 0.00023-0.00023 |
| **Hf** | *36.7* | 37.2 | 0.848 | 12 | 2.28 | 1.31 | 0.00089-0.00124 | 37.9 | 1.45 | 11 | 3.82 | 3.37 | 0.00075-0.00108 |
| **Ta** | *37.6* | 37.2 | 0.555 | 6 | 1.49 | -1.05 | 0.00015-0.0007 | 37.4 | 0.783 | 6 | 2.09 | -0.634 | 0.00009-0.00017 |
| **W** | *38.0* | 38.5 | 0.745 | 6 | 1.94 | 1.22 | 0.00091-0.00091 | 38.8 | 0.892 | 5 | 2.30 | 2.08 | 0 |
| **Re** | *6.6* | 6.73 | 0.174 | 6 | 2.58 | 1.53 | 0.00032-0.00051 | 6.72 | 0.243 | 5 | 3.61 | 1.33 | 0.00016-0.00023 |
| **Tl** | *14.9* | 14.1 | 0.491 | 6 | 3.49 | -5.45 | 0.00074-0.00363 | 11.3 | 0.728 | 5 | 6.46 | **-24.4** | 0.00045-0.00217 |
| **Pb** | *38.6* | 36.4 | 1.92 | 12 | 5.29 | -5.69 | 0.000572-0.00909 | 36.8 | 1.18 | 11 | 3.20 | -4.51 | 0.00376-0.00689 |
| **Bi** | *30.2* | 32.3 | 1.85 | 12 | 5.71 | 7.11 | 0.00168-0.00613 | 32.9 | 0.855 | 11 | 2.60 | 8.97 | 0.00177-0.00499 |
| **Th** | *37.8* | 37.8 | 0.739 | 12 | 1.95 | 0.099 | 0.00044-0.00077 | 38.6 | 1.46 | 11 | 3.79 | 2.01 | 0.0002-0.00063 |
| **U** | *37.4* | 37.3 | 0.789 | 12 | 2.12 | -0.332 | 0.00033-0.00054 | 37.9 | 0.797 | 11 | 2.10 | 1.49 | 0.00023-0.00038 |

Bold numbers are >10% difference between measured concentrations and GeoReM preferred reference values.
Avrg = average concentration in µg $g^{-1}$; SD = standard deviation; n = number of analyses; RSD % = relative standard deviation in per cent; diff.% = difference in per cent with GeoReM preferred values; LOD = limit of detection.

from 0.0051 to 0.0007 µg $g^{-1}$ and in Yb from 0.0072 to 0.0004 µg $g^{-1}$. The improvement in LOD values enables the acquisition of ultra-trace elements that were below the limit of detection in normal mode measurements but are now accessible in hydrogen mode, e.g., both Nd and Gd detection limits are ranging from 1–2 ng $g^{-1}$ in normal mode with concentrations being below detection limit and in $H_2$ mode LODs decrease to ranges between 0.6–1.0 ng $g^{-1}$ and 0.7–1.3 ng $g^{-1}$, respectively.

Many ultra-trace element concentrations show lower values when $H_2$ is used. As shown for the basaltic reference material BCR-2G the lower abundances for some elements (e.g., Ga, Ge, Lu, Re, Pb etc.) with added hydrogen gas are not a deterioration from the GeoReM preferred value but represent a more

Table 5 BCR-2G concentrations (µg $g^{-1}$) acquired in normal and hydrogen mode. Measurement results are compared to published preferred GeoReM abundances.

| *BCR-2G* | | normal mode | | | | | | hydrogen mode | | | | | |
|---|---|---|---|---|---|---|---|---|---|---|---|---|---|
| | *GeoReM* | Avrg | SD | n | RSD % | diff.% | LOD (range) | Avrg | SD | n | RSD % | diff.% | LOD (range) |
| **Li** | *9* | 9.30 | 0.496 | 6 | 5.34 | 3.28 | 0.117-0.164 | 8.89 | 0.432 | 6 | 4.86 | -1.19 | 0.0555-0.0639 |
| **Sc** | *33* | 33.0 | 2.52 | 12 | 7.63 | 0.104 | 0.0219-0.0457 | 34.7 | 1.31 | 12 | 3.78 | 5.07 | 0.0322-0.0531 |
| **Ti** | *14100* | 12627 | 180 | 6 | 1.43 | **-10.4** | 0.0803-0.133 | 12596 | 208 | 6 | 1.65 | **-10.7** | 0.122-0.183 |
| **V** | *425* | 423 | 12.3 | 12 | 2.91 | -0.576 | 0.0024-0.0082 | 414 | 5.49 | 12 | 1.33 | -2.64 | 0.00197-0.00538 |
| **Cr** | *17* | 14.9 | 1.33 | 6 | 8.92 | **-12.1** | 0.182-0.257 | 15.0 | 1.14 | 6 | 7.57 | **-11.7** | 0.186-0.216 |
| **Mn** | *1550* | 1466 | 29.8 | 6 | 2.04 | -5.43 | 0.0879-0.104 | 1525 | 24.8 | 6 | 1.63 | -1.62 | 0.0773-0.0902 |
| **Co** | *38* | 37.2 | 0.664 | 6 | 1.79 | -2.07 | 0.002-0.00304 | 37.0 | 0.932 | 6 | 2.52 | -2.58 | 0.0029-0.0029 |
| **Cu** | *21* | 17.4 | 0.911 | 12 | 5.22 | **-16.9** | 0.017-0.0239 | 16.4 | 0.565 | 12 | 3.45 | **-22.1** | 0.0075-0.0144 |
| **Zn** | *125* | 151 | 5.49 | 12 | 3.64 | **20.6** | 0.127-0.168 | 145 | 5.46 | 12 | 3.76 | **16.4** | 0.0572-0.0853 |
| **Ga** | *23* | 21.7 | 0.575 | 12 | 2.65 | -5.57 | 0.0019-0.00559 | 21.9 | 0.380 | 12 | 1.73 | -4.71 | 0.00122-0.00221 |
| **Ge** | *1.5* | 2.21 | 0.956 | 6 | 43.3 | **47.2** | 0.0624-0.0825 | 1.66 | 0.0844 | 6 | 5.10 | **10.4** | 0.0472-0.0676 |
| **As** | – | 1.13 | 0.135 | 6 | 11.9 | – | 0.0532-0.087 | 0.852 | 0.0920 | 6 | 10.8 | – | 0.0326-0.0475 |
| **Rb** | *47* | 47.6 | 0.604 | 6 | 1.27 | 1.37 | 0.0032-0.00499 | 46.9 | 0.660 | 6 | 1.41 | -0.305 | 0.0115-0.0127 |
| **Sr** | *342* | 323 | 10.7 | 12 | 3.30 | -5.56 | 0 | 323 | 9.54 | 12 | 2.95 | -5.52 | 0.00103-0.00103 |
| **Y** | *35* | 29.9 | 1.20 | 12 | 4.01 | **-14.6** | 0.0006-0.00055 | 30.1 | 1.23 | 12 | 4.08 | **-14.0** | 0.00061-0.00087 |
| **Zr** | *184* | 177 | 42.4 | 12 | 23.9 | -3.82 | 0.0012-0.00124 | 163 | 6.62 | 12 | 4.06 | **-11.4** | 0.0008-0.00104 |
| **Nb** | *12.5* | 11.5 | 0.274 | 12 | 2.38 | -8.13 | 0.0007-0.0007 | 11.5 | 0.335 | 12 | 2.91 | -8.10 | 0 |
| **Mo** | *270* | 254 | 5.73 | 12 | 2.26 | -5.87 | 0.0027-0.00447 | 250 | 3.67 | 12 | 1.47 | -7.58 | 0.00164-0.0022 |
| **Ag** | *0.5* | 0.337 | 0.0885 | 6 | 26.2 | **-32.5** | 0.006-0.0135 | 1.02 | 0.132 | 6 | 12.9 | **104** | 0.00548-0.00792 |
| **Cd** | *0.2* | 0.283 | 0.225 | 6 | 79.6 | **41.3** | 0.0074-0.0158 | 0.183 | 0.0317 | 6 | 17.4 | -8.67 | 0.00276-0.00854 |
| **In** | *0.11* | 0.123 | 0.0351 | 6 | 28.5 | **11.8** | 0.0007-0.00196 | 0.0927 | 0.00832 | 6 | 8.97 | **-15.7** | 0.00124-0.00211 |
| **Sb** | *0.35* | 0.467 | 0.193 | 6 | 41.3 | **33.5** | 0.0216-0.0302 | 0.301 | 0.0131 | 6 | 4.35 | **-14.0** | 0.0187-0.0252 |
| **Cs** | *1.16* | 1.14 | 0.0269 | 6 | 2.36 | -1.74 | 0.0011-0.00223 | 1.13 | 0.0286 | 6 | 2.53 | -2.70 | 0.00306-0.00357 |
| **Ba** | *683* | 646 | 8.89 | 6 | 1.38 | -5.36 | 0.0035-0.00574 | 656 | 13.5 | 6 | 2.05 | -3.93 | 0.00556-0.00789 |
| **La** | *24.7* | 23.1 | 0.797 | 12 | 3.44 | -6.28 | 0.0004-0.00057 | 23.5 | 0.800 | 12 | 3.41 | -4.96 | 0.00035-0.0005 |
| **Ce** | *53.3* | 51.2 | 1.69 | 12 | 3.30 | -4.02 | 0.0004-0.00066 | 51.1 | 1.16 | 12 | 2.27 | -4.21 | 0.00035-0.00043 |
| **Pr** | *6.7* | 6.12 | 0.115 | 6 | 1.88 | -8.66 | 0 | 6.25 | 0.100 | 6 | 1.60 | -6.69 | 0 |
| **Nd** | *28.9* | 25.6 | 0.623 | 6 | 2.44 | **-11.5** | 0.0014-0.00172 | 26.0 | 0.510 | 6 | 1.96 | -9.99 | 0.00122-0.00241 |
| **Sm** | *6.59* | 5.89 | 0.108 | 6 | 1.83 | **-10.6** | 0.0024-0.00293 | 6.05 | 0.182 | 6 | 3.01 | -8.27 | 0.00104-0.00235 |
| **Eu** | *1.97* | 1.86 | 0.114 | 12 | 6.11 | -5.35 | 0.0004-0.00064 | 1.86 | 0.0638 | 12 | 3.43 | -5.47 | 0.00027-0.00044 |
| **Gd** | *6.71* | 5.98 | 0.239 | 6 | 4.00 | **-11.0** | 0.002-0.00199 | 5.98 | 0.209 | 6 | 3.50 | **-10.9** | 0.00097-0.0027 |
| **Tb** | *1.02* | 0.884 | 0.0323 | 6 | 3.66 | **-13.4** | 0.0002-0.00035 | 0.892 | 0.0341 | 6 | 3.82 | **-12.6** | 0.00021-0.00021 |
| **Dy** | *6.44* | 5.50 | 0.137 | 6 | 2.50 | **-14.6** | 0.001-0.0016 | 5.63 | 0.189 | 6 | 3.37 | **-12.7** | 0.00106-0.00106 |
| **Ho** | *1.27* | 1.09 | 0.0330 | 6 | 3.02 | **-14.0** | 0.0003-0.0003 | 1.13 | 0.0352 | 6 | 3.11 | **-10.9** | 0.00019-0.00019 |
| **Er** | *3.7* | 3.25 | 0.198 | 12 | 6.08 | **-12.2** | 0.0012-0.00118 | 3.27 | 0.108 | 12 | 3.31 | **-11.7** | 0.00055-0.0009 |
| **Tm** | *0.51* | 0.441 | 0.0278 | 6 | 6.32 | **-13.6** | 0.0002-0.00069 | 0.443 | 0.0172 | 6 | 3.88 | **-13.2** | 0.00035-0.00035 |
| **Yb** | *3.39* | 2.97 | 0.226 | 12 | 7.62 | **-12.4** | 0.0017-0.00175 | 2.98 | 0.178 | 12 | 5.99 | **-12.2** | 0 |
| **Lu** | *0.503* | 0.423 | 0.0102 | 6 | 2.41 | **-15.9** | 0.0003-0.00059 | 0.440 | 0.0261 | 6 | 5.92 | **-12.5** | 0.00031-0.00031 |
| **Hf** | *4.84* | 5.00 | 1.59 | 12 | 31.9 | 3.31 | 0.001-0.00119 | 4.43 | 0.259 | 12 | 5.83 | -8.40 | 0.00068-0.00094 |
| **Ta** | *0.78* | 0.646 | 0.0140 | 6 | 2.18 | **-17.2** | 0.0002-0.00037 | 0.672 | 0.0302 | 6 | 4.49 | **-13.9** | 0.00011-0.00026 |
| **W** | *0.5* | 0.573 | 0.107 | 6 | 18.6 | **14.6** | 0 | 0.486 | 0.0333 | 6 | 6.86 | -2.80 | 0 |
| **Re** | *0.006* | 0.0121 | 0.00917 | 6 | 75.8 | **95.2** | 0.0005-0.0008 | 0.00677 | 0.00273 | 6 | 40.3 | 9.17 | 0.00031-0.00055 |
| **Tl** | *0.3* | 0.235 | 0.0411 | 6 | 17.5 | **-21.6** | 0.0005-0.00317 | 0.233 | 0.0185 | 6 | 7.93 | **-22.4** | 0.00042-0.00179 |
| **Pb** | *11* | 10.5 | 0.253 | 12 | 2.42 | -4.90 | 0.0072-0.0121 | 10.4 | 0.223 | 12 | 2.14 | -5.41 | 0.00575-0.0102 |
| **Bi** | *0.05* | 0.0685 | 0.0582 | 12 | 84.9 | **37.0** | 0.0023-0.00605 | 0.0369 | 0.00764 | 12 | 20.7 | **-26.2** | 0.00247-0.00535 |
| **Th** | *5.9* | 5.33 | 0.233 | 12 | 4.38 | -9.66 | 0.0003-0.00062 | 5.40 | 0.253 | 12 | 4.70 | -8.52 | 0.00029-0.00043 |
| **U** | *1.69* | 1.70 | 0.0923 | 12 | 5.43 | 0.464 | 0.0004-0.00071 | 1.64 | 0.0382 | 12 | 2.32 | -2.73 | 0.0003-0.00052 |

Bold numbers are >10% difference between measured concentrations and GeoReM preferred reference values.
Avrg = average concentration in µg $g^{-1}$; SD = standard deviation; n = number of analyses; RSD % = relative standard deviation in per cent; diff.% = difference in per cent with GeoReM preferred values; LOD = limit of detection.

accurate value. Thus, the lower concentration in hydrogen mode in Mt Gambier olivines (Table 6) represent more accurate concentration with possible minor interferences being successfully eliminated. Significant improvement in the quantification of the absolute abundance and precision of elements at low levels was observed in Ga, Y, Zr, Nb, Ag, In, Ce, Nd, Sm, Gd, Yb, Lu, Hf, Pb, Bi and Th.

Table 6 Representative trace (μg $g^{-1}$) and ultra-trace (ng $g^{-1}$) element concentration of Mt Gambier olivines (sample GamTR1) measured in normal and hydrogen mode.

| | normal mode | | | | hydrogen mode | | | |
|---|---|---|---|---|---|---|---|---|
| | Avrg (n=6) | SD | RSD% | LOD (range) | Avrg (n=6) | SD | RSD% | LOD (range) |
| ***Trace elements in μg $g^{-1}$*** | | | | | | | | |
| **Li** | 1.61 | 0.145 | 8.99 | 0.04-0.06 | 1.72 | 0.144 | 8.35 | 0.025-0.029 |
| **Sc** | 3.48 | 0.361 | 10.4 | 0.01-0.018 | 5.19 | 0.274 | 5.27 | 0.015-0.024 |
| **Ti** | 4.03 | 0.822 | 20.4 | 0.02-0.04 | 4.77 | 1.12 | 23.4 | 0.07-0.08 |
| **V** | 0.670 | 0.0310 | 4.63 | 0.001-0.002 | 0.684 | 0.0658 | 9.62 | 0.001-0.002 |
| **Cr** | 7.11 | 0.235 | 3.31 | 0.06-0.10 | 7.38 | 0.986 | 13.4 | 0.08-0.09 |
| **Mn** | 1143 | 30.4 | 2.66 | 0.03-0.04 | 1168 | 19.5 | 1.67 | 0.034-0.039 |
| **Co** | 152 | 5.11 | 3.36 | 0.0006-0.0006 | 152 | 2.22 | 1.46 | 0.0007-0.0009 |
| **Cu** | 0.429 | 0.0550 | 12.8 | 0.006-0.01 | 0.412 | 0.0495 | 12.0 | 0.004-0.006 |
| **Zn** | 40.9 | 2.73 | 6.67 | 0.05-0.08 | 38.4 | 1.74 | 4.53 | 0.02-0.04 |
| **Ga** | 0.0231 | 0.0158 | 68.5 | 0.001-0.003 | 0.00847 | 0.00287 | 33.9 | 0.00053-0.00053 |
| **Ge** | 0.876 | 0.0186 | 2.12 | 0.028-0.031 | 0.836 | 0.103 | 12.3 | 0.025-0.028 |
| **As** | 0.0970 | 0.0271 | 27.9 | 0.028-0.032 | 0.0970 | 0.0282 | 29.0 | 0.017-0.018 |
| **Rb** | 0.00182 | – | | 0.001-0.002 | 0.00620 | – | | 0.005-0.006 |
| **Zr** | 0.230 | 0.262 | 114 | 0.0003-0.0007 | 0.00443 | 0.00389 | 88.0 | 0.0006-0.0009 |
| ***Ultra-trace elements in ng $g^{-1}$*** | | | | | | | | |
| **Sr** | 10.15 | 11.4 | 112 | 0.3–0.5 | 6.80 | – | | 0.2–0.4 |
| **Y** | 7.62 | 12.7 | 167 | 0.4–0.7 | 1.36 | 0.610 | 44.9 | 0.4–0.5 |
| **Nb** | 9.70 | 5.09 | 52.5 | 0.3–0.6 | 2.98 | 1.45 | 48.7 | 0.3–0.5 |
| **Mo** | 14.27 | 4.27 | 29.9 | 1.6–2.1 | 11.5 | 2.87 | 25.0 | 0.6–2.0 |
| **Ag** | 12.90 | – | | 5.2–5.6 | 3.90 | – | | 3.2–3.5 |
| **Cd** | 19.10 | 11.2 | 58.5 | 2.9–3.1 | 27.5 | 0.778 | 2.83 | 2.3–2.3 |
| **In** | 14.93 | 5.10 | 34.2 | 0.6–0.7 | 6.57 | 0.723 | 11.0 | 0.7–0.9 |
| **Sb** | 30.67 | 13.7 | 44.6 | 11.5–11.6 | 28.2 | 16.3 | 57.7 | 9.6–10.4 |
| **Cs** | 1.93 | 0.926 | 48.1 | 0.69–0.76 | – | – | | 1.5–1.7 |
| **Ba** | 14.75 | 13.9 | 94.4 | 3.5–3.8 | 9.30 | – | | 5–6 |
| **La** | 6.20 | 7.22 | 117 | 0.3–0.4 | 1.13 | – | | 0.2–0.5 |
| **Ce** | 4.01 | 5.49 | 137 | 0.2–0.5 | 1.17 | 1.24 | 106 | 0.1–0.4 |
| **Pr** | 0.29 | – | | 0.2–0.4 | 0.790 | – | | 0.19–0.21 |
| **Nd** | – | – | | 1.0–2.0 | 1.60 | 0.624 | 39.0 | 0.6–1.0 |
| **Sm** | – | – | | 1.0–2.0 | 1.80 | – | | 1.0–2.0 |
| **Eu** | 2.54 | 3.08 | 121 | 0.2–0.4 | 1.18 | – | | 0.3–0.6 |
| **Gd** | – | – | | 1.0–2.0 | 1.31 | 0.410 | 31.3 | 0.7–1.3 |
| **Tb** | 0.10 | – | | 0.1–0.4 | 0.310 | – | | 0.15–0.23 |
| **Dy** | 1.54 | – | | 0.5–1.1 | – | – | | 0.4–0.9 |
| **Ho** | 0.23 | 0.0902 | 39.8 | 0.2–0.3 | 0.290 | – | | 0.1–0.3 |
| **Er** | 2.93 | 3.65 | 124.8 | 0.3–1.2 | 2.39 | – | | 0.8–1.0 |
| **Tm** | 1.26 | 0.735 | 58.4 | 0.2–0.3 | 0.520 | – | | 0.1–0.3 |
| **Yb** | 7.92 | 7.21 | 91.0 | 1.07–1.43 | 2.10 | 0.424 | 20.2 | 0.6–1.0 |
| **Lu** | 1.25 | 0.359 | 28.7 | 0.2–0.3 | 0.880 | 0.453 | 51.4 | 0.2–0.4 |
| **Hf** | 8.00 | 6.75 | 84.4 | 0.7–1.6 | 1.02 | – | | 0.3–1.0 |
| **Ta** | 0.54 | 0.212 | 39.3 | 0.1–0.3 | 0.400 | – | | 0.1–0.2 |
| **W** | 2.14 | 0.993 | 46.3 | – | 1.68 | – | | – |
| **Re** | 0.66 | 0.445 | 67.4 | 0.18–0.22 | 0.540 | – | | 0.15–0.16 |
| **Tl** | 2.01 | – | | 0.3–0.9 | 0.400 | – | | 0.2–0.3 |
| **Pb** | 10.55 | 2.25 | 21.3 | 3.0–5.0 | 5.18 | 0.870 | 16.8 | 2.6–4.2 |
| **Bi** | 4.23 | 2.21 | 52.3 | 1.0–2.0 | 2.60 | 0.849 | 32.6 | 1.0–2.0 |
| **Th** | 2.54 | 3.32 | 130.8 | 0.2–0.4 | 0.685 | 0.460 | 67.1 | 0.1–0.4 |
| **U** | 3.47 | 5.20 | 149.9 | 0.2–0.3 | – | – | | 0.1–0.3 |

Avrg = average concentrations in μg $g^{-1}$ (traces) and ng $g^{-1}$ (ultra-traces); SD = standard deviation; n = number of total spot analyses; RSD % = relative standard deviation in per cent; LOD = limit of detection

The use of $H_2$-mode as an analysis routine enhancement facilitates the acquisition of a complete REE pattern in natural silicate samples with low-level elements such as in olivines, which in previous LA-ICP-MS analyses was problematic and incomplete. This advancement also enables the examination of hitherto "ignored" elements because of their low abundances, which attract increasing attention because of their potential to investigate magmatic and metasomatic processes in the Earth's upper mantle. An example for such overlooked elements in olivines would be the chalcophile group of elements.

## 2.4 Conclusions

The motivation for this study was to improve the LA-ICP-MS analytical routine for the acquisition of trace elements at low concentration levels in natural silicate phases such as olivine. We have applied and compared two LA-ICP-MS methods, (1) 'normal mode' acquisition, which is the standard set-up at our laboratory using He-Ar carrier gas, and (2) an improved 'hydrogen mode' method, where 5 mL $min^{-1}$ of molecular hydrogen gas was added to the He-ablated sample mixture before being mixed with Ar gas. The hydrogen-mode method achieved consistently higher sensitivities for all measured elements by a factor 1.5 and resulted in slightly lower limits of detection in certified reference materials. The most significant enhancement in sensitivity was observed for Zn, As and Cd, which was demonstrated to be a function of higher $1^{st}$ ionisation potentials, i.e., these elements with high $1^{st}$ ionization potential are being ionized to a much greater extent with the use of hydrogen mode. The most insightful results were achieved for the olivine measurements with improvements in precision and limits of detection, which now enable acquisition of ultra-trace elements that were too low to determine in 'normal mode' analysis routine. This advancement facilitates new possibilities in natural olivine characterisation (and other low-level content minerals), such as the acquisition of complete REE pattern, which so far was either incomplete or ignored altogether, as well as expanding the palette of analysed elements to include the chalcophile and siderophile group of elements (such as Mo, In, Cd, Ag) which are almost non-existent in literature for natural olivines.


### ACKNOWLEDGEMENTS

This work was carried out as part of a PhD study of MV at Macquarie University and was supported by the Australian Government International Research Training Program (iRTP) Scholarship (No. 2017056).

# CHAPTER 3

# RECONSTRUCTION OF THE CONTINENTAL MANTLE COMPOSITION FROM MANTLE XENOLITH MINERALS IN MT GAMBIER, SOUTHEASTERN AUSTRALIA

Marina **Veter**[1]*, Stephen F. **Foley**[1,2], Olivier **Alard**[1,2,3]

[1] Department of Earth and Environmental Sciences, Macquarie University, NSW 2109, Australia

[2] ARC Centre of Excellence for Core to Crust Fluid Systems, Department of Earth and Environmental Sciences, Macquarie University, NSW 2109, Australia

[3] Géosciences Montpellier, UMR 5243, CNRS & Université Montpellier, 34095 Montpellier, France

* Corresponding author: marina.veter@mq.edu.au

## ABSTRACT

The composition of the continental lithospheric mantle has drawn the attention of many researchers. Samples of the lithosphere are found on the Earth's surface in form of mantle xenoliths entrained in alkali basalts or kimberlites, or as orogenic peridotite blocks. Thus, we are able to characterise the lithospheric mantle and determine estimates of the primitive mantle composition. However, processes of mantle modification and xenolith transport almost universally affect the original lithospheric composition by complex, often multiple, episodes of melt and/or fluid action. Therefore, it is difficult to assess the original composition and its relation to primitive mantle, and caution must be applied in sample selection and analytical methods.

We present new trace element compositions of the mantle forming phases olivine, orthopyroxene and clinopyroxene in spinel-peridotite xenoliths hosted in alkali-basalts from Mt Gambier, Newer Volcanic Province in southeastern Australia. Mt Gambier is a well-studied locality in southern Australia that represents relatively unmetasomatised continental mantle. The samples exhibit especially fresh and homogeneous minerals, which are excellent for characterisation of element budgets in lithospheric mantle, overcoming the common problem of metasomatic overprinting of original element abundances. Precise *in-situ* LA-ICP-MS analyses enable the acquisition of low-level trace elements, such as rare earth element (REE) and volatile chalcophile and siderophile element (VCSE) abundances in silicate phases from mantle peridotite xenoliths. The VCSE in mantle silicate phases have received little attention to date since they are not considered major host phases for these elements. As a consequence, little is known about the distribution

and behaviour of the VCSE in the petrogenesis of the continental lithosphere. Our improved *in-situ* hydrogen-mode LA-ICP-MS method enables the characterisation of a wide range (almost complete set) of elements, including several that are rarely analysed due to detection limitations, in all the major mantle silicate phases olivine, orthopyroxene and clinopyroxene. That allows us to reconstruct the lithospheric mantle composition and propose Mt Gambier mantle xenoliths as a keystone for composition of continental lithospheric mantle to which other areas can be compared. The presented results should form a fundament for understanding the processes and agents of mantle metasomatism in relatively young continental lithosphere.

**Keywords:** Mantle xenoliths; Mt Gambier; continental lithosphere; trace elements; metasomatism; chalcophile and siderophile elements

## 3.1 Introduction

Characterising the chemical composition of the Earth's subcontinental lithospheric mantle (SCLM) and the distribution of elements within the mantle and its constituent minerals has been the focus of numerous studies. Acquiring this information is of substantial value for the reconstruction of, and our understanding of, the Earth's evolution and composition of the Bulk Silicate Earth (BSE). Luckily, samples of the continental lithosphere are brought to the Earth's surface by different processes, e.g., orogenic peridotites, mantle peridotite xenoliths hosted in alkali basalts (off-cratonic regions) or hosted in kimberlites and lamproites (cratonic regions) and as mineral inclusions in diamonds (e.g., O'Neill and Palme, 1998). Orogenic (or massif) peridotites are bodies of shallow (<100 km) lithospheric mantle that have been tectonically exposed on the Earth's surface preserving the field relationships as within the mantle (e.g., Pearson *et al.*, 2003; Lorand and Luguet, 2016). A drawback of these bodies is their chemically altered composition evident as serpentinization and re-equilibration within the crust. Mineral inclusions in diamonds sample deeper levels of lithosphere, on rare occasions even from the lower mantle, but their small size/amount and rarity are rather unrepresentative. Mantle xenoliths sample large vertical sections of the SCLM, which is systematic but may be unrepresentative. The rapid transport in kimberlites from within the mantle to the Earth's surface preserves the equilibration P-T conditions in the mineralogical composition from depths where it was sampled.

There are generally two types of magmas that carry mantle xenoliths: (1) alkaline basalts that sample predominantly the spinel-lherzolite facies in the lithospheric mantle from depths ranging from 40–70 km, in rare cases the xenoliths may be garnet-bearing which indicates equilibration at higher pressures with maximum depths of 80–90 km; and (2) kimberlites and lamproites that sample predominantly garnet-bearing peridotite xenoliths corresponding to pressures up to 7 GPa (depths ≈ 220 km), as well as spinel-facies lherzolites (O'Neill and Palme, 1998; Pearson *et al.*, 2003). Thus, kimberlitic and basaltic xenoliths provide insights into different levels of the SCLM, whereas the former suite primarily sampled the Archaean cratonic lithosphere, the latter are characteristic for post-Archaean off-craton lithosphere.

Studies of major and trace element abundances in mantle xenoliths indicate that they are residues of more fertile protoliths that experienced some degree of melt extraction (e.g.Walter, 1999). However, the residues have usually been subsequently overprinted by metasomatic enrichment events. Kimberlite-derived mantle xenoliths have been shown to have experienced extensive, multi-stage metasomatic overprints, known as modal metasomatism characterised by apparent petrographic alterations evident in modified mineral assemblages (Dawson, 1980; Griffin *et al.*, 1988; O'Reilly and Griffin, 1988). Common phases precipitated during metasomatic enrichment processes in cratonic xenoliths are predominantly clinopyroxene and garnet (Shimizu, 1999; Pearson and Nowell, 2002) along with amphibole and phlogopite, whereas non-cratonic samples may, to a lesser extent, have apatite and carbonate (Pearson *et al.*, 2003).

Peridotite xenoliths hosted in alkali basalts generally experienced less enrichment caused by infiltration of the host magma than xenoliths in kimberlitic rocks. Nevertheless, this can produce important modifications in the abundances of a large number of trace element without causing the growth of new minerals, which is known as cryptic metasomatism (e.g. Dawson, 1980; Griffin *et al.*, 1988; O'Neill and Palme, 1998). Nevertheless, modal metasomatism can occur in xenoliths carried by kimberlite and alkali basalt.

Rocks with chemical and isotopic abundances matching the primitive mantle are unknown amongst the samples available at the Earth's surface, since depletion and enrichment processes have substantially obscured their original composition. In order to reconstruct the chemical composition of the primitive mantle (i.e., before depletion by melt loss and re-enrichment), the modifying processes need to be accounted for and excluded from the element budget. The primitive mantle composition (synonymously used for BSE) describes the bulk chemical composition of the mantle after core segregation but before the extraction of the crust. Different approaches to reconstruct the initial bulk Earth mantle abundances were derived from primitive meteorite concentrations and cosmochemical models (e.g. O'Neill and Palme, 1998). The first method is based on acquiring a ratio of refractory elements to trace elements from different mantle reservoirs (Wänke *et al.*, 1984; Jochum *et al.*, 1993; O'Neill and Palme, 1998; Salters and Stracke, 2004), but this approach has its limitations as it was shown to be reliable only for highly incompatible elements, which are insensitive to the degree and mechanism of partial melting (Witt-Eickschen *et al.*, 2009).

The alternative method is to analyse mantle peridotite xenoliths that show the least differentiated "primitive" chemical composition (e.g. O'Neill and Palme, 1998). The best-known examples are spinel lherzolite xenoliths from San Carlos, Arizona, SC1 described by (Jagoutz *et al.*, 1979; Wänke *et al.*, 1984; Jochum *et al.*, 1989) and from Dreiser Weiher, Germany, Ib/8 (Stosch and Seck, 1980). The problem with this approach is establishing whether these samples represent truly primitive composition or experienced by chance the "right" amount of melt extraction and metasomatic re-enrichment to match the primitive mantle composition. However, O'Neill and Palme (1998) argued that this approach is still reliable as long as the consistency in the LREE-enriching metasomatism is maintained.

Trace elements with lithophile affinities in mantle rocks have been studied abundantly and used to reconstruct the bulk Earth mantle composition. Numerous studies of the distribution of REE and other incompatible elements between peridotite minerals established that clinopyroxene (cpx) and garnet (grt; if present) are their major hosts, with orthopyroxene (opx) playing only a minor role (e.g. Frey and Green, 1974; Shimizu, 1975; Salters and Shimizu, 1988) and olivine being mostly ignored as insignificant or having abundances that are unmeasurably low.

Relative to the lithophile elements, the volatile chalcophile and siderophile elements (VCSE) are rarely analysed and estimates of their abundances in the Earth's mantle and/or in mineral phases are underrepresented. Furthermore, the concentration of VCSE can be altered, e.g., by metasomatic sulphide enrichment or reduced by percolating high temperature silicate melts with low S abundances (e.g. Lorand, 1990; Lorand and Alard, 2001; Luguet *et al.*, 2004; Witt-Eickschen *et al.*, 2009). Analytical advances in

recent years, especially in LA-ICP-MS enable rapid, multi-element *in-situ* measurements of trace and ultra-trace elements with low abundances in individual mineral phases. We highlight here two studies that used these analytical advances to measure trace elements in mantle phases. Eggins *et al.* (1998b) presented a thorough LA-ICP-MS analysis of trace elements with a focus on incompatible elements, in which they measured the bulk rock composition of mantle peridotite xenoliths and its constituent silicate phases including amphiboles/glass pockets. This is probably the most complete attempt to acquire incompatible trace elements from olivine, opx and cpx. A second study was carried out by Witt-Eickschen *et al.* (2009) using *in-situ* LA-ICP-MS to determine the composition of some VCSE (As, Cd, Ga, In and Sn) in spinel-lherzolite mantle xenoliths and the constituent phases olivine, opx, cpx and spinel. This is the first study presenting values for these elements in all silicate phases of spinel lherzolites and determines the intercrystalline partition coefficients.

We have focussed in this study on "combining" the advantages and approaches of these two highlighted works above and have acquired the most extensive set of elements yet measured by using a new, enhanced LA-ICP-MS method (see Veter et al., Chapter 2). We have chosen five spinel peridotite mantle xenoliths from Mt Gambier, southeastern South Australia, which are thought to represent pristine mantle compositions and exhibit exceptionally fresh minerals that are affected by minimal melt infiltration. The melt infiltration, where present, is very clear in petrographic images and so can be characterised and stripped to arrive at the best available model for the original pre-metasomatic substrate. Element abundances were determined for the major silicate phases olivine, opx and cpx and were used to derive bulk rock compositions by mass balance. The results can be used as a model for relatively young sub-continental mantle away from cratons: we present the most complete element set yet for young continental lithosphere and investigate the partitioning of trace and ultra-trace elements between the phases. This includes a full data set for olivine and opx, for which data has been conspicuously sparse in the past.

## 3.2 Geological Setting

Australia has been subject to repeated compressional and rifting events during its history, which are relevant to the origin of its continental lithosphere. In the late Proterozoic, Australia has been forming a part of the supercontinent Rodinia (1300–1100 Ma; Johnson (2009)) with neighbouring Antarctica, India and probably parts of North America (Dalziel, 1991; Moores, 1991) or South China (Li *et al.*, 1995; Li *et al.*, 1996) until Rodinia's breakup around 830 to 745 Ma (Powell *et al.*, 1994; Wingate *et al.*, 1998; Johnson, 2009). After the breakup the drifting continental masses amalgamated in Early Cambrian to form Gondwana with Australia, Antarctica, India and New Zealand juxtaposed representing the eastern part of Gondwana where Australia was positioned on the eastern margin; Africa, Madagascar and South America were building the western part of Gondwana (Johnson, 2009). During this time, Australia generally remained a passive margin with episodes of collision with oceanic plates and accretion of terranes throughout the Paleozoic resulting in the formation of the Tasman Fold Belt stretching from North

Queensland down to Tasmania (e.g. Duncan and McDougall, 1989; Wyborn, 1989; Coney *et al.*, 1990; Handler, 1998). Around 154 Ma the breakup of Gondwana commenced, with the western terranes splitting away by 120 Ma, followed by India's separation and rapid northwards movement around 99 Ma (e.g. Duncan and McDougall, 1989; Johnson, 2009). To the south, separation of Australia from Antarctica was initiated at approximately 90 Ma (e.g. Johnson *et al.*, 1989; Coney *et al.*, 1990) first spreading at a slower rate and increasing later in time resulting in the opening of the Great Australian Bight and the Southern Ocean (e.g. Johnson *et al.*, 1989; Coney *et al.*, 1990; Johnson, 2009). During this fracturing in the south, Tasmania was isolated from Australia – but did not break away – by opening the Bass Strait which represents stretched continental crust overlain by a thick sedimentary sequence (Johnson, 2009). At the same time (around 84 Ma) along the eastern coast of Australia, the opening of the Tasman Sea was initiated by eastward drift of New Zealand. This rifting propagated northwards and eventually around 56 Ma the Coral Sea was open, and the Queensland Plateau separated from the north-eastern coast of Queensland (e.g. Duncan and McDougall, 1989; Coney *et al.*, 1990; Johnson, 2009).

During the Cenozoic to Recent (around 70 Ma to 4600 yr B.P.), the last episode of basaltic intraplate volcanism was active along eastern Australia, producing two distinct types of volcanic provinces – lava field and central volcanoes that stretch from northern Queensland to Tasmania (Wyborn, 1989; Johnson, 2009) (Figure 7). However, the most recent eruptions in Australia are found in northern Queensland (not subject of this study), western Victoria and southeastern South Australia in the Newer Volcanic Province (NVP), covering an area of 15000 $km^2$ with more than 400 known eruption centres and stretching around 400 km E-W from Melbourne to Mt Gambier, South Australia (Joyce and Day, 1989; Johnson, 2009; Van Otterloo *et al.*, 2014). The NVP can be further subdivided into three sub-provinces: Central Highlands, Western Plains, and Mt Gambier, the latter being the focus of this study. The volcanic features in NVP are characterized by scoria cones, maars, tuffs and lava flows of mainly alkaline basalts (e.g. Nicholls and Joyce, 1989). The youngest volcanic activity was dated back to approximately 4600 yr B.P. and occurred at Mt Gambier (Nicholls and Joyce, 1989) with two distinguished magmatic activities, (1) major phreatomagmatic activity resulting in a number of maar deposits and (2) minor magmatic activity producing lava flows and scoria cones (Sheard and Nicholls, 1989).

The volcanic basalt penetrated the Proterozoic SCLM that experienced late Proterozoic folding (Griffin *et al.*, 1999a). The Tertiary volcanic deposits carry xenoliths collected from the wall-rock during the rapid ascent of the magma and are mainly characterised as Cr-diopside spinel-bearing peridotites (e.g. Nicholls and Joyce, 1989; O'Reilly *et al.*, 1989; Sheard and Nicholls, 1989; Yaxley *et al.*, 1991; Yaxley *et al.*, 1997).

Re–Os isochron ages for the Mt Gambier xenoliths yielded Proterozoic ages of 1.9 Ga and two younger ages to the east in the NVP around 800–1000 Ma and ≤500 Ma. These three episodes of mantle depletion suggest a younging towards the east, with the oldest ages found only in Mt Gambier, and Paleozoic ages in the eastern localities of NVP (Handler *et al.*, 1997).

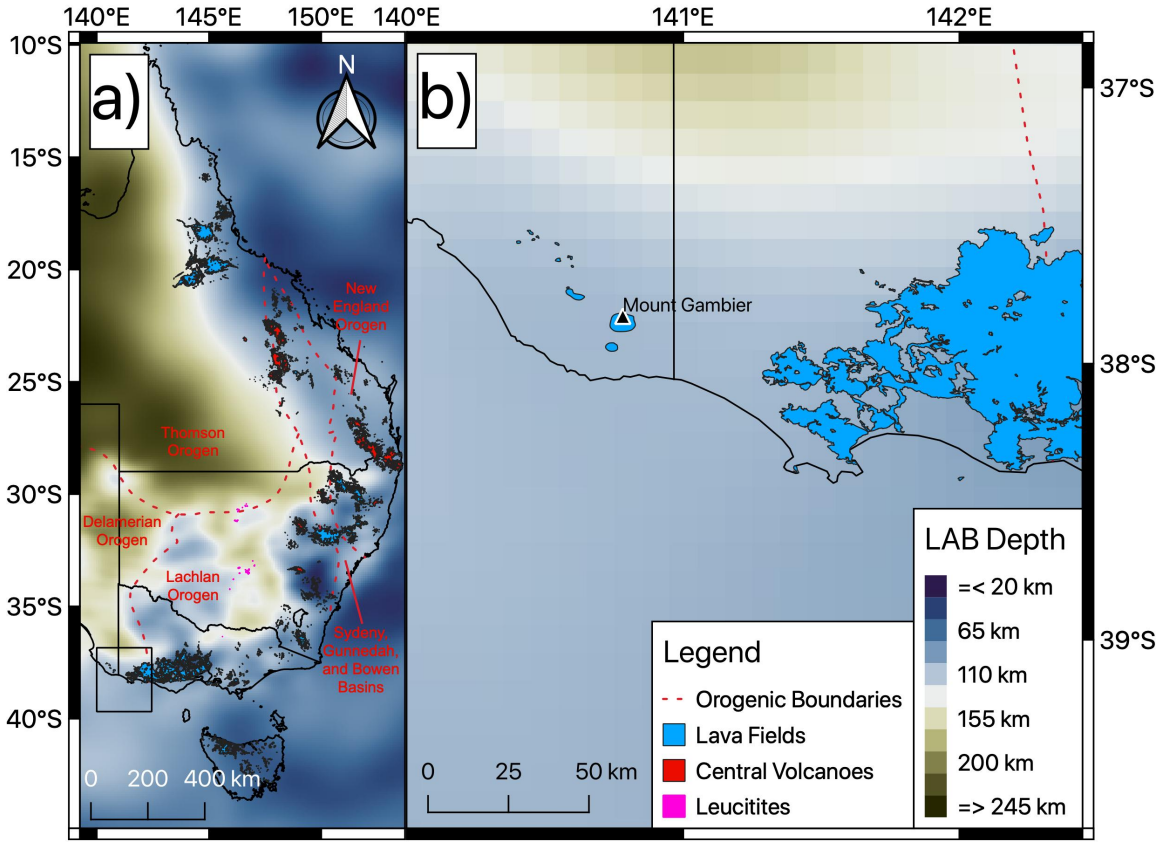


Figure 7 Distribution of eastern Australian Cenozoic intraplate volcanism combined with the lithosphere-asthenosphere boundary (LAB) depth. (a) Dark blue and dark yellow colours indicate the shallowest and deepest LAB depth, respectively, and light colours represent intermediate depths. (b) Defines the close-up area representing the eastern part of NVP and the location of Mt Gambier, showing an intermediate LAB depth of ~110 km below this area. The figure was provided by Shea et al. (unpublished); LAB depths are after Rawlinson *et al.* (2017).

## 3.3 Analytical methods

All analyses for this study were performed in the facilities of Macquarie GeoAnalytical (MQGA), at the Department of Earth and Environmental Sciences at Macquarie University, Australia. The EPMA analyses were run at the Geoscience facilities at Johannes Gutenberg-University Mainz, Germany.

### 3.3.1 Petrography, Micro-XRF and FE-SEM

Petrographic descriptions of polished thick sections (100 µm) were carried out using a polarising microscope in combination with qualitative elemental distribution maps acquired with a Bruker M4 Tornado Micro-XRF (µXRF). For high-resolution petrographic observations and backscatter electron images acquisition a FEI Field Emission SEM was used. The µXRF measuring parameters were set to 200 µA, 50 kV, scanning time of 10 ms per pixel with 35 µm step size (distance). This scanning method was primarily used in addition to petrographic microscopy observations for mineral identification and distribution, and the maps generate a clearer overview of the textural structures in samples (see Figure 8b).

For backscatter electron imaging (Figure 8d) and mineral identification a FEI Teneo Field Emission Scanning Electron Microscope was used equipped with secondary and backscatter-electron detectors and an integrated Bruker Energy Dispersive X-ray Spectroscopy (EDX; Bruker XFlash Series 6) analyser. The analyses were run at 12.0 mm working distance and 15 kV acceleration voltage.

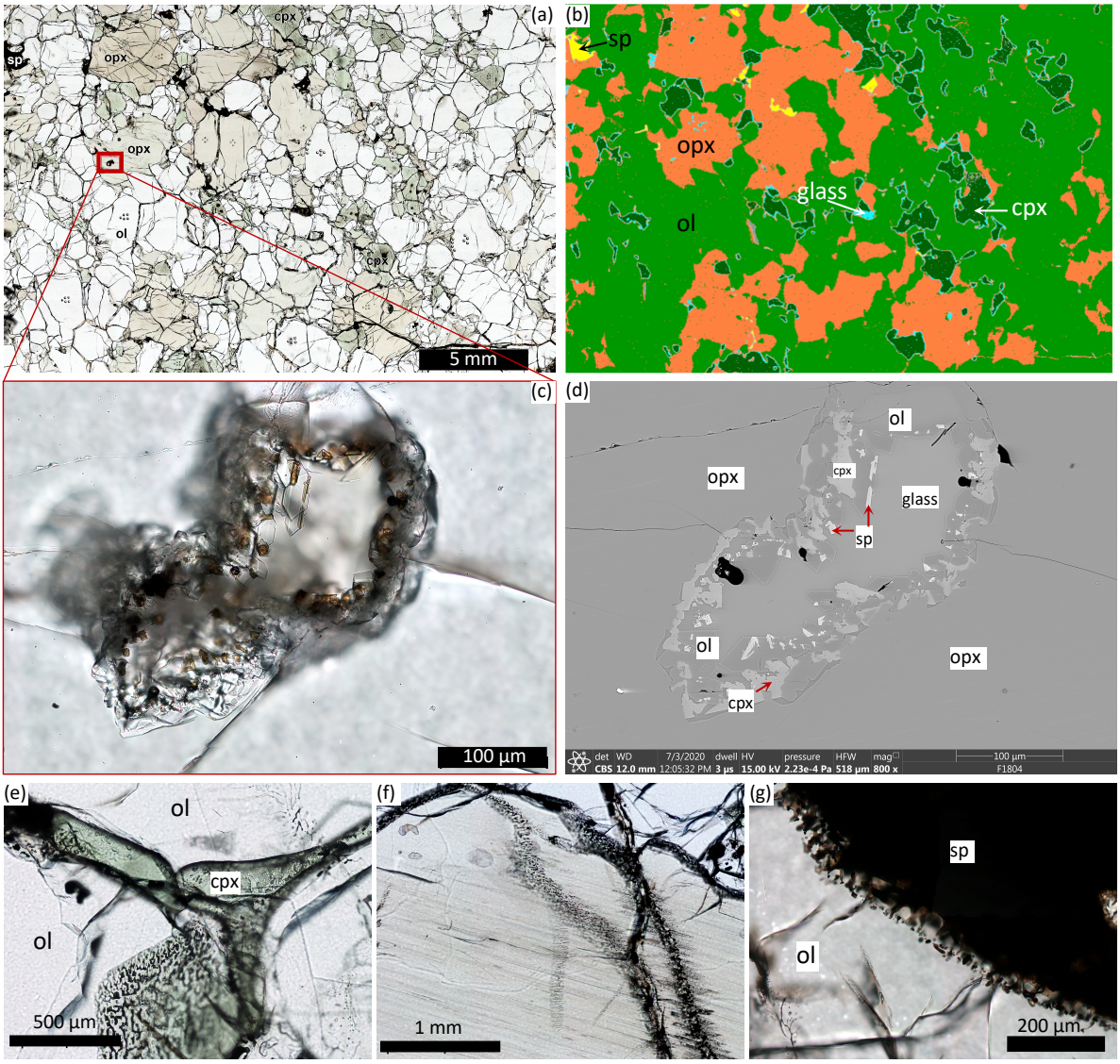


Figure 8 Photomicrographs taken with a polarizing microscope under a plain polarized light (PPL) and backscatter electron images of the samples. (a) Photomicrograph shows a protogranular representative sample of the spinel lherzolite suite from Mt Gambier with constituent phases olivine (white), orthopyroxene (light green and reddish, effect of pleochroism), clinopyroxene (dark green) and spinels (black). Small holes are LA-ICP-MS spot analyses The red box indicates the area of (c) and (d); (b) Modal abundance map acquired with µXRF of the same sample area as in (a), green = olivine, orange = orthopyroxene, dark green = clinopyroxene, yellow = spinel, light blue = areas of glass pockets as shown in (c) and (d); (c) shows a close-up of the highlighted area in (a) which is a glass pocket inclusion within an orthopyroxene with a rim of secondary euhedral crystals of olivine, clinopyroxene and spinel; (d) exhibits a backscatter electron image of same area as shown in (c) with a higher resolution of single minerals in the crystal "rim" and the glass patch filling in the middle; (e) Clinopyroxene crystallized in a triple junction between olivine grains; (f) "Cloudy" bands in an orthopyroxene which are melt infiltrations, usually occurring along grain boundaries or in cracks and grain defects; (g) shows olivine and spinel in contact with each other and tiny spinel inclusions in olivine.

### 3.3.2 Whole Rock Trace Element Analyses by Standard Solution ICP-MS

Whole rock trace and rare earth element compositions were determined for selected samples with a standard solution ICP-MS procedure using an Agilent 7500cs quadrupole mass spectrometer with an integrated Agilent autosampler. The unknown samples were bracketed by the analysis of three USGS reference materials, the synthetic glasses produced from natural basalt samples BCR-2 was used for calibration, and BHVO-2 and BIR-1 were measured as the quality control materials. The reference materials were prepared in three different dilution factors and were always measured in order of decreasing dilution (1:5000, 1:2000 and 1:1000). Each run started with the analysis of 2% $HNO_3$ + trace HF solution for the background measurement, as well as the rinsing solution.

For the analyses, the powdered rock samples were chemically digested in sealed Teflon beakers using a 1:1 mixture of concentrated $HNO_3$ and HF at 150°C overnight, then dried down and repeated. Dried samples were then dissolved and heated at 190°C in $HClO_4$ for 24 hours. Since the samples are spinel bearing peridotites, an extra digestion step was added, where dried samples were diluted in 1:3 mixture of $HNO_3$ and HCl (aqua regia) at 150°C overnight, then dried down and subsequently digested in a 3:1:1:1 mixture of HF:$HClO_4$:$HNO_3$:$H_2O$ at 170°C for 8 days, then dried down. Afterwards, samples were digested in 6N (molar) $HNO_3$ at 80°C for 1 hour, then diluted to a ratio of 1:1000 with 2% $HNO_3$ and trace HF. Each sample was individually spiked with an aliquot of $^{6}$Li, As, Rh, In and Bi in 2% $HNO_3$.

### 3.3.3 Major Element Analyses of minerals by EPMA

Major element concentrations of olivines, opxs and cpxs were obtained using a JEOL JXA-8200 electron microprobe at the Institute for Geoscience of the Johannes Gutenberg-University Mainz, Germany. For the analyses, the thick sections were checked to be polished and cleaned, before coating with 20 nm thin layer of carbon. Quantitative data was acquired using the standard silicate routine with 105 s acquisition time per point including the major elements Mg, Si, and Fe and the minor elements Na, Al, Cr, Mn, Ti, K, Ca, and Ni. The operating conditions were set at 15 kV acceleration voltage, 12 nA beam current and 2 µm probe diameter. Calibration was performed on natural and synthetic standards and are given in Appendix A-1.

### 3.3.4 Trace Element Analyses by LA-ICP-MS

Quantitative minor, trace and ultra-trace element analyses were carried out using an Agilent 7700cs quadrupole ICP-mass spectrometer, coupled with a Photon Analyte G2 193nm ArF Excimer laser system equipped with a HelEx II Active 2-Volume Cell. An improved measurement method (hydrogen mode) was applied, where the ablation was performed in a helium atmosphere, then mixed with a hydrogen gas before the main carrier gas argon was added to the mixture. A detailed description of the set-up and "hydrogen mode" method development is outlined in Chapter 2.

The instrument was auto tuned for stable ion beam, low ThO/Th oxide production and low values of doubly charged ions using a synthetic silicate reference glass NIST SRM 610. The laser was run with operating parameters of 5 Hz pulse repetition rate and 7.6–5.2 J $cm^{-2}$ laser fluence. The additional $H_2$ gas flow was set to 5 mL $min^{-1}$. Background time was set to 150 s followed by 60 s ablation time. The spot size on olivines was adjusted between 85 110 µm, depending on the size of olivines, opx was set to 85 µm, and cpx and all reference materials were measured with 65 µm spot diameter. Certified reference materials bracketing the samples were measured as the calibration material (NIST SRM 612) and as quality control materials (NIST SRM 610, USGS BCR-2G, BHVO-2G and BIR-1G) to monitor accuracy and reproducibility. A wide range of masses (in total 72 masses) was acquired in two separate runs with two different element lists focussing on (1) 'standard' silicate elements including all REEs and (2) 'transition' elements including the volatile chalcophile and siderophile elements. The detailed element lists can be seen in Chapter 2.

Automated data processing of time-resolved LA-ICP-MS raw data was done using the GLITTER software (Macquarie University, Sydney). Quantitative concentrations were acquired with NIST 612 as the external standard for calibration of measurements and $^{29}Si$ as the internal standard, with $SiO_2$ wt.% concentrations previously determined by electron microprobe analyses. Analyses of natural samples were screened and filtered for outliers that resulted from mixed analyses or inclusions.

## 3.4 Results

### 3.4.1 Petrographic observations

The samples exhibit a coarse grained, protogranular to porphyroclastic texture with anhedral to sub-rounded equant grains of predominantly olivine and opx as porphyroclastic phases ranging up to 5 mm in size, and cpx and spinel as minor phases (summary in Appendix A-2). Figure 8a shows the exceptional freshness of the samples, with no sign of abundant alteration on grain boundaries that is commonly observed in kimberlite hosted xenoliths but also in other Australian off-craton xenoliths (e.g. Yaxley *et al.*, 1997). Where melt infiltration can be optically observed, it is recent, can be well characterised and easily avoided during *in-situ* measurements.

Clinopyroxene and spinel crystallise in some samples in bands and describe a well-developed foliation. Orthopyroxenes and cpxs exhibit parallel lineations, which were identified as cleavages or occasional exsolution lamellae of cpx and opx, respectively. Figure 8e shows a cpx grain crystallising between grain boundaries in a triple junction with low angle faces that indicates crystallisation from the infiltrated melt just before the eruption, so that there was no time for the cpxs to equilibrate; in some cases, cpx precipitate around another phase, thus completely enclosing single minerals. Spinels display an irregular shape and usually occur in clusters with pyroxenes. Figure 8g display olivine in contact with spinel and tiny (>5 µm) inclusions of solid phase spinel trapped in the neighbouring olivine. Sample GamTR1

and MGam1 exhibit rare, inhomogeneously distributed glass pockets (≤2 mm) with a rim of small (≤50 µm) recrystallized euhedral olivine, cpx and spinel grains (Figure 8c and d). On one occasion, a melt pocket with quenched minerals was observed, which included euhedral spinel, olivine and cpx crystals as well as relic amphibole crystals (≤30 µm) within the glass patch. Similar occurrences of melt pockets with secondary crystals have been previously observed and described as amphibole and/or mica breakdown products (e.g. Frey and Green, 1974; Dasch and Green, 1975; Yaxley *et al.*, 1997; Eggins *et al.*, 1998b). All samples exhibit thin melt and/or fluid infiltrations with tiny crystallites along some grain boundaries or thin selvages of melt/fluid inclusions running through minerals along cracks and/or grain defects, as shown in Figure 8f.

### 3.4.2 Whole rock geochemistry

Numerous studies from the NVP region have shown a variety of peridotite xenolith types, ranging from anhydrous, hydrous mineral-rich to hydrous minerals ±apatite-bearing peridotites (e.g. Frey and Green, 1974; O'Reilly *et al.*, 1989; Yaxley *et al.*, 1998). The rock types in this study represent anhydrous Cr-diopside spinel-bearing lherzolites and harzburgites, also classified as Group I peridotite xenoliths after Frey and Prinz (1978). The mineral proportions were determined by least squares mass fraction calculations from bulk and mineral major element analyses and range from 50–73 % olivine, 18–27 % opx, 3–28 % cpx and 0.7–3.9 % spinel (Table 7). The occurrence of grt-bearing xenoliths in the NVP is recorded in grt-pyroxenites (websterites) only, and is limited to few localities, e.g., Bullenmerri/Gnotuk maars, and Mt Leura and Mt Shadwell (e.g. Irving, 1974; Nickel and Green, 1984; O'Reilly and Griffin, 1985), and are not part of this study.

Sample GamTR3 is a cpx-rich spinel lherzolite with the highest modal proportion in cpx (28 %), whereas sample MGam2 represents a depleted spinel harzburgite with 3 % modal cpx. Calculated equilibrium temperatures (Table 7) with the Ca-in-opx geothermometer (T[Ca-opx-BK]; from Brey and Köhler (1990)) yield temperatures ranging between 834–954ºC. The calculated temperatures with the two-pyroxene geothermometer (T[2px–BK]; Brey and Köhler (1990)) result in lower temperature ranges, varying between 732–825°C. However, due to the increased sensitivity to minor CaO changes at low temperatures, the two-pyroxene geothermometer was shown to yield unreliable equilibrium temperatures, thus the Ca-in-opx thermometer is recommended instead (Brey and Köhler, 1990; De Hoog *et al.*, 2010). In comparison, the two-pyroxene geothermometer after Wells (1977) (T[2px–W]) yielded equilibrium temperatures ranging from 775°C to 831°C (Table 7).

Whole rock geochemical analyses of the mantle xenoliths are presented in Table 7. The samples plot within the range of published spinel peridotite xenoliths and the correlations of $Al_2O_3$ and CaO vs. MgO are characteristic of varying degrees of melt extraction from primitive peridotites, leaving behind refractory residues (e.g. Nickel and Green, 1984; Frey *et al.*, 1985; McDonough, 1990; Yaxley *et al.*, 1998). The variability in $Al_2O_3$ (1.01–3.21 wt%), CaO (0.82–6.25 wt%) and MgO (36.4–45.3 wt%) concentrations indicate some range in fertility, GamTR3 (3.21 wt% $Al_2O_3$ and 36.4 wt% MgO) represents the most fertile

Table 7 Bulk composition for analysed mantle peridotites.

| Sample | MGam1 | MGam2 | GamTR1 | GamTR3 | GamTR4 | this study | | | Sp-π [a] | PM[b] | calculated bulk | | calculated melt | |
|---|---|---|---|---|---|---|---|---|---|---|---|---|---|---|
| Rocktype | Sp-Lhz | Sp-Hzb | Sp-Lhz | Sp-Lhz | Sp-Lhz | Avrg | SD | Median | Avrg | | Avrg | Median | Avrg | Median |
| ***Mass proportion% (normalised to 100%)*** | | | | | | | | | | | | | | |
| Ol | 61.7 | 73.2 | 68.1 | 50.0 | 67.0 | 64.0 | 8.8 | 67.0 | 62 | 56 [a] | | | | |
| Opx | 26.5 | 23.0 | 21.8 | 18.2 | 24.1 | 22.7 | 3.0 | 23.0 | 24 | 22 [a] | | | | |
| Cpx | 10.3 | 3.2 | 8.8 | 27.9 | 8.1 | 11.7 | 9.4 | 8.8 | 12 | 19 [a] | | | | |
| Sp | 1.5 | 0.7 | 1.3 | 3.9 | 0.7 | 1.6 | 1.3 | 1.3 | 2 | 3 [a] | | | | |
| ***Geothermometer (°C)*** | | | | | | | | | | | | | | |
| T[1] | 834 | 871 | 954 | 857 | 886 | 880 | 45 | 871 | | | | | | |
| T[2] | 825 | 732 | 747 | 799 | 744 | 769 | 40 | 747 | | | | | | |
| T[3] | 830 | 775 | 785 | 831 | 779 | 800 | 28 | 785 | | | | | | |
| ***Major elements (wt% oxide; XRF)*** [c] | | | | | | | | | | | | | | |
| $SiO_2$ | 45.9 | 44.4 | 44.2 | 45.2 | 44.9 | 44.9 | 0.665 | 44.9 | 44.0 | 44.8 [a] | | | | |
| $TiO_2$ | 0.0915 | 0.0100 | 0.0200 | 0.409 | 0.0600 | 0.118 | 0.166 | 0.0600 | 0.0900 | 0.21 [a] | | | | |
| $Al_2O_3$ | 2.28 | 1.01 | 2.04 | 3.21 | 1.97 | 2.10 | 0.786 | 2.04 | 2.27 | 4.45 [a] | | | | |
| FeO(tot) | 7.23 | 8.16 | 8.04 | 8.00 | 7.31 | 7.75 | 0.441 | 8.00 | 8.43 | 8.4 [a] | | | | |
| MnO | 0.142 | 0.120 | 0.140 | 0.150 | 0.130 | 0.136 | 0.0116 | 0.140 | 0.140 | 0.14 [a] | | | | |
| MgO | 41.8 | 45.3 | 43.4 | 36.4 | 43.6 | 42.1 | 3.41 | 43.4 | 41.4 | 37.2 [a] | | | | |
| CaO | 2.32 | 0.819 | 2.11 | 6.25 | 1.91 | 2.68 | 2.08 | 2.11 | 2.15 | 3.6 [a] | | | | |
| $Na_2O$ | 0.193 | 0.180 | 0.0702 | 0.319 | 0.0500 | 0.162 | 0.108 | 0.180 | 0.240 | 0.34 [a] | | | | |
| $K_2O$ | 0.0102 | 0.0200 | 0 | 0.0498 | 0 | 0.0160 | 0.0207 | 0.0102 | 0.0540 | 0.028 [a] | | | | |
| Mg# | 91.2 | 90.8 | 90.6 | 89.0 | 91.4 | 90.6 | 0.9 | 90.8 | 89.8 | 88.8 [a] | | | | |
| ***Trace elements (µg $g^{-1}$; LA-ICP-MS)*** | | | | | | | | | | | *calculated bulk* | | *calculated melt* | |
| Li | 2.22 | 1.99 | 2.10 | 1.24 | 1.05 | 1.72 | 0.53 | 1.99 | 1.5 | 1.6 | 1.4 | 1.4 | 0.302 | 0.548 |
| Sc | 12.4 | 6.9 | 10.5 | 18.4 | 11.3 | 11.9 | 4.2 | 11.3 | 12.2 | 16.2 | 14.2 | 13.0 | -2.30 | -1.76 |
| Ti | 612 | 84 | 199 | 1975 | 426 | 659 | 763 | 426 | - | 1205 | 290 | 286 | 369 | 140 |
| V | 56.0 | 28.3 | 57.4 | 86.5 | 51.8 | 56.0 | 20.7 | 56.0 | 56.0 | 82.0 | 52.6 | 48.5 | 3.43 | 7.51 |
| Cr | 3124 | 2400 | 2184 | 2603 | 2572 | 2577 | 348 | 2572 | 2690 | 2625 | 1609 | 1615 | 968 | 957 |
| Co | 97.5 | 103 | 103 | 85.9 | 96.5 | 97.1 | 6.86 | 97.5 | 112 | 105 | 108 | 113 | -10.6 | -15.0 |
| Ni | 2091 | 2373 | 2175 | 1704 | 2173 | 2103 | 246 | 2173 | 2160 | 1960 | 2231 | 2305 | -128 | -133 |
| Cu | 11.1 | 4.98 | 3.94 | 14.2 | 10.6 | 8.96 | 4.36 | 10.6 | 11.0 | 30.0 | 0.300 | 0.377 | 8.66 | 10.2 |
| Zn | 53.3 | 39.6 | 50.6 | 44.2 | 44.4 | 46.4 | 5.50 | 44.4 | 65.0 | 55.0 | 29.2 | 31.5 | 17.2 | 13.0 |
| Ga | 2.17 | 0.636 | 1.83 | 3.33 | 1.56 | 1.90 | 0.978 | 1.83 | 2.40 | 4.00 | 0.917 | 0.943 | 0.988 | 0.890 |
| Rb | 0.103 | 0.0805 | 0.0255 | 1.12 | 0.0645 | 0.278 | 0.469 | 0.0805 | 1.90 | 0.600 | 0.0250 | 0.00438 | 0.253 | 0.0761 |
| Sr | 9.89 | 1.82 | 3.13 | 34.8 | 6.08 | 11.1 | 13.6 | 6.08 | 49.0 | 19.9 | 6.63 | 4.11 | 4.51 | 1.97 |
| Y | 2.33 | 0.224 | 1.07 | 4.06 | 1.55 | 1.85 | 1.45 | 1.55 | 4.40 | 4.30 | 1.32 | 1.14 | 0.530 | 0.411 |
| Zr | 7.44 | 0.970 | 2.06 | 13.2 | 2.91 | 5.33 | 5.07 | 2.91 | 21.0 | 10.5 | 2.22 | 1.68 | 3.11 | 1.23 |
| Nb | 0.112 | 0.157 | 0.0707 | 0.843 | 0.117 | 0.260 | 0.327 | 0.117 | 4.80 | 0.658 | 0.0169 | 0.00753 | 0.243 | 0.110 |
| Cs | 0.00185 | 0.00184 | 0.00110 | 0.0122 | 0.00126 | 0.00364 | 0.00477 | 0.00184 | 0.0100 | 0.0210 | 0.00185 | 0.00178 | 0.00179 | 0.000058 |
| Ba | 1.14 | 1.49 | 0.642 | 14.5 | 1.12 | 3.78 | 6.00 | 1.14 | 33.0 | 6.60 | 0.110 | 0.00319 | 3.67 | 1.14 |
| Hf | 0.177 | 0.0182 | 0.0543 | 0.438 | 0.0813 | 0.154 | 0.170 | 0.0813 | 0.270 | 0.283 | 0.0694 | 0.0507 | 0.0845 | 0.0306 |
| Ta | 0.00710 | 0.00856 | 0.00367 | 0.0732 | 0.00526 | 0.0195 | 0.0300 | 0.00710 | 0.400 | 0.0370 | 0.00541 | 0.00114 | 0.0141 | 0.00596 |
| Pb | 0.237 | 0.183 | 1.39 | 0.443 | 0.417 | 0.534 | 0.492 | 0.417 | 0.160 | 0.150 | 0.0240 | 0.0149 | 0.510 | 0.402 |
| Th | 0.00887 | 0.0117 | 0.00587 | 0.0922 | 0.0212 | 0.0280 | 0.0364 | 0.0117 | 0.710 | 0.0795 | 0.0200 | 0.00164 | 0.00792 | 0.0101 |
| U | 0.00418 | 0.00269 | 0.00121 | 0.0177 | 0.00507 | 0.00616 | 0.00659 | 0.00418 | 0.120 | 0.0203 | 0.00590 | 0.00049 | 0.00026 | 0.00369 |
| ***REE (µg $g^{-1}$; LA-ICP-MS)*** | | | | | | | | | | | | | | |
| La | 0.251 | 0.104 | 0.098 | 1.34 | 0.216 | 0.403 | 0.530 | 0.216 | 2.60 | 0.648 | 0.281 | 0.0862 | 0.122 | 0.130 |
| Ce | 0.758 | 0.204 | 0.275 | 3.70 | 0.516 | 1.09 | 1.48 | 0.516 | 6.29 | 1.68 | 0.755 | 0.304 | 0.336 | 0.213 |
| Pr | 0.138 | 0.0261 | 0.0507 | 0.602 | 0.0804 | 0.179 | 0.240 | 0.0804 | 0.560 | 0.254 | 0.113 | 0.0532 | 0.0660 | 0.0273 |
| Nd | 0.723 | 0.105 | 0.248 | 2.96 | 0.379 | 0.884 | 1.18 | 0.379 | 2.67 | 1.25 | 0.529 | 0.299 | 0.354 | 0.0804 |
| Sm | 0.239 | 0.0273 | 0.0807 | 0.833 | 0.129 | 0.262 | 0.329 | 0.129 | 0.470 | 0.406 | 0.150 | 0.108 | 0.112 | 0.0216 |
| Eu | 0.0844 | 0.0108 | 0.0302 | 0.271 | 0.0486 | 0.0890 | 0.105 | 0.0486 | 0.160 | 0.154 | 0.0529 | 0.0422 | 0.0361 | 0.00634 |
| Gd | 0.306 | 0.0293 | 0.113 | 0.878 | 0.180 | 0.301 | 0.338 | 0.180 | 0.600 | 0.544 | 0.181 | 0.154 | 0.120 | 0.0255 |
| Tb | 0.0525 | 0.00467 | 0.0206 | 0.133 | 0.0328 | 0.0487 | 0.0502 | 0.0328 | 0.0700 | 0.0990 | 0.0324 | 0.0284 | 0.0162 | 0.00442 |
| Dy | 0.340 | 0.0321 | 0.145 | 0.743 | 0.221 | 0.296 | 0.274 | 0.221 | 0.510 | 0.674 | 0.226 | 0.199 | 0.0702 | 0.0224 |
| Ho | 0.0741 | 0.00683 | 0.0350 | 0.142 | 0.0524 | 0.0621 | 0.0510 | 0.0524 | 0.120 | 0.149 | 0.0510 | 0.0451 | 0.0110 | 0.00734 |
| Er | 0.215 | 0.0208 | 0.107 | 0.374 | 0.156 | 0.175 | 0.132 | 0.156 | 0.300 | 0.438 | 0.154 | 0.131 | 0.0209 | 0.0244 |
| Yb | 0.208 | 0.0277 | 0.120 | 0.301 | 0.154 | 0.162 | 0.102 | 0.154 | 0.260 | 0.441 | 0.166 | 0.135 | -0.0034 | 0.0194 |
| Lu | 0.0313 | 0.00499 | 0.0200 | 0.0427 | 0.0250 | 0.0248 | 0.0139 | 0.0250 | 0.0430 | 0.068 | 0.0262 | 0.0213 | -0.0014 | 0.00370 |

[a] All average spinel peridotite xenolith values are from McDonough (1990); [b] Primitive mantle (PM) values are from McDonough & Sun (1995), except where otherwise denoted, [c] Bulk rock major element measurements are taken from Alard, O. (2000).
MGam = Mt Gambier; PM = Primitive Mantle; Sp-π = Spinel-peridotite xenoliths; Lhz = Lherzolite; Hzb = Harzburgite.
Avrg = average concentration; SD = standard deviation
T[1] = Ca-opx, Brey & Köhler (1990); T[2] = 2-pyroxene, Brey & Köhler (1990); T[3] = 2-pyroxene, Wells (1977).

and MGam2 (1.01 wt% $Al_2O_3$ and 45.26 wt% MgO) the most depleted samples in this suite. The range in fertility is further reflected in the relative abundance of minerals, with olivine decreasing from 73 to 50 % and cpx increasing from 3 to 28 %, respectively. In general, when compared with primitive mantle values from McDonough and Sun (1995) our measured whole rock data show higher Mg# of 90.6 (see Table 7;

PM value 88.8), and higher oxide contents in MgO and slightly increased $Cr_2O_3$ (42.1 and 0.47 wt%, PM values: 37.2 and 0.43 wt%, respectively). However, the majority of average oxide contents are depleted relative to primitive mantle, such as $TiO_2$ (this study 0.12 wt% vs. PM 0.21 wt%), $Al_2O_3$ (2.10 vs. 4.45 wt%), CaO (2.68 vs. 3.60 wt%), $Na_2O$ (0.16 vs. 0.34 wt%) and $K_2O$ (0.016 vs. 0.028 wt%). Sample GamTR3 is the most similar of the five samples with the published primitive mantle values (oxides as well as modal abundances), however, its high $(La/Yb)_N$ value of 3.04 exceeds the recommended value of ≤2 (McDonough and Sun, 1995), and thus indicates modification by secondary enrichment processes.

The presence of accessory apatite is unlikely in the samples analysed in this study. Yaxley *et al.* (1998) showed apatite bearing xenoliths from NVP have high $CaO/Al_2O_3$ (average 2.62) in the whole-rock composition, whereas our samples have an average value of 1.16 and no apatite was observed in thin section. Also, our average value is closer to the average subcontinental lithosphere of 0.95, as reported by McDonough (1990). Another indicator for the presence of accessory apatite in peridotites is the fractionation of Ti and REE during partial melting, resulting in lower whole-rock Ti/Eu values (average 830; Yaxley *et al.* (1998)), whereas our samples yield much higher average values of 7535. Mantle-derived peridotites and primitive basalts on the other hand show no decoupling of these elements and result in Ti/Eu values similar to primitive mantle (7600 from McDonough (1990)), which is in agreement with our average Ti/Eu value of 7535.

No quantitative data for the glasses was acquired, but qualitative EDS analyses show an enrichment in $Al_2O_3$, $SiO_2$ and alkalis, which is in agreement with compositions determined in previous studies on glasses from the NVP spinel xenoliths (e.g. Yaxley *et al.*, 1997; Eggins *et al.*, 1998b).

### 3.4.3 Geochemistry of silicate mineral phases

Chemical major and trace element compositions for olivine, opx and cpx phases are given in Table 8, Table 9 and Table 10, respectively. This data array presents the most complete element set yet measured for minerals in upper mantle peridotite xenoliths, and includes several elements rarely analysed in silicate phases, particularly the volatile chalcophile and siderophile elements.

The silicate phases are homogeneous with no chemical zonation, thus, measurements for each phase were acquired in the core only. Olivine Mg#s ($100\times Mg/[Mg+Fe^{tot}]$) are high and show little variation with values ranging from 90.6–91.8, and when plotted versus modal olivine (%) the samples plot on the upper edge of the depletion array described by off-craton xenoliths (Boyd, 1989). Concentrations of Ni (3163–3268 μg $g^{-1}$), Mn (917–1114 μg $g^{-1}$), Ti (4.5–11.4 μg $g^{-1}$) and Ca (59–553 μg $g^{-1}$) are low and span a narrow range. Titanium and Ca contents fall within the range of typical pristine mantle olivines (Ti <70 and Ca <700 μg $g^{-1}$; after Foley *et al.* (2013)). Vanadium concentrations for the olivines are low (0.43–1.13 μg $g^{-1}$) and result in low V/Sc ratios (average 0.21), which indicate crystallisation in an oxidised environment (Lee *et al.*, 2005).

Table 8 Olivine major, trace and ultra-trace element concentrations from Mt Gambier peridotite xenoliths. Concentrations are averages from n analyses.

| Sample | MGam1 | MGam2 | GamTR1 | GamTR3 | GamTR4 | Avrg | SD | Median |
|---|---|---|---|---|---|---|---|---|
| Rocktype | Sp-Lhz | Sp-Hzb | Sp-Lhz | Sp-Lhz | Sp-Lhz | | | |
| *n EPMA* | *8* | *12* | *29* | *8* | *41* | | | |
| *n LAICPMS* | *16* | *6* | *8* | *10* | *8* | | | |
| ***Major elements (wt% oxide; EPMA)*** | | | | | | | | |
| **SiO2** | 40.7 | 40.8 | 40.5 | 41.0 | 40.8 | 40.8 | 0.172 | 40.8 |
| **TiO2** | 0.00408 | 0.00784 | 0.00515 | 0.00374 | 0.00714 | 0.00559 | 0.00183 | 0.00515 |
| **Al2O3** | 0.00500 | 0.00628 | 0.0129 | 0.0317 | 0.0107 | 0.0133 | 0.0107 | 0.0107 |
| **Cr2O3** | 0.0138 | 0.0267 | 0.0220 | 0.00921 | 0.0218 | 0.0187 | 0.00704 | 0.0218 |
| **FeO(tot)** | 9.29 | 8.17 | 9.50 | 9.19 | 8.74 | 8.98 | 0.530 | 9.19 |
| **MnO** | 0.151 | 0.123 | 0.157 | 0.145 | 0.130 | 0.141 | 0.0144 | 0.145 |
| **MgO** | 50.3 | 51.3 | 50.0 | 50.4 | 50.8 | 50.6 | 0.503 | 50.4 |
| **CaO** | 0.0124 | 0.0124 | 0.0116 | 0.0188 | 0.0217 | 0.0154 | 0.00456 | 0.0124 |
| **Na2O** | 0.00265 | 0.010 | 0.014 | 0.00593 | 0.00839 | 0.00823 | 0.00436 | 0.00839 |
| **K2O** | 0.00293 | 0.00471 | 0.00444 | 0.00505 | 0.00330 | 0.00408 | 0.00092 | 0.00444 |
| **NiO** | 0.401 | 0.409 | 0.367 | 0.330 | 0.337 | 0.369 | 0.03580 | 0.367 |
| **Total** | 100.9 | 100.9 | 100.6 | 101.1 | 100.8 | 100.9 | 0.197 | 100.9 |
| **Mg#** | 90.6 | 91.8 | 90.4 | 90.7 | 91.2 | 90.9 | 0.6 | 90.7 |
| ***Trace elements (µg $g^{-1}$ ; LA-ICP-MS)*** | | | | | | | | |
| **Li** | 1.91 | 1.64 | 1.64 | 1.79 | 1.56 | 1.71 | 0.139 | 1.64 |
| **Al** | 21.7 | 4.07 | 12.6 | 218 | 9.93 | 53.3 | 92.4 | 12.6 |
| **Ca** | 137 | 59.4 | 96.5 | 554 | 97.9 | 189 | 206 | 97.9 |
| **Sc** | 4.24 | 5.14 | 3.73 | 1.72 | 3.71 | 3.71 | 1.25 | 3.73 |
| **Ti** | 11.4 | 5.12 | 4.47 | 5.69 | 6.86 | 6.71 | 2.76 | 5.69 |
| **V** | 1.13 | 0.433 | 0.657 | 0.611 | 0.673 | 0.700 | 0.256 | 0.657 |
| **Cr** | 19.4 | 5.56 | 6.77 | 8.60 | 6.66 | 9.39 | 5.69 | 6.77 |
| **Mn** | 1064 | 917 | 1114 | 1022 | 936 | 1011 | 83.7 | 1022 |
| **Co** | 155 | 143 | 151 | 141 | 141 | 146 | 6.58 | 143 |
| **Ni** | 3258 | 3176 | 3179 | 3268 | 3161 | 3209 | 50.3 | 3179 |
| **Cu** | 0.363 | 0.0791 | 0.389 | 0.278 | 0.180 | 0.257 | 0.129 | 0.278 |
| **Zn** | 45.8 | 34.0 | 39.0 | 24.4 | 32.5 | 35.1 | 7.96 | 34.0 |
| **Ga** | 0.0156 | 0.00772 | 0.0103 | 0.0242 | 0.00951 | 0.0135 | 0.00669 | 0.0103 |
| **Ge** | 0.691 | 0.738 | 0.676 | 0.630 | 0.644 | 0.676 | 0.0424 | 0.676 |
| ***Ultra-trace elements (ng $g^{-1}$ ; LA-ICP-MS)*** | | | | | | | | |
| **As** | 58.4 | 66.0 | 54.4 | 73.1 | 48.8 | 60.2 | 9.56 | 58.4 |
| **Rb** | 2.83 | *3.72* | 3.40 | 129 | 3.30 | 28.4 | 56.0 | 3.40 |
| **Sr** | 0.571 | 2.05 | 0.513 | 458 | 1.44 | 92.4 | 204 | 1.44 |
| **Y** | 6.54 | 2.94 | 0.780 | 11.6 | 2.62 | 4.90 | 4.31 | 2.94 |
| **Zr** | 4.27 | 2.60 | 2.37 | 563 | 2.11 | 115 | 251 | 2.60 |
| **Nb** | 0.363 | 1.24 | 0.440 | 5.50 | 0.230 | 1.55 | 2.24 | 0.44 |
| **Mo** | 12.6 | 12.6 | 16.3 | 17.4 | 9.46 | 13.6 | 3.19 | 12.6 |
| **Ag** | 3.40 | 3.40 | 2.50 | 19.6 | 2.10 | 6.20 | 7.51 | 3.40 |
| **Cd** | 22.6 | 5.05 | 9.92 | 9.56 | 10.6 | 11.5 | 6.55 | 9.92 |
| **In** | 5.94 | 6.37 | 4.98 | 53.8 | 5.54 | 15.3 | 21.5 | 5.94 |
| **Sb** | 15.3 | 14.7 | 9.78 | 12.5 | 11.7 | 12.8 | 2.23 | 12.5 |
| **Cs** | 1.51 | 1.47 | 1.33 | 2.89 | 1.22 | 1.68 | 0.685 | 1.47 |
| **Ba** | 8.41 | 1.25 | 0.558 | 598 | 1.83 | 122 | 266 | 1.83 |
| **La** | 0.174 | 1.08 | 0.236 | 116 | 0.385 | 23.6 | 51.8 | 0.385 |
| **Ce** | 0.368 | 0.607 | 0.510 | 25.3 | 0.490 | 5.45 | 11.1 | 0.510 |
| **Pr** | 0.278 | 0.317 | 0.387 | 27.1 | 0.248 | 5.67 | 12.0 | 0.317 |
| **Nd** | 1.12 | 0.900 | 1.49 | 92.2 | 2.04 | 19.5 | 40.6 | 1.49 |
| **Sm** | 3.97 | 1.13 | 0.650 | 21.5 | 3.20 | 6.09 | 8.72 | 3.20 |
| **Eu** | 0.180 | 0.440 | 0.770 | 1.03 | 0.287 | 0.542 | 0.354 | 0.440 |
| **Gd** | 0.791 | 1.10 | 1.30 | 17.9 | 1.09 | 4.44 | 7.53 | 1.10 |
| **Tb** | 0.171 | 0.410 | 0.310 | 2.45 | 0.155 | 0.700 | 0.986 | 0.310 |
| **Dy** | 0.994 | 1.22 | 0.720 | 12.5 | 1.93 | 3.47 | 5.05 | 1.22 |
| **Ho** | 0.225 | 0.265 | 0.383 | 2.93 | 0.305 | 0.821 | 1.18 | 0.305 |
| **Er** | 0.950 | 0.723 | 0.852 | 0.380 | 1.14 | 0.808 | 0.283 | 0.852 |
| **Tm** | 0.355 | 0.0850 | 0.170 | 1.42 | 0.358 | 0.478 | 0.541 | 0.355 |
| **Yb** | 3.76 | 2.08 | 0.828 | 2.96 | 0.916 | 2.11 | 1.28 | 2.08 |
| **Lu** | 1.71 | 0.858 | 0.853 | 1.74 | 1.12 | 1.26 | 0.441 | 1.12 |
| **Hf** | 0.694 | 0.615 | 0.480 | 4.01 | 0.620 | 1.28 | 1.53 | 0.620 |
| **Ta** | 1.96 | 0.155 | 0.163 | 1.16 | 0.193 | 0.727 | 0.812 | 0.193 |
| **W** | 0.515 | *0.215* | 0.435 | 0.478 | 0.665 | 0.462 | 0.163 | 0.478 |
| **Re** | 0.154 | *0.150* | 0.240 | 0.0943 | 0.200 | 0.168 | 0.06 | 0.154 |
| **Tl** | 0.390 | *0.513* | 0.308 | 0.357 | 0.407 | 0.395 | 0.08 | 0.390 |
| **Pb** | 4.63 | 6.40 | 3.90 | 11.8 | 3.20 | 5.99 | 3.47 | 4.63 |
| **Bi** | 1.19 | *1.27* | 0.680 | 2.62 | 1.42 | 1.44 | 0.718 | 1.27 |
| **Th** | 0.240 | 0.533 | 0.172 | 4.18 | 0.155 | 1.06 | 1.75 | 0.240 |
| **U** | 0.150 | 0.330 | 0.145 | 1.82 | 0.200 | 0.529 | 0.725 | 0.200 |

*italics* represent DL values

Avrg = average concentration; SD = standard deviation; n = number of total spot analyses

Table 9 Orthopyroxene major, trace and ultra-trace element concentrations from Mt Gambier peridotite xenoliths. Concentrations are averages from n analyses.

| Sample | MGam1 | MGam2 | GamTR1 | GamTR3 | GamTR4 | Avrg | SD | Median |
|---|---|---|---|---|---|---|---|---|
| Rocktype | Sp-Lhz | Sp-Hzb | Sp-Lhz | Sp-Lhz | Sp-Lhz | | | |
| *n EPMA* | *8* | *9* | *35* | *10* | *41* | | | |
| *n LAICPMS* | *8* | *6* | *6* | *8* | *8* | | | |
| ***Major elements (wt% oxide; EPMA)*** | | | | | | | | |
| **SiO2** | 55.2 | 56.3 | 54.8 | 55.9 | 55.4 | 55.5 | 0.585 | 55.4 |
| **TiO2** | 0.143 | 0.0283 | 0.0351 | 0.0289 | 0.0956 | 0.0661 | 0.0512 | 0.0351 |
| **Al2O3** | 4.20 | 2.66 | 4.05 | 3.01 | 3.97 | 3.58 | 0.693 | 3.97 |
| **Cr2O3** | 0.605 | 0.580 | 0.563 | 0.354 | 0.596 | 0.540 | 0.105 | 0.580 |
| **FeO(tot)** | 6.02 | 5.37 | 6.22 | 6.23 | 5.75 | 5.92 | 0.364 | 6.02 |
| **MnO** | 0.150 | 0.140 | 0.162 | 0.162 | 0.140 | 0.151 | 0.0110 | 0.150 |
| **MgO** | 33.6 | 34.9 | 33.4 | 34.2 | 33.9 | 34.0 | 0.582 | 33.9 |
| **CaO** | 0.362 | 0.444 | 0.657 | 0.409 | 0.478 | 0.470 | 0.113 | 0.444 |
| **Na2O** | 0.0754 | 0.0271 | 0.0525 | 0.0209 | 0.0458 | 0.0443 | 0.0217 | 0.0458 |
| **K2O** | 0.00333 | 0.00627 | 0.00481 | 0.00348 | 0.00480 | 0.00454 | 0.00120 | 0.00480 |
| **NiO** | 0.0949 | 0.0900 | 0.0803 | 0.0559 | 0.0677 | 0.0778 | 0.0161 | 0.0803 |
| **Total** | 100.5 | 100.5 | 100.0 | 100.4 | 100.5 | 100.4 | 0.219 | 100.5 |
| **Mg#** | 90.9 | 92.1 | 90.5 | 90.7 | 91.3 | 91.1 | 0.606 | 90.9 |
| ***Trace elements (µg $g^{-1}$; LA-ICP-MS)*** | | | | | | | | |
| **Li** | 1.20 | 0.965 | 1.16 | 1.04 | 1.06 | 1.09 | 0.0963 | 1.06 |
| **Sc** | 15.5 | 16.8 | 18.9 | 16.1 | 16.4 | 16.7 | 1.31 | 16.4 |
| **Ti** | 787 | 192 | 264 | 205 | 639 | 417 | 276 | 264 |
| **V** | 94.4 | 77.7 | 108 | 89.0 | 102 | 94.2 | 11.7 | 94.4 |
| **Cr** | 3852 | 3828 | 3566 | 2257 | 4007 | 3502 | 714 | 3828 |
| **Mn** | 1088 | 952 | 1159 | 1137 | 992 | 1066 | 90.2 | 1088 |
| **Co** | 56.2 | 50.2 | 55.5 | 48.2 | 52.7 | 52.6 | 3.43 | 52.7 |
| **Ni** | 698 | 639 | 674 | 552 | 674 | 648 | 57.4 | 674 |
| **Cu** | 0.340 | 0.102 | 0.379 | 0.408 | 0.163 | 0.278 | 0.137 | 0.340 |
| **Zn** | 28.2 | 27.8 | 27.5 | 18.5 | 24.6 | 25.3 | 4.07 | 27.5 |
| **Ga** | 3.34 | 1.53 | 2.98 | 1.96 | 2.82 | 2.53 | 0.752 | 2.82 |
| **Ge** | 1.48 | 1.42 | 1.48 | 1.48 | 1.37 | 1.44 | 0.0497 | 1.48 |
| **Sr** | 0.503 | 0.0364 | 0.0713 | 0.344 | 0.224 | 0.236 | 0.194 | 0.224 |
| **Y** | 0.661 | 0.214 | 0.373 | 0.326 | 0.567 | 0.428 | 0.182 | 0.373 |
| **Zr** | 2.09 | 0.219 | 0.583 | 0.504 | 0.900 | 0.858 | 0.728 | 0.583 |
| ***Ultra-trace elements (ng $g^{-1}$; LA-ICP-MS)*** | | | | | | | | |
| **As** | 50.9 | 73.5 | 46.4 | 64.3 | 48.5 | 56.7 | 11.7 | 50.9 |
| **Rb** | 7.25 | *5.55* | *4.93* | 89.6 | *4.91* | 22.4 | 37.5 | 5.55 |
| **Nb** | 1.37 | 8.40 | 0.497 | 3.56 | 2.30 | 3.22 | 3.11 | 2.30 |
| **Mo** | 16.2 | 13.7 | 10.0 | 13.4 | 6.50 | 11.9 | 3.75 | 13.4 |
| **Ag** | 4.80 | *4.20* | 9.40 | 20.9 | 3.95 | 8.64 | 7.18 | 4.80 |
| **Cd** | 36.6 | 8.00 | 25.6 | 19.6 | 18.1 | 21.6 | 10.5 | 19.6 |
| **In** | 19.3 | 10.8 | 18.7 | 58.6 | 16.6 | 24.8 | 19.2 | 18.7 |
| **La** | 12.3 | 0.653 | 2.98 | 66.4 | 4.96 | 17.5 | 27.7 | 4.96 |
| **Ce** | 57.9 | 3.17 | 11.0 | 186.43 | 19.6 | 55.6 | 76.1 | 19.6 |
| **Pr** | 9.62 | 0.46 | 1.09 | 19.2 | 3.05 | 6.69 | 7.89 | 3.05 |
| **Nd** | 53.4 | 4.52 | 4.53 | 62.2 | 15.5 | 28.0 | 27.7 | 15.5 |
| **Sm** | 22.7 | 2.14 | 3.90 | 12.9 | 8.75 | 10.1 | 8.22 | 8.75 |
| **Eu** | 8.64 | 1.03 | 1.56 | 4.00 | 4.61 | 3.97 | 3.03 | 4.00 |
| **Gd** | 39.9 | 6.22 | 11.3 | 13.4 | 24.6 | 19.1 | 13.5 | 13.4 |
| **Tb** | 10.1 | 2.39 | 3.39 | 3.91 | 7.46 | 5.44 | 3.22 | 3.91 |
| **Dy** | 88.4 | 23.7 | 41.2 | 35.6 | 67.3 | 51.2 | 26.2 | 41.2 |
| **Ho** | 25.1 | 7.11 | 12.9 | 11.7 | 21.8 | 15.7 | 7.46 | 12.9 |
| **Er** | 96.7 | 33.4 | 55.7 | 52.0 | 81.8 | 63.9 | 25.2 | 55.7 |
| **Tm** | 20.3 | 6.70 | 12.4 | 12.0 | 17.1 | 13.7 | 5.20 | 12.4 |
| **Yb** | 167 | 70.1 | 113 | 133 | 151 | 127 | 37.6 | 133 |
| **Lu** | 31.8 | 13.6 | 23.2 | 26.4 | 28.4 | 24.7 | 6.94 | 26.4 |
| **Sb** | 16.5 | 13.2 | 16.0 | 11.9 | 16.0 | 14.7 | 2.06 | 16.0 |
| **Cs** | *2.16* | *2.07* | 3.55 | 2.08 | 1.90 | 2.35 | 0.677 | 2.08 |
| **Ba** | 0.993 | 0.865 | 0.480 | 456 | 0.663 | 91.9 | 204 | 0.865 |
| **Hf** | 67.8 | 9.55 | 21.5 | 12.0 | 34.8 | 29.1 | 23.8 | 21.5 |
| **Ta** | 0.290 | 0.220 | 0.253 | 0.587 | *0.234* | 0.317 | 0.153 | 0.253 |
| **W** | 0.730 | *0.440* | *0.580* | 0.735 | 1.92 | 0.881 | 0.593 | 0.730 |
| **Re** | 0.445 | 0.250 | 0.310 | 0.312 | 0.250 | 0.313 | 0.0796 | 0.310 |
| **Tl** | 0.750 | *0.675* | 0.270 | 0.535 | 0.340 | 0.514 | 0.207 | 0.535 |
| **Pn** | 6.50 | 10.35 | 5.17 | 55.03 | 7.18 | 16.84 | 21.43 | 7.18 |
| **Bi** | 1.65 | 1.30 | 2.74 | 1.48 | 1.28 | 1.69 | 0.606 | 1.48 |
| **Th** | 0.484 | 2.01 | 1.01 | 22.05 | 0.450 | 5.20 | 9.44 | 1.01 |
| **U** | *0.170* | 0.845 | 0.255 | 7.55 | 0.455 | 1.86 | 3.19 | 0.455 |

*italics* represent DL values

Avrg = average concentration; SD = standard deviation; n = number of total spot analyses

Table 10 Clinopyroxene major, trace and ultra-trace element concentrations from Mt Gambier peridotite xenoliths. Concentrations are averages from n analyses.

| Sample | MGam1 | MGam2 | GamTR1 | GamTR3 | GamTR4 | Avrg | SD | Median |
|---|---|---|---|---|---|---|---|---|
| Rocktype | Sp-Lhz | Sp-Hzb | Sp-Lhz | Sp-Lhz | Sp-Lhz | | | |
| *n EPMA* | *8* | *7* | *33* | *10* | *33* | | | |
| *n LAICPMS* | *8* | *6* | *8* | *10* | *8* | | | |
| ***Major elements (wt% oxide; EPMA)*** | | | | | | | | |
| **SiO2** | 51.9 | 52.9 | 52.1 | 52.7 | 52.1 | 52.4 | 0.422 | 52.1 |
| **TiO2** | 0.625 | 0.151 | 0.186 | 0.149 | 0.458 | 0.314 | 0.217 | 0.186 |
| **Al2O3** | 6.40 | 4.11 | 5.41 | 4.69 | 5.91 | 5.31 | 0.923 | 5.41 |
| **Cr2O3** | 1.28 | 1.45 | 1.13 | 0.93 | 1.30 | 1.22 | 0.195 | 1.28 |
| **FeO(tot)** | 2.01 | 1.81 | 2.27 | 2.02 | 2.01 | 2.02 | 0.163 | 2.01 |
| **MnO** | 0.0840 | 0.0972 | 0.0867 | 0.0874 | 0.0861 | 0.0883 | 0.00516 | 0.0867 |
| **MgO** | 14.6 | 15.7 | 15.0 | 15.7 | 14.7 | 15.1 | 0.540 | 15.0 |
| **CaO** | 21.0 | 22.3 | 22.1 | 22.3 | 21.9 | 21.9 | 0.526 | 22.1 |
| **Na2O** | 1.85 | 1.37 | 1.39 | 1.17 | 1.61 | 1.48 | 0.259 | 1.39 |
| **K2O** | 0.00476 | 0.00711 | 0.00297 | 0.00326 | 0.00473 | 0.00457 | 0.00164 | 0.00473 |
| **NiO** | 0.0385 | 0.0355 | 0.0305 | 0.0397 | 0.0258 | 0.0340 | 0.00579 | 0.0355 |
| **Total** | 99.8 | 99.9 | 99.8 | 99.8 | 100.1 | 99.9 | 0.109 | 99.8 |
| **Mg#** | 92.8 | 93.9 | 92.2 | 93.3 | 92.9 | 93.0 | 0.637 | 92.9 |
| **Ca#** | 0.490 | 0.489 | 0.494 | 0.487 | 0.498 | 0.491 | 0.00415 | 0.490 |
| ***Trace elements (µg $g^{-1}$ ; LA-ICP-MS)*** | | | | | | | | |
| **Li** | 0.918 | 0.703 | 1.34 | 0.441 | 0.787 | 0.837 | 0.329 | 0.787 |
| **Sc** | 60.9 | 65.6 | 72.9 | 72.4 | 57.5 | 65.8 | 6.86 | 65.6 |
| **Ti** | 3514 | 752 | 1040 | 882 | 2490 | 1736 | 1216 | 1040 |
| **V** | 253 | 219 | 277 | 271 | 253 | 254 | 22.5 | 253 |
| **Cr** | 7872 | 8757 | 6669 | 5867 | 7922 | 7418 | 1142 | 7872 |
| **Mn** | 591 | 494 | 614 | 589 | 542 | 566 | 47.9 | 589 |
| **Co** | 17.8 | 16.1 | 17.3 | 16.9 | 17.2 | 17.1 | 0.614 | 17.2 |
| **Ni** | 291 | 264 | 282 | 280 | 294 | 282 | 11.7 | 282 |
| **Cu** | 0.608 | 0.409 | 0.555 | 0.822 | 0.373 | 0.553 | 0.179 | 0.555 |
| **Zn** | 6.38 | 5.54 | 5.03 | 5.16 | 4.94 | 5.41 | 0.590 | 5.16 |
| **Ga** | 4.06 | 1.75 | 2.91 | 2.27 | 3.18 | 2.83 | 0.883 | 2.91 |
| **Ge** | 1.39 | 1.46 | 1.41 | 1.52 | 1.24 | 1.41 | 0.104 | 1.41 |
| **Sr** | 78.5 | 17.7 | 27.5 | 62.7 | 49.8 | 47.2 | 24.9 | 49.8 |
| **Y** | 16.9 | 5.48 | 8.32 | 8.62 | 12.3 | 10.3 | 4.41 | 8.62 |
| **Zr** | 52.0 | 8.52 | 12.9 | 4.70 | 20.5 | 19.7 | 19.0 | 12.9 |
| **La** | 1.72 | 0.520 | 0.544 | 3.59 | 1.04 | 1.48 | 1.27 | 1.04 |
| **Ce** | 6.84 | 1.54 | 2.04 | 8.87 | 3.67 | 4.59 | 3.16 | 3.67 |
| **Pr** | 1.30 | 0.261 | 0.385 | 1.13 | 0.642 | 0.745 | 0.458 | 0.642 |
| **Nd** | 7.27 | 1.44 | 2.09 | 4.63 | 3.61 | 3.81 | 2.31 | 3.61 |
| **Sm** | 2.43 | 0.459 | 0.733 | 1.03 | 1.27 | 1.19 | 0.761 | 1.03 |
| **Eu** | 0.859 | 0.195 | 0.283 | 0.349 | 0.503 | 0.438 | 0.261 | 0.349 |
| **Gd** | 2.92 | 0.683 | 1.03 | 1.11 | 1.81 | 1.51 | 0.889 | 1.11 |
| **Tb** | 0.498 | 0.133 | 0.198 | 0.194 | 0.325 | 0.270 | 0.146 | 0.198 |
| **Dy** | 3.30 | 0.953 | 1.35 | 1.39 | 2.23 | 1.85 | 0.938 | 1.39 |
| **Ho** | 0.687 | 0.212 | 0.315 | 0.320 | 0.487 | 0.404 | 0.186 | 0.320 |
| **Er** | 1.84 | 0.623 | 0.944 | 1.03 | 1.36 | 1.16 | 0.463 | 1.03 |
| **Tm** | 0.267 | 0.0907 | 0.138 | 0.148 | 0.189 | 0.166 | 0.0660 | 0.148 |
| **Yb** | 1.64 | 0.622 | 0.986 | 1.08 | 1.20 | 1.11 | 0.368 | 1.08 |
| **Lu** | 0.250 | 0.0865 | 0.149 | 0.156 | 0.168 | 0.162 | 0.06 | 0.156 |
| **Hf** | 1.51 | 0.277 | 0.439 | 0.167 | 0.710 | 0.620 | 0.537 | 0.439 |
| ***Ultra-trace elements (ng $g^{-1}$ ; LA-ICP-MS)*** | | | | | | | | |
| **As** | 80.8 | 97.0 | 80.7 | 101 | 65.7 | 85.1 | 14.3 | 80.8 |
| **Rb** | 10.9 | 9.10 | 8.85 | 96.0 | 12.1 | 27.4 | 38.4 | 10.9 |
| **Nb** | 46.2 | 393 | 80.5 | 171 | 52.9 | 149 | 145 | 80.5 |
| **Mo** | 2.86 | 4.07 | 8.03 | 6.85 | 6.67 | 5.70 | 2.15 | 6.67 |
| **Ag** | 5.55 | 10.2 | 5.70 | 8.07 | 4.05 | 6.71 | 2.42 | 5.70 |
| **Cd** | 111 | 79.5 | 97.5 | 92.7 | 70.3 | 90.2 | 15.8 | 92.7 |
| **In** | 50.7 | 34.4 | 45.7 | 87.9 | 35.6 | 50.9 | 21.8 | 45.7 |
| **Sb** | 25.3 | *25.0* | 32.0 | 20.7 | *23.4* | 25.3 | 4.18 | 25.0 |
| **Cs** | *2.69* | 3.10 | 2.90 | 2.00 | *3.05* | 2.75 | 0.449 | 2.90 |
| **Ba** | 30.1 | 14.5 | 11.8 | 550 | 22.2 | 126 | 237 | 22.2 |
| **Ta** | 18.1 | 30.8 | 3.27 | 74.7 | 7.59 | 26.9 | 28.8 | 18.1 |
| **W** | 1.28 | *1.02* | 3.86 | 0.967 | 1.38 | 1.70 | 1.22 | 1.28 |
| **Re** | 0.653 | *0.305* | 0.320 | 0.775 | 0.663 | 0.543 | 0.216 | 0.653 |
| **Tl** | 1.11 | *1.06* | 1.24 | 0.420 | *0.733* | 0.912 | 0.332 | 1.06 |
| **Pb** | 109 | 49.6 | 35.1 | 207 | 135 | 107 | 69.6 | 109 |
| **Bi** | 2.48 | 7.60 | 2.70 | 2.10 | 1.65 | 3.31 | 2.43 | 2.48 |
| **Th** | 8.10 | 24.9 | 14.7 | 320 | 4.76 | 74.5 | 137 | 14.7 |
| **U** | 2.27 | 5.96 | 3.80 | 91.1 | 1.34 | 20.9 | 39.3 | 3.80 |

*italics* represent DL values

Avrg = average concentration; SD = standard deviation; n = number of total spot analyses

Orthopyroxenes have high Mg# ranging between 90.5–92.1, high $Al_2O_3$ contents (2.7–4.2 wt%) and $Cr_2O_3$ (0.35–0.61 wt%), and relatively low CaO (0.36–0.66 wt%) and $TiO_2$ (0.03–0.14 wt%) concentrations. The $Al_2O_3$ and MgO (33.4–34.9 wt%) values compared with contents from a metasomatized peridotite suite in southeastern Australia in Yaxley *et al.* (1998) show that our results overlap with the field of opxs from unmetasomatised and amphibole ±phlogopite ±glass–bearing peridotite xenoliths, which is consistent with our petrographic observation.

Clinopyroxenes were all identified as Cr-rich diopsides with $Cr_2O_3$ values ranging between 0.93–1.45 wt%. Calcium oxide mass fractions are relatively high and show little variation (21.05–22.31 wt%), $TiO_2$ (0.15–0.63 wt%) and $Al_2O_3$ (4.11–6.40 wt%) show a wider range and are relatively low. Sodium oxide values vary between 1.17–1.85 wt% and are comparable to cpx values (average 1.49 ±0.15 wt%) from Eggins *et al.* (1998b).

### 3.4.4 Primitive mantle normalised incompatible elements

Figure 9 illustrates the primitive mantle (PM; McDonough and Sun (1995)) normalised rare-earth and other incompatible element distribution for bulk-rock peridotites and their minerals olivine, opx and cpx. The majority of REE whole rock concentrations are below those of the primitive mantle, with the exception of sample GamTR3, and span a wide range of concentrations. Sample GamTR4 describes an exceptionally flat REE pattern parallel to the primitive mantle but at lower levels around 0.3×PM, almost exactly matching chondritic concentrations (see Appendix A-3 for chondrite normalised REE). Samples MGam1 and GamTR1 plot slightly above and below GamTR4, respectively, and show slightly lower concentrations in La and Ce, and a rather flat distribution of remaining rare-earth elements. However, samples MGam2 (harzburgite) and GamTR3 (cpx-rich lherzolite) show the most divergent patterns in bulk composition, “bracketing” the other samples. MGam2 is the most depleted sample and describes a slightly convex pattern, with LREE enrichment decreasing towards MREEs and slightly increasing $Yb_N$ and $Lu_N$ values. GamTR3 on the other hand, is the most enriched sample, displaying enriched LREE and MREE values and continuous depletion towards HREE. The overall enriched LREE over HREE pattern in MGam2 (harzburgite) and the depletion in LREE abundances for MGam1, GamTR1 and GamTR4 (lherzolites) indicate differences in fertility of these samples. Nevertheless, a pronounced fractionation in the patterns is absent. The normalised ratio of LREE to HREE expressed as $(La/Yb)_N$ shows little variation for MGam1, GamTR1 and GamTR4, varying between 0.55–0.95, and is consistent with no metasomatic enrichment (McDonough and Sun, 1995). However, samples GamTR3 and MGam2 show an enrichment in LREE concentrations with higher $(La/Yb)_N$ ratios of 3.03 and 2.55, respectively, implying a metasomatic influence.

The primitive mantle normalised REE distribution in cpxs spans a wide range with a maximum deviation factor of 5 (e.g., Nd PM normalised value varies between 1.2 in MGam2 and in 5.8 MGam1). All samples except GamTR3 describe an almost flat pattern, with slightly lower concentrations in LREE compared to HREE. GamTR3 shows the opposite behaviour with pronounced LREE enrichment gradually

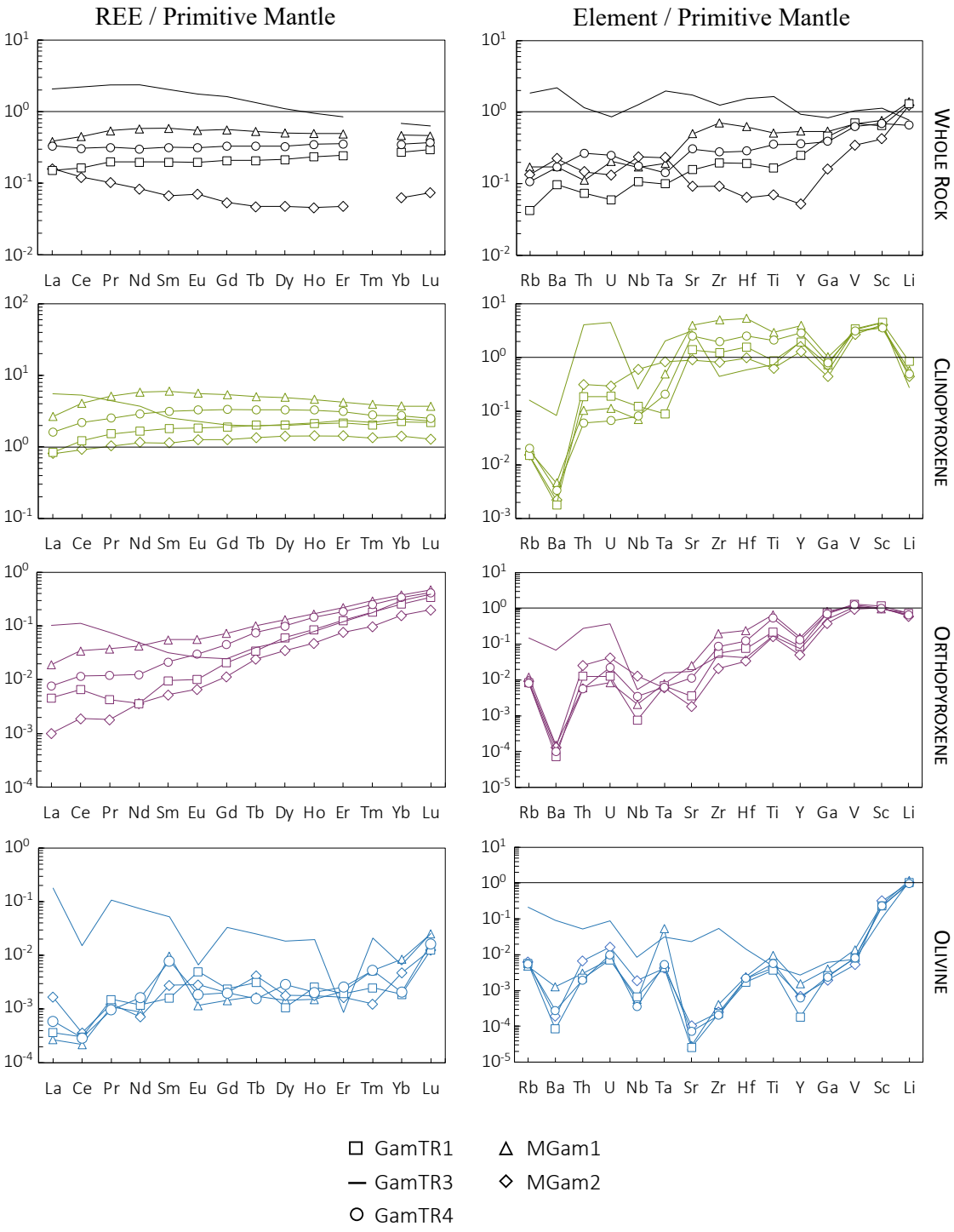


Figure 9 Primitive mantle normalised REEs and other incompatible elements for bulk-rock (black), cpx (green), opx (purple) and olivine (blue). The normalised REE bulk rock concentrations span a wide range and show a rather flat pattern plotting below the PM values, with two deviating samples describing a slightly more enriched pattern (GamTR3) and more depleted behaviour (MGam2). Clinopyroxenes span a wide range in LREE and are more confined towards HREE. They describe the same flat pattern as bulk rock data but at higher concentrations, thus determining the bulk rock pattern. Orthopyroxene shows the same behaviour as cpx, with higher variability in LREE and narrower range in HREE, however, in contrary to cpx, opx exhibits a pronounced LREE-depletion and significant increase towards HREE. Olivines show the most confined range in all incompatible elements with the lowest concentrations. The REE has a slightly increasing trend from LREE to HREE. Sample GamTR3 in all three phases exhibits a LREE enriched trend and a flat MREE–HREE in cpx, a dip in the MREE (lowest at Gd) and increasing HREE in opx and a continuously decreasing trend from LREE to HREE in olivine with negative anomalies in Ce, Eu and Er. PM values from McDonough and Sun (1995).

decreasing towards MREE and describing a flat pattern in HREE, overlapping with GamTR1. All values plot above or close to primitive mantle values. Interestingly, the cpx REE pattern in the most cpx-poor sample (MGam2) does not describe the same behaviour as its bulk-rock pattern, where the latter shows a LREE enrichment with depletion towards MREE and slight enrichment in Yb and Lu, describing a slightly convex pattern.

The REE distribution in opx shows a general depletion and higher variability in concentration in LREEs and constantly increases towards HREEs, spanning a narrower range in concentration. The La/Yb pattern is highly fractionated in opx, in comparison to cpx and olivine. However, GamTR3 describes a strongly convex pattern with a LREE and HREE enrichment and a dip in MREE.

The normalised REE distribution in olivines show lower concentrations than opx (up to 1 order of magnitude lower than opx) and cpx (2 to 4 orders of magnitude lower than cpx). In comparison to opx, the relative concentrations in olivine, with the exception of sample GamTR3, show less scatter and span a much narrower range. The La/Yb fractionation is lower than in opx, with a predominantly flat MREE pattern. Sample GamTR3 deviates from other samples and describes a steadily depleting pattern from LREE to HREE with distinct negative anomalies in Ce, Eu, Er and Yb.

Relative concentrations of incompatible, non-rare-earth elements normalised to primitive mantle values for bulk rock and silicate phases are presented in Figure 10 (right column). As in the REE plot, cpx is the defining phase for the bulk rock signal and contains the highest concentrations with olivine having the lowest contents. Orthopyroxene falls in between these phases and has concentrations similar to olivines on the more incompatible left-hand side of the plot and closer to cpx on the right-hand side. As noted by Eggins *et al.* (1998b), Li can substitute for Mg because of their similar ionic radii (0.80 and 0.82 Å) and thus is distributed equally amongst all three silicate phases.

## 3.5 Discussion

### 3.5.1 Mass balance: reconstruction of pre-metasomatic whole-rock compositions

The trace element analyses of olivine, opx and cpx were used with mineral mass fractions to calculate the whole-rock (silicate bulk) trace element compositions by mass balance shown in Figure 10. The mineral modal abundances were derived by calculating the residual least sum of squares of major oxide compositions. The lherzolite sample MGam1 shows the best match overall between measured and calculated bulk rock budget despite the significant deviation for the highly incompatible trace elements Rb, Ba, Th, U, Nb and Ta (>55 % deficit), and moderate shortages for La, Sr, Zr, Y, Lu, Ga and Li (13–40 % deficit). Samples GamTR1 and GamTR4 show a similar trend with large deficiencies (>50 %) for highly incompatible elements and deficiencies <40 % for the moderately incompatible elements. Samples GamTR3 and MGam2 display less agreement between the measured and calculated budgets. Overall, the comparison of incompatible elements normalised to primitive mantle values (from McDonough and Sun,

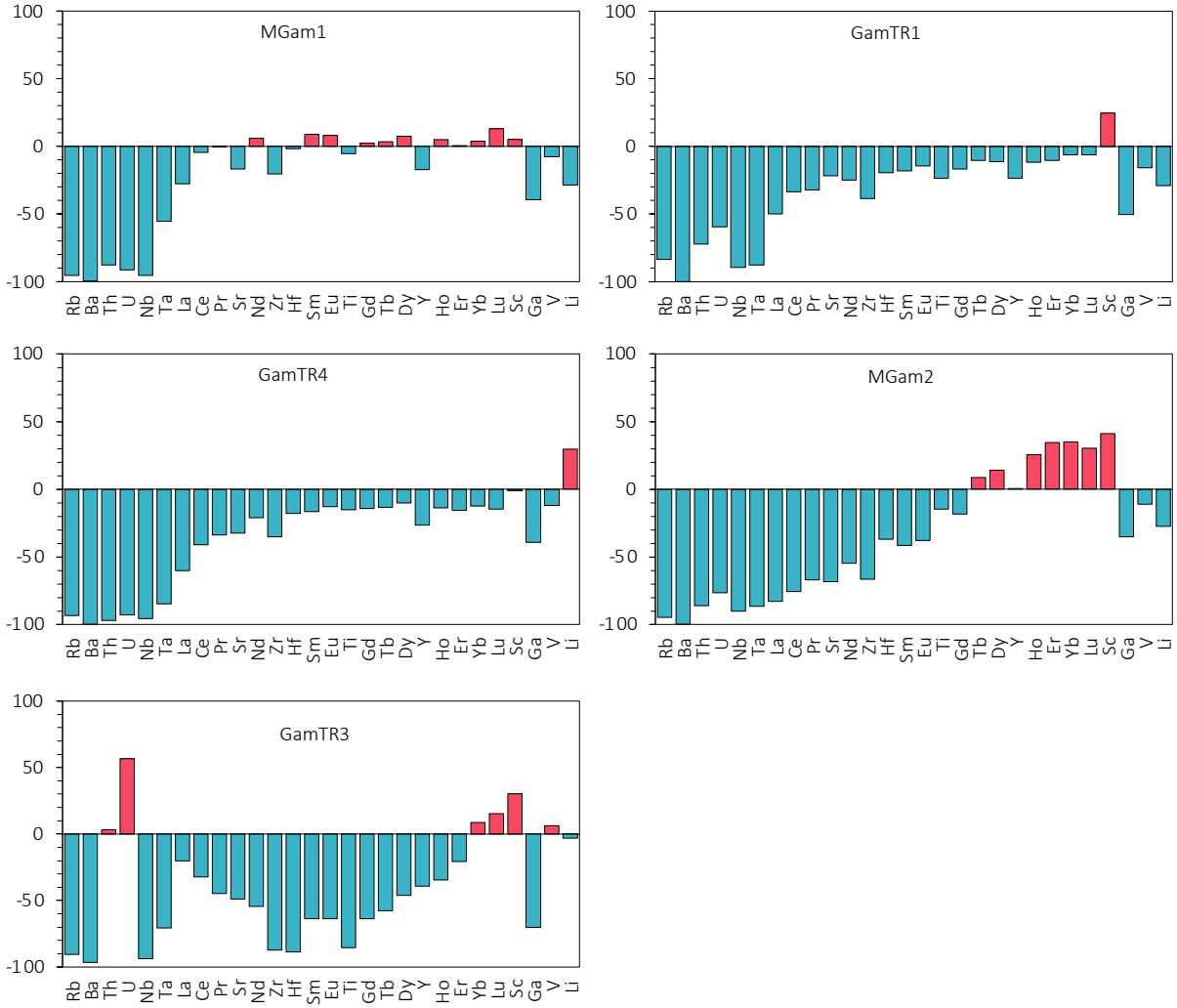


Figure 10 Incompatible element mass-balance results showing the net deficiency (blue) or excess (red) in percent, calculated from the sum of the constituent silicate phases (calculated silicate bulk) in comparison to their measured bulk rock abundances. Sample MGam1 shows the best fit, with high deficiency (>55 %) in highly incompatible elements Rb, Ba, Th, U, Nb, and Ta and a moderate (13–40 %) deficiency in La, Sr, Zr, Y, Lu, Ga, and Li, otherwise excellent (<9 %) agreement between the calculated and measured bulk. This deficiency may be explained by the presence of glass pockets, which were not measured in this study and thus are not considered.

1995) between measured and calculated bulk rock budget (Figure 11) demonstrates a strong deficiency for calculated highly incompatible elements (left-hand side) and otherwise excellent agreement for the remaining incompatible elements (right-hand side).

Figure 12 displays the relative distribution of elements between the mantle silicate phases and shows the preference of particular elements for individual phases as their major host. The order of elements for this figure was sorted by decreasing incorporation into cpx for the sample MGam1. This diagram shows that cpx is the major host for the majority of incompatible elements, even for some elements in MGam2, which has only 3% cpx. Orthopyroxene seems to be the major host for only a few minor/trace elements, including V, Cr and Ga, which is due to its relatively low modal abundance within the xenoliths coupled with low contents of most elements. In contrast, olivine incorporates the majority of chalcophile and siderophile elements (e.g., Ag, Cd, Sb, Mo, Zn) due to its high modal abundance, despite low concentrations

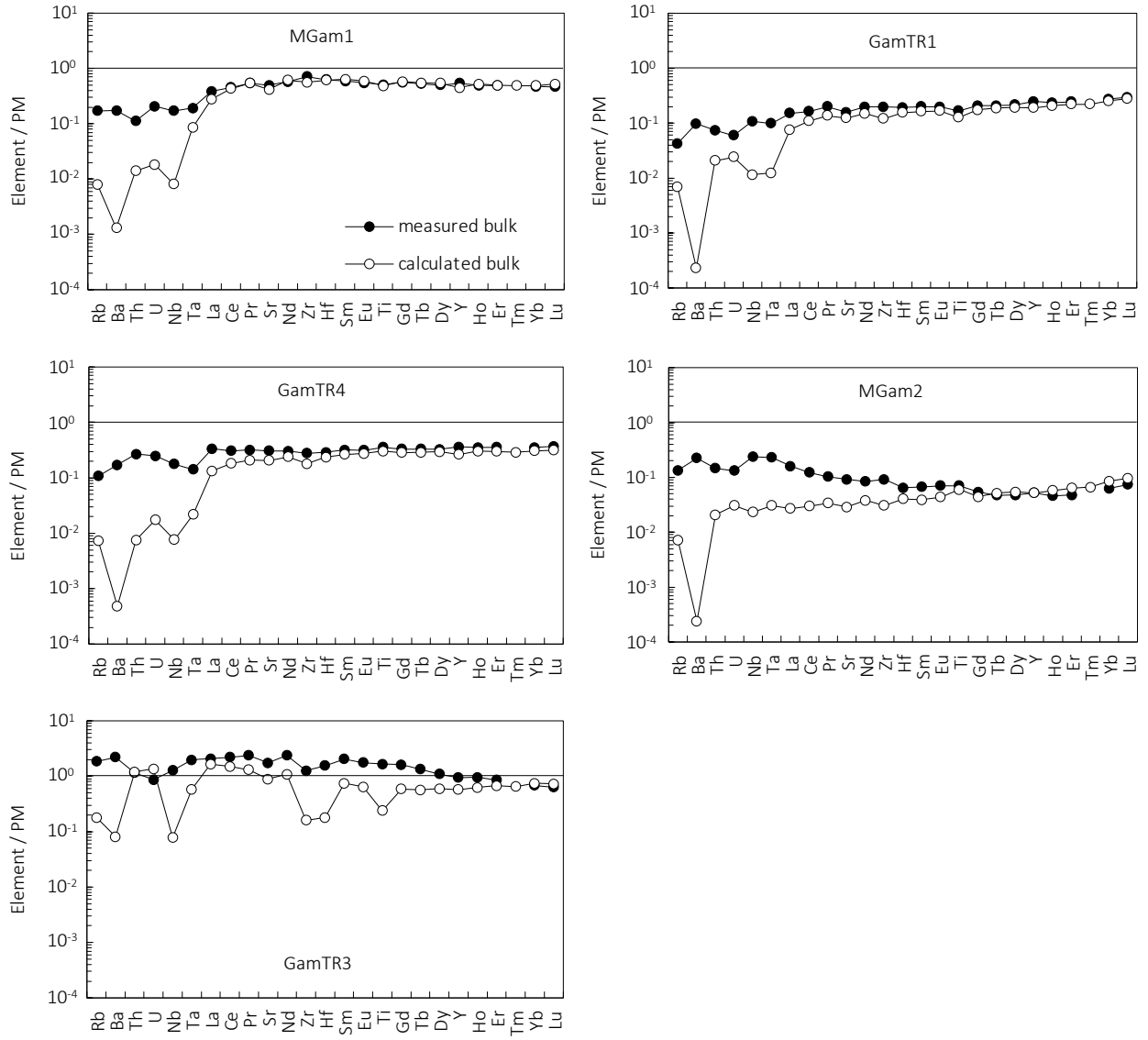


Figure 11 Comparison of measured bulk (closed circle) and calculated silicate bulk (open circle) incompatible elements normalised to primitive mantle values (McDonough and Sun, 1995). The patterns show an excellent agreement for elements on the right-hand side, and higher discrepancies on the left-hand side elements (highly incompatible) including Rb, Ba, Th, U, ±La, ±Ce. Sample MGam2 and GamTR3 show larger discrepancies between the measured and calculated bulk compositions.

of many elements. Sample GamTR3 exhibits the most distinctive distribution with cpx (28% mode) dominating the budget for many more elements with few in opx.

### 3.5.2 Comparison of reconstructed and measured rock compositions

Establishing the composition of the primitive mantle is crucial for reconstructing the composition of the Earth and has been a subject of interest for many decades. Extensive work on geochemical and isotopic composition of volcanic rocks and mantle xenoliths has culminated in our understanding that peridotite xenoliths are almost universally overprinted by metasomatic additions to the original lithospheric mantle composition and mineralogy. In order to arrive at a reasonable estimate of the original lithospheric composition, the effects of these later processes need to be stripped. One method of proceeding is by

investigating mantle xenoliths that are (relatively) unaffected by secondary enrichment events. This combined with continuing analytical progress enables the acquisition of more precise data, facilitating refinement of the geochemical composition of the lithosphere and its source.

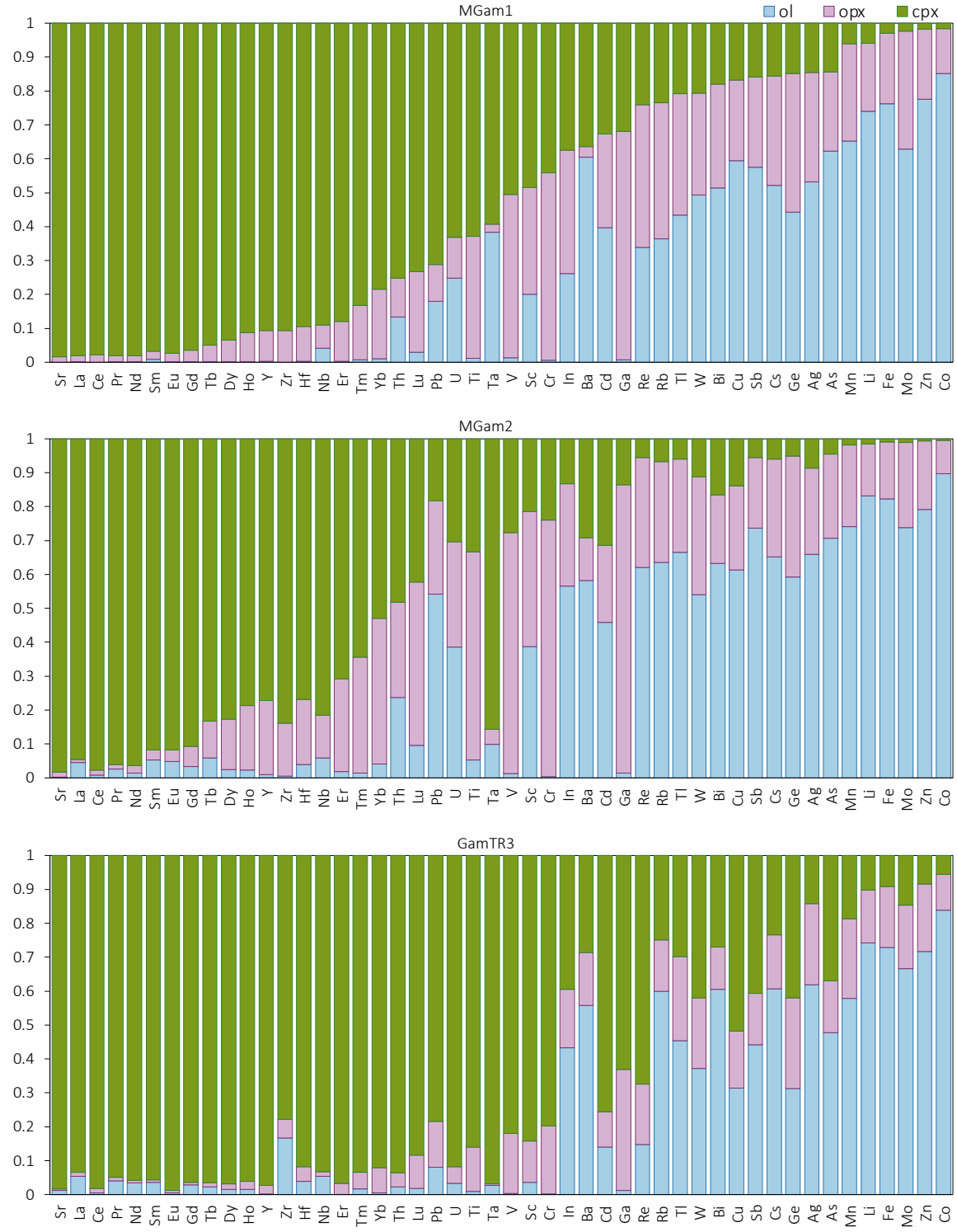


Figure 12 Representative histograms showing the fractional contribution of silicate phases to the trace-element budgets for the bulk rocks. Elements were sorted by decreasing contribution of cpx in the representative sample MGam1, thus slight variations between samples are unavoidable. The histograms demonstrate that cpx is the major host for a majority of elements, especially incompatible elements like REEs, LILEs, HFSEs, even though olivine is the major silicate phase in the mantle. Nevertheless, olivine and to a lesser degree opx are important contributors to the trace-element budget. Vanadium, Cr, Ga and ±Ti are preferentially incorporated into opx; olivines are the major hosts for some chalcophile and siderophile transition elements e.g., Ag, Cd, Sb, Mo, Zn.

The Mt Gambier mantle-derived peridotite xenoliths have exceptionally fresh and homogeneous minerals that facilitate accurate *in-situ* analysis using large ablation craters. Later metasomatism is also petrographically readily characterized in thin reaction rims and glass material along grain boundaries (Figure 8), which thus can be easily avoided during analysis. The difference between measured whole rock compositions and those reconstructed using *in-situ* analyses of minerals in combination with mass fraction estimates of minerals are illustrated in Figure 11. The main differences are in the highly incompatible elements towards the left-hand side of the plot. This difference is attributable to the unanalysed glass and reaction rims and corresponds to a trace element pattern that is strongly enriched in these elements (see 3.5.5). Eggins *et al.* (1998b) showed in their analyses that precursor amphiboles, now represented as glass pockets, are the major hosts for Ba, Nb and Ta at upper-mantle conditions, whereas spinel dominates the Ga and V budget. They also excluded exotic accessory minerals as major contributors that explain the deficient concentrations in mass balance. Thus, in this study the deficiencies of the above-mentioned elements are explained by the lack of measurements for glass and spinels. Calculations of the budget including spinel concentrations after Eggins *et al.* (1998b) show no significant improvement except for minimising the deficiencies in Ga and V, so that the contribution of spinels is considered negligible. Niobium and Ta deficiencies can be ascribed to the presence of spinels covered by thin reaction layers of mainly Ti-oxides and phlogopite, which are the main hosts for these elements (Bodinier *et al.*, 1996). During the preparation for solution bulk-rock analyses, these spinels with the reaction rims were digested and measured, whereas the calculated (silicate) whole-rock composition successfully avoids these phases.

### 3.5.3 Partition coefficients

The wide range of elements acquired here for upper mantle silicate phases presents a unique opportunity to quantify mineral partitioning in peridotites for a large number of elements, including several rarely measured elements. The partition coefficients ($D$) for mineral pairs are presented in Table 11 and summarised in Figure 13, where they are ordered by atomic number. The partitioning between opx/cpx shows the least variation between the samples; average and median values are mostly in excellent agreement. Large variation of $D^{Opx/Cpx}$ between individual samples is observed only in the highly incompatible elements Nb, Ba, Ta and LREE, and some siderophile elements Mo, Ag, W, Tl and Bi. In comparison to cpx, Li, Zn, Ge, Mo, Ag, and first row transition elements (Mn, Fe, Co, Ni) are preferentially incorporated into opx. The olivine/opx and olivine/cpx partitioning both show more scatter, especially for Sr, Zr, Nb, Ta, Ba and REEs. For the majority of the elements, average partitioning values provide a good estimate of the true partitioning value, however, for the highly scattered elements, the median values may provide a better estimate.

Relative to both pyroxenes, olivine incorporates Li, the heavier first row transition elements (Fe, Co, Ni, ±Mn), Zn and Mo more readily, as well as As, Ba and Ta relative to opx. Overall, $D^{Ol/Opx}$ show the largest scatter between samples, $D^{Opx/Cpx}$ least scatter, whereas $D^{Ol/Cpx}$ show intermediate behaviour. This implies an approach to equilibrium for opx/cpx pairs, whereas olivine may preserve earlier information.

The partition coefficients in combination with the histogram plots visualising the fractional contributions of individual phases to whole-rock budgets (Figure 12) show that cpx dominates the budget for most trace elements, as expected, even though it is the least abundant silicate phase in this suite (olivine > opx > cpx).

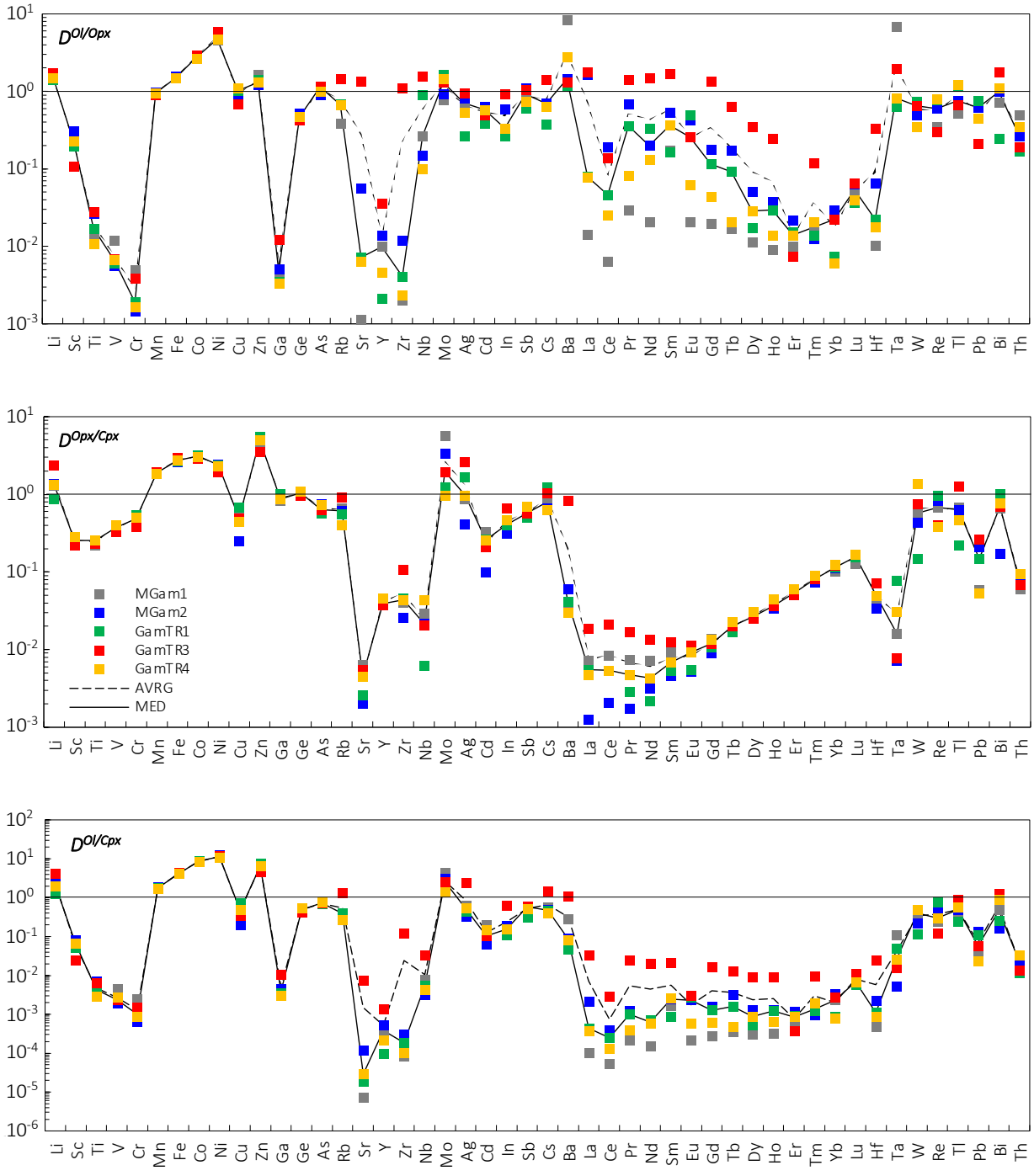


Figure 13 Partition coefficients for mineral pairs olivine/opx, opx/cpx and olivine/cpx, with calculated averages and medians.

Table 11 Calculated average and median partition coefficient values for the mineral pairs ol/opx, opx/cpx and ol/cpx.

| | Ol/Opx | | | Opx/Cpx | | | Ol/Cpx | | |
|---|---|---|---|---|---|---|---|---|---|
| | Avrg | SD | Median | Avrg | SD | Median | Avrg | SD | Median |
| **Li** | 1.58 | 0.137 | 1.59 | 1.45 | 0.545 | 1.35 | 2.34 | 1.05 | 2.08 |
| **Sc** | 0.222 | 0.0768 | 0.227 | 0.256 | 0.0222 | 0.256 | 0.0575 | 0.0213 | 0.0646 |
| **Ti** | 0.019 | 0.00754 | 0.0170 | 0.244 | 0.0150 | 0.254 | 0.00471 | 0.00184 | 0.00430 |
| **V** | 0.00741 | 0.00257 | 0.00661 | 0.370 | 0.0293 | 0.373 | 0.00274 | 0.00110 | 0.00237 |
| **Cr** | 0.00277 | 0.00157 | 0.00190 | 0.470 | 0.0596 | 0.489 | 0.00128 | 0.000726 | 0.00101 |
| **Mn** | 0.949 | 0.0305 | 0.961 | 1.88 | 0.0466 | 1.89 | 1.79 | 0.054 | 1.80 |
| **Fe** | 1.52 | 0.0305 | 1.51 | 2.77 | 0.140 | 2.71 | 4.20 | 0.177 | 4.08 |
| **Co** | 2.79 | 0.0962 | 2.76 | 3.08 | 0.141 | 3.11 | 8.58 | 0.299 | 8.73 |
| **Ni** | 4.99 | 0.533 | 4.71 | 2.30 | 0.188 | 2.39 | 11.4 | 0.482 | 11.3 |
| **Cu** | 0.930 | 0.190 | 1.03 | 0.485 | 0.160 | 0.497 | 0.462 | 0.202 | 0.482 |
| **Zn** | 1.38 | 0.151 | 1.32 | 4.69 | 0.720 | 4.98 | 6.48 | 1.15 | 6.58 |
| **Ga** | 0.00578 | 0.00374 | 0.00469 | 0.894 | 0.0767 | 0.873 | 0.00509 | 0.00317 | 0.00385 |
| **Ge** | 0.468 | 0.0340 | 0.466 | 1.03 | 0.0590 | 1.05 | 0.483 | 0.0409 | 0.499 |
| **As** | 1.07 | 0.117 | 1.14 | 0.667 | 0.0777 | 0.635 | 0.709 | 0.0298 | 0.722 |
| **Rb** | 0.771 | 0.392 | 0.672 | 0.634 | 0.192 | 0.610 | 0.533 | 0.455 | 0.384 |
| **Sr** | 0.281 | 0.588 | 0.00720 | 0.00421 | 0.00186 | 0.00450 | 0.00150 | 0.00325 | 0.000029 |
| **Y** | 0.0132 | 0.0134 | 0.00989 | 0.0414 | 0.00380 | 0.0392 | 0.000516 | 0.000496 | 0.000387 |
| **Zr** | 0.227 | 0.497 | 0.00407 | 0.0524 | 0.0317 | 0.0440 | 0.0241 | 0.0535 | 0.000184 |
| **Nb** | 0.589 | 0.621 | 0.265 | 0.0243 | 0.0136 | 0.0214 | 0.0106 | 0.0122 | 0.00546 |
| **Mo** | 1.21 | 0.356 | 1.30 | 2.64 | 1.92 | 1.95 | 2.69 | 1.13 | 2.54 |
| **Ag** | 0.651 | 0.262 | 0.708 | 1.30 | 0.846 | 0.975 | 0.867 | 0.880 | 0.519 |
| **Cd** | 0.542 | 0.103 | 0.584 | 0.232 | 0.0848 | 0.258 | 0.125 | 0.0539 | 0.103 |
| **In** | 0.483 | 0.275 | 0.333 | 0.447 | 0.134 | 0.408 | 0.236 | 0.0353 | 0.156 |
| **Sb** | 0.888 | 0.212 | 0.926 | 0.588 | 0.0791 | 0.573 | 0.521 | 0.128 | 0.586 |
| **Cs** | 0.762 | 0.376 | 0.696 | 0.872 | 0.256 | 0.805 | 0.668 | 0.440 | 0.474 |
| **Ba** | 3.03 | 3.11 | 1.45 | 0.199 | 0.353 | 0.0408 | 0.317 | 0.105 | 0.0868 |
| **La** | 0.716 | 0.802 | 0.0792 | 0.00744 | 0.00655 | 0.00548 | 0.00708 | 0.000901 | 0.000434 |
| **Ce** | 0.0809 | 0.0791 | 0.0464 | 0.00845 | 0.00738 | 0.00538 | 0.000736 | 0.00119 | 0.000250 |
| **Pr** | 0.513 | 0.303 | 0.356 | 0.00674 | 0.00609 | 0.00476 | 0.00535 | 0.000480 | 0.00100 |
| **Nd** | 0.433 | 0.597 | 0.199 | 0.00608 | 0.00454 | 0.00430 | 0.00439 | 0.000249 | 0.000627 |
| **Sm** | 0.581 | 0.174 | 0.366 | 0.00773 | 0.00320 | 0.00689 | 0.00566 | 0.000776 | 0.00247 |
| **Eu** | 0.252 | 0.211 | 0.258 | 0.00830 | 0.00277 | 0.00918 | 0.00174 | 0.00127 | 0.00226 |
| **Gd** | 0.339 | 0.0712 | 0.116 | 0.0119 | 0.00192 | 0.0120 | 0.00398 | 0.000513 | 0.00126 |
| **Tb** | 0.186 | 0.0883 | 0.0915 | 0.0197 | 0.00228 | 0.0201 | 0.00362 | 0.00155 | 0.00157 |
| **Dy** | 0.092 | 0.145 | 0.0287 | 0.0276 | 0.00262 | 0.0268 | 0.00239 | 0.00369 | 0.000867 |
| **Ho** | 0.0680 | 0.117 | 0.0298 | 0.0385 | 0.00496 | 0.0365 | 0.00251 | 0.00406 | 0.00122 |
| **Er** | 0.0136 | 0.00550 | 0.0139 | 0.0552 | 0.00422 | 0.0536 | 0.000757 | 0.000265 | 0.000835 |
| **Tm** | 0.0367 | 0.0460 | 0.0175 | 0.0823 | 0.00789 | 0.0808 | 0.00300 | 0.00370 | 0.00133 |
| **Yb** | 0.0176 | 0.0116 | 0.0222 | 0.116 | 0.00933 | 0.115 | 0.00199 | 0.00124 | 0.00230 |
| **Lu** | 0.0517 | 0.0133 | 0.0537 | 0.156 | 0.0172 | 0.157 | 0.00806 | 0.00234 | 0.00683 |
| **Hf** | 0.0900 | 0.139 | 0.0223 | 0.0498 | 0.0136 | 0.0490 | 0.00574 | 0.0103 | 0.00109 |
| **Ta** | 2.18 | 2.62 | 0.825 | 0.0279 | 0.0293 | 0.0160 | 0.0409 | 0.0518 | 0.0255 |
| **W** | 0.588 | 0.178 | 0.650 | 0.661 | 0.465 | 0.570 | 0.340 | 0.191 | 0.402 |
| **Re** | 0.565 | 0.255 | 0.600 | 0.650 | 0.258 | 0.681 | 0.380 | 0.280 | 0.302 |
| **Tl** | 0.857 | 0.338 | 0.760 | 0.654 | 0.391 | 0.639 | 0.498 | 0.137 | 0.486 |
| **Pb** | 0.549 | 0.137 | 0.618 | 0.147 | 0.0926 | 0.147 | 0.0726 | 0.0514 | 0.0569 |
| **Bi** | 0.966 | 0.557 | 0.981 | 0.666 | 0.309 | 0.705 | 0.601 | 0.310 | 0.479 |
| **Th** | 0.293 | 0.133 | 0.265 | 0.0746 | 0.0134 | 0.0689 | 0.0217 | 0.00937 | 0.0214 |
| **U** | 0.504 | 0.242 | 0.440 | 0.141 | 0.114 | 0.0828 | 0.0656 | 0.0492 | 0.0553 |

Avrg = average; SD = standard deviation

### 3.5.4 Composition of the non-cratonic sub-continental mantle

There has been more emphasis on defining the original composition and characterizing metasomatic changes for the cratonic mantle lithosphere than for younger mantle lithosphere away from the cratons, even though the latter underlies a much greater area of the continents and could therefore be viewed as "normal" sub-continental lithosphere.

The clean and homogeneous minerals in the Mt Gambier xenoliths enable reconstruction of whole-rock compositions that eliminate the infiltrated melt component. It should be emphasized here that the present work focuses on spinel-facies peridotite xenoliths only, which are representative of the upper lithospheric mantle and not the grt-facies peridotite domains that would occur at greater depths wherever the lithosphere is thicker. Nonetheless, Maaløe and Aoki (1977) suggested that spinel peridotite xenoliths may cover a range of depleted and undepleted compositions, and proposed a representative composition for the primitive mantle in the range of spinel lherzolite.

Figure 14 compares reconstructed and measured bulk average and median compositions (see Table 7 and Table 12) normalised to primitive mantle abundances (McDonough and Sun, 1995). The order of elements was chosen to show declining values for primitive mantle-normalised abundances to the left of the diagram. This plot illustrates the complete range of measured elements for the calculated whole-rock. The median and/or average of all samples demonstrate that Mt Gambier's pre-metasomatic composition is depleted in most elements relative to this proposed undifferentiated primitive mantle composition, which may represent depletion in a melt component. The divergent values between the average and median patterns (e.g., Ba, Rb, Th, Ag, In) demonstrate the degree of variation between individual samples, in which case the median values may present more accurate estimates.

The differences between measured and calculated bulk composition on the left-hand third of Figure 14 represents highly incompatible elements such as Ba, Rb, Nb, Th, U, Ta and the LREEs, which may be ascribed to the presence of infiltrated melt components (see 3.5.5), which are measured in powdered rock

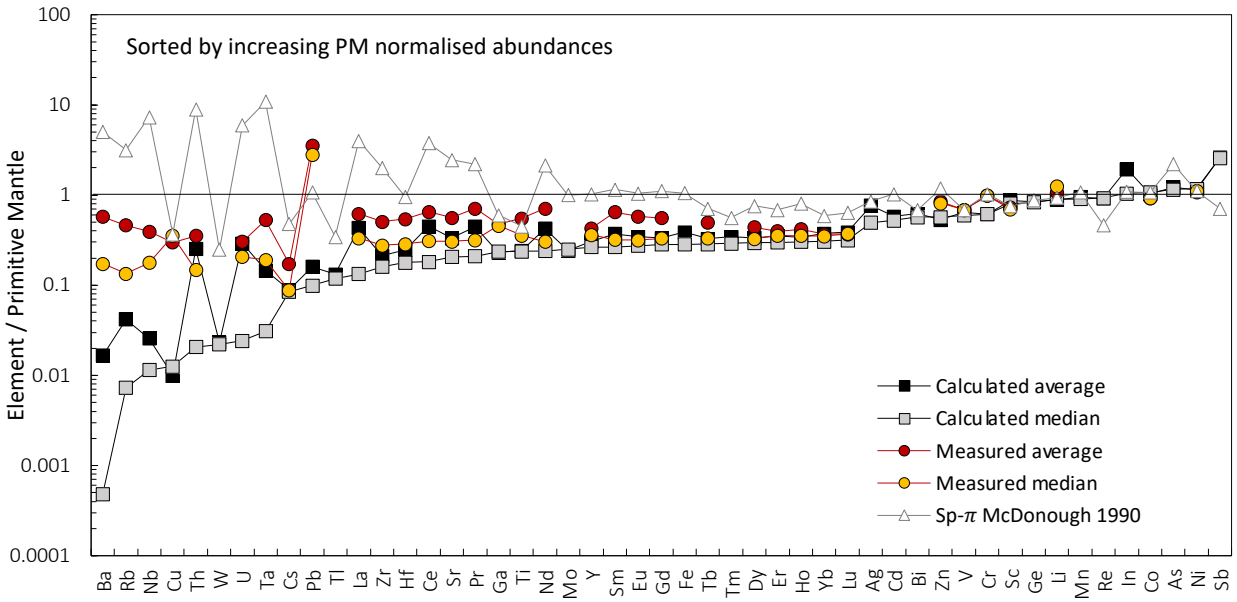


Figure 14 Primitive mantle normalised abundances of elements for reconstructed whole rock (average and median) in comparison to measured bulk rock (average and median) and published data for a spinel peridotite from McDonough (1990). The discrepancy between measured and calculated whole rock in the highly incompatible trace elements is the result of the precise *in-situ* LA-ICP-MS measurement vs. powdered rock samples, where incompatible element-enriched melt infiltrations and glass pockets cannot be excluded. Thus, the calculated whole rock abundance is stripped off the melt infiltration signal and gives a more precise composition. Primitive mantle values after McDonough and Sun (1995).

samples but may be bypassed with *in-situ* ablation analysis. Thus, the apparent deficit of these elements in the reconstructed whole rock is most probably representative of the composition of the melt infiltration, present along grain boundaries and in pockets of glass (see Figure 8).

The high discrepancy in Cu between measured and reconstructed bulk may be attributable to unanalysed sulphide minerals, which are known to occur in Mt Gambier samples (Alard *et al.*, 2000). Lead composition in measured whole rocks shows highly enriched abundances relative to the primitive mantle, however, reconstructed bulk eliminates this trend. Since Pb is a mobile element, it may be introduced by melt infiltration.

The results of this study are further compared to the published average spinel peridotite xenolith abundances from McDonough (1990), which are based on an extensive study of the composition of the continental lithospheric mantle, comprising 375 spinel peridotite xenoliths hosted in alkali basalts from continental regions. Our reconstructed bulk rock abundances are up to three orders of magnitude lower than the average spinel peridotite values for the highly incompatible elements (left-hand side of Figure 14), whereas the measured Mt Gambier whole-rock concentrations plot at intermediate values. Interestingly, the calculated and published averages demonstrate a similar behaviour for the elements Cu, W, Cs, Tl, Ga and Ti showing negative dips, whereas Ba, Nb, Th, U, Ta, Pb, La, Hf and Nd display positive anomalies. However, the zig-zag pattern of the calculated average abundances is imposed by the enriched GamTR3 sample (cpx-rich lherzolite), which is not representative of the whole spinel-peridotite xenolith suite, and for which the calculated median composition is likely to be a better estimate, eliminating the observed positive and negative dips seen in the calculated average values. The REE abundances in the analysed suite are below the primitive mantle and describe a flat trend, whereas the published spinel peridotite xenoliths show a clear LREE enrichment, intermediate MREE pattern consistent with PM values, and slightly depleted HREEs. Taking these observations in consideration, the question arises how much modification does the published average spinel peridotite reflect by enrichment processes compared to samples in this study, and is the nature of these processes evident in the differences in this plot?

The dominance of cpx for most elements is demonstrated in Figure 12 on the right-hand side with samples MGam2 (depleted harzburgite) and GamTR3 (cpx-rich lherzolite) plotting in one column for easier visual comparison. Clinopyroxene concentrates the majority of incompatible trace elements, but in case of strong mantle depletion (MGam2), significant proportions of these elements are redistributed into opx and olivine. The new full analyses of opx and olivine in the cpx-poor sample MGam2 show the sequestration sites of elements in harzburgites, when melting occurs at relatively shallow mantle levels. Figure 12 (compare MGam2 and GamTR3) demonstrates that a substantial number of elements are redistributed predominantly into opx, most strikingly Ti, V, Ga and intermediate to heavy rare-earths, and to a lesser degree Zr, Y, Th, Sc, Cr. Olivine generally dominates the elements on the right-hand side of GamTR3 (cpx-rich lherzolite) in Figure 12 with distinguished increases in Th, U, Pb, Sc, Cd, Re, Cu and Ge in the depleted harzburgite (MGam2). Combining these observations with the partitioning of elements between the silicate minerals pairs (Table 11 and Figure 13) the data suggests that olivine dominates incorporation of Li, Fe,

Co, Ni, Zn and Mo, and in cpx-free or poor samples it hosts the majority of As, Ba and Ta, whereas opx mainly hosts Mn, Ge and Ag, and in cpx-depleted samples it is also the main host for V, Cr, Ga, Y, Ce and Dy–Ho.

### 3.5.5 Distribution of chalcophile and other rarely analysed elements

At present little is known about the distribution of volatile chalcophile and siderophile elements in silicate phases from continental lithospheric mantle and their abundance in the Earth's upper mantle is poorly constrained. Probably the most comprehensive study to date is presented by Witt-Eickschen *et al.* (2009), who performed thorough *in-situ* LA-ICP-MS analysis of off-craton mantle xenoliths from different localities, focussing on the volatile trace elements Sd, Cd, Ga, In and Sn. In the present study, we used the same approach and report an even more complete set of elements in mantle forming minerals olivine, opx and cpx for the first time, enabled by the hydrogen method of LA-ICP-MS analysis. In addition to the standard major, minor and trace elements, we were able to acquire concentrations for the ultra-trace elements Cu, Ge, As, Mo, Ag, Cd, In, Sb, W, Re, Tl, and Bi in all three major minerals of the Mt Gambier spinel peridotites (Table 8, Table 9, Table 10). Cadmium and In are classified as highly volatile chalcophile elements and the remaining elements range from refractory to highly volatile siderophile elements (McDonough and Sun, 1995), although their geochemical character is highly dependent on prevailing oxygen and sulphur partial pressures, which determine their siderophile, chalcophile or lithophile affinities (e.g. Witt-Eickschen *et al.*, 2009; Wang *et al.*, 2015).

Figure 14 illustrates the bulk rock composition calculated from the individual mineral phase analyses. Antimony is the only trace element measured here that is notably enriched relative to primitive mantle. This indicates compatible behaviour in silicates and no control by, e.g. sulphides. Witt-Eickschen *et al.* (2009) demonstrated the preferred incorporation of In and Cd into cpx and amphibole, if present, whereas As demonstrates a more chalcophile nature partitioning more readily into sulphides. Our calculated average whole rock In (21 ±23 ng $g^{-1}$) and Cd (23 ±12 ng $g^{-1}$) abundances (Table 12) agree within error with the published values by Witt-Eickschen *et al.* (2009) (18 ±3 and 35 ±7 ng $g^{-1}$, respectively). Arsenic abundances in this study are consistent with compatible behaviour and are slightly higher than primitive mantle values, which indicates compatibility with silicate phases, and is not in agreement with the observations made by Witt-Eickschen *et al.* (2009). However, the high values may be explained by the very high mobility of As within the upper mantle, which was shown to be "one of the most readily transported trace elements in metasomatic fluids" (Witt-Eickschen *et al.*, 2009).

Copper is widely accepted to be a chalcophile element, but recent experimental studies proposed significant partitioning into the modally dominant silicate phases olivine and opx (Liu *et al.*, 2014), which was contradicted by Lorand and Luguet (2016), who demonstrated that Cu abundance in silicate phases is negligible and the major host remains the base metal sulphides (BMS).

Thallium is suggested to be a highly incompatible element during melting and sensitive indicator for sulphide saturation (McDonough and Sun, 1995). The high incompatibility and strong depletion of Cu and

Tl (left-hand side of Figure 14) relative to primitive mantle may be explained by the presence of sulphides in the Mt Gambier suite. This observation is further supported by the large discrepancy between measured (powdered rock samples) and calculated bulk rock abundances (Figure 14 and Table 7).

Table 12 Calculated whole rock composition for spinel peridotite xenolith suite, compared to average spinel peridotite (McDonough, 1990) and primitive mantle (McDonough & Sun, 1995) contents.

| | this study | | | (1) | (2) |
|---|---|---|---|---|---|
| | Avrg | SD | Median | Sp-$\pi$ (Avrg) | PM |
| ***Trace elements in µg g$^{-1}$*** | | | | | |
| **Li** | 1.42 | 0.144 | 1.45 | 1.5 | 1.6 |
| **Sc** | 14.2 | 5.65 | 13.0 | 12.2 | 16.2 |
| **Ti** | 290 | 197 | 286 | 540 | 1205 |
| **V** | 52.6 | 24.3 | 48.5 | 56 | 82 |
| **Cr** | 1609 | 356 | 1615 | 2690 | 2625 |
| **Mn** | 954 | 78.2 | 910 | 1084 | 1045 |
| **Fe** | 24171 | 15439 | 17812 | 65526 | 6.26 |
| **Co** | 108 | 13.8 | 113 | 112 | 105 |
| **Ni** | 2231 | 252 | 2305 | 2160 | 1960 |
| **Cu** | 0.300 | 0.150 | 0.377 | 11 | 30 |
| **Zn** | 29.2 | 7.44 | 31.5 | 65 | 55 |
| **Sr** | 6.63 | 6.83 | 4.11 | 49 | 19.9 |
| **Y** | 1.32 | 0.890 | 1.14 | 4.4 | 4.3 |
| **Zr** | 2.22 | 2.16 | 1.68 | 21 | 10.5 |
| ***Ultra-trace elements in ng g$^{-1}$*** | | | | | |
| **Ga** | 917 | 324 | 943 | 2400 | 14000 |
| **Ge** | 930 | 56.2 | 912 | 960 | 1100 |
| **As** | 61.3 | 10.9 | 57.9 | 110 | 50 |
| **Rb** | 25.0 | 46.0 | 4.38 | 1900 | 600 |
| **Nb** | 16.9 | 19.6 | 7.53 | 4800 | 658 |
| **Mo** | 12.0 | 2.11 | 12.5 | 50 | 50 |
| **Ag** | 6.10 | 5.48 | 3.94 | 7 | 8 |
| **Cd** | 23.1 | 11.5 | 20.9 | 41 | 40 |
| **In** | 21.3 | 22.9 | 11.5 | 12 | 11 |
| **Sb** | 14.3 | 1.30 | 14.2 | 4 | 6 |
| **Cs** | 1.85 | 0.333 | 1.78 | 10 | 21 |
| **Ba** | 110 | 238 | 3.19 | 33000 | 6600 |
| **La** | 281 | 445 | 86.2 | 2600 | 648 |
| **Ce** | 755 | 1016 | 304 | 6290 | 1675 |
| **Pr** | 113 | 132 | 53.2 | 560 | 254 |
| **Nd** | 529 | 531 | 299 | 2670 | 1250 |
| **Sm** | 150 | 124 | 108 | 470 | 406 |
| **Eu** | 52.9 | 40.4 | 42.2 | 160 | 154 |
| **Gd** | 181 | 132 | 154 | 600 | 544 |
| **Tb** | 32.4 | 22.3 | 28.4 | 70 | 99 |
| **Dy** | 226 | 155 | 199 | 510 | 674 |
| **Ho** | 51.0 | 34.3 | 45.1 | 120 | 149 |
| **Er** | 154 | 105 | 131 | 300 | 438 |
| **Tm** | 23.3 | 15.6 | 19.7 | 38 | 68 |
| **Yb** | 166 | 110 | 135 | 260 | 441 |
| **Lu** | 26.2 | 16.4 | 21.3 | 43 | 68 |
| **Hf** | 69.4 | 62.0 | 50.7 | 270 | 283 |
| **Ta** | 5.41 | 9.06 | 1.14 | 400 | 37 |
| **W** | 0.672 | 0.263 | 0.643 | 7 | 29 |
| **Re** | 0.257 | 0.0525 | 0.259 | 0.13 | 0.28 |
| **Tl** | 0.461 | 0.0907 | 0.414 | 1.2 | 3.5 |
| **Pb** | 24.0 | 28.1 | 14.9 | 160 | 150 |
| **Th** | 20.0 | 42.0 | 1.64 | 710 | 80 |
| **U** | 5.90 | 12.2 | 0.490 | 120 | 20 |

Avrg = average; SD = standard deviation
Sp-$\pi$ = spinel peridotite; PM = Primitive Mantle
(1) McDonough, 1990; average values of spinel peridotite xenolith suite
(2) McDonough & Sun, 1995

Tungsten is a refractory siderophile element, but in the absence of metal extraction it shows highly incompatible geochemical affinity similar to Ba, Th, U, Nb and Ta (Newsom *et al.*, 1996; König *et al.*, 2011), consistent with our observation of a highly depleted abundance relative to primitive mantle in vicinity of aforementioned elements.

The remaining elements on the right-hand third of Figure 14 demonstrate minor to moderate incompatibility with very slight depletion relative to PM, sorted by decreasing abundances in the order Re>Ge>Bi>Ag>Mo. Wang and Becker (2015) analysed Cu and Ag abundances in mantle peridotites by isotope dilution ICP-MS and demonstrated that silicate phases may host a small fraction of these elements, while sulphides remain the predominant hosts. However, our results support this as an inference but indicate Ag behaves similarly to Cd and HREE, which we interpret as cpx ±opx ±olivine as possible important silicate hosts.

### 3.5.6 Nature of the metasomatic agent

The presented whole rock data measured by solution ICP-MS and calculated whole rock composition from mineral mass abundances and trace elements in silicates acquired by *in-situ* LA-ICP-MS analyses demonstrates good agreement for moderate to mildly incompatible elements but a significant difference in highly incompatible element concentrations (Figure 10 and Figure 11). This discrepancy is attributed to the presence of melt infiltration, which is visible along grain boundaries and as glass pockets and growth of new, small cpxs (Figure 8). During sample preparation for solution ICP-MS analysis the addition of these secondary precipitations is inevitably included in the powdered rock, thus the trace element signal is "enhanced". However, *in-situ* LA-ICP-MS analysis can easily eliminate this problem by analysing clean areas on mineral phases only. The origin of these glasses has been widely debated and shall not be the main focus of this study but needs some mentioning. The difference between whole-rock and reconstituted whole rock by mass balance aided by the petrographic observations (Figure 8) quantify the metasomatic agent quite well. Previous studies have identified carbonatitic melt metasomatism in southeast Australian peridotite xenoliths, where residual peridotitic wall-rock interacts with passing carbonatitic melts. The decarbonation reaction of dolomite and opx results in the production of olivines and cpxs, changing the bulk composition towards wherlites, and precipitation of accessory apatite (e.g. Green and Wallace, 1988; Yaxley *et al.*, 1991; Yaxley, 1993). The geochemical fingerprints of the carbonatitic melt enrichment are characterised by high LREEs along with strong depletion in Ti relative to Eu, and increased Ca/Al values in the peridotites. On this basis, a carbonatitic re-enrichment in the Mt Gambier peridotite xenoliths in this study can be excluded. Ti/Eu ratios of 7535 (average) in our mantle xenoliths are close to the primitive mantle (7600; (McDonough, 1990)) and combined with low $(La/Yb)_N$ values (average 1.5) indicate no carbonatitic metasomatism. Furthermore, the influence of a carbonatitic melt can be excluded on the basis of petrographic observations and phase compositions, as no evidence of apatite or modally high cpx presence was observed.

## 3.6 Conclusions

We have determined the concentrations of major and trace elements of mantle-forming silicate phases olivine, opx and cpx in five spinel–peridotite xenoliths entrained in alkali-basalt volcanic rocks from Mt Gambier, NVP in southeastern Australia. We applied an improved LA-ICP-MS method (see Chapter 2) where hydrogen gas was admixed to the helium-sample-aerosol before mixing with Ar gas and entering the ICP. This measurement protocol enhancement has been shown to increase sensitivity (higher cps μg $g^{-1}$) and improve limits of detection (normal vs. hydrogen mode, e.g., Li: 104 vs. 45 ng $g^{-1}$, Ga: 3.2 vs. 1.6 ng $g^{-1}$, U: 0.45 vs. 0.33 ng $g^{-1}$).

The key mantle minerals olivine and opx make up 80–95% of most mantle peridotites, yet their concentration in trace elements is in μg $g^{-1}$ to ng $g^{-1}$ levels, thus making this information hard to access. However, laser ablation-ICP-MS analysis in hydrogen mode enables the determination of trace- and ultra-trace-element abundances, such as REE and the rarely analysed volatile chalcophile and siderophile elements (VCSE) in olivines and opxs. This means we can produce complete REE patterns for olivine and opx, as well as present new data on VCSE and characterise their distribution between the mantle xenolith phases olivine, opx and cpx. For this purpose, the Mt Gambier mantle xenoliths were chosen as representatives of a relatively unmetasomatised lithospheric mantle, which is supported by exceptionally fresh and clean samples with no signs of modal metasomatism. Minor melt and/or fluid infiltrations, in form of glass pockets, oxide precipitation along grain boundaries or along defects can be easily identified and avoided during *in-situ* analysis. The bulk composition of the lithospheric mantle sample beneath Mt Gambier have been reconstructed of bulk rock on the basis of mineral mass abundance estimates and measured trace elements, avoiding inclusion of elements that have been added through interaction with metasomatic melts and fluids. Our results show good agreement between reconstructed and measured bulk rock for moderate incompatible elements. A large discrepancy is observed in the highly incompatible elements, which can be explained in part by the different methods of estimating bulk rock compositions – powdered rock samples include observed glass pockets and melt infiltration along grain boundaries that are inferred to be enriched in these incompatible elements.


### ACKNOWLEDGEMENTS

This work was carried out as part of a PhD study of MV at Macquarie University and was supported by the Australian Government International Research Training Program (iRTP) Scholarship (No. 2017056). Stephan Buhre and Nora Groschopf (Johannes Gutenberg-University, Mainz) are thanked for assistance with EPMA analyses acquisition. We acknowledge Peter Wieland (MQGA) for his assistance with solution ICP-MS and Tim Murphy with his assistance with μXRF. We thank Josh Shea for his help in creating the map of eastern/southeastern Australia, Chutian Shu for his help with AMICS software and Chunfei Chen for his help with modal abundance calculations.

# CHAPTER 4

# COMPARATIVE CRATONOLOGY – TRACE ELEMENT COMPOSITIONS OF MANTLE MINERALS IN THE KAAPVAAL AND NORTH ATLANTIC CRATONS

Marina **Veter**[1]*, Stephen F. **Foley**[1,2], Olivier **Alard**[1,2,3], D. Graham **Pearson**[4], Dorrit E. **Jacob**[5]

[1] Department of Earth and Environmental Sciences, Macquarie University, NSW 2109, Australia.

[2] ARC Centre of Excellence for Core to Crust Fluid Systems, Department of Earth and Environmental Sciences, Macquarie University, NSW 2109, Australia.

[3] Géosciences Montpellier, UMR 5243, CNRS & Université Montpellier, 34095 Montpellier, France.

[4] Department of Earth and Atmospheric Sciences, University of Alberta, Edmonton, Alberta, Canada.

[5] Research School of Earth Sciences, Australian National University, Canberra, ACT 0200, Australia.

* Corresponding author: marina.veter@mq.edu.au

## ABSTRACT

A new, improved method for analysing trace and ultra-trace elements by Laser-ICP-MS enables a full palette of elements for olivine and orthopyroxene as well as the more commonly analysed clinopyroxene and garnet to be analysed *in situ* in mantle peridotites. Much more data exists for clinopyroxene and garnet because of their higher trace element abundances, but they are often introduced during later metasomatic events and so cannot record earlier events witnessed by olivine and orthopyroxene, which are the most abundant minerals in peridotites and have great potential to record differences in cratonic root formation and modification. Here, we present trace element data for minerals in cratonic mantle xenoliths from the North Atlantic craton (West Greenland) and the Kaapvaal craton (southern Africa), comparing and contrasting them with each other and with non-cratonic continental mantle xenoliths from Mt Gambier in South Australia.

The higher modal orthopyroxene content of Kaapvaal peridotites (28 ±10 %) relative to West Greenland (11 ±12%) is consistent with addition of silica in melts or fluids from a subducting slab, whereas addition of carbonate-rich melts may increase the olivine/orthopyroxene ratio by a wehrlitization reaction.

Both cratons experienced a high degree of partial melting that resulted in (i) negative correlation of Li, Mn, Co and Zn with Mg# in both olivine and orthopyroxene, (ii) similar $D^{ol/opx}$ partition coefficients for

these elements, and (iii) HREE depletion in orthopyroxene. A positive correlation of Ni in olivine with modal olivine/orthopyroxene in Kaapvaal is related to crystallization of secondary orthopyroxene at the expense of olivine during reaction with a $SiO_2$-rich melt. This is accompanied by (i) higher Al in orthopyroxenes in Kaapvaal than in West Greenland peridotites and (ii) low REE contents in orthopyroxenes. Increased light and middle REE in orthopyroxenes from both West Greenland and Kaapvaal peridotites reflect the presence of, and equilibration with, secondary clinopyroxene.

West Greenland peridotites are generally richer in Li, Ti, Ga, Zn and Cu, whereas Kaapvaal peridotites have higher P, Cr and Al. Low-level concentration trace elements acquired in hydrogen mode LA-ICP-MS demonstrate slightly higher Ag and In abundances in West Greenland peridotites, but predominantly higher Nb, Ta and Mo concentrations in Kaapvaal, and similar Cd contents in both cratons.

The calculated partitioning between olivine and orthopyroxene for the cratonic Kaapvaal and West Greenland peridotites in comparison with the off-craton peridotite xenoliths from Mt Gambier demonstrate significantly lower values of Sc, Ti, V, Cr, Ga and HREE, and higher partition coefficients for the LREE at Mt Gambier.

**Keywords:** Orthopyroxene; Olivine; trace elements; Kaapvaal craton; mantle xenoliths; North Atlantic craton; peridotite

## 4.1 Introduction

Many years of investigation into mantle xenoliths have outlined compositional differences between lithospheric mantle beneath cratons and younger areas of continental crust (Menzies, 1983; McDonough, 1990), as well as between cratons that are probably related to distinct Archaean blocks (Boyd, 1989; Pearson *et al.*, 1995; Bernstein *et al.*, 1998). The ages of cratons are traditionally thought to be Archaean and to have been stable since then primarily due to being thicker, colder, and more depleted (Fe-poor) in composition than surrounding Proterozoic and Phanerozoic areas (Pearson, 1999a; Pearson *et al.*, 2003; King, 2005). Although the surface area of cratons forms a small part of the continents, their thickness means that the volume of Archaean cratonic lithosphere is about equal to the continental lithosphere outside the cratons (Foley and Fischer, 2017). The cratonic lithosphere was assembled during a period in which the tectonic style differed from modern plate tectonics, making the processes of formation difficult to ascertain. The internal events experienced by individual cratons within the Archaean differ, and post-Archaean magmatic events have overprinted and masked geochemical evidence for many of the early events.

Xenolith samples from sub-cratonic lithospheric mantle provide evidence that cratonic roots form in several stages, beginning with high degree partial melting (40% or more), which has been interpreted by some to have occurred at low pressures (1–4 GPa) in Archaean subduction zones (Simon *et al.*, 2007a; Pearson and Wittig, 2008; Wittig *et al.*, 2008). Although the majority of peridotites from the different cratons are similar to each other in terms of high Mg# (100*Mg/[Mg+Fe]) and depletion in basaltic components such as Na, Ca and Al (Boyd and Mertzman, 1987), a major difference has been identified in whole-rock $SiO_2$ composition, which expresses itself as the ratio of modal olivine to orthopyroxene (opx). Many peridotites, notably from the Kaapvaal and Siberian cratons (Canil, 1992; Boyd *et al.*, 1997), are $SiO_2$-rich and contain considerably more opx than expected to result from the extraction of partial melt, which leads rapidly to olivine modes of 70–90% (Boyd, 1989; Herzberg, 1993). Major and trace elements, isotope compositions, element partitioning, and textural evidence indicate that much of this opx probably crystallized from a $SiO_2$-rich melt or fluid long after the major melt depletion event (Kelemen *et al.*, 1998; Bell *et al.*, 2005a; Lee, 2006; Rehfeldt *et al.*, 2008a). Other cratons, notably the Tanzania and North Atlantic cratons, have not experienced this strong opx-enrichment. Mantle peridotites from the North Atlantic craton are olivine-rich and appear to be closer to representing pristine, metasomatically unmodified depleted mantle compositions (Bernstein *et al.*, 1998; Bernstein *et al.*, 2006b; Wittig *et al.*, 2008).

Peridotites of the Kaapvaal craton and North Atlantic craton are chosen here to represent these two extremes. A third stage post-dates this opx-enrichment process, where present, consisting of one or more episodes of mineralogical change related to strong enrichments in trace elements, which are probably related to magmatic events which may or may not result in volcanism at the Earth's surface. The Kaapvaal peridotites have experienced multiple and strong metasomatic re-enrichment after silica enrichment, reflected by the reintroduction of clinopyroxene (cpx) and garnet (grt) (Simon *et al.*, 2007a; Rehfeldt *et al.*, 2008a; O'Reilly and Griffin, 2013). North Atlantic craton peridotites in West Greenland represent mantle lithosphere that has experienced extensive melt depletion during the Archaean and are generally interpreted

to have experienced only very limited secondary metasomatic overprinting. However, the effects of low-silica, carbonate-rich melts may have little effect on olivine/opx ratios whilst introducing significant amounts of trace elements (Ammannati *et al.*, 2016; Aulbach *et al.*, 2020b). The melts that cause these third-stage processes may be related to forerunners of the magmas that host the xenoliths (widely labelled as "proto-kimberlite" in Kaapvaal) or may have been active at much earlier times, intermediate between craton stabilization and the host magmatism, as occurred in several episodes in West Greenland (Larsen and Rex, 1992; Secher *et al.*, 2009).

Olivine and opx are the two most abundant minerals in mantle peridotites, especially in the subcratonic lithosphere, where they comprise an average 92 vol.% of the rocks (Pearson *et al.*, 2003). Although trace element concentrations in olivine have been sporadically documented for many years (Stosch and Seck, 1980; Glaser *et al.*, 1999; Grégoire *et al.*, 2003; Rehfeldt *et al.*, 2008a), their interpretation has mostly been neglected. Recent studies have shown that trace element concentrations in olivine can differ according to geodynamic setting, equilibration temperature and pressure, degree of melt depletion and metasomatic re-enrichment (De Hoog *et al.*, 2010; Foley *et al.*, 2013; Prelević *et al.*, 2013). Olivine compositions may record the depletion event in their compatible trace elements, and also later overprinting by reaction with passing melts (Foley *et al.*, 2013).

Trace elements in opx have been studied even less, although they have the potential to shed light on the intermediate stages of development of some cratons, namely the opx-enrichment. Furthermore, reactions of several types of melt with peridotites have recently been invoked to explain changes – both increases and decreases – in the opx/olivine ratio of peridotites: these include silica-rich melts that increase opx/olivine and carbonatitic melts that decrease opx/olivine (Yaxley *et al.*, 1991; Ammannati *et al.*, 2016). These can result in websterites and wehrlites in extreme cases (Aulbach *et al.*, 2020a; Zhang *et al.*, 2020). Thus, much of the opx in cratonic peridotites is probably secondary, and different generations may prove to be distinguishable by their trace element signatures. Previous studies on Kaapvaal mantle peridotites have shown multiple opx generations (e.g. Dawson, 2004; Bell *et al.*, 2005a) that may have different trace element compositions.

Even though cpx and grt are modally subordinate (together averaging <10 vol. %) they have been studied more intensively due to their higher concentrations of minor and trace elements (Shimizu, 1975). However, it is now recognized that cpx and grt are secondary minerals that crystallized during later metasomatic events in many peridotites, mostly during the Phanerozoic (Shimizu, 1999; Simon *et al.*, 2003; Rehfeldt *et al.*, 2008a; O'Reilly and Griffin, 2013). Their major and trace element compositions thus do not reflect primary, or even early, processes of craton formation.

In this study, we present trace element compositions of all silicate minerals from peridotite xenoliths from the North Atlantic and Kaapvaal cratons, hereafter referred to as West Greenland and Kaapvaal peridotites/samples, respectively. We systematically analysed 72 trace elements, employing an optimised method for low-level trace elements (Veter et al., Chapter 2) in order to access elements that are seldom analysed. These help to identify differences between the two cratons, between different opx generations,

and further document the differences between lithospheric mantle beneath cratons and in younger continental areas.

## 4.2 Geological setting and samples

The geological setting and development of the mantle lithosphere of the North Atlantic and Kaapvaal cratons is summarized in Table 13. We report here data for 14 selected peridotite xenoliths from the northern edge of the North Atlantic craton in West Greenland (Figure 15) that form part of a previously studied set (Wittig *et al.*, 2008). These were chosen to represent the whole geochemical range of northern margin North Atlantic craton mantle peridotites. All contain minor amounts of cpx (<2.5%). Samples with Mg# <89 were excluded, as they have been interpreted to have experienced FeO enrichment by later melts (Wittig *et al.*, 2008). The 23 Kaapvaal craton samples selected from Kimberley and Jagersfontein include 9 cpx-free and 14 cpx-bearing peridotite xenoliths (Table 14). Most are previously unstudied or reported in (Rehfeldt *et al.*, 2008a), supplemented by three samples from the Erlank and Gurney collections. Literature data was used to complete information presented for the North Atlantic craton (Bernstein *et al.*, 2006b; Wittig *et al.*, 2008) and Kaapvaal craton peridotites (Grégoire *et al.*, 2002; Grégoire *et al.*, 2003; Simon *et al.*, 2003; Dawson, 2004; Van Achterbergh, 2004; Simon *et al.*, 2007a; Rehfeldt *et al.*, 2008a).

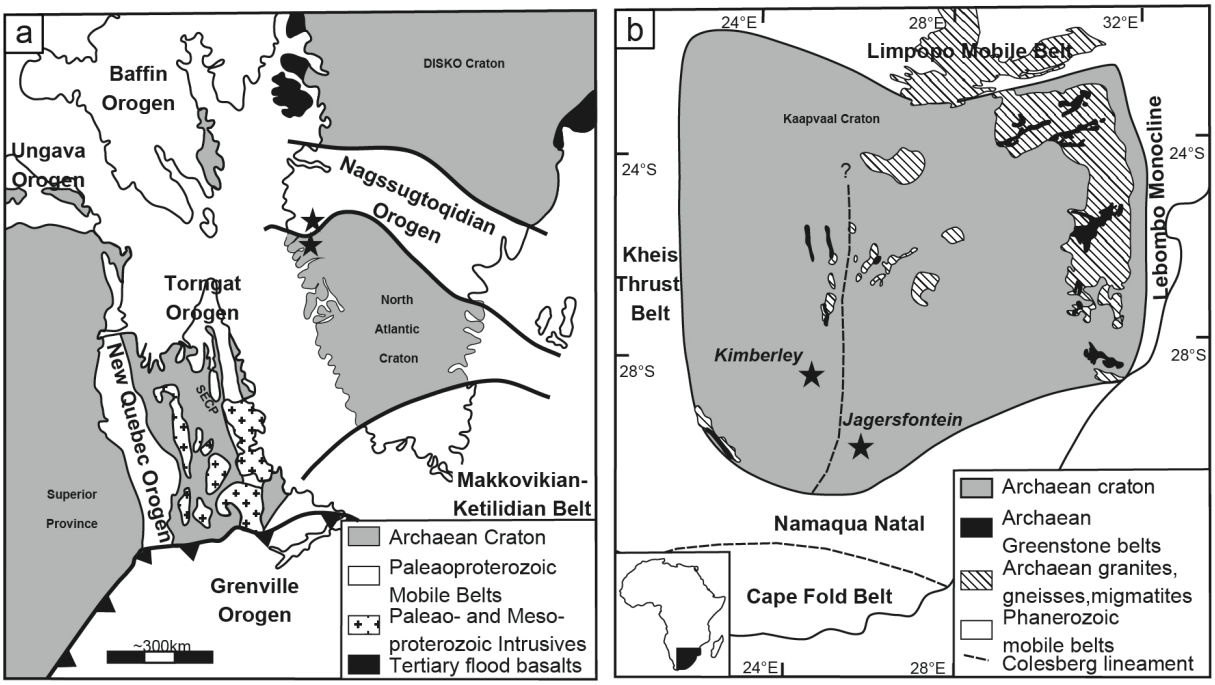


Figure 15 Simplified geological maps of Kaapvaal and North Atlantic cratons. (a) the Archaean North Atlantic and adjacent cratons (modified after Connelly et al., 2000 and Tappe et al., 2006) and (b) the Kaapvaal craton (modified after Rehfeldt et al., 2008). Sample localities are indicated with black stars. Abbreviations: SECP = Southeast Churchill Province.

Table 13 Comparison of the geological development of the Kaapvaal and North Atlantic cratons.

| | | Kaapvaal craton | | | | North Atlantic craton | | | |
|---|---|---|---|---|---|---|---|---|---|
| | | **Crustal evolution**[1. 2. 3. 4] | | **Cratonic root evolution** | | **Crustal evolution**[17. 18. 19. 20] | | **Cratonic root evolution** | |
| **Formation and stabilization** | | **~3.5 Ga** | Ancient Gneiss and southern Barberton terrain. Oldest rocks of the eastern Witwatersrand block. | **>2.5-3.6 Ga** | Several episodes of partial melting[5. 6. 7. 8. 9] | **~3.8 Ga** | Amîtsoq gneiss and Ameralik dyke swarm in west Greenland | | |
| | | **3.2-3.3 Ga** | Oldest crust component in the western Kimberley block. | **3.2-3.3 Ga** | Diamond formation[10] | **2.7-2.8. 2.9-3.0. 3.2. 3.6. 3.8 Ga** | Stages of continental crustal accretion | **2.7-3.3 Ga** | High degree partial melting[21. 22] |
| | | **2.88-2.94 Ga** | Amalgamation of Kimberley and Witwatersrand block by subduction convergence | **~2.9 Ga** | Subduction-related metasomatic silica and trace element enrichment[7. 8. 11] and diamond formation[10. 12. 13] | **~2.7 Ga** | Terrane assembly by continent-continent collision Stabilization and separation from border zones | | |
| | | **2.7-2.8 Ga** | Post-tectonic granites and Venterstorp extension and volcanism | | | **>2.8 Ga** | Granulite or amphibolite-facies metamorphism | **2.6-2.3 Ga** | FeO-enrichment overprinting[22] |
| **Modification** | **old** | **2.0 Ga** | Intrusion of the Bushveld complex at northern margin | **2.0 Ga** | Cryptic Fe-. Ti. and Al-enrichment[14] and diamond formation[12]. | **2.0 Ga** | Kangamiut dyke swarm emplacement | **2.0 Ga** | Melt extraction and metasomatic enrichment[22] |
| | | | | **1.5-1.9 Ga** | | | | | |
| | | | | **1.3-1.8 Ga** | Multiple metasomatism by subduction-related fluid phase[9] | **~1.8 Ga** | Ketilidian orogen accretion at the southern margin | | |
| | | **50 Ma-1.6 Ga** | Group I kimberlite magmatism | **1.15 Ga** | Diamond formation with eclogitic inclusions[12] | **1.1-1.3 Ga** | Alkaline and carbonatitic intrusions related to the Gardar rift | | |
| | **young** | | | **400 Ma** | Melt metasomatism[9] | **555-585 Ma** | Kimberlite volcanism at northern margin | **Kimberlite emplacement** | Low degree metasomatic addition of pyroxene and reequilibration of mineral and isotopic composition[22] |
| | | **~200 Ma** | Karoo flood basalt magmatism | **~200 Ma** | Diopside crystallization from kimberlite-like melt[7. 8. 15] | **150-200 Ma** | Kimberlite volcanism at southern margin | | |
| | | **110-200 Ma** | Group II kimberlite magmatism occurring only locally | **~90 Ma** | MARID and cryptic metasomatism of near vein assemblages[8. 16] | **47-61 Ma** | Rifting and passage of Iceland mantle plume along eastern Greenland | **Iceland plume related** | Modal metasomatism and reequilibration in eastern Greenland xenoliths[23] |

1 De Wit *et al.* (1992). 2 Anhaeusser and Walraven (1999). 3 Poujol *et al.* (2003). 4 Schmitz *et al.* (2004b). 5 Pearson *et al.* (1995). 6 Carlson *et al.* (1999b). 7 Simon *et al.* (2007b). 8 Rehfeldt *et al.* (2008b). 9 Lazarov *et al.* (2009). 10 Shirey *et al.* (2003). 11 Bell *et al.* (2005b). 12 Richardson *et al.* (1993). 13 Jagoutz *et al.* (1984). 14 Hoal (2003). 15 Griffin *et al.* (2003). 16 Konzett *et al.* (1998b). 17 Oxford-Isotope-Geology-Laboratory and McGregor (1971). 18 Bridgwater *et al.* (1973). 19 Nutman *et al.* (2004). 20 Holm and Prægel (2006). 21 Bernstein *et al.* (2006a). 22 Wittig *et al.* (2010b). 23 Hanghøj *et al.* (2001a)

### 4.2.1 North Atlantic craton

The North Atlantic craton is exposed in parts of Greenland, Labrador and northwest Scotland and is surrounded by early Proterozoic mobile belts of the Nagssugtoqidian and Torngat Orogens to the north and west and the Makkovikian-Ketilidian Belt to the south (Figure 15a). It is dominated by high-grade gneisses that developed from trondhjemite-tonalite-granodiorite (TTG) protoliths interpreted to be of subduction-related origin (Steenfelt *et al.*, 2005). The oldest rocks of the North Atlantic craton occur as the ~3.8 Ga old Amîtsoq gneisses located in the Færingehavn terrane of Greenland (Black *et al.*, 1971) and the Uivak Gneiss in the Saglek area of northern Labrador (Komiya *et al.*, 2015). The North Atlantic craton is characterized by several stages of continental crust accretion at 3.8 Ga, 3.6 Ga, 3.2 Ga, 3.0–2.9 Ga and 2.8–2.7 Ga (Steenfelt *et al.*, 2005) and stabilization occurred at approximately 2.7 Ga (Friend *et al.*, 1988).

Mineralogical and chemical overprinting of the North Atlantic craton lithospheric mantle could have occurred during any of several episodes of incomplete rifting. The first at ca. 2.0 Ga is represented at the surface by the Kangamiut dyke swarm in Greenland (Nutman *et al.*, 1999), but is also detected in the isotopic signatures of ≈1.4 Ga olivine lamproites in Labrador, interpreted to reflect the formation of pyroxenites in the lower lithosphere (Tappe *et al.*, 2007). This second phase (ca. 1.4–1.1 Ga) led to alkaline and carbonatitic intrusions associated with the Gardar rift and olivine lamproites of the Canadian mainland (Tappe *et al.*, 2007; Secher *et al.*, 2009) and was followed by a break of ≈500 million years by extensive carbonate-rich magmatism (ultramafic lamprophyres and carbonatites) at 585–555 Ma on both margins of the Labrador Sea (Larsen and Rex, 1992; Tappe *et al.*, 2007; Secher *et al.*, 2009). The final opening of the Labrador Sea resulted in further kimberlites, lamprophyres, nephelinites and melilitites (200-115 Ma) that post-date the magmatism that brought the samples of this study to the surface. Rifting of cratons is generally associated with a prolonged history of carbonate-rich melt mobilization at the base of cratons, linked to later focusing of carbonate-rich magmatism in rifts and at their margins (Foley *et al.*, 2012; Foley and Fischer, 2017). Evidence for these magmatic episodes may be stored as enrichment events in xenoliths.

Mantle peridotites occur at several localities in the North Atlantic craton; the Wiedemann Fjord in East Greenland (Bernstein *et al.*, 1998) from the northern and southern cratonic margins in West Greenland (Emeleus and Andrews, 1975; Bizzarro and Stevenson, 2003; Wittig *et al.*, 2008), and from Baffin Island (Fig.1; Kopylova *et al.*, 2019). Also, mantle xenoliths from Ubekendt Ejland in the Disko Province further north (Figure 15a) show similar features to mantle peridotites of the North Atlantic craton (Bernstein *et al.*, 2006b), exhibiting high modal olivine and low opx contents (Bernstein *et al.*, 1998; Bernstein *et al.*, 2006b; Wittig *et al.*, 2008) with high Mg# (average 92.7), high whole-rock Mg/Si but low Al/Si, $Al_2O_3$ and CaO contents. These features are characteristic for the North Atlantic cratonic mantle and have been interpreted to reflect extensive melt depletion (>40%; Bernstein *et al.*, 1998; Bizzarro and Stevenson, 2003; Wittig *et al.*, 2008).

Low heavy rare earth element (HREE) abundances in the peridotites have been explained by high degree melting at depths shallower than grt stability related to a subduction zone (Wittig *et al.*, 2008).

Rhenium-Os and PGE analyses indicate that this strong depletion occurred in two episodes at 2.7– 3.2 and 2.0 Ga, and a few West Greenland mantle xenoliths document interaction with an Fe-rich basaltic liquid at 2.3–2.6 Ga (Wittig *et al.*, 2008; Wittig *et al.*, 2010a). The low modal opx and consequent low bulk-rock $SiO_2$-contents discount significant later modification by siliceous melts or fluids. West Greenland peridotites show only minor metasomatic addition of cpx ±grt (Hanghøj *et al.*, 2001b; Wittig *et al.*, 2008); Hf-Nd ages indicate that this event is of Phanerozoic age, probably related to kimberlite emplacement. Overall, the mantle lithosphere beneath the North Atlantic craton seems to have mostly escaped post-Archaean deformation and has experienced only very limited metasomatic overprinting compared to the Kaapvaal mantle.

### 4.2.2 Kaapvaal craton

The Kaapvaal craton of southern Africa is surrounded by Proterozoic mobile belts (Figure 15b). Its oldest rocks are in the Ancient Gneiss Complex of Swaziland (~3.7 Ga; Kröner *et al.*, 1996) (Table 13) and it was compiled during several episodes of crust assembly (De Wit *et al.*, 1992), the youngest marked by westward subduction along the Colesberg lineament at ~2.9 Ga which fused the western and eastern blocks (Schmitz *et al.*, 2004a). At the northern margin of the Kaapvaal craton, collision with the Zimbabwe craton at 2.7 Ga (De Wit *et al.*, 1992) led to the formation of the Limpopo mobile belt. The Kaapvaal craton was essentially stable by ~2.7 Ga.

Mg-rich mineral compositions, high Cr# (100*Cr/[Cr+Al]) in spinels, low whole-rock CaO and $Al_2O_3$ contents, depleted HREE compositions and low Re and Os concentrations are evidence of strong depletion by up to 40% melt loss, for which Re-depletion ages cluster around 2.9 Ga (Griffin *et al.*, 1999b; Grégoire *et al.*, 2003; Simon *et al.*, 2007a; Lazarov *et al.*, 2009). Several episodes of partial melting between 3.6 and >2.5 Ga ago can be identified from Lu-Hf and Sm-Nd isotopes of subcalcic grts from Finsch (Lazarov *et al.*, 2009), and many studies document disturbance of the Re-Os isotope system during and after the Archaean (Carlson *et al.*, 1999a; Rehfeldt *et al.*, 2007; Simon *et al.*, 2007a).

Kaapvaal mantle peridotites have been studied extensively and appear to show a more complex petrogenetic history than those of the North Atlantic craton (Nixon and Boyd, 1973; Gurney and Harte, 1980; Erlank, 1987; Hawkesworth *et al.*, 1990), including a similar Archaean episode of depletion by melt loss, but multiple metasomatic re-enrichments, including some of the first recognized as mantle metasomatism (Gurney *et al.*, 1975; Harte *et al.*, 1975). Proterozoic modification of the SCLM was related to several regional events, most notably the intrusion of the Bushveld complex (2.05 Ga; Buchanan *et al.*, 2004), but with minor kimberlitic events at 1.6 and 1.1 Ga (Allsopp *et al.*, 1989). Strong metasomatic overprinting is indicated by (i) high modal opx (Bell *et al.*, 2005a; Simon *et al.*, 2007a; Pearson and Wittig, 2008; Wasch *et al.*, 2009), (ii) addition of cpx and grt, frequently with amoeboid textures (Erlank, 1987; Rehfeldt *et al.*, 2008a; O'Reilly and Griffin, 2013), (iii) oxygen isotope and trace element disequilibria between minerals (Zhang *et al.*, 2000; Rehfeldt *et al.*, 2008a), and (iv) disturbance of several radiogenic

isotope systems with ages clustering at 2.1–1.3 Ga and 400–200 Ma (Simon *et al.*, 2007a; Lazarov *et al.*, 2009).

### 4.2.3 Petrographic observations

The characterisation of lithologies followed the traditionally used terminology for Kaapvaal craton kimberlites, where all cpx-bearing peridotite xenoliths are termed lherzolites, to reflect metasomatic input, and cpx-free xenoliths are classified as harzburgites. Garnet-bearing samples are indicated with the prefix grt, if composition was >1 %, two harzburgites from Kaapvaal have grt modal abundances of 0.2 % (DJ0224) and 0.4 %(KIM4) and are indicated as harzburgite only. The modal abundances are summarized in Table 14.

Figure 16 shows photomicrographs of studied lithologies observed in Kaapvaal and West Greenland samples, indicating the variety in rock types and texture that range from refractory dunites to grt-bearing lherzolites. This variability in samples demonstrates the heterogeneity of mantle xenoliths and sampling bias. Generally, peridotite xenoliths in this sample set from West Greenland and Kaapvaal exhibit similar petrographic textures, but differ in frequency, i.e., samples from Kaapvaal are predominantly granular with only three sheared fine-grained samples (total n=23), compared to West Greenland (n=14) with 7 granular/porphyroclastic and 7 sheared samples (Table 14). These contrasts are also expressed in the

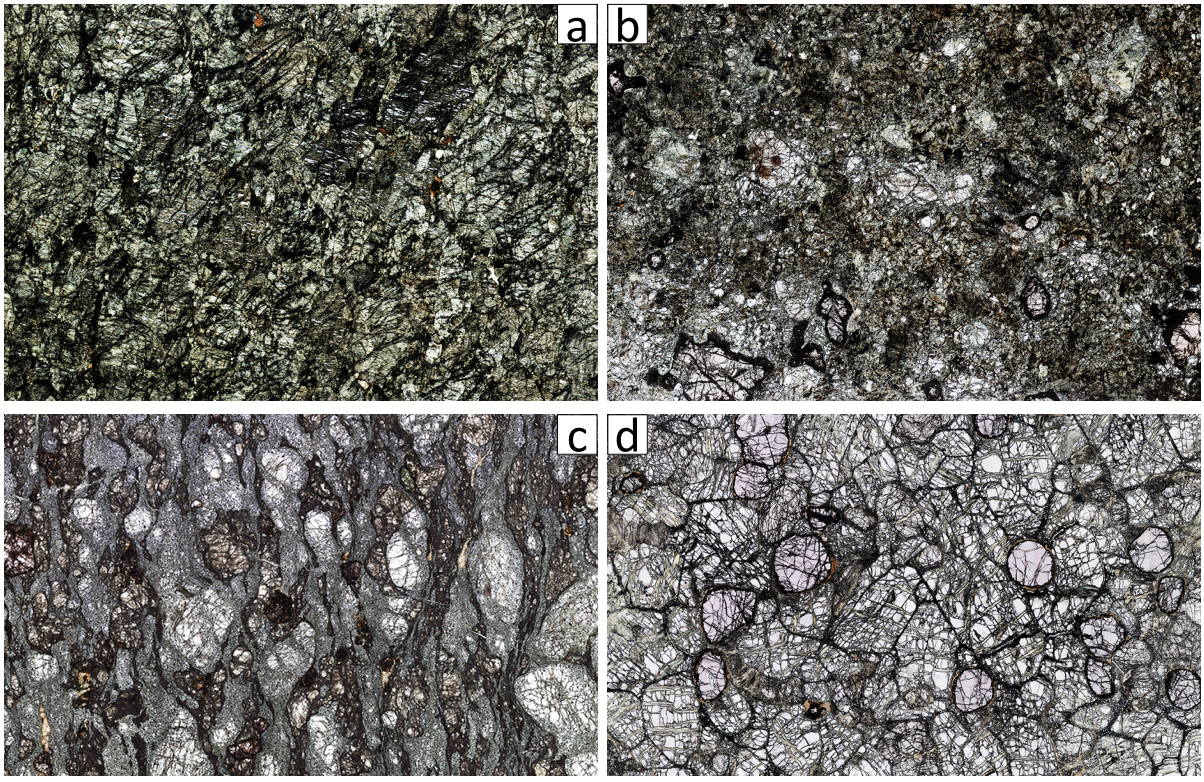


Figure 16 Representative photomicrographs of West Greenland (a–b) and Kaapvaal (c–d) peridotites. (a) shows sample 474544, a dunite with predominantly olivine and some minor phlogopite and spinel minerals; (b) shows a grt-harzburgite (474575) with highly kelyphitized grts; (c) is a sheared porphyroclastic grt-harzburgite with olivine, opx and grt as the major porphyroclasts and olivine and opx as fine-grained matrix; (d) sample KIM.FLOOR, equigranular grt-harzburgite with coarse olivine, opx and rounded grts.

diversity of modal composition and in the chemical characteristics between the two cratons. Kaapvaal samples are predominantly grt-bearing harzburgites and lherzolites with coarse granular to porphyroclastic textures and clearly distinctive olivine, opx, cpx and grt phases ±phlogopite and ±spinel grains. Samples DJ0277, DJ0298 and DJ2104 are sheared, with fine-grained olivine neoblasts and porphyroclastic olivine, opx ±grt (Figure 16). The amoeboid and vermicular texture of grt and cpx is evident of their later introduction. West Greenland peridotite lithologies in this sample set are harzburgites and dunites that may carry secondary grt and to a lesser degree cpx and phlogopites. The samples display largely sheared textures with olivine, opx and ±cpx and ±grt as common porphyroclastic minerals, and exhibit to a lesser degree granular to porphyroclastic textures (Figure 16).

West Greenland peridotite xenoliths in this study are comprised of dunites, harzburgites, lherzolites and one wehrlite. The modal composition in olivine ranges from 59.5–99.7 % (Table 14). Orthopyroxene contents are generally <24.4 %, with the exception of sample 474577 for which a modal abundance of 32.6 % is reported. Clinopyroxene abundances are very low (<0.7 %), with sample 474557 demonstrating the highest content of 2.5 %. Garnet-bearing samples report abundance of <5.4 %. In contrast, Kaapvaal peridotite lithologies in this sample set are predominantly lherzolites and harzburgites, with one dunite (Table 14). Modal contents of olivine in Kaapvaal samples range between 47.0 and 86.4 %, with the highest content in sample DJ2104 (dunite) of 97.6 %. Orthopyroxene modal abundances range between 1.4–38.5 % and are slightly higher compared to West Greenland peridotites. Clinopyroxene abundances are predominantly <4 %, except two samples where cpx modal content values of 15.5 % (AJE464) and 28 % (DJ0262) are reported. Garnet contents in Kaapvaal are <9.6 % and comprise mostly fresh grains, displaying only slight kelyphitization, opposed to usually strongly kelyphitized grts in West Greenland peridotites (Figure 16b, d).

## 4.3 Analytical methods

### 4.3.1 Electron microprobe

Minerals were analysed for major elements by electron microprobe at the Department of Geosciences, University of Mainz, Germany (JEOL JXA 8900 RL) using wavelength dispersive analysis and a range of natural and synthetic standards (see Appendix A-1 for operating parameters and list of standards). Quantitative data was acquired using the standard silicate routine with 105 s acquisition time per point including the major elements Mg, Si and Fe and the minor elements Na, Al, Cr, Mn Ti, K, Ca and Ni. The operating parameters were set at 15 kV acceleration voltage, 12 nA beam current and 2 µm probe diameter. The data were corrected using the CITZAF procedure (Armstrong, 1995), and detection limits are between 0.01 and 0.07 wt.%.

Table 14 Modal abundance (vol%), textural information and geothermometry for analysed Kaapvaal and West Greenland peridotite xenoliths.

| | | | modal composition | | | | | | | *T* [°C] | | |
|---|---|---|---|---|---|---|---|---|---|---|---|---|
| Sample | Rocktype | Texture | Ol | Opx | Cpx | Grt | Phl | Oxides | Others | 2-px | Ca-opx | Ol-grt |
| ***Kaapvaal Craton*** | | | | | | | | | | | | |
| *cpx- & grt-free* | | | | | | | | | | | | |
| AJE407 | Hzb | granular | 84.0 | 14.0 | 0 | 0 | 0 | 0.3 | 1.8 | - | 951 | - |
| DJ0250 | Hzb | granular | 76.5 | 23.1 | 0 | 0 | 0 | 0 | 0.4 | - | 952 | - |
| DJ2104 | Dun | sheared fine-grained, ol neoblast | 97.6 | 1.4 | 0 | 0 | 1.0 | 0 | | - | 1176 | - |
| *cpx-free & grt-bearing* | | | | | | | | | | | | |
| DJ0203 | Grt-hzb | granular | 67.8 | 27.3 | 0 | 4.5 | 0.4 | 0 | 0 | - | 846 | 1393 |
| DJ0224 | Hzb | granular | 61.9 | 37.6 | 0 | 0.2 | 0 | 0 | 0.3 | - | 1063 | - |
| DJ0254 | Grt-hzb | granular | 50.6 | 38.5 | 0 | 8.5 | 2.4 | 0 | 0 | - | 875 | 1210 |
| DJ0264 | Grt-hzb | granular | 85.5 | 12.5 | 0 | 1.3 | 0.4 | 0 | 0.3 | - | 780 | 1061 |
| KIM4 | Hzb | granular | 63.0 | 34.4 | 0 | 0.4 | 2.1 | 0 | 0.01 | - | 804 | - |
| KIM.FLOOI | Grt-hzb | granular | 71.5 | 18.6 | 0 | 9.6 | 0.4 | 0 | 0 | - | 902 | 1326 |
| *cpx-bearing & grt-free* | | | | | | | | | | | | |
| AJE439* | Lhz | granular | 73.6 | 21.5 | 4.0 | 0 | 1.0 | 0.03 | 0 | 878 | 849 | - |
| AJE464 | Lhz | granular | 76.5 | 8.0 | 15.5 | 0 | 0 | 0 | 0 | 1130 | 1001 | - |
| DJ0278 | Lhz | granular | 64.9 | 32.7 | 0.2 | 0 | 2.2 | 0 | 0 | 743 | 804 | 1023 |
| KDJ6 | Lhz | granular | 69.8 | 24.7 | 3.6 | 0 | 1.7 | 0.1 | 0.1 | 877 | 822 | - |
| YC2 | Lhz | granular | 57.1 | 36.1 | 2.5 | 0 | 5.7 | 0.1 | 0 | 1062 | 768 | - |
| *cpx- & grt-bearing* | | | | | | | | | | | | |
| DJ0205* | Grt-lhz | granular | 54.1 | 35.6 | 1.4 | 9.0 | 0 | 0 | 0 | 761 | 796 | 1053 |
| DJ0261 | Grt-lhz | granular | 57.0 | 24.6 | 3.6 | 8.3 | 1.1 | 5.4 | 0 | 903 | 816 | 1076 |
| DJ0262* | Grt-lhz | granular | 47.0 | 19.8 | 28.0 | 2.2 | 2.2 | 0 | 0.8 | 892 | 835 | 1143 |
| DJ0277* | Grt-lhz | sheared fine-grained, ol neoblast | 59.9 | 35.5 | 0.05 | 3.2 | 0.8 | 0 | 0.6 | 980 | 886 | 1161 |
| DJ0298 | Grt-lhz | sheared fine-grained, ol neoblast | 75.8 | 20.4 | 0.01 | 2.9 | 0.9 | 0 | 0 | 1244 | 1001 | 1266 |
| DJ02152 | Lhz | granular | 70.3 | 26.2 | 0.5 | 2.6 | 0.4 | 0 | 0 | 822 | 809 | - |
| JJG6356* | Grt-lhz | granular | 86.4 | 9.4 | 0.7 | 2.8 | 0 | 0.5 | 0.3 | 1127 | 967 | 1224 |
| KDJ5* | Grt-lhz | granular | 58.9 | 33.1 | 3.3 | 4.7 | 0 | 0.03 | 0 | 879 | 840 | 1119 |
| KIM5 | Grt-lhz | granular | 55.5 | 34.7 | 2.3 | 1.7 | 5.8 | 0 | 0.01 | 1060 | 929 | 1235 |
| *MIN* | | | *47.0* | *1.4* | *0* | *0* | *0* | *0* | *0* | *743* | *768* | *1023* |
| *MAX* | | | *97.6* | *38.5* | *28.0* | *9.6* | *5.8* | *5.4* | *1.8* | *1244* | *1176* | *1393* |
| ***North Atlantic Craton - West Greenland*** | | | | | | | | | | | | |
| *cpx- & grt-free (±opx-free)* | | | | | | | | | | | | |
| 474544 | Dun | sheared fine-grained | 99.7 | 0 | 0 | 0 | 0.1 | 0.2 | 0 | - | - | - |
| 477421 | Dun | porphyroclastic, UML | 59.5 | 0 | 0 | 0 | 2.7 | 1.9 | 35.9 | - | - | - |
| 488802 | Dun | granular, UML | 97.8 | 0 | 0 | 0 | 0.7 | 0.1 | 1.5 | - | - | - |
| 488836 | Dun | sheared coarse, UML | 88.8 | 0 | 0 | 0 | 1.4 | 0 | 9.8 | - | - | - |
| 474570* | Dun | granular | 97.0 | 2.8 | 0 | 0 | 0 | 0 | 0.2 | - | 984 | *1174*[#] |
| *cpx-free &grt-bearing* | | | | | | | | | | | | |
| 474573 | Grt-dun | sheared coarse | 97.6 | 0 | 0 | 2.4 | 0 | 0 | 0 | - | - | 1374 |
| 474538 | Grt-hzb | sheared fine-grained | 71.2 | 24.4 | 0 | 4.4 | 0 | 0 | 0 | - | 1032 | 1472 |
| 474575 | Grt-hzb | granular, porphyrocalstic | 72.3 | 22.1 | 0 | 5.4 | 0.1 | 0 | 0.1 | - | 979 | 1391 |
| *cpx-bearing ±grt-free* | | | | | | | | | | | | |
| 474557 | Weh | sheared coarse | 92.6 | 0 | 2.5 | 0 | 4.5 | 0 | 0.4 | - | - | - |
| 474527* | Grt-lhz | granular | 86.3 | 11.7 | 0.7 | 1.3 | 0 | 0 | 0 | 1246 | 1085 | - |
| 474545* | Grt-lhz | sheared fine-grained, porphyrocl | 77.9 | 19.5 | 0.4 | 1.6 | 0 | 0 | 0.6 | 1140 | 925 | 1208 |
| 474551* | Grt-lhz | granular | 74.9 | 21.9 | 0.1 | 2.6 | 0 | 0.4 | 0 | 1224 | 1008 | 1366 |
| 474555* | Grt-lhz | granular | 76.1 | 21.1 | 0.5 | 1.7 | 0 | 0 | 0.5 | 1197 | 1036 | 1272 |
| 474577* | Grt-lhz | sheared coarse, porphyroclastic | 65.7 | 32.6 | 0.5 | 1.0 | 0 | 0 | 0.2 | 1278 | 1149 | - |
| *MIN* | | | *59.5* | *0* | *0* | *0* | *0* | *0* | *0* | *1140* | *925* | *1208* |
| *MAX* | | | *99.7* | *32.6* | *2.5* | *5.4* | *4.5* | *1.9* | *35.9* | *1278* | *1149* | *1472* |

Modal compositions were determined with µXRF elemental map distribution at MQGA (Macquarie University), using AMICS software for calculation of phases mod%. T(2-px) = Brey & Kohler, 1990; T(Ca-opx) = Brey & Kohler, 1990; T(Ol-grt) = O'Neill & Wood, 1979. – = not available; Ol = olivine; Opx = orthopyroxene; Cpx = clinopyroxene; Grt = garnet; Phl = phlogopite; Hzb = harzburgite; Lhz = lherzolite; Dun = dunite; Weh = wehrlite; UML = ultramafic lamprophyre. * Samples that were used for $H_2$ mode LA-ICP-MS analyses; [#] T(ol-grt) calculated with concentrations acquired for micro-grt with EPMA, but too small for LA-ICP-MS and µXRF analyses

### 4.3.2 Laser Ablation – Inductively Coupled Plasma – Mass Spectrometry (LA-ICP-MS)

Quantitative minor and trace element compositions of olivine, opx, cpx and grt were determined by LA-ICP-MS in the facilities of Macquarie GeoAnalytical (MQGA), at the Department of Earth and Environmental Sciences, Macquarie University in Sydney, the Department of Geosciences, Mainz University and the GeoZentrum Nordbayern, University of Erlangen-Nuremberg. The analytical equipment and measurement conditions from all institutions are detailed in Appendix B-1. Analyses were carried out on polished thick sections (~100 µm thick) with ablation spot sizes for olivines varying between 110–85 µm, and pyroxenes and grts between 85–50 µm diameter, depending on grain size. The ablation was

performed in a helium atmosphere with He as the only carrier gas (Jacob, 2006) and before entering the torch mixed with Ar as make-up gas. Plasma torch conditions were optimised so that ThO/Th ratios were <0.5%; no further corrections for oxide production were applied.

GLITTER software (Macquarie University, Sydney) was used for automated data processing of time-resolved LA-ICP-MS raw data using NIST SRM 612 glass as external standard (Jochum *et al.*, 2011). Internal standardization used $^{29}Si$ for olivine and opx and $^{43}Ca$ for cpx and grt analyses with $SiO_2$ and CaO wt% concentrations calculated from electron microprobe analyses. The accuracy of results was confirmed by analyses of USGS reference glass BCR-2G (Jochum *et al.*, 2006) (Appendix B-2). The analyses carried out in Mainz and Erlangen also analysed several USGS reference glasses, GSA-1G, GSC-1G, GSD-1G and GSE-1G; the measured values are mostly within the range of elemental concentrations given by USGS preliminary results (Appendix B-2). The isotopes $^{66}Zn$ and $^{63}Cu$ were used to avoid interferences (Foley *et al.*, 2011).

Additional analysis with the improved measurement method in hydrogen mode (Veter et al., Chapter 2) was applied on six samples from each locality, Kaapvaal and West Greenland. The measurements were carried out using an 8900 Agilent Triple Quadrupole ICP-MS in single MS mode coupled with a Photon Analyte G2 193nm ArF Excimer laser system equipped with a HelEx II Cell in the facilities of Macquarie GeoAnalytical (MQGA). The operating parameters were set at 10 Hz repetition rate, 5–7 J $cm^{-2}$ laser fluence and 60 s ablation time following 150 s of gas blank measurement. Spot sizes varied between 110–85 µm for olivines and between 85–65 µm for both pyroxenes and grts, depending on grain size. A set of 72 masses was acquired in two separate analysis programs, focussing on 'standard' silicates including REE and 'transition' silicate elements including volatile chalcophile and siderophile elements. Quantitative concentrations were acquired by automated data reduction with GLITTER software, where NIST 612 was used as the external standard for calibration of measurements and $^{29}Si$ as the internal standard with $SiO_2$ wt% values previously determined by EPMA. A detailed description of the operating parameters and analysis programs is presented in Appendix A-1.

## 4.4 Results

### 4.4.1 Modal analyses and whole rock composition

The modal abundances (vol%) of minerals in the xenoliths for Kaapvaal and West Greenland samples were determined with a Bruker M4 Tornado Micro-XRF (µXRF) by acquiring elemental distribution maps that were used to identify different phases and extract mineral spectra, which were imported into the AMICS (Advanced Mineral Identification and Characterization System) software to calculate the modal distribution of the phases. The acquired modal abundances and mineral major and trace element concentrations from fresh core analyses were used to calculate the whole rock compositions and are presented in Table 15. The advantageous reconstruction of bulk rock composition avoids kimberlite

infiltrations, of which small amounts were shown to modify the incompatible element composition in the xenoliths (Barth *et al.*, 2001). The bulk rock abundances from West Greenland are more refractory with high MgO and FeO (45.7 and 7.8 wt%) and low $SiO_2$, $Al_2O_3$, and CaO (40.7, 0.33 and 0.26 wt%, respectively) contents. In contrast, the Kaapvaal samples have higher $SiO_2$, $Al_2O_3$ and CaO (44.7, 0.80 and 0.76 wt%, respectively) and lower MgO and FeO (44.9 and 6.3 wt%) values. Thus, North Atlantic craton peridotite xenoliths exhibit higher Mg/Si ratio compared to Kaapvaal, which is supported by the divergent opx/ol between the two cratons. This difference is expressed in a space of Mg# vs. olivine modal abundance (after Boyd, 1989) shown in Figure 17, where the two localities are clearly separated. Both cratons follow the oceanic depletion trend terminating at the refractory end characterised by high Mg# and high olivine mod%. The majority of Kaapvaal samples plot off the 'oceanic trend' predominantly towards lower modal olivine at slightly decreasing Mg# (Figure 17). This trend reflects opx enrichment (green arrow) that does not change the Mg-rich nature of the peridotites. West Greenland, on the other hand, are clearly separated from Kaapvaal predominantly plotting to the lower left, with a higher range in Mg# but principally preserving higher modal olivine contents.

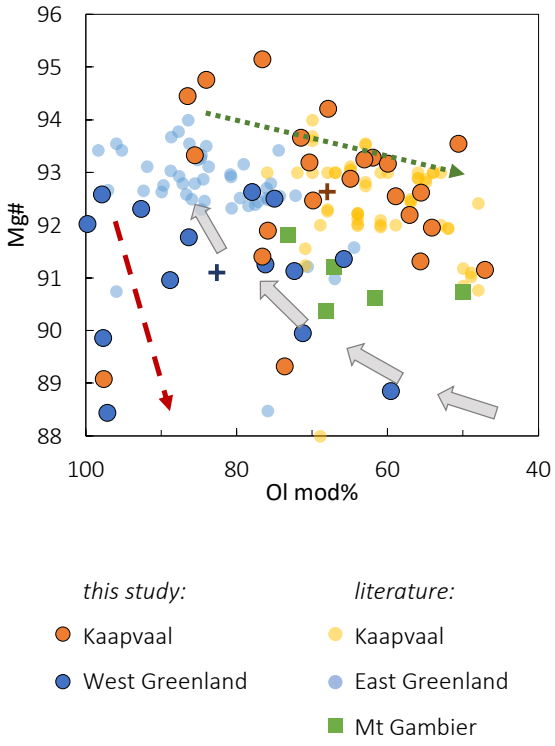


Figure 17 Mg# (100*Mg/(Mg+Fe)) versus modal olivine in peridotite xenoliths from West Greenland (dark blue this study; light symbols Bernstein et al., 1998) and Kaapvaal (dark orange this study; light symbols Simon et al., 2003; Simon et al., 2007). The 'oceanic trend' (grey arrows) reflects enrichment in modal olivine and Mg # during partial mantle melting (Boyd, 1989). The trend for opx-enrichment (green arrow) is taken from Bell et al. (2005).

### 4.4.2 Major element composition of minerals

Representative major and trace element compositions for Kaapvaal and West Greenland olivines are presented in Table 16 and Table 17, and for opx in Table 18 and Table 19, respectively. Element compositions for cpx and grt are included in the Electronic Supplement B2.

Table 15 Reconstructed Kaapvaal and West Greenland whole rock major and trace elements calculated from mineral modal abundances (mod%) and measured major (EPMA) and trace element (LA-ICP-MS) compositions in hydrogen mode.

| | Kaapvaal | | | | | | West Greenland | | | | | |
|---|---|---|---|---|---|---|---|---|---|---|---|---|
| Sample | AJE439 | DJ0205 | DJ0262 | DJ0277 | JJG6356 | KDJ5 | 474527 | 474545 | 474551 | 474555 | 474570 | 474577 |
| Rocktype | Lhz | Grt-lhz | Grt-lhz | Grt-lhz | Grt-lhz | Grt-lhz | Grt-lhz | Grt-lhz | Grt-lhz | Grt-lhz | Dun | Grt-lhz |
| ***Major element (wt%)*** | | | | | | | | | | | | |
| **$SiO_2$** | 44.0 | 47.6 | 46.5 | 46.1 | 42.3 | 46.8 | 42.5 | 44.0 | 44.4 | 44.1 | 40.5 | 45.8 |
| **$TiO_2$** | 0.0315 | 0.0121 | 0.0605 | 0.0288 | 0.0300 | 0.0160 | 0.0672 | 0.0300 | 0.0473 | 0.0896 | 0.0334 | 0.0156 |
| **$Al_2O_3$** | 0.122 | 2.22 | 1.26 | 0.926 | 0.528 | 1.41 | 0.106 | 0.403 | 0.536 | 0.448 | 0.0253 | 0.246 |
| **$Cr_2O_3$** | 0.134 | 0.340 | 0.632 | 0.293 | 0.430 | 0.357 | 0.133 | 0.283 | 0.503 | 0.293 | 0.0552 | 0.219 |
| **FeO** | 9.21 | 6.75 | 6.02 | 5.78 | 5.24 | 6.29 | 7.53 | 6.66 | 6.63 | 7.80 | 11.08 | 7.23 |
| **MnO** | 0.140 | 0.140 | 0.108 | 0.108 | 0.0886 | 0.119 | 0.115 | 0.115 | 0.114 | 0.129 | 0.143 | 0.124 |
| **MgO** | 44.3 | 41.5 | 35.6 | 44.6 | 49.6 | 43.8 | 47.6 | 47.5 | 46.8 | 46.2 | 47.7 | 44.5 |
| **CaO** | 0.886 | 0.811 | 5.88 | 0.302 | 0.382 | 0.980 | 0.259 | 0.250 | 0.376 | 0.366 | 0.0435 | 0.478 |
| **$Na_2O$** | 0.107 | 0.0481 | 0.601 | 0.0474 | 0.0574 | 0.123 | 0.0592 | 0.0627 | 0.0632 | 0.0685 | 0.0166 | 0.0798 |
| **$K_2O$** | 0.00561 | 0.00405 | 0.00485 | 0.00649 | 0.00358 | 0.00456 | 0.00672 | 0.00246 | 0.00623 | 0.00445 | 0.00490 | 0.00385 |
| **NiO** | 0.293 | 0.268 | 0.202 | 0.262 | 0.320 | 0.282 | 0.333 | 0.273 | 0.277 | 0.298 | 0.339 | 0.285 |
| **Total** | 99.2 | 99.7 | 96.9 | 98.4 | 98.9 | 100.2 | 98.7 | 99.5 | 99.8 | 99.8 | 99.9 | 98.9 |
| **Mg#** | 89.5 | 91.6 | 91.3 | 93.2 | 94.4 | 92.5 | 91.8 | 92.7 | 92.6 | 91.4 | 88.5 | 91.6 |
| ***Trace elements ($\mu g\ g^{-1}$)*** | | | | | | | | | | | | |
| **Li** | 1.78 | 1.16 | 1.28 | 1.29 | 1.43 | 1.24 | 1.91 | 1.20 | 1.64 | 2.38 | 2.21 | 1.16 |
| **Na** | 750 | 11.6 | 4485 | 490 | 412 | 7.07 | - | 438 | 1054 | 19.3 | 160 | 609 |
| **Al** | 640 | 11789 | 6525 | 4739 | 2744 | 6525 | 495 | 1932 | 2511 | 2102 | 131 | 1275 |
| **P** | 51.7 | 8.15 | 72.2 | 91.6 | 46.0 | 3.55 | - | 30.9 | 30.7 | 1.59 | 37.4 | 26.0 |
| **K** | 18.8 | 5.23 | 279 | 62.4 | 25.0 | 5.14 | - | 88.4 | 70.8 | 13.6 | 190 | 149 |
| **Ca** | 6271 | 6158 | 42454 | 2335 | 2557 | 6370 | 1591 | 1758 | 2664 | 2396 | 270 | 3240 |
| **Sc** | 6.18 | 10.9 | 14.0 | 6.15 | 7.29 | 8.12 | 4.17 | 4.35 | 11.2 | 5.78 | 2.07 | 2.98 |
| **Ti** | 211 | 99.4 | 433 | 203 | 208 | 94.0 | 326 | 148 | 273 | 489 | 205 | 107 |
| **V** | 22.6 | 29.3 | 101 | 19.6 | 12.1 | 29.2 | 15.4 | 18.5 | 21.7 | 24.8 | 8.23 | 21.3 |
| **Cr** | 785 | 2364 | 4057 | 1879 | 2866 | 2138 | 693 | 1705 | 3176 | 1877 | 224 | 1396 |
| **Mn** | 1094 | 1003 | 795 | 815 | 694 | 848 | 790 | 821 | 918 | 968 | 1049 | 920 |
| **Co** | 146 | 102 | 88.8 | 114 | 110 | 103 | 114 | 116 | 113 | 120 | 161 | 114 |
| **Ni** | 2731 | 2145 | 1895 | 2491 | 2884 | 2319 | 2487 | 2735 | 2538 | 2645 | 2919 | 2507 |
| **Cu** | 0.223 | 0.251 | 0.619 | 0.523 | 1.880 | 0.123 | 6.83 | 1.94 | 5.48 | 5.37 | 4.33 | 4.52 |
| **Zn** | 75.2 | 46.5 | 43.0 | 43.5 | 39.5 | 45.2 | 58.3 | 48.7 | 49.2 | 65.2 | 84.2 | 49.9 |
| **Ga** | 0.522 | 1.08 | 1.82 | 0.430 | 0.270 | 0.542 | 0.401 | 0.362 | 0.560 | 1.16 | 0.248 | 0.567 |
| **Ge** | 0.776 | 0.952 | 1.35 | 0.710 | 0.578 | 0.806 | 0.823 | 1.04 | 1.01 | 1.02 | 0.904 | 0.921 |
| **As** | 0.114 | 0.0689 | 0.163 | 0.0929 | 0.0840 | 0.120 | 0.0592 | 0.0651 | 0.0688 | 0.0664 | 0.0667 | 0.0787 |
| **Rb** | 0.00642 | 0.0971 | 0.527 | 0.208 | 0.00922 | 0.00367 | 0.0525 | 0.00442 | 0.0906 | 0.0602 | 0.00193 | 0.0133 |
| **Sr** | 23.5 | 11.8 | 152 | 5.36 | 1.06 | 27.8 | 0.880 | 1.01 | 0.992 | 0.992 | 0.0145 | 1.03 |
| **Y** | 0.503 | 1.03 | 1.29 | 0.535 | 1.27 | 0.616 | 0.0313 | 0.161 | 0.165 | 0.393 | 0.00422 | 0.0130 |
| **Zr** | 2.29 | 0.879 | 19.4 | 4.18 | 5.12 | 2.94 | 0.235 | 1.85 | 2.29 | 2.03 | 0.264 | 0.117 |
| **Nb** | 0.288 | 0.756 | 1.49 | 1.06 | 0.121 | 0.392 | 0.0473 | 0.173 | 0.0611 | 0.0786 | 0.171 | 0.0372 |
| ***Ultra-trace elements ($ng\ g^{-1}$)*** | | | | | | | | | | | | |
| **Mo** | 28.9 | 15.1 | 64.2 | 37.5 | 50.1 | 10.6 | 12.5 | 12.1 | 13.5 | 16.0 | 15.1 | 12.9 |
| **Ag** | 1.26 | 2.65 | 6.64 | 1.40 | 1.49 | 3.81 | 2.64 | 5.92 | 0.949 | 1.05 | 1.45 | 1.91 |
| **Cd** | 35.5 | 15.9 | 50.9 | 27.0 | 30.0 | 21.6 | 21.8 | 24.1 | 21.1 | 26.3 | 17.6 | 16.1 |
| **In** | 9.18 | 11.8 | 17.4 | 6.41 | 19.3 | 11.6 | 8.21 | 86.2 | 99.4 | 12.1 | 95.0 | 116 |
| **Sb** | 11.0 | 18.6 | 17.1 | 12.8 | 16.1 | 12.9 | 12.6 | 176 | 13.0 | 22.9 | 20.5 | 18.4 |
| **Cs** | 6.62 | 5.62 | 28.3 | 127 | 3.12 | 0.666 | 1.81 | 2.19 | 2.22 | 3.81 | 0.717 | 1.39 |
| **Ba** | 101 | 21.0 | 7931 | 4093 | 50.8 | 18.4 | 31.4 | 15.2 | 400 | 8.09 | 4.51 | 11.8 |
| **La** | 779 | 607 | 5092 | 512 | 15.7 | 495 | 12.0 | 20.3 | 16.1 | 10.0 | 0.865 | 12.3 |
| **Ce** | 2328 | 1785 | 15768 | 1276 | 72.8 | 1821 | 48.4 | 68.1 | 74.7 | 46.8 | 2.45 | 47.9 |
| **Pr** | 343 | 189 | 2179 | 146 | 17.3 | 294 | 9.04 | 13.5 | 16.3 | 10.3 | 0.401 | 8.45 |
| **Nd** | 1497 | 742 | 8556 | 625 | 131 | 1343 | 47.3 | 87.2 | 117 | 70.5 | 1.76 | 44.7 |
| **Sm** | 259 | 169 | 1219 | 158 | 85.3 | 261 | 13.6 | 46.6 | 58.2 | 38.3 | 0.836 | 12.8 |
| **Eu** | 64.5 | 53.5 | 298 | 56.3 | 40.3 | 75.2 | 4.52 | 20.3 | 23.0 | 17.6 | 0.421 | 3.60 |
| **Gd** | 170 | 141 | 664 | 167 | 158 | 195 | 13.1 | 52.1 | 65.6 | 62.0 | 0.612 | 7.83 |
| **Tb** | 21.6 | 23.5 | 70.8 | 23.3 | 32.7 | 26.6 | 1.70 | 7.69 | 8.83 | 11.8 | 0.143 | 0.743 |
| **Dy** | 114 | 162 | 307 | 119 | 235 | 135 | 8.69 | 39.1 | 43.7 | 74.4 | 0.813 | 2.77 |
| **Ho** | 20.0 | 39.3 | 47.6 | 20.4 | 51.5 | 21.4 | 1.32 | 6.58 | 6.99 | 14.1 | 0.189 | 0.401 |
| **Er** | 50.1 | 127 | 114 | 48.8 | 152 | 50.2 | 3.30 | 15.1 | 14.9 | 36.1 | 0.741 | 1.07 |
| **Tm** | 6.41 | 20.7 | 13.2 | 6.41 | 21.9 | 5.92 | 0.636 | 1.92 | 1.83 | 2.53 | 0.083 | 0.200 |
| **Yb** | 39.7 | 159 | 86.6 | 40.4 | 154 | 41.3 | 2.17 | 11.0 | 13.1 | 17.2 | 0.461 | 0.885 |
| **Lu** | 4.82 | 25.8 | 11.3 | 6.29 | 23.3 | 6.83 | 0.579 | 1.98 | 2.64 | 2.05 | 0.135 | 0.100 |
| **Hf** | 123 | 15.5 | 848 | 66.2 | 109 | 88.6 | 9.41 | 50.9 | 64.4 | 55.9 | 7.84 | 4.22 |
| **Ta** | 6.38 | 6.21 | 67.3 | 38.6 | 9.27 | 17.2 | 2.93 | 10.8 | 4.65 | 5.47 | 9.25 | 3.44 |
| **W** | 3.23 | 3.73 | 36.0 | 10.0 | 8.44 | 1.17 | 1.63 | 1.65 | 1.12 | 0.986 | 0.192 | 1.74 |
| **Re** | 0.347 | 0.184 | 0.346 | 0.357 | 0.543 | 0.457 | 0.616 | 0.653 | 1.03 | 0.383 | 0.575 | 0.743 |
| **Tl** | 0.103 | 0.691 | 24.5 | 1.13 | 0.619 | 0.835 | 0.622 | 0.394 | 0.361 | 0.524 | 0.406 | 0.567 |
| **Pb** | 177 | 79.7 | 746 | 523 | 184 | 233 | 553 | 55 | 126 | 34 | 4 | 53.3 |
| **Bi** | 1.50 | 1.64 | 6.58 | 1.52 | 1.23 | 2.37 | 2.41 | 2.04 | 2.46 | 1.82 | 1.03 | 1.62 |
| **Th** | 14.0 | 89.4 | 265 | 70.9 | 1.11 | 20.5 | 0.700 | 1.54 | 6.16 | 0.757 | 0.246 | 0.460 |
| **U** | 2.52 | 34.7 | 37.2 | 19.5 | 1.21 | 3.65 | 0.302 | 1.15 | 5.06 | 0.705 | 0.206 | 0.185 |

Avrg = average; SD = standard deviation; - = not available

West Greenland olivines have high Mg# of 91 (88–93) which coupled with high modal abundances of olivine places them at the end of the 'oceanic-trend' in Figure 17 (Boyd, 1989). In contrast, Kaapvaal olivines have a slightly higher average of Mg# 93 and a larger range 89–95, plotting off the 'oceanic-trend' to the right. Major element compositions of olivine are generally similar in West Greenland and Kaapvaal peridotites with high MgO (50.1 vs. 51.3 wt%) and NiO (0.34 vs. 0.38 wt%) and low FeO (8.7 vs. 7.3 wt%). West Greenland olivines have a restricted range of NiO contents (0.29–0.37 wt.%) compared to Kaapvaal olivines (0.26–0.46 wt.%).

West Greenland opx demonstrate Mg# ranging between 90–94, in contrast to Kaapvaal spanning a larger range of 89–96. Kaapvaal opx generally show lower CaO averages (0.38 wt%) but span a large range (0.17–1.16 wt%), whereas West Greenland vary between 0.42–1.07 wt% with a higher average of 0.678 wt%, in keeping with the ubiquitous presence of cpx. Orthopyroxene $TiO_2$ and $Na_2O$ values are much higher in West Greenland peridotites with average values 0.13 and 0.17 wt%, respectively, whereas Kaapvaal is characterised by 0.048 wt% $TiO_2$ and 0.084 wt% $Na_2O$.

Clinopyroxenes from both localities are represented by Cr-diopsides. Following the trend observed in olivine and opx, the cpx Mg# are slightly higher in Kaapvaal compared to West Greenland peridotites (93 vs. 92). The $Na_2O$ abundances are similar with contents in Kaapvaal being 1.3–2.8 wt% (average 2.1 wt%) and in West Greenland 1.3–2.6 wt% (average 1.98 wt%). The CaO and $Al_2O_3$ averages in Kaapvaal are higher and range 18.1–22.3 and 0.33–2.90 wt%, respectively. In contrast, concentrations in West Greenland cpxs span a narrower array between 17.3–21.1 and 0.08–0.46 wt%, respectively. However, $TiO_2$ abundances in cpx follow the same trend as in olivine and opx and are higher in West Greenland with an average of 0.25 wt%, compared to Kaapvaal average of 0.16 wt%.

Garnets from both cratons are magnesian and show similar average values in Mg# of 84 (81–90) in Kaapvaal and 82 (77–86) in West Greenland. The latter exhibit higher concentrations in $TiO_2$ 0.57 wt%, $Cr_2O_3$ 7.0 wt%, CaO 6.2 wt% and $Na_2O$ 0.065 wt%, in contrast to Kaapvaal grt with 0.07 wt% $TiO_2$, 4.0 wt% $Cr_2O_3$, 4.7 wt% CaO and 0.033 wt% $Na_2O$.

### 4.4.3 Trace element concentrations

#### *4.4.3.1 Olivine*

Trace elements are dominated by the doubly charged transition metal ions Mn, Co, Ni and Zn that are able to replace Mg and Fe due to the same charge and similar ionic radii, fitting well into the olivine M1 and M2 sites (73–76.7 pm in Mg-rich olivine; Zanetti et al. (2004)). These elements correlate negatively with Mg# (Figure 18) in West Greenland and Kaapvaal peridotites. Additionally, the singly charged Li behaves like Zn in decreasing with increasing Mg#.

Table 16 Kaapvaal peridotite olivine major, trace and ultra-trace elements compositions. Values are averages of a number (n) of analyses. LA-ICP-MS data presented here was acquired in hydrogen mode.

| | Kaapvaal | | | | | | | | | | | |
|---|---|---|---|---|---|---|---|---|---|---|---|---|
| Sample | AJE439 | | DJ0205 | | DJ0262 | | DJ0277 | | JJG6356 | | KDJ5 | |
| Rocktype | Lhz | | Grt-lhz | | Grt-lhz | | Grt-lhz | | Grt-lhz | | Grt-lhz | |
| *n EPMA* | *19* | | *6* | | *26* | | *31* | | *12* | | *27* | |
| *n LAICPMS* | *12* | | *12* | | *12* | | *12* | | *12* | | *12* | |
| | Avrg | SD | Avrg | SD | Avrg | SD | Avrg | SD | Avrg | SD | Avrg | SD |
| ***Major elements (wt%; EPMA)*** | | | | | | | | | | | | |
| **$SiO_2$** | 40.2 | 0.2 | 41.4 | 0.1 | 40.5 | 0.2 | 40.7 | 0.1 | 40.9 | 0.1 | 40.9 | 0.2 |
| **$TiO_2$** | 0.0148 | 0.0192 | bdl | bdl | 0.0139 | 0.0151 | 0.0145 | 0.0135 | 0.0120 | 0.0131 | 0.00739 | 0.01471 |
| **$Al_2O_3$** | 0.0088 | 0.0130 | 0.0112 | 0.0195 | 0.0104 | 0.0137 | 0.0115 | 0.0158 | 0.00708 | 0.00871 | 0.0109 | 0.0136 |
| **$Cr_2O_3$** | 0.0198 | 0.0207 | 0.0255 | 0.0086 | 0.0323 | 0.0185 | 0.0363 | 0.0248 | 0.0575 | 0.0158 | 0.0389 | 0.0288 |
| **FeO** | 10.5 | 0.1 | 7.79 | 0.06 | 8.74 | 0.86 | 6.80 | 0.09 | 5.52 | 0.05 | 7.35 | 0.09 |
| **MnO** | 0.139 | 0.019 | 0.0948 | 0.0191 | 0.113 | 0.029 | 0.095 | 0.017 | 0.0826 | 0.0206 | 0.100 | 0.018 |
| **MgO** | 49.1 | 0.2 | 49.9 | 0.4 | 50.4 | 0.7 | 51.9 | 0.2 | 52.6 | 0.1 | 51.1 | 0.2 |
| **CaO** | 0.0233 | 0.0119 | 0.0199 | 0.0078 | 0.0225 | 0.0129 | 0.0245 | 0.0125 | 0.0238 | 0.0086 | 0.0174 | 0.0115 |
| **$Na_2O$** | 0.0136 | 0.0195 | 0.0135 | 0.0127 | 0.0123 | 0.0154 | 0.0172 | 0.0201 | 0.0223 | 0.0166 | 0.0158 | 0.0180 |
| **$K_2O$** | 0.00587 | 0.00812 | 0.00150 | 0.00260 | 0.00455 | 0.00683 | 0.00604 | 0.00935 | 0.00283 | 0.00674 | 0.00377 | 0.00641 |
| **NiO** | 0.372 | 0.044 | 0.432 | 0.0247 | 0.366 | 0.055 | 0.375 | 0.048 | 0.361 | 0.022 | 0.421 | 0.033 |
| **Total** | 100.4 | 0.3 | 99.7 | 0.5 | 100.2 | 0.2 | 99.9 | 0.3 | 99.6 | 0.2 | 100.0 | 0.3 |
| **Mg#** | 89.3 | 0.1 | 91.9 | 0.1 | 91.1 | 0.9 | 93.2 | 0.1 | 94.4 | 0.1 | 92.5 | 0.1 |
| **Cr#** | 0.636 | 0.426 | 0.746 | 0.441 | 0.721 | 0.332 | 0.704 | 0.385 | 0.896 | 0.145 | 0.721 | 0.309 |
| ***Trace elements (µg $g^{-1}$; LA-ICP-MS)*** | | | | | | | | | | | | |
| **Li** | 2.15 | 0.11 | 1.64 | 0.11 | 1.73 | 0.17 | 1.45 | 0.14 | 1.57 | 0.10 | 1.59 | 0.05 |
| **Na** | 90.1 | 3.8 | n.a. | – | 147 | 67 | 186 | 71 | 169 | 5 | n.a. | – |
| **Al** | 28.9 | 0.6 | 7.27 | 0.13 | 38.4 | 2.9 | 51.5 | 8.5 | 62.8 | 3.2 | 14.8 | – |
| **P** | 59.5 | 7.0 | n.a. | – | 69.5 | 15.9 | 105 | 36 | 45.3 | 3.7 | n.a. | – |
| **K** | 18.0 | – | n.a. | – | 43.7 | 47.3 | 18.2 | 12.9 | 8.67 | 7.73 | n.a. | – |
| **Ca** | 101 | 40 | 66 | 13 | 250 | 116 | 378 | 260 | 170 | 16 | 100 | 20 |
| **Sc** | 2.42 | 0.05 | 2.32 | 0.06 | 1.90 | 0.05 | 2.02 | 0.05 | 2.38 | 0.04 | 2.44 | 0.06 |
| **Ti** | 113 | 6 | 33.9 | 0.9 | 110 | 10 | 93.5 | 6.5 | 95.4 | 5.1 | 37.9 | 0.9 |
| **V** | 3.23 | 0.09 | 1.77 | 0.04 | 3.01 | 0.25 | 3.68 | 0.14 | 3.51 | 0.08 | 2.84 | 0.09 |
| **Cr** | 72.3 | 1.7 | 36.3 | 1.2 | 65.6 | 1.8 | 134 | 2 | 374 | 11 | 71.6 | 1.7 |
| **Mn** | 1102 | 13 | 693 | 11 | 808 | 18 | 731 | 9 | 650 | 17 | 713 | 7 |
| **Co** | 180 | 2 | 148 | 2 | 153 | 6 | 156 | 2 | 121 | 3 | 142 | 1 |
| **Ni** | 3478 | 72 | 3520 | 58 | 3540 | 59 | 3658 | 44 | 3243 | 76 | 3492 | 63 |
| **Cu** | 0.239 | 0.012 | 0.295 | 0.019 | 0.575 | 0.075 | 0.346 | 0.038 | 2.01 | 0.04 | 0.126 | 0.008 |
| **Zn** | 86.6 | 1.2 | 61.2 | 2.4 | 67.1 | 3.3 | 53.7 | 1.0 | 42.4 | 1.1 | 57.1 | 2.0 |
| **Ga** | 0.0227 | 0.0019 | 0.0153 | 0.0059 | 0.0380 | 0.0114 | 0.0369 | 0.0197 | 0.0428 | 0.0030 | 0.0168 | 0.0040 |
| **Ge** | 0.500 | – | 0.536 | 0.042 | 0.620 | – | 0.420 | – | 0.467 | – | 0.491 | 0.030 |
| **As** | 0.111 | 0.011 | 0.0688 | 0.0093 | 0.123 | 0.026 | 0.0844 | 0.0125 | 0.0736 | 0.0099 | 0.106 | 0.012 |
| ***Ultra-trace elements (ng $g^{-1}$; LA-ICP-MS)*** | | | | | | | | | | | | |
| **Rb** | 2.90 | 0.71 | 3.40 | – | 63.7 | 42.9 | 26.6 | 18.4 | 8.70 | 3.25 | – | – |
| **Sr** | 1.91 | 1.58 | 2.88 | 1.39 | 720 | 447 | 1807 | 1390 | 1.00 | 0.44 | 4.09 | 3.10 |
| **Y** | 5.22 | 1.14 | 0.822 | 0.426 | 40.6 | 29.6 | 29.5 | 19.4 | 3.72 | 0.68 | 1.29 | 0.99 |
| **Zr** | 225 | 22 | 23.4 | 8.7 | 776 | 550 | 1084 | 635 | 323 | 36 | 146 | 22 |
| **Nb** | 352 | 52 | 1064 | 249 | 1044 | 245 | 1169 | 394 | 117 | 13 | 564 | 28 |
| **Mo** | 27.6 | 2.9 | 5.58 | 2.51 | 49.1 | 20.7 | 32.2 | 15.7 | 18.5 | 5.6 | 9.25 | 4.50 |
| **Ag** | 0.557 | 0.436 | 2.29 | 0.54 | 1.17 | 0.59 | 0.813 | 0.385 | 0.663 | 0.078 | 2.97 | 0.76 |
| **Cd** | 29.1 | 5.6 | 6.86 | 1.97 | 24.8 | 5.7 | 24.2 | 4.2 | 26.3 | 4.8 | 6.54 | 2.29 |
| **In** | 5.59 | 0.49 | 4.97 | 0.76 | 3.96 | 1.02 | 3.28 | 0.37 | 4.32 | 0.73 | 5.76 | 1.00 |
| **Sb** | 11.5 | 1.6 | 11.1 | 3.7 | 11.3 | 3.6 | 11.3 | 4.9 | 8.09 | 2.89 | 9.10 | – |
| **Cs** | bdl | bdl | bdl | bdl | 3.95 | 1.43 | 4.04 | 2.72 | 2.50 | 0.70 | bdl | bdl |
| **Ba** | 0.787 | 1.103 | 0.510 | 0.170 | 911 | 390 | 1713 | 1307 | 0.274 | 0.213 | 0.960 | 0.297 |
| **La** | 0.294 | 0.228 | 1.31 | 0.96 | 211 | 142 | 214 | 161 | 0.555 | 0.489 | 0.686 | 0.472 |
| **Ce** | 0.538 | 0.451 | 0.529 | 0.271 | 478 | 323 | 531 | 405 | 0.126 | 0.067 | 25.3 | 22.0 |
| **Pr** | 0.0567 | 0.0273 | 0.727 | 0.481 | 18.8 | 12.4 | 48.6 | 35.4 | 0.0550 | 0.0227 | 0.348 | 0.059 |
| **Nd** | 0.374 | 0.242 | 1.26 | 0.42 | 64.6 | 41.0 | 174 | 128 | 0.832 | 0.678 | 1.55 | 0.31 |
| **Sm** | 0.303 | 0.134 | 1.03 | – | 9.17 | 6.30 | 24.2 | 17.6 | 0.408 | 0.254 | 2.98 | 1.48 |
| **Eu** | 0.217 | 0.158 | 0.405 | 0.085 | 6.37 | 3.80 | 5.38 | 3.57 | 0.127 | 0.069 | 1.90 | 2.61 |
| **Gd** | 0.286 | 0.161 | 1.35 | 0.44 | 6.36 | 3.37 | 15.4 | 9.8 | 0.465 | 0.266 | 2.02 | – |
| **Tb** | 0.0613 | 0.0544 | 0.193 | 0.127 | 0.834 | 0.366 | 1.69 | 1.07 | 0.0700 | 0.0482 | 0.270 | 0.071 |
| **Dy** | 0.622 | 0.376 | 1.34 | 0.66 | 3.89 | 2.51 | 6.48 | 4.12 | 0.513 | 0.299 | 0.930 | 0.486 |
| **Ho** | 0.196 | 0.094 | 0.150 | 0.057 | 0.715 | 0.349 | 0.954 | 0.662 | 0.174 | 0.081 | 0.317 | 0.230 |
| **Er** | 0.857 | 0.305 | 0.840 | 0.113 | 3.44 | 2.25 | 2.09 | 1.30 | 0.472 | 0.190 | 0.720 | 0.049 |
| **Tm** | 0.225 | 0.080 | bdl | bdl | 0.416 | 0.353 | 0.485 | 0.353 | 0.131 | 0.072 | 0.110 | – |
| **Yb** | 2.45 | 1.02 | 1.40 | – | 2.49 | 1.75 | 1.30 | 0.73 | 0.878 | 0.355 | 1.30 | 0.02 |
| **Lu** | 0.781 | 0.220 | 0.170 | – | 0.286 | 0.190 | 0.147 | 0.098 | 0.141 | 0.075 | 0.445 | 0.219 |
| **Hf** | 4.17 | 0.97 | 0.925 | 0.180 | 15.4 | 9.8 | 13.8 | 4.7 | 7.26 | 1.29 | 2.35 | 1.23 |
| **Ta** | 7.96 | 0.87 | 6.03 | 1.11 | 34.0 | 12.8 | 40.3 | 11.5 | 7.95 | 1.18 | 18.6 | 1.0 |
| **W** | 3.50 | 2.00 | 0.980 | 0.292 | 18.1 | 10.7 | 3.99 | 2.26 | 0.294 | 0.131 | 1.15 | 0.74 |
| **Re** | 0.377 | 0.230 | bdl | bdl | 0.428 | 0.133 | 0.334 | 0.135 | 0.334 | 0.134 | 0.343 | 0.150 |
| **Tl** | bdl | bdl | 0.480 | 0.240 | 6.09 | 5.68 | 0.658 | 0.394 | 0.255 | 0.007 | 0.970 | – |
| **Pb** | 14.8 | 2.4 | 47.9 | 9.3 | 60.2 | 30.8 | 521 | 204 | 116 | 66 | 155 | 61 |
| **Bi** | 0.642 | 0.237 | 1.12 | 0.34 | 1.15 | 0.26 | 1.70 | 0.69 | 0.764 | 0.277 | 1.66 | 0.67 |
| **Th** | 0.170 | 0.100 | 0.310 | 0.096 | 38.8 | 29.5 | 23.1 | 15.6 | 0.360 | 0.173 | 3.24 | 1.03 |
| **U** | 0.251 | 0.132 | 0.545 | 0.247 | 10.7 | 7.4 | 7.10 | 4.69 | 0.167 | 0.125 | 0.907 | 0.811 |

n = number of spot analyses; Avrg = average concentration; SD = standard deviation; n.a. = not acquired;
bdl = below detection limit; – = not available.

Table 17 West Greenland olivine major, trace and ultra-trace elements compositions. Values are averages of a number (n) of analyses. LA-ICP-MS data presented here was acquired in hydrogen mode.

| | West Greenland | | | | | | | | | | | |
|---|---|---|---|---|---|---|---|---|---|---|---|---|
| Sample | 474527 | | 474545 | | 474551 | | 474555 | | 474570 | | 474577 | |
| Rocktype | Grt-lhz | | Grt-lhz | | Grt-lhz | | Grt-lhz | | Dun | | Grt-lhz | |
| *n EPMA* | *20* | | *9* | | *21* | | *20* | | *22* | | *32* | |
| *n LAICPMS* | *7* | | *3* | | *10* | | *8* | | *10* | | *10* | |
| | Avrg | SD | Avrg | SD | Avrg | SD | Avrg | SD | Avrg | SD | Avrg | SD |
| ***Major elements (wt%; EPMA)*** | | | | | | | | | | | | |
| **$SiO_2$** | 41.0 | 0.1 | 40.9 | 0.2 | 40.9 | 0.2 | 40.7 | 0.2 | 40.1 | 0.2 | 40.7 | 0.3 |
| **$TiO_2$** | 0.0432 | 0.0249 | 0.0217 | 0.0180 | 0.0258 | 0.0232 | 0.0383 | 0.0231 | 0.0309 | 0.0218 | 0.00829 | 0.01119 |
| **$Al_2O_3$** | 0.0148 | 0.0181 | 0.0103 | 0.0174 | 0.0248 | 0.0358 | 0.0108 | 0.0181 | 0.00962 | 0.01408 | 0.0262 | 0.0202 |
| **$Cr_2O_3$** | 0.0793 | 0.0269 | 0.0626 | 0.0271 | 0.0988 | 0.0366 | 0.0621 | 0.0246 | 0.0482 | 0.0371 | 0.0839 | 0.0265 |
| **FeO** | 8.05 | 0.09 | 7.29 | 0.09 | 7.40 | 0.42 | 8.62 | 0.13 | 11.23 | 0.13 | 8.47 | 0.08 |
| **MnO** | 0.116 | 0.020 | 0.109 | 0.013 | 0.106 | 0.029 | 0.122 | 0.020 | 0.143 | 0.016 | 0.121 | 0.023 |
| **MgO** | 50.2 | 0.3 | 51.3 | 0.2 | 51.1 | 0.4 | 50.3 | 0.2 | 48.1 | 0.2 | 50.1 | 0.2 |
| **CaO** | 0.0527 | 0.0242 | 0.0224 | 0.0164 | 0.0630 | 0.0227 | 0.0315 | 0.0120 | 0.0291 | 0.0113 | 0.0711 | 0.0175 |
| **$Na_2O$** | 0.0242 | 0.0197 | 0.0282 | 0.0196 | 0.0296 | 0.0260 | 0.0235 | 0.0212 | 0.0133 | 0.0205 | 0.0252 | 0.0215 |
| **$K_2O$** | 0.00667 | 0.00906 | 0.00197 | 0.00327 | 0.00644 | 0.00952 | 0.00417 | 0.00618 | 0.00502 | 0.00584 | 0.00394 | 0.00617 |
| **NiO** | 0.371 | 0.036 | 0.329 | 0.052 | 0.335 | 0.044 | 0.362 | 0.029 | 0.347 | 0.028 | 0.374 | 0.039 |
| **Total** | 99.9 | 0.3 | 100.1 | 0.1 | 100.1 | 0.3 | 100.3 | 0.3 | 100.0 | 0.3 | 100.0 | 0.3 |
| **Mg#** | 91.8 | 0.1 | 92.6 | 0.1 | 92.5 | 0.4 | 91.2 | 0.1 | 88.4 | 0.1 | 91.3 | 0.1 |
| **Cr#** | 0.808 | 0.185 | 0.871 | 0.181 | 0.779 | 0.200 | 0.834 | 0.225 | 0.731 | 0.355 | 0.692 | 0.185 |
| ***Trace elements ($\mu g\ g^{-1}$; LA-ICP-MS)*** | | | | | | | | | | | | |
| **Li** | 2.05 | 0.07 | 1.31 | 0.06 | 1.85 | 0.18 | 2.71 | 0.08 | 2.25 | 0.09 | 1.40 | 0.04 |
| **Na** | n.a. | – | 148 | 3 | 760 | 409 | n.a. | – | 133 | 3 | 194 | 5 |
| **Al** | 64.1 | – | 62.0 | 5.8 | 144 | 19 | 49.7 | 1.7 | 52.3 | 2.5 | 143 | 16 |
| **P** | n.a. | – | 32.5 | 1.8 | 31.6 | 1.8 | n.a. | – | 38.0 | 4.0 | 31.1 | 1.8 |
| **K** | n.a. | – | 74.7 | – | 56.6 | 45.8 | n.a. | – | 191 | – | 213 | – |
| **Ca** | 279 | 34 | 190 | 2 | 644 | 186 | 202 | 16 | 174 | 7 | 484 | 60 |
| **Sc** | 3.95 | 0.22 | 1.90 | 0.04 | 2.55 | 0.47 | 3.18 | 0.05 | 2.03 | 0.04 | 2.44 | 0.08 |
| **Ti** | 208 | 18 | 86.6 | 3.3 | 157 | 28 | 208 | 6 | 190 | 5 | 52.1 | 15.5 |
| **V** | 9.65 | 0.44 | 6.66 | 0.14 | 9.01 | 0.79 | 9.27 | 0.21 | 7.11 | 0.19 | 9.50 | 0.29 |
| **Cr** | 357 | 15 | 292 | 10 | 563 | 112 | 279 | 8 | 178 | 7 | 512 | 25 |
| **Mn** | 791 | 30 | 771 | 3 | 881 | 82 | 915 | 14 | 1048 | 19 | 905 | 18 |
| **Co** | 125 | 5 | 134 | 1 | 133 | 4 | 141 | 3 | 164 | 2 | 143 | 1 |
| **Ni** | 2766 | 142 | 3296 | 34 | 3130 | 72 | 3217 | 76 | 2985 | 106 | 3314 | 30 |
| **Cu** | 7.28 | 0.68 | 2.11 | 0.10 | 6.39 | 0.66 | 6.02 | 0.15 | 4.38 | 0.11 | 5.25 | 0.18 |
| **Zn** | 62.9 | 4.2 | 54.6 | 0.4 | 57.1 | 5.3 | 74.3 | 2.5 | 85.4 | 1.5 | 59.2 | 1.8 |
| **Ga** | 0.144 | 0.017 | 0.0516 | 0.0084 | 0.175 | 0.021 | 0.199 | 0.012 | 0.145 | 0.011 | 0.099 | 0.015 |
| **Ge** | 0.758 | 0.034 | 0.879 | – | 0.775 | – | 0.842 | 0.036 | 0.877 | – | 0.698 | – |
| **As** | 0.0602 | 0.0116 | 0.0609 | 0.0070 | 0.0675 | 0.0103 | 0.0668 | 0.0193 | 0.0666 | 0.0084 | 0.0786 | 0.0097 |
| ***Ultra-trace elements ($ng\ g^{-1}$; LA-ICP-MS)*** | | | | | | | | | | | | |
| **Rb** | 16.0 | 7.5 | 1.80 | – | 73.6 | 48.4 | 5.10 | – | 1.90 | – | 3.03 | 0.23 |
| **Sr** | 2.30 | 0.98 | 12.5 | 0.3 | 534 | 243 | 1.92 | 1.13 | 4.35 | 1.12 | 9.65 | 3.41 |
| **Y** | 5.52 | 1.74 | 6.47 | 2.66 | 12.5 | 5.6 | 3.87 | 1.25 | 2.63 | 0.91 | 4.42 | 2.16 |
| **Zr** | 150 | 16 | 329 | 105 | 262 | 102 | 229 | 53 | 262 | 11 | 82.5 | 12.1 |
| **Nb** | 47.7 | 9.3 | 194 | 17 | 35.6 | 17.2 | 80 | 7 | 174 | 19 | 21.3 | 7.9 |
| **Mo** | 13.6 | 7.5 | 11.9 | 0.1 | 13.6 | 4.6 | 14.1 | 3.6 | 15.3 | 4.3 | 12.6 | 3.3 |
| **Ag** | 2.60 | 1.18 | 4.45 | 1.21 | 0.670 | 0.368 | – | – | 1.42 | 0.17 | 2.10 | – |
| **Cd** | 21.0 | 6.2 | 23.3 | 1.9 | 16.9 | 5.1 | 21.6 | 6.3 | 17.1 | 6.7 | 10.3 | 5.0 |
| **In** | 8.39 | 1.50 | 84.7 | 11.5 | 100 | 12 | 9.22 | 1.05 | 95.2 | 6.2 | 129 | 11 |
| **Sb** | 12.6 | 1.2 | 205 | 84 | 12.8 | 2.9 | 14.1 | 2.0 | 20.8 | 9.3 | 19.8 | 7.5 |
| **Cs** | 1.63 | – | 1.05 | 0.05 | 1.34 | 0.53 | 3.60 | – | 0.685 | 0.049 | 1.33 | 0.39 |
| **Ba** | 33.2 | 24.8 | 4.27 | 0.42 | 337 | 133 | 0.578 | 0.316 | 3.93 | 2.71 | 0.633 | 0.513 |
| **La** | 1.91 | 1.30 | 1.39 | 1.03 | 7.06 | 5.06 | 0.359 | 0.151 | 0.665 | 0.268 | 1.38 | 0.82 |
| **Ce** | 6.71 | 4.64 | 0.965 | 0.042 | 28.0 | 22.1 | 0.798 | 0.287 | 1.50 | 0.84 | 0.746 | 0.348 |
| **Pr** | 1.56 | 1.22 | 0.630 | 0.523 | 3.12 | 2.48 | 0.288 | 0.050 | 0.226 | 0.126 | 0.233 | 0.085 |
| **Nd** | 5.22 | 2.25 | 0.675 | 0.120 | 10.2 | 7.3 | 0.875 | 0.120 | 0.698 | 0.436 | 1.29 | 0.52 |
| **Sm** | 1.49 | 0.45 | 1.90 | 2.12 | 1.28 | 0.40 | 0.900 | – | 0.504 | 0.195 | 0.603 | 0.276 |
| **Eu** | 0.534 | 0.166 | 2.20 | 1.82 | 0.738 | 0.442 | 0.451 | 0.146 | 0.307 | 0.215 | 0.238 | 0.044 |
| **Gd** | 1.38 | 0.08 | 0.235 | 0.007 | 1.37 | 0.56 | 1.07 | 0.32 | 0.254 | 0.071 | 0.883 | 0.337 |
| **Tb** | 0.238 | 0.172 | 0.230 | 0.113 | 0.155 | 0.124 | 0.347 | 0.172 | 0.0843 | 0.0294 | 0.179 | 0.109 |
| **Dy** | 1.51 | 0.93 | 0.690 | 0.085 | 1.68 | 0.76 | 1.20 | 0.30 | 0.457 | 0.229 | 0.643 | 0.200 |
| **Ho** | 0.240 | 0.122 | 0.225 | 0.078 | 0.647 | 0.123 | 0.235 | 0.113 | 0.118 | 0.054 | 0.166 | 0.064 |
| **Er** | 1.19 | 0.56 | 0.908 | 0.060 | 1.21 | 0.70 | 0.856 | 0.290 | 0.630 | 0.292 | 0.449 | 0.188 |
| **Tm** | 0.437 | 0.101 | 0.255 | 0.304 | 0.145 | 0.071 | 0.270 | 0.092 | 0.0733 | 0.0437 | 0.172 | 0.033 |
| **Yb** | 1.41 | 0.59 | 0.665 | 0.368 | 1.53 | 0.90 | 0.848 | 0.266 | 0.398 | 0.230 | 0.698 | 0.208 |
| **Lu** | 0.533 | 0.437 | 0.550 | 0.317 | 0.338 | 0.115 | 0.306 | 0.098 | 0.128 | 0.072 | 0.0720 | 0.0130 |
| **Hf** | 3.05 | 1.38 | 10.3 | 7.0 | 5.40 | 2.40 | 5.44 | 1.84 | 7.51 | 1.99 | 2.36 | 0.99 |
| **Ta** | 2.74 | 0.66 | 11.2 | 1.4 | 1.69 | 0.54 | 4.65 | 0.73 | 9.31 | 0.91 | 1.67 | 0.69 |
| **W** | 1.50 | 0.94 | 1.12 | 0.04 | 0.240 | 0.042 | 0.675 | 0.219 | 0.190 | – | 1.88 | 0.82 |
| **Re** | 0.670 | 0.221 | 0.540 | 0.028 | 1.10 | 0.29 | 0.295 | 0.049 | 0.574 | 0.126 | 0.577 | 0.085 |
| **Tl** | 0.640 | 0.244 | 0.330 | 0.141 | 0.340 | – | 0.533 | 0.181 | 0.410 | 0.028 | 0.540 | 0.085 |
| **Pb** | 625 | 648 | 45.1 | 4.9 | 127 | 53 | 28.1 | 11.0 | 3.87 | 1.25 | 55.0 | 22.1 |
| **Bi** | 2.57 | 1.72 | 1.85 | 0.97 | 2.15 | 0.92 | 1.51 | 0.59 | 0.970 | 0.159 | 1.56 | 0.11 |
| **Th** | 0.645 | 0.377 | 0.748 | 0.350 | 4.70 | 3.35 | 0.392 | 0.207 | 0.242 | 0.136 | 0.318 | 0.305 |
| **U** | 0.280 | 0.046 | 0.633 | 0.357 | 3.71 | 2.65 | 0.288 | 0.042 | 0.201 | 0.046 | 0.120 | 0.067 |

n = number of spot analyses; Avrg = average concentration; SD = standard deviation; n.a. = not acquired;
bdl = below detection limit; – = not available.

Table 18 Kaapvaal orthopyroxene major, trace and ultra-trace elements compositions. Values are averages of a number (n) of analyses. LA-ICP-MS data presented here was acquired in hydrogen mode.

| | Kaapvaal | | | | | | | | | | | |
|---|---|---|---|---|---|---|---|---|---|---|---|---|
| Sample | AJE439 | | DJ0205 | | DJ0262 | | DJ0277 | | JJG6356 | | KDJ5 | |
| Rocktype | Lhz | | Grt-lhz | | Grt-lhz | | Grt-lhz | | Grt-lhz | | Grt-lhz | |
| *n EPMA* | *38* | | *12* | | *10* | | *19* | | *9* | | *36* | |
| *n LAICPMS* | *8* | | *4* | | *5* | | *8* | | *10* | | *6* | |
| | Avrg | SD | Avrg | SD | Avrg | SD | Avrg | SD | Avrg | SD | Avrg | SD |
| ***Major elements (wt%; EPMA)*** | | | | | | | | | | | | |
| **$SiO_2$** | 57.2 | 0.2 | 58.1 | 0.2 | 57.1 | 0.1 | 57.3 | 0.2 | 57.7 | 0.4 | 57.7 | 0.2 |
| **$TiO_2$** | 0.0666 | 0.0305 | 0.0246 | 0.0261 | 0.0548 | 0.0262 | 0.0457 | 0.0260 | 0.0707 | 0.0185 | 0.0235 | 0.0246 |
| **$Al_2O_3$** | 0.293 | 0.028 | 0.622 | 0.028 | 0.734 | 0.032 | 0.753 | 0.026 | 0.674 | 0.025 | 0.772 | 0.042 |
| **$Cr_2O_3$** | 0.183 | 0.030 | 0.203 | 0.031 | 0.260 | 0.041 | 0.360 | 0.028 | 0.602 | 0.049 | 0.291 | 0.032 |
| **FeO** | 6.40 | 0.07 | 4.92 | 0.07 | 5.21 | 0.05 | 4.20 | 0.06 | 3.38 | 0.06 | 4.61 | 0.07 |
| **MnO** | 0.160 | 0.018 | 0.122 | 0.016 | 0.110 | 0.025 | 0.111 | 0.018 | 0.0896 | 0.0180 | 0.112 | 0.025 |
| **MgO** | 35.1 | 0.2 | 35.1 | 0.2 | 35.6 | 0.2 | 36.2 | 0.2 | 36.7 | 0.2 | 36.7 | 0.2 |
| **CaO** | 0.274 | 0.018 | 0.200 | 0.026 | 0.253 | 0.022 | 0.339 | 0.050 | 0.512 | 0.028 | 0.265 | 0.105 |
| **$Na_2O$** | 0.0652 | 0.0257 | 0.0389 | 0.0187 | 0.0569 | 0.0305 | 0.098 | 0.031 | 0.180 | 0.019 | 0.0835 | 0.0384 |
| **$K_2O$** | 0.00463 | 0.00591 | 0.00757 | 0.00652 | 0.00581 | 0.00790 | 0.00753 | 0.00875 | 0.00388 | 0.00855 | 0.00624 | 0.00841 |
| **NiO** | 0.0836 | 0.0295 | 0.0917 | 0.0240 | 0.0914 | 0.0222 | 0.102 | 0.029 | 0.0822 | 0.0328 | 0.0978 | 0.0311 |
| **Total** | 99.8 | 0.3 | 99.4 | 0.4 | 99.5 | 0.2 | 99.5 | 0.3 | 99.3 | 0.6 | 100.7 | 0.2 |
| **Mg#** | 90.7 | 0.1 | 92.7 | 0.1 | 92.4 | 0.1 | 93.9 | 0.1 | 95.1 | 0.1 | 93.4 | 0.1 |
| **Cr#** | 0.295 | 0.037 | 0.179 | 0.021 | 0.191 | 0.022 | 0.243 | 0.017 | 0.374 | 0.021 | 0.202 | 0.018 |
| ***Trace elements (µg $g^{-1}$ ; LA-ICP-MS)*** | | | | | | | | | | | | |
| **Li** | 0.800 | 0.050 | 0.731 | 0.018 | 1.17 | 0.20 | 1.14 | 0.47 | 0.724 | 0.062 | 0.824 | 0.163 |
| **Na** | 461 | 46 | n.a. | – | 910 | 196 | 1007 | 311 | 1270 | 101 | n.a. | – |
| **Al** | 1518 | 48 | 3331 | 260 | 3591 | 156 | 4167 | 308 | 3722 | 269 | 3688 | 86 |
| **P** | 26.8 | 2.4 | n.a. | – | 58.0 | 2.4 | 57.0 | 21.0 | 23.5 | 3.2 | n.a. | – |
| **K** | 15.7 | 4.2 | n.a. | – | 542 | 301 | 134 | 103 | 101 | – | n.a. | – |
| **Ca** | 1818 | 44 | 3110 | 405 | 2525 | 439 | 2821 | 588 | 3174 | 219 | 1466 | 17 |
| **Sc** | 4.37 | 0.03 | 3.73 | 0.19 | 3.50 | 0.11 | 3.98 | 0.66 | 3.66 | 0.17 | 3.79 | 0.08 |
| **Ti** | 425 | 8 | 158 | 6 | 382 | 54 | 345 | 30 | 503 | 44 | 137 | 3 |
| **V** | 24.0 | 0.5 | 38.8 | 2.8 | 32.9 | 1.6 | 35.6 | 1.3 | 26.0 | 2.2 | 33.3 | 0.5 |
| **Cr** | 1027 | 22 | 1679 | 195 | 1555 | 71 | 2364 | 107 | 4166 | 294 | 1838 | 50 |
| **Mn** | 1192 | 10 | 813 | 15 | 921 | 31 | 812 | 34 | 701 | 46 | 821 | 13 |
| **Co** | 58.7 | 0.3 | 50.9 | 0.8 | 55.3 | 0.5 | 53.1 | 1.2 | 49.5 | 4.5 | 53.0 | 1.0 |
| **Ni** | 743 | 6 | 665 | 22 | 721 | 15 | 837 | 25 | 831 | 65 | 760 | 15 |
| **Cu** | 0.160 | 0.010 | 0.232 | 0.031 | 0.612 | 0.227 | 0.878 | 0.528 | 1.34 | 0.15 | 0.112 | 0.013 |
| **Zn** | 51.3 | 1.1 | 35.4 | 0.7 | 40.8 | 1.2 | 31.0 | 0.7 | 27.1 | 4.2 | 33.2 | 1.1 |
| **Ga** | 1.45 | 0.04 | 1.97 | 0.13 | 1.97 | 0.05 | 0.957 | 0.062 | 1.26 | 0.07 | 1.05 | 0.04 |
| **Ge** | 1.42 | – | 1.31 | 0.03 | 1.69 | – | 1.15 | – | 1.20 | – | 1.21 | 0.05 |
| **As** | 0.0971 | 0.0071 | 0.0614 | 0.0133 | 0.125 | 0.023 | 0.109 | 0.019 | 0.171 | 0.065 | 0.0860 | 0.0249 |
| **Rb** | 0.0143 | 0.0180 | 0.266 | 0.124 | 1.33 | 1.37 | 0.513 | 0.460 | 0.00566 | 0.00248 | 0.00630 | 0.00099 |
| **Sr** | 0.192 | 0.015 | 8.89 | 1.56 | 14.6 | 0.4 | 9.10 | 7.98 | 0.660 | 0.478 | 0.295 | 0.104 |
| **Y** | 0.147 | 0.016 | 0.0235 | 0.0056 | 0.193 | 0.066 | 0.158 | 0.098 | 0.0917 | 0.0085 | 0.0443 | 0.0043 |
| **Zr** | 0.187 | 0.013 | 0.259 | 0.070 | 3.06 | 0.62 | 2.46 | 1.60 | 0.655 | 0.092 | 0.295 | 0.040 |
| **Nb** | 0.0478 | 0.0043 | 0.443 | 0.062 | 1.28 | 0.43 | 0.966 | 0.711 | 0.0790 | 0.0104 | 0.101 | 0.013 |
| ***Ultra-trace elements (ng $g^{-1}$ ; LA-ICP-MS)*** | | | | | | | | | | | | |
| **Mo** | 30.6 | 3.8 | 15.5 | 9.1 | 69.8 | 34.6 | 45.0 | 10.3 | 347 | 312 | 7.49 | 1.54 |
| **Ag** | 0.835 | 0.120 | 3.00 | – | 1.76 | 0.73 | 2.28 | 1.04 | 7.42 | 4.15 | 3.60 | – |
| **Cd** | 42.1 | 7.6 | 15.2 | 3.0 | 35.3 | 7.5 | 29.6 | 5.9 | 31.0 | 10.9 | 31.4 | 7.7 |
| **In** | 6.34 | 0.60 | 5.07 | 1.04 | 5.18 | 0.51 | 4.73 | 0.74 | 124 | 13 | 6.76 | 2.38 |
| **Sb** | 7.99 | 2.07 | 13.4 | 0.3 | 17.9 | 6.4 | 13.0 | 5.3 | 84.3 | 37.8 | 13.7 | 0.1 |
| **Cs** | 29.9 | – | 15.4 | 3.0 | 111 | 55 | 333 | 236 | 7.63 | 6.65 | bdl | bdl |
| **Ba** | 2.46 | 1.05 | 38.7 | 0.3 | 8235 | 294 | 7609 | 4307 | 359 | 422 | 2.38 | 0.63 |
| **La** | 14.8 | 0.9 | 495 | 115 | 1298 | 412 | 985 | 718 | 7.09 | 3.63 | 11.8 | 2.2 |
| **Ce** | 57.6 | 3.5 | 1434 | 324 | 2851 | 844 | 2374 | 1691 | 28.7 | 6.0 | 63.1 | 9.9 |
| **Pr** | 9.75 | 0.6 | 101 | 33 | 274 | 13 | 266 | 213 | 5.23 | 1.11 | 10.4 | 2.2 |
| **Nd** | 51.8 | 2.4 | 366 | 75 | 998 | 47 | 1001 | 747 | 36.7 | 12.7 | 51.6 | 8.9 |
| **Sm** | 15.1 | 1.4 | 55.8 | 25.2 | 142 | 9 | 144 | 94 | 17.3 | 3.8 | 14.8 | 2.8 |
| **Eu** | 4.32 | 0.56 | 14.5 | 3.4 | 39.3 | 10.6 | 38.1 | 22.0 | 7.22 | 2.09 | 4.61 | 1.23 |
| **Gd** | 16.6 | 2.4 | 20.3 | 2.9 | 96.2 | 6.6 | 92.6 | 56.6 | 20.1 | 3.4 | 12.8 | 3.6 |
| **Tb** | 2.97 | 0.50 | 2.48 | 1.07 | 10.6 | 0.9 | 10.1 | 6.3 | 2.95 | 0.77 | 1.65 | 0.44 |
| **Dy** | 25.7 | 4.6 | 6.10 | 1.84 | 51.1 | 3.9 | 39.1 | 25.8 | 19.3 | 3.5 | 11.6 | 3.1 |
| **Ho** | 5.52 | 0.68 | 1.59 | 0.67 | 8.51 | 1.35 | 5.44 | 3.87 | 3.21 | 1.29 | 1.07 | 0.35 |
| **Er** | 17.5 | 2.4 | 1.50 | 0.79 | 18.5 | 4.9 | 12.3 | 7.7 | 9.84 | 3.05 | 2.91 | 1.77 |
| **Tm** | 3.19 | 0.51 | 0.427 | 0.064 | 1.93 | 0.55 | 1.11 | 0.93 | 1.03 | 0.41 | 0.530 | 0.139 |
| **Yb** | 24.8 | 2.6 | 1.73 | 0.57 | 12.7 | 3.7 | 7.83 | 5.45 | 5.24 | 2.68 | 3.85 | 1.01 |
| **Lu** | bdl | 0.64 | 0.370 | – | 1.78 | 0.34 | 0.957 | 0.693 | 0.714 | 0.339 | 0.490 | 0.130 |
| **Hf** | 8.10 | 1.49 | 8.65 | 3.48 | 72.9 | 19.9 | 66.6 | 33.8 | 27.5 | 6.5 | 6.96 | 1.91 |
| **Ta** | bdl | 2.25 | 6.94 | 1.16 | 69.2 | 8.7 | 38.1 | 20.9 | 14.0 | 4.6 | 11.5 | 1.5 |
| **W** | 1.95 | 0.86 | 8.57 | 2.48 | 49.4 | 14.7 | 20.1 | 9.0 | 85.9 | 73.7 | 0.630 | – |
| **Re** | 0.267 | 0.133 | 0.290 | 0.098 | 0.190 | 0.071 | 0.345 | 0.124 | 2.19 | 0.75 | 0.530 | 0.113 |
| **Tl** | 0.375 | 0.007 | 0.910 | – | 97.9 | 41.8 | 2.00 | 0.68 | 3.92 | 2.14 | bdl | bdl |
| **Pb** | 15.7 | 3.3 | 69.0 | 25.1 | 227 | 84 | 503 | 161 | 801 | 674 | 57.7 | 13.3 |
| **Bi** | 1.07 | 0.71 | 2.00 | 0.75 | 1.00 | 0.24 | 1.18 | 0.46 | 4.82 | 1.74 | 1.03 | 0.23 |
| **Th** | 3.51 | 0.58 | 207 | 34 | 194 | 40 | 154 | 98 | 1.30 | 1.16 | 2.59 | 0.57 |
| **U** | 1.59 | 0.33 | 51.4 | 6.2 | 47.1 | 11.5 | 38.5 | 22.3 | 3.37 | 2.30 | 0.761 | 0.205 |

n = number of spot analyses; Avrg = average concentration; SD = standard deviation; n.a. = not acquired;
bdl = below detection limit; – = not available.

Table 19 West Greenland orthopyroxene major, trace and ultra-trace elements compositions. Values are averages of a number (n) of analyses. LA-ICP-MS data presented here was acquired in hydrogen mode.

| | West Greenland | | | | | | | | | | | |
|---|---|---|---|---|---|---|---|---|---|---|---|---|
| Sample | 474527 | | 474545 | | 474551 | | 474555 | | 474570 | | 474577 | |
| Rocktype | Grt-lhz | | Grt-lhz | | Grt-lhz | | Grt-lhz | | Dun | | Grt-lhz | |
| *n EPMA* | *18* | | *29* | | *19* | | *23* | | *12* | | *28* | |
| *n LAICPMS* | *6* | | *8* | | *8* | | *6* | | *6* | | *8* | |
| | Avrg | SD | Avrg | SD | Avrg | SD | Avrg | SD | Avrg | SD | Avrg | SD |
| ***Major elements (wt%; EPMA)*** | | | | | | | | | | | | |
| **$SiO_2$** | 57.6 | 0.3 | 57.9 | 0.2 | 57.9 | 0.2 | 57.5 | 0.3 | 57.0 | 0.2 | 57.5 | 0.2 |
| **$TiO_2$** | 0.230 | 0.029 | 0.0420 | 0.0202 | 0.0910 | 0.0397 | 0.186 | 0.023 | 0.121 | 0.020 | 0.0300 | 0.0244 |
| **$Al_2O_3$** | 0.690 | 0.035 | 0.527 | 0.028 | 0.477 | 0.031 | 0.621 | 0.032 | 0.570 | 0.024 | 0.683 | 0.027 |
| **$Cr_2O_3$** | 0.441 | 0.029 | 0.448 | 0.029 | 0.580 | 0.037 | 0.394 | 0.033 | 0.302 | 0.012 | 0.478 | 0.039 |
| **FeO** | 4.83 | 0.04 | 4.42 | 0.07 | 4.23 | 0.08 | 5.18 | 0.05 | 6.73 | 0.07 | 5.06 | 0.06 |
| **MnO** | 0.126 | 0.023 | 0.120 | 0.020 | 0.117 | 0.023 | 0.136 | 0.022 | 0.167 | 0.020 | 0.134 | 0.025 |
| **MgO** | 35.2 | 0.1 | 36.3 | 0.2 | 36.2 | 0.2 | 35.4 | 0.1 | 34.5 | 0.1 | 35.0 | 0.2 |
| **CaO** | 0.846 | 0.026 | 0.419 | 0.021 | 0.619 | 0.037 | 0.693 | 0.029 | 0.549 | 0.023 | 1.072 | 0.026 |
| **$Na_2O$** | 0.215 | 0.036 | 0.156 | 0.025 | 0.169 | 0.028 | 0.183 | 0.028 | 0.134 | 0.026 | 0.176 | 0.028 |
| **$K_2O$** | 0.00682 | 0.00641 | 0.00404 | 0.00737 | 0.00565 | 0.00808 | 0.00513 | 0.00719 | 0.00080 | 0.00211 | 0.00339 | 0.00525 |
| **NiO** | 0.107 | 0.037 | 0.0830 | 0.0307 | 0.118 | 0.025 | 0.106 | 0.030 | 0.103 | 0.036 | 0.120 | 0.031 |
| **Total** | 100.2 | 0.4 | 100.5 | 0.3 | 100.5 | 0.3 | 100.4 | 0.3 | 100.1 | 0.3 | 100.3 | 0.2 |
| **Mg#** | 92.8 | 0.1 | 93.6 | 0.1 | 93.9 | 0.1 | 92.4 | 0.1 | 90.1 | 0.1 | 92.5 | 0.1 |
| **Cr#** | 0.300 | 0.020 | 0.363 | 0.018 | 0.449 | 0.017 | 0.299 | 0.019 | 0.262 | 0.010 | 0.320 | 0.023 |
| ***Trace elements (µg $g^{-1}$ ; LA-ICP-MS)*** | | | | | | | | | | | | |
| **Li** | 1.10 | 0.24 | 0.902 | 0.153 | 1.10 | 0.25 | 1.43 | 0.12 | 0.882 | 0.255 | 0.725 | 0.045 |
| **Na** | n.a. | – | 1270 | 23 | 2079 | 654 | n.a. | – | 1114 | 7 | 1350 | 8 |
| **Al** | 3159 | 88 | 2773 | 74 | 2455 | 72 | 3143 | 61 | 2860 | 37 | 3521 | 42 |
| **P** | n.a. | – | 17.32 | 2.11 | 17.1 | 2.6 | n.a. | – | 18.3 | 1.8 | 16.7 | 1.8 |
| **K** | n.a. | – | 154 | 125 | 57.3 | 8.8 | n.a. | – | 178 | – | 19.5 | – |
| **Ca** | 4934 | 145 | 2910 | 213 | 4206 | 248 | 4403 | 224 | 3590 | 95 | 7186 | 153 |
| **Sc** | 5.36 | 0.16 | 3.14 | 0.15 | 3.74 | 0.14 | 4.76 | 0.16 | 3.62 | 0.06 | 4.02 | 0.07 |
| **Ti** | 1108 | 24 | 272 | 27 | 507 | 137 | 1001 | 10 | 759 | 8 | 217 | 16 |
| **V** | 46.3 | 0.5 | 38.8 | 0.7 | 33.8 | 2.2 | 48.8 | 0.6 | 47.5 | 1.1 | 43.6 | 0.8 |
| **Cr** | 2585 | 64 | 2867 | 49 | 3854 | 89 | 2523 | 65 | 1842 | 62 | 3096 | 55 |
| **Mn** | 866 | 24 | 893 | 59 | 877 | 53 | 1033 | 31 | 1146 | 15 | 983 | 15 |
| **Co** | 52.7 | 1.8 | 54.0 | 0.8 | 54.1 | 0.7 | 58.8 | 1.0 | 65.2 | 0.4 | 61.9 | 0.6 |
| **Ni** | 826 | 35 | 842 | 11 | 868 | 12 | 916 | 12 | 765 | 8 | 998 | 10 |
| **Cu** | 4.39 | 0.22 | 1.46 | 0.12 | 3.09 | 0.17 | 3.59 | 0.16 | 2.91 | 0.24 | 3.25 | 0.09 |
| **Zn** | 33.7 | 2.5 | 30.6 | 1.9 | 28.3 | 0.7 | 39.9 | 3.3 | 48.3 | 1.8 | 33.4 | 0.5 |
| **Ga** | 2.13 | 0.12 | 1.24 | 0.03 | 1.56 | 0.22 | 3.69 | 0.15 | 3.85 | 0.08 | 1.51 | 0.03 |
| **Ge** | 1.37 | 0.07 | 1.66 | – | 1.65 | – | 1.53 | 0.07 | 1.90 | – | 1.40 | – |
| **As** | 0.0569 | 0.0162 | 0.0798 | 0.0129 | 0.0700 | 0.0143 | 0.0622 | 0.0171 | 0.0736 | 0.0153 | 0.0808 | 0.0261 |
| **Rb** | 0.329 | 0.063 | 0.01 | 0.01 | 0.113 | 0.070 | 0.251 | 0.221 | 0.00305 | 0.00021 | 0.0340 | 0.0132 |
| **Sr** | 0.701 | 0.154 | 0.472 | 0.137 | 1.19 | 0.45 | 1.61 | 1.06 | 0.370 | 0.093 | 1.08 | 0.13 |
| **Y** | 0.0896 | 0.0087 | 0.0247 | 0.0061 | 0.0625 | 0.0085 | 0.0866 | 0.0092 | 0.0598 | 0.0047 | 0.0239 | 0.0026 |
| **Zr** | 0.287 | 0.020 | 0.311 | 0.036 | 0.515 | 0.170 | 0.347 | 0.015 | 0.353 | 0.024 | 0.157 | 0.020 |
| **Nb** | 0.0426 | 0.0048 | 0.0808 | 0.0062 | 0.0933 | 0.0351 | 0.0518 | 0.0081 | 0.0646 | 0.0063 | 0.0681 | 0.0128 |
| ***Ultra-trace elements (ng $g^{-1}$ ; LA-ICP-MS)*** | | | | | | | | | | | | |
| **Mo** | 6.00 | 1.93 | 11.1 | 6.0 | 10.5 | 4.1 | 17.8 | 8.0 | 7.63 | 3.49 | 12.9 | 4.9 |
| **Ag** | 2.97 | 0.38 | 11.3 | 5.0 | 1.35 | 0.35 | 3.43 | 0.75 | 2.65 | 0.06 | 1.54 | 0.39 |
| **Cd** | 25.9 | 3.9 | 23.4 | 10.2 | 29.7 | 7.4 | 32.2 | 6.4 | 34.7 | 5.7 | 27.8 | 10.5 |
| **In** | 7.11 | 1.04 | 93.8 | 4.2 | 99.9 | 7.3 | 9.82 | 1.81 | 93.3 | 7.0 | 93.6 | 6.2 |
| **Sb** | 14.5 | 0.8 | 80.2 | 71.5 | 11.7 | 1.5 | 13.8 | 4.3 | 12.5 | 2.4 | 16.3 | 3.2 |
| **Cs** | 3.07 | 1.55 | 6.41 | 6.66 | 3.72 | 1.19 | 3.70 | 3.29 | 1.89 | 0.43 | 1.41 | 0.33 |
| **Ba** | 13.5 | 13.0 | 41.3 | 37.2 | 539 | 330 | 12.5 | 8.3 | 24.6 | 15.2 | 9.02 | 1.34 |
| **La** | 6.61 | 2.11 | 32.3 | 26.3 | 21.5 | 13.0 | 6.91 | 2.00 | 7.88 | 1.11 | 12.3 | 1.8 |
| **Ce** | 43.2 | 9.9 | 66.6 | 25.4 | 87.9 | 47.1 | 34.9 | 4.9 | 35.8 | 4.0 | 64.6 | 19.8 |
| **Pr** | 5.34 | 0.47 | 9.64 | 2.58 | 11.4 | 4.5 | 5.67 | 1.03 | 6.51 | 0.69 | 11.4 | 2.5 |
| **Nd** | 45.3 | 6.8 | 55.7 | 11.2 | 59.9 | 21.8 | 39.3 | 4.4 | 38.9 | 4.9 | 64.9 | 8.3 |
| **Sm** | 16.7 | 3.6 | 14.9 | 2.2 | 12.8 | 3.8 | 14.1 | 3.8 | 12.4 | 3.3 | 21.0 | 2.9 |
| **Eu** | 7.37 | 1.06 | 6.16 | 1.42 | 6.15 | 2.23 | 5.92 | 1.06 | 4.40 | 0.74 | 6.17 | 0.85 |
| **Gd** | 25.9 | 2.2 | 14.7 | 2.3 | 18.8 | 5.9 | 17.3 | 5.8 | 13.1 | 1.9 | 13.6 | 2.2 |
| **Tb** | 3.69 | 0.66 | 1.61 | 0.43 | 2.74 | 0.97 | 3.21 | 1.21 | 2.20 | 0.43 | 1.27 | 0.23 |
| **Dy** | 19.8 | 4.4 | 5.60 | 0.81 | 13.3 | 4.1 | 19.8 | 2.2 | 13.2 | 2.7 | 4.88 | 1.23 |
| **Ho** | 3.003 | 0.324 | 1.21 | 0.39 | 2.19 | 0.74 | 3.22 | 1.02 | 2.66 | 0.31 | 0.610 | 0.224 |
| **Er** | 8.39 | 1.43 | 2.53 | 1.05 | 6.08 | 1.35 | 6.95 | 2.76 | 4.62 | 0.98 | 1.80 | 0.69 |
| **Tm** | 1.02 | 0.60 | 0.315 | 0.093 | 0.573 | 0.263 | 0.688 | 0.218 | 0.440 | 0.208 | 0.202 | 0.058 |
| **Yb** | 3.11 | 1.29 | 2.09 | 0.79 | 3.08 | 1.14 | 5.05 | 2.06 | 2.68 | 0.99 | 0.955 | 0.456 |
| **Lu** | 0.473 | 0.212 | 0.195 | 0.049 | 0.435 | 0.223 | 0.678 | 0.304 | 0.373 | 0.167 | 0.106 | 0.046 |
| **Hf** | 15.7 | 2.4 | 18.4 | 4.6 | 14.5 | 4.4 | 17.5 | 3.5 | 19.8 | 2.9 | 6.08 | 1.64 |
| **Ta** | 4.34 | 0.81 | 9.23 | 1.28 | 11.2 | 4.0 | 6.71 | 1.25 | 7.82 | 1.08 | 7.03 | 1.02 |
| **W** | 2.87 | 2.29 | 3.84 | 1.76 | 4.10 | 1.05 | 1.55 | – | 0.260 | – | 1.18 | 0.84 |
| **Re** | 0.320 | 0.057 | 0.968 | 0.268 | 0.875 | 0.193 | 0.275 | 0.120 | 0.657 | 0.064 | 1.09 | 0.35 |
| **Tl** | 0.590 | – | 0.600 | 0.227 | 0.373 | 0.111 | 0.400 | 0.057 | 0.300 | – | 0.615 | 0.403 |
| **Pb** | 98.7 | 44.3 | 76.0 | 27.0 | 116 | 51 | 43.3 | 14.9 | 5.39 | 0.97 | 48.7 | 8.8 |
| **Bi** | 1.43 | – | 2.82 | 0.46 | 3.42 | 2.02 | 2.51 | 1.30 | 3.10 | – | 1.80 | 0.65 |
| **Th** | 0.543 | 0.190 | 3.72 | 2.03 | 9.02 | 5.45 | 0.608 | 0.294 | 0.394 | 0.141 | 0.493 | 0.181 |
| **U** | 0.347 | 0.150 | 1.61 | 0.83 | 5.89 | 3.14 | 0.515 | 0.127 | 0.415 | 0.269 | 0.254 | 0.167 |

n = number of spot analyses; Avrg = average concentration; SD = standard deviation; n.a. = not acquired;
bdl = below detection limit; – = not available.

In West Greenland peridotites, Ni has a restricted range of 2900–3500 µg $g^{-1}$ in olivine and shows a slightly negative correlation with decreasing Mg# content up to 90–91 where it appears to change to a positive correlation delineated by the two lowest Mg# (~89) and Ni values (2900 µg $g^{-1}$), which are described by a typical fractionation trend. However, Kaapvaal peridotite olivine demonstrates a larger range of Ni (2600–3900 µg $g^{-1}$) and describes the same trend as seen in West Greenland – a negative correlation with decreasing Mg# (95–91) and an apparent change towards the fractionation trend, that is indicated by two points with Mg# ~89 (Figure 18a).

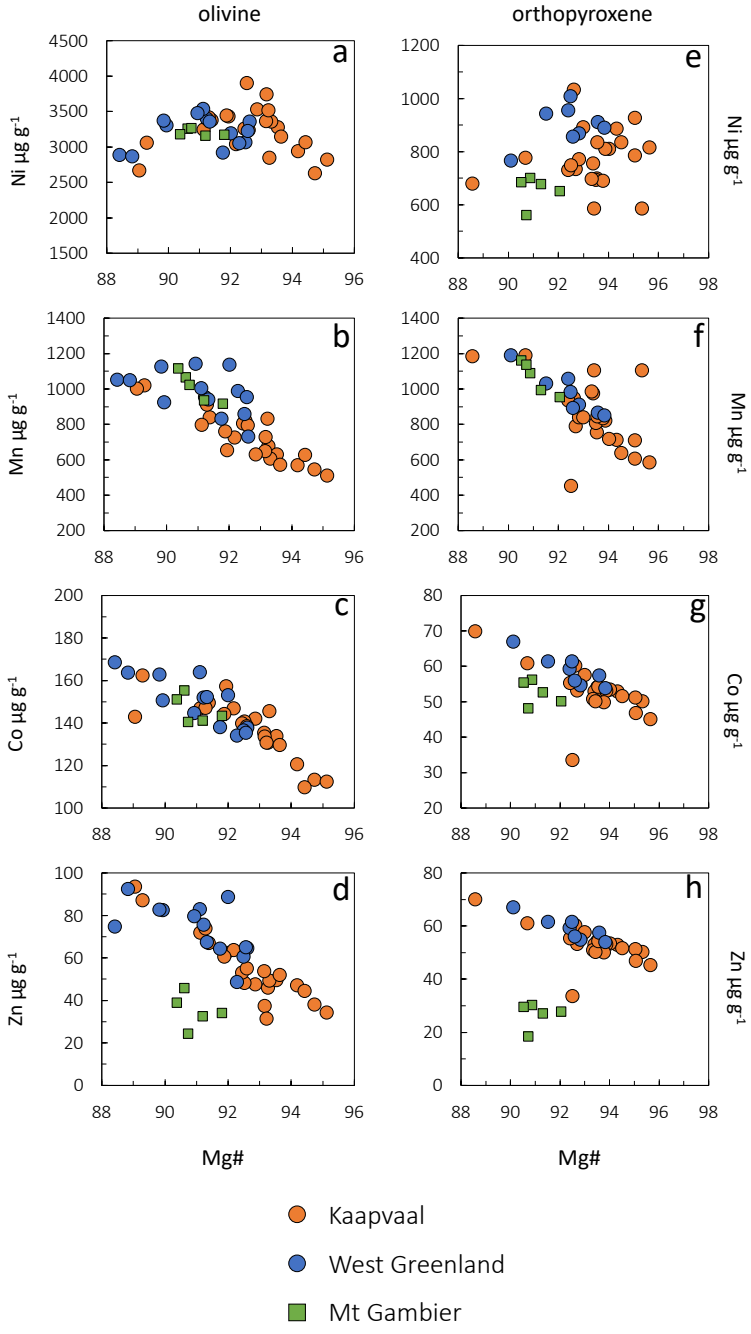


Figure 18 Bivariate plots showing Ni, Mn, Co and Zn variation vs. Mg# for olivines (left column) and opxs (right column) from Kaapvaal (orange) and West Greenland (blue) in comparison with Mt Gambier samples (green squares). Both phases show negative correlation of element abundances with Mg# which indicates melt depletion. Nickel shows a slight negative correlation in Kaapvaal olivines, whereas no correlation in Ni with Mg# is observed in opx.

Overall, most trace elements, including Al, Ca, Sc, Ti, V, Cr, Cu, Ga, and Y have higher to similar concentrations in olivines from West Greenland compared to Kaapvaal peridotites. Aluminium has large concentration ranges with similar to slightly higher concentrations in West Greenland compared to Kaapvaal (4.3–181 vs. 0.5–124 μg $g^{-1}$; Figure 19a). Copper contents in West Greenland olivines (0.5–10.5 μg $g^{-1}$) are universally higher than in Kaapvaal olivines (0.1–2.2 μg $g^{-1}$; Figure 20). Much higher Cu contents have been measured in olivines from ocean island or rift settings (Neumann *et al.*, 2002; Neumann *et al.*, 2004; Kaeser *et al.*, 2006).

Titanium in olivine differs slightly between West Greenland and Kaapvaal (Figure 19b) with ranges between 50–280 and 1–150 μg $g^{-1}$, respectively. However, Ti concentrations in Kaapvaal define two separate groups, low-Ti and high-Ti, where the latter overlap to some degree with olivines from West Greenland olivines. The low-Ti group has concentrations < 20 μg $g^{-1}$ and correlates with high Mg# (92–95). This group is also observed to be predominantly cpx-free.

Calcium in olivine have strong concentration differences between West Greenland and Kaapvaal peridotites (Figure 19a). West Greenland peridotites have a larger range (Ca: 80–600 μg $g^{-1}$) and generally higher Ca average contents (310 μg $g^{-1}$), compared to lower Ca averages in Kaapvaal (123 μg $g^{-1}$).

#### *4.4.3.2 Orthopyroxene*

As for olivines, the most abundant trace elements in opx are the divalent elements Ni, Mn, Co and Zn, although they have lower concentrations than in olivine, resulting in olivine/opx partition coefficients between 1.7 and 4.6 (Table 20). Manganese has partition coefficients slightly below 1 (Kaapvaal = 0.89 and West Greenland = 0.92).

Similar behaviour to olivines is observed in Li, Zn Mn and Co contents in opx that decrease with increasing Mg# in the peridotites of both cratons (Figure 18). Also following the behaviour of olivine, Ni has a restricted range (760–1007 μg $g^{-1}$) in West Greenland peridotites, whereas Ni in Kaapvaal opx shows a slightly larger spread (580–1030 μg $g^{-1}$). No clear correlation of Ni with Mg# is evident in opx from either craton (Figure 18e). Cobalt in opx shows similar behaviour to Ni (Figure 19), with a more restricted range in West Greenland compared to Kaapvaal (54–67 vs. 34–77 μg $g^{-1}$).

West Greenland peridotites have intermediate Cr, Al, V and Sc contents in opx with more restricted ranges than those from Kaapvaal peridotites (Table 19 and Table 18, respectively). Titanium concentrations in opx are variable and Kaapvaal peridotites are characterised by a larger range compared to West Greenland peridotites (5.9–1660 vs. 220–1330 μg $g^{-1}$, respectively). As shown for Ti in olivine, Kaapvaal opx can be divided in high-Ti and low-Ti (<100 μg $g^{-1}$) groups, with the latter being predominantly observed in the cpx-free peridotite xenoliths. Copper contents in West Greenland opx (2.9 μg $g^{-1}$) are consistently higher compared to Kaapvaal (0.57 μg $g^{-1}$) and plotted against Cu in olivine (Figure 20) the West Greenland peridotites extend the trend to higher abundances, indicating the enrichment in Cu in West Greenland a characteristic of the different cratons.

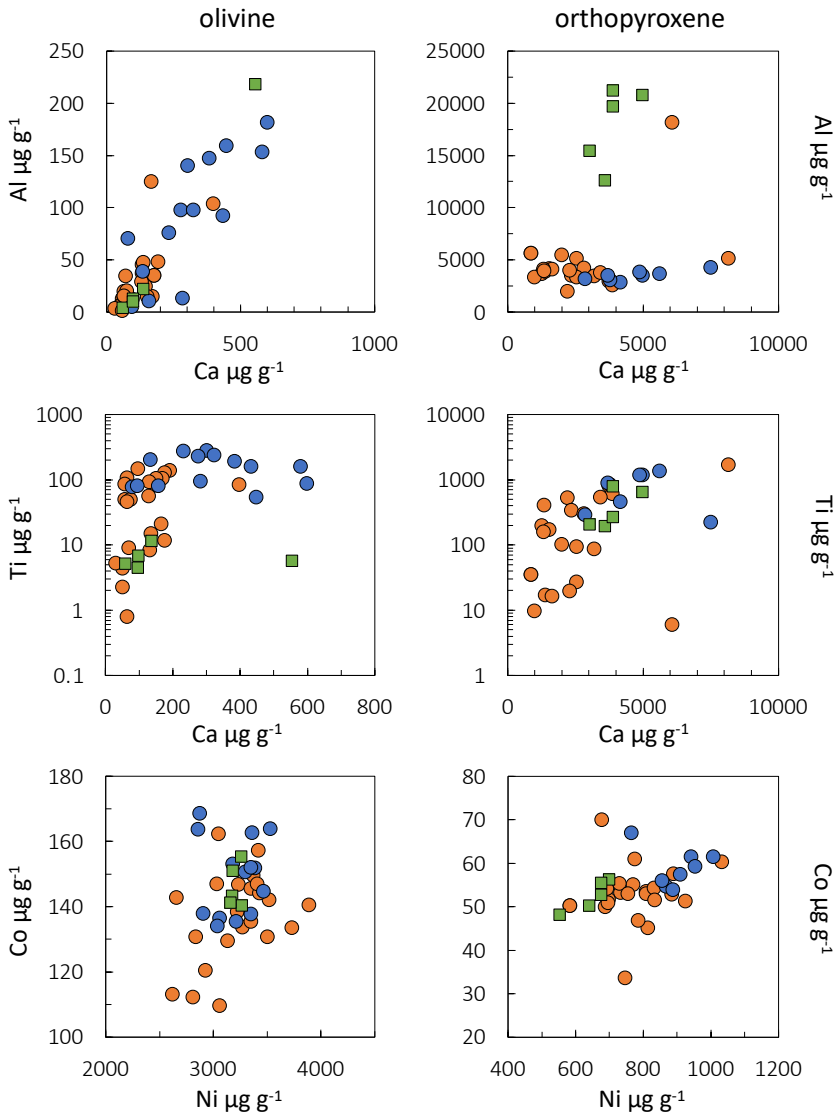


Figure 19 Bivariate plots showing Al and Ti concentrations vs. Ca, and Co vs. Ni in olivines (left column) and opxs (right column). Symbols as in Figure 18.

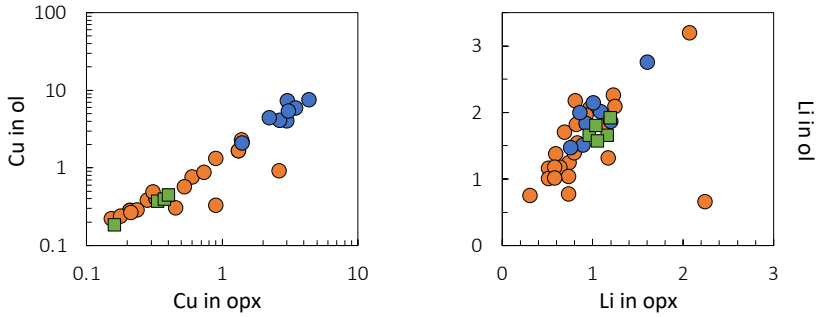


Figure 20 Plots showing Cu in olivine vs. Cu in opx (left) and Li in olivine vs. Li in opx (right). Both elements show a positive correlation in abundances. Note the much higher Cu concentrations in West Greenland for both olivine and opx in comparison to Kaapvaal. Symbols as in Figure 18.

#### *4.4.3.3 Clinopyroxene*

Kaapvaal cpx has higher Sc, V, Cr, Mn, Sr, Y Zr and REE concentrations compared to West Greenland xenolith cpx. On the contrary, higher abundances of Li, Ti, Co, Ni, Cu, Zn and Ga are characteristic for West Greenland cpx (Electronic Supplement B-2). Concentrations of Ti (366–2660 μg $g^{-1}$) and Cu (1.1–11 μg $g^{-1}$) are systematically higher in West Greenland cpx in contrast to Kaapvaal (22–2740 and 0.2–1.5 μg $g^{-1}$, respectively). This trend is also observed in olivine, opx and grt phases, indicating that Ti and Cu enrichment is a characteristic of West Greenland. Clinopyroxene is the main host for V and Sc (next to grt) which is also shown in the partitioning values between the silicate phases (Table 20). Kaapvaal cpx are characterised by higher Sc (25–304 vs. 15–46 μg $g^{-1}$) and V (144–750 vs. 170–370 μg $g^{-1}$) contents compared to West Greenland. However, olivine, opx, and grt show the opposite trend and exhibit higher values in West Greenland peridotites. This observation can be ascribed to higher cpx-content in Kaapvaal samples. Thus, higher concentrations of Sc and V in phases other than cpx indicate that less or no cpx is available, and the excess Sc and V is incorporated in olivine, opx and grt, as observed in West Greenland peridotites.

#### *4.4.3.4 Garnet*

West Greenland grts are characterised by higher concentrations in the majority of elements, e.g., Li, Sc, Ti, V, Cr, Ni, Cu, Zn, Ga and Zr, compared to Kaapvaal grts, which on the other hand, demonstrate enrichment in P, Mn, Y and REE (Electronic Supplement B-2). The higher Ti and Cu contents in West Greenland grts are universally higher in all other phases, whereas greater REE enrichment for cpx and grt is a typical feature of Kaapvaal peridotites.

#### *4.4.3.5 Mantle normalised incompatible elements*

Rare earth and other incompatible elements normalised to primitive mantle (McDonough and Sun, 1995) are presented in Figure 21. Abundances for olivines from West Greenland and Kaapvaal are highly depleted relative to primitive mantle, with exceptions for Li, Co, Ni and in few samples Nb and Ta concentrations having approximately PM abundances. In general, West Greenland olivines show a relatively flat REE distribution with concentrations ranging between 0.01–0.001 mantle abundances. Kaapvaal olivines broadly overlap with this range and additionally have two samples (DJ0262 and DJ0277) with increased LREE contents with up to 0.3 PM abundance. These two samples exhibit higher abundances in highly incompatible elements Ba, Th, U, Nb and Ta ranging 0.1–1 PM abundance. However, the majority of elements are overlapping for both cratons, with pronounced positive anomalies in Ti, and to a lesser degree in the HFSEs Zr, Hf, Nb and Ta.

Orthopyroxenes from both cratons show low incompatible element concentrations, but slightly higher compared to olivines, and demonstrate a more confined range in MREE (0.05–0.03) with a slightly wider range in LREE (0.01–0.05) and highest range in HREE (0.002–0.03) mantle abundances. West Greenland opx show a tendency to slightly decreasing HREE, whereas three Kaapvaal opx (DJ0205, DJ0262 and DJ0277) demonstrate high LREE/HREE ratios with LREE being similar to or just above PM abundances. The incompatible trace element pattern demonstrates more depletion in highly incompatible

and HREE elements, with some scatter. West Greenland opx show a ubiquitous strong positive Ti anomaly. In comparison, most Kaapvaal peridotites display a positive Ti anomaly as well, but less pronounced. Lithium, Rb, and Ga and to a lesser degree Sc, V, Co and Ni show abundances equal or close to primitive mantle abundances. Kaapvaal samples DJ0262 and DJ0277 exhibit almost constant abundances in highly incompatible and light rare earth elements at around 1–2 PM.

Clinopyroxenes from Kaapvaal peridotites predominantly display higher incompatible trace element abundances compared to West Greenland cpx. The former is characterised by a strong LREE enrichment

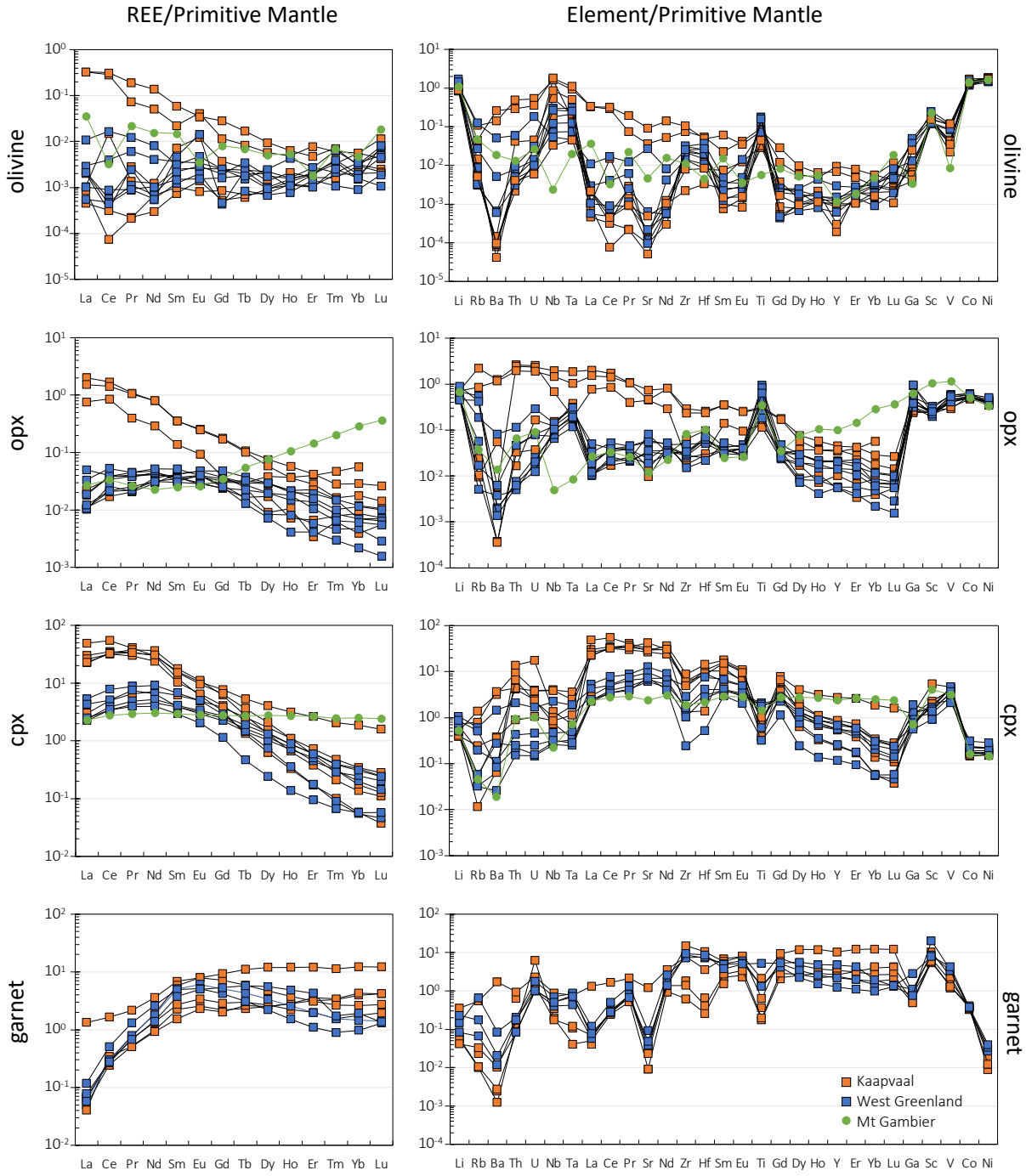


Figure 21 Primitive mantle normalized REE patterns and incompatible elements for mantle silicate phases olivine, opx, cpx and grt. Kaapvaal = orange square, West Greenland = blue square, Mt Gambier = green circle (data from Chapter 3). Primitive mantle values after McDonough and Sun (1995).

with abundances 20–60 above primitive mantle, and a strong decline towards HREE. West Greenland cpx generally describe the same trend as Kaapvaal but with less enriched LREE (2–10 mantle abundance) and same range in HREE, which is expressed in much lower $(La/Yb)_N$ values (West Greenland = 35 vs. Kaapvaal = 206). Both localities show strong negative Ti anomalies, where West Greenland peridotite cpx show slightly more variation (0.3–2 PM vs. 0.4–1 PM). The negative Ti anomalies were shown to be counterbalanced by positive anomalies in opx (Rampone *et al.*, 1991a; Rehfeldt *et al.*, 2008a). However, Kaapvaal peridotite cpx are more enriched in REE compared to West Greenland, which is supported by a significant difference in cpx Ti/Eu values between the cratons of 750 and 3300, respectively.

Garnets from West Greenland are generally more Ca- and Cr-rich compared to Kaapvaal grts. However, the mantle normalised REEs display similar trends for both localities, with a slightly humped pattern in the MREEs, with HREE ranging between 1–10 PM and LREE on the lower side around 0.1 mantle abundance. Kaapvaal grt shows two outliers, the first has slightly more enriched LREE but overlaps with general MREE–HREE signal, whereas the second shows same LREE abundances but a flat MREE-HREE enrichment at abundances 10 primitive mantle. The normalised incompatible element pattern in both settings is relatively homogeneous and demonstrate good overlap with some exceptions in the LILEs (Rb, Ba) and HFSEs (Ta, Zr, Hf and Ti), where West Greenland grts are more enriched relative to Kaapvaal peridotite. However, both samples display strong negative anomalies in Ba, La, Sr and Ti.

## 4.5 Discussion

The diversity of olivine and opx trace element compositions in the West Greenland and Kaapvaal peridotite xenoliths can be related to differences in lithospheric root formation and its later modification. The stages of cratonic crust and lithospheric root formation that have been recognized for the Kaapvaal and North Atlantic cratons are summarized in Table 13. Cratonic lithosphere development can be subdivided into three phases: (i) Archaean melt depletion; (ii) metasomatic modification related to craton stabilization in the late Archaean; and (iii) Proterozoic and Phanerozoic overprint(s) caused by percolating melts or fluids. Although the formation histories may be broadly similar due to similar geological processes that operated in Earth's early history (Foley, 2008; Pearson and Wittig, 2008; Condie *et al.*, 2009), the North Atlantic and Kaapvaal cratons differ in terms of the timing and the nature of craton stabilization and modification (Table 13). The formation of the Kaapvaal craton involved the collision of two major continental blocks and westward subduction of the Witwatersrand block underneath the Kimberley block at ~2.9 Ga (Schmitz *et al.*, 2004a). Most Re-Os data on peridotites of the Kaapvaal craton reflect this amalgamation age (Walker *et al.*, 1989; Pearson *et al.*, 1995; Menzies *et al.*, 1999; Irvine *et al.*, 2001; Carlson and Moore, 2004).

The North Atlantic craton has generally been summarized as having had a simpler history, because of the opx-poor, olivine-rich mineral assemblages that place the North Atlantic craton xenoliths (West Greenland sample set in this study) at the end of the depletion trend in Figure 17 (Bernstein *et al.*, 1998;

Wittig *et al.*, 2008). However, some dunites contain cpx but not opx, which may indicate reaction with infiltrating melts that produce a wehrlitic trend (Yaxley *et al.*, 1991), which does not show up on Figure 17. The magmatic history of the North Atlantic craton in West Greenland has seen the emplacement of abundant carbonate-rich, silica-poor melts such as carbonatites, ultramafic lamprophyres and kimberlites, which could induce a wehrlitic trend, increasing olivine and cpx abundance (Ammannati *et al.*, 2016; Aulbach *et al.*, 2020b). Although widespread, these are low-volume melts that will have affected the base of the lithosphere at least locally. Furthermore, much of the North Atlantic craton is under the Greenland ice sheet, which restricts the sample population and may shroud complexities in the history of the cratonic mantle lithosphere.

The Kaapvaal lithospheric mantle is known to have experienced a complex history including several melt depletion events, the youngest at ~2.5 Ga, followed by multiple events of strong metasomatic overprinting, including an episode of silica-enrichment that caused the high modal opx (Carlson and Moore, 2004; Simon *et al.*, 2007a; Rehfeldt *et al.*, 2008a; Lazarov *et al.*, 2009). This is also reflected in whole-rock compositions with slightly lower $SiO_2$, $Al_2O_3$, CaO and $Na_2O$ contents in the West Greenland relative to Kaapvaal (Wittig *et al.*, 2008). In Al/Si versus Mg/Si space, West Greenland peridotites plot at the lower end of the restite peridotite field (Herzberg, 2004) with only slight deviation towards opx and cpx, while Kaapvaal peridotites have similar to lower Mg/Si, mostly higher Al/Si ratios, and plot off the restite peridotite field towards modal enrichment in opx, cpx and grt.

### 4.5.1 Geothermometry

Different generations of minerals in peridotites and the uncertainty, if equilibrium between these minerals has been attained or not, complicate the assessment of the partitioning of trace elements between minerals. These include minerals that remain in the residue after partial melting and are thus stripped of all but the more compatible elements, those that are newly grown from infiltrating melts with different compositions, and those that are reaction products between infiltrating melts and pre-existing minerals. To assess if equilibrium between phases in both cratonic peridotites, the Kaapvaal and West Greenland, were achieved, we calculated the equilibration temperatures based on three widely used geothermometers – the two-pyroxene and the Ca-in-opx thermometer (Brey and Köhler, 1990) and the grt-olivine thermometer, which is based on Fe–Mg partitioning between coexisting grt and olivine (O'Neill and Wood, 1979). All temperatures (ºC) were calculated at constant pressures of 3 GPa and are presented in Table 14. Kaapvaal samples show similar ranges for the two-pyroxene and Ca-in-opx thermometers ranging between 743–1244 ºC and 768–1176 ºC, respectively, whereas the grt-olivine thermometer yields higher temperatures (1023–1393 ºC). West Greenland xenoliths resulted overall in slightly higher temperatures, where grt-olivine thermometer yields the highest (1208–1472 ºC), the two-pyroxene intermediate (1140–1278 ºC) and Ca-in-opx the lowest (925–1149 ºC) temperatures. Figure 22 demonstrates that Kaapvaal and West Greenland peridotites are characterised by lower Ca-in-opx temperatures (except for two samples in the Ca-opx vs. two-pyroxene space), which indicates that opx did not attain equilibrium with cpx and grt. This

observation encourages the idea to find 'older' signals that are still preserved in opx in comparison to the later introduced cpx and grt, which bear 'new' signals.

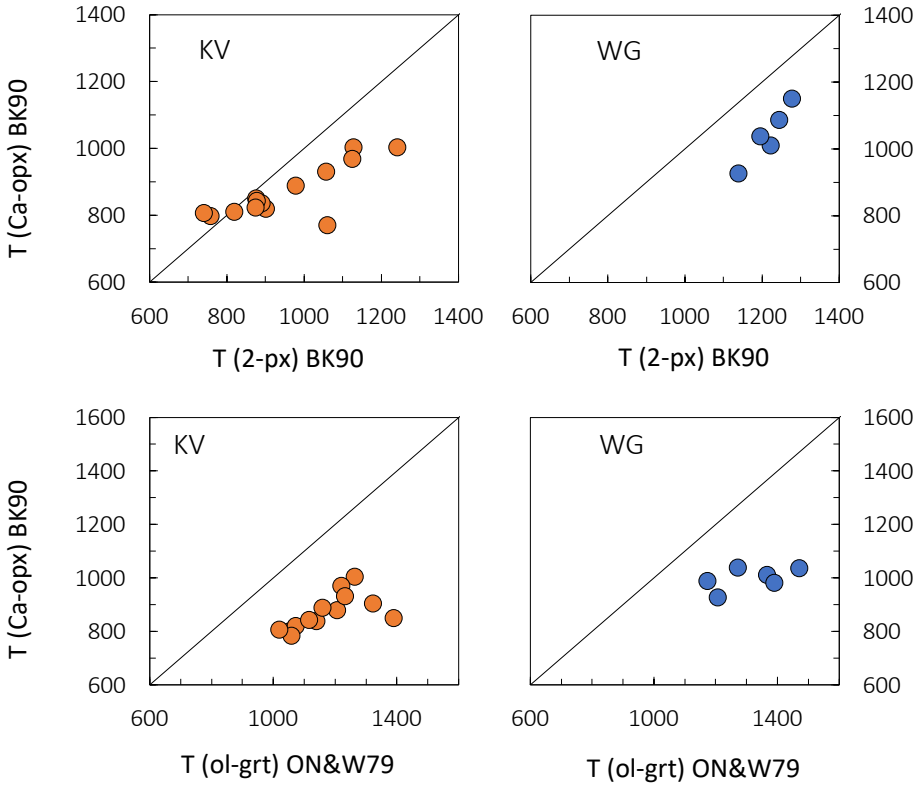


Figure 22 Calculated equilibrium temperatures for three widely used geothermometers, (1) two-pyroxene thermometer (Brey&Köhler, 1990), (2) Ca-in-opx (Brey&Köhler, 1990) and (3) grt-olivine thermometer based on the Fe-Mg partitioning between coexisting grt and olivine (O'Neill&Wood, 1979). The comparison between the calculated equilibrium temperatures demonstrates that opx is in disequilibrium with coexisting grts and cpxs. Thus, opxs likely preserve 'old' signatures, which were not eradicated by the introduction of the later cpx and grt.

### 4.5.2 Trace element partitioning between olivine and orthopyroxene

Table 20 compares the partition coefficients calculated for olivine/opx pairs in West Greenland and Kaapvaal peridotites with off-craton mantle xenoliths from Mt Gambier, southeastern Australia (Veter et al., Chapter 3) and with published equilibrium values derived from experiments on olivine/melt and opx/melt pairs, where available (Le Roux *et al.*, 2011; Foley *et al.*, 2013). There is still a dearth of experimental values for many elements, particularly for opx, and a few major discrepancies are still present, such as for Co and Ni, which lead to an contrary results for $K_{DNi/Co}^{ol/opx}$ ($D^{ol/opx}$ 2.21 for Co and 2.04 for Ni according to Le Roux *et al.* (2011), and 1.88 and 3.63 according to Foley *et al.* (2013)). The former study is internally consistent but on a single composition, whereas the latter draws on more experimental data from more bulk compositions, filtering out unnatural compositions. The less incompatible elements generally have smaller uncertainties on the $D^{ol/opx}$ values (standard deviations may be <10% for Co, Mn, Ni, Cu, Zn), whereas uncertainties may be higher for elements with low concentrations. These higher uncertainties are expressed in the standard deviations of the averages, so that the D-values listed for Sr, Zr, Nb, Ce, Eu and Pb are the least reliable (Table 20). Nevertheless, consistencies are seen, such as lower values for Sr and higher values for Nb and Zr relative to the non-cratonic xenoliths from Mt Gambier and

Vitim, so that the large number of data may offer indications as to element behaviour even if the absolute values may need later revision.

Within the natural cratonic samples, there is a noticeable preference of olivine for Co, Ni, Cu and Zn, but also for Li, P, Nb and in some cases Mo and In (Table 20). The West Greenland peridotites, which correspond to strongly depleted compositions with only a small degree of later overprint, have higher $D^{ol/opx}$ for several elements (Sc, Ti, V, Co and Zn) with respect to experimentally determined partitioning values, whereas values for Cr, Mn and Cu overlap. Kaapvaal peridotites have lower $D^{ol/opx}$ than both sets of experimental estimates for Cr and Cu, but higher for Co (as are the West Greenland samples). The same features were found in spinel lherzolites thought to represent cratonic remnants in eastern Antarctica (Foley *et al.*, 2006).

For Ti, both cratonic peridotites have higher $D^{ol/opx}$ than the experimental equilibrium values. The partitioning data for the most compatible trace elements, Co and Ni, show that equilibrium between olivine and opx has been achieved in the Kaapvaal samples: no excess from the conversion of olivine to opx by the reaction with the silica-rich melt remains.

The cratonic samples have significantly higher $D^{ol/opx}$ for Sc, Ti, V, Cr and Ga relative to off-cratonic samples from Mt Gambier. Similar values between West Greenland, Kaapvaal and Mt Gambier are calculated for Li, Mn, Co, Ni, Cu and Zn. Olivine/opx partition coefficients for REE exhibit that LREE–MREE are higher in samples away from the craton, whereas determined partitioning values for HREE are higher in cratonic samples. The calculated standard deviations for REE show quite consistent values, predominantly around 12 % (some larger deviations in HREE from West Greenland), however, these calculations are considered to be representative.

### 4.5.3 Archaean melt depletion

The main similarity between West Greenland and Kaapvaal peridotites is their strong melt depletion corresponding to up to 40 % partial melting, assuming a primitive mantle starting point (Simon *et al.*, 2007a; Wittig *et al.*, 2008). The decrease of Mn, Co, Zn and Li with increasing Mg# in olivine and opx (Figure 18) and similar Li, Mn, Ni, Co, Zn and Ga $D^{ol/opx}$ partition coefficients (Table 20) in West Greenland and Kaapvaal peridotites reflects this similar history (O'Reilly *et al.*, 1997; De Hoog *et al.*, 2010). This strong depletion event is thought to be an essential prerequisite for the survival of the cratonic root over time (Lee, 2006).

Orthopyroxenes in West Greenland peridotites have roughly flat REE patterns (Figure 21), whereas Kaapvaal opxs describe two trends, first overlapping with West Greenland opx abundances and the second characterised by higher LREE abundances. During mantle melting, first cpx and then grt are consumed into the melt, followed by opx at much higher degrees of melting (Walter, 2003). Therefore, low trace element compositions in opx and olivine in the residue should result, whereby the remaining REE will be hosted principally in opx. During later metasomatism by melts with high LREE/HREE, light and middle REE may

be re-enriched in opx, while HREE continue to reflect the composition of the original restite (Kelemen *et al.*, 1998). Orthopyroxene in West Greenland and Kaapvaal xenoliths in this study demonstrate low HREE concentrations (0.002–0.03 PM abundances), in agreement with the restitic signature, whereas the flat LREE-MREE pattern may be due to slight re-enrichment.

The flat REE pattern with low HREE favours low pressure melting in the spinel peridotite facies (2–3 GPa; Takazawa *et al.*, 2003; Wittig *et al.*, 2008), as grt would store higher amounts of the HREE. Similarly, low V and Sc concentrations in opx in West Greenland peridotites (32–58 and 3–8 µg $g^{-1}$, respectively) may reflect equilibration with melt in the spinel facies (Canil, 2004). Orthopyroxene in Kaapvaal peridotites has similar to higher V and Sc compositions (17–70 and 1–27 µg $g^{-1}$, respectively) relative to West Greenland xenolith opx, which may indicate equilibration with secondary metasomatic grt or more reducing conditions.

Different Cu $D^{ol/opx}$ between West Greenland and Kaapvaal xenoliths are caused by higher Cu in olivine in West Greenland samples (Figure 20). High Cu contents in olivine in mantle rocks are known from ocean island and rift environments (Neumann *et al.*, 2002; Neumann *et al.*, 2004; Kaeser *et al.*, 2006) and may reflect a different melting environment for West Greenland compared to Kaapvaal. Overall, high degrees of shallow melt extraction may support the interpretation that both West Greenland and Kaapvaal lithospheric mantle experienced hydrous melting related to Archaean subduction (Pearson and Wittig, 2008).

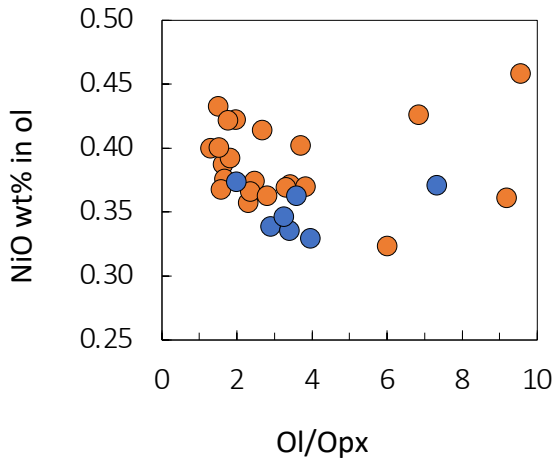


Figure 23 Modal olivine/opx plotted vs. NiO wt% in olivine shows the correlation of high-Ni olivines in opx-rich peridotites, whereas rocks with higher modal olivine demonstrate lower Ni abundances in olivines. Kaapvaal samples demonstrate a slight negative trend, which agrees with the observed higher modal opx composition in peridotite xenoliths, whereas West Greenland samples show slightly less Ni-enriched olivines and are supported by the higher olivine/opx mode.

Table 20 Olivine/opx partition coefficients ($D^{ol/opx}$) for trace elements in West Greenland and Kaapvaal peridotites. Partition coefficients from off-cratonic continental lithospheric mantle Mt Gambier (Veter *et al.*, Chapter 3) and from Vitim, Siberia are listed for comparison.

| | Kaapvaal | | | | | | | | West Greenland | | | | | | | | Mt Gambier | | Vitim, Siberia | | A | B |
|---|---|---|---|---|---|---|---|---|---|---|---|---|---|---|---|---|---|---|---|---|---|---|
| Sample | AJE439 | DJ0205 | DJ0262 | DJ0277 | JJG6356 | KDJ5 | | | 474527 | 474545 | 474551 | 474555 | 474570 | 474577 | | | | | | | | |
| Rocktype | Lhz | Grt-lhz | Grt-lhz | Grt-lhz | Grt-lhz | Grt-lhz | Avrg | SD | Grt-lhz | Grt-lhz | Grt-lhz | Grt-lhz | Dun | Grt-lhz | Avrg | SD | Avrg | SD | Avrg | SD | | |
| n | | | | | | | | | | | | | | | | | | | | | | |
| **Li** | 2.69 | 2.24 | 1.48 | 1.27 | 2.17 | 1.93 | 1.96 | 0.522 | 1.87 | 1.45 | 1.68 | 1.89 | 2.56 | 1.93 | 1.90 | 0.370 | 1.58 | 0.137 | 1.5 | 0.11 | – | – |
| **Na** | 0.195 | – | 0.162 | 0.185 | 0.133 | – | 0.169 | 0.0275 | – | 0.117 | 0.366 | – | 0.119 | 0.144 | 0.186 | 0.120 | – | – | – | – | – | – |
| **Al** | 0.0190 | 0.00218 | 0.0107 | 0.0124 | 0.0169 | 0.00402 | 0.0109 | 0.00675 | 0.0203 | 0.0224 | 0.0587 | 0.0158 | 0.0183 | 0.0405 | 0.0293 | 0.0169 | – | – | – | – | – | – |
| **P** | 2.22 | – | 1.20 | 1.84 | 1.93 | – | 1.80 | 0.430 | – | 1.88 | 1.85 | – | 2.08 | 1.87 | 1.92 | 0.11 | – | – | – | – | – | – |
| **K** | 1.14 | – | 0.0806 | 0.136 | 0.0860 | – | 0.361 | 0.521 | – | 0.485 | 0.987 | – | 1.07 | 10.9 | 3.37 | 5.04 | – | – | – | – | – | – |
| **Ca** | 0.056 | 0.0211 | 0.0990 | 0.134 | 0.0536 | 0.0679 | 0.0719 | 0.0395 | 0.0565 | 0.0654 | 0.153 | 0.0459 | 0.0486 | 0.0673 | 0.0728 | 0.0403 | – | – | – | – | – | – |
| **Sc** | 0.554 | 0.622 | 0.542 | 0.507 | 0.651 | 0.643 | 0.586 | 0.0600 | 0.737 | 0.605 | 0.681 | 0.667 | 0.560 | 0.607 | 0.643 | 0.0640 | 0.222 | 0.0768 | 0.41 | 0.41 | – | 0.36 |
| **Ti** | 0.267 | 0.215 | 0.288 | 0.271 | 0.190 | 0.275 | 0.251 | 0.0391 | 0.188 | 0.318 | 0.310 | 0.208 | 0.250 | 0.240 | 0.252 | 0.0528 | 0.0193 | 0.00754 | – | – | – | 0.16 |
| **V** | 0.135 | 0.0458 | 0.0915 | 0.104 | 0.135 | 0.0851 | 0.0993 | 0.0337 | 0.208 | 0.172 | 0.267 | 0.190 | 0.150 | 0.218 | 0.201 | 0.0407 | 0.00741 | 0.00257 | 0.06 | 0.17 | – | 0.11 |
| **Cr** | 0.0704 | 0.0217 | 0.0422 | 0.0567 | 0.0898 | 0.0390 | 0.0533 | 0.0244 | 0.138 | 0.102 | 0.146 | 0.110 | 0.097 | 0.165 | 0.126 | 0.0275 | 0.00277 | 0.00157 | 0.07 | 0.43 | – | 0.16 |
| **Mn** | 0.925 | 0.853 | 0.877 | 0.900 | 0.927 | 0.868 | 0.892 | 0.0307 | 0.914 | 0.863 | 1.01 | 0.886 | 0.914 | 0.920 | 0.917 | 0.0484 | 0.949 | 0.0305 | 1.13 | 0.17 | 1.11 | 1.06 |
| **Co** | 3.07 | 2.91 | 2.76 | 2.94 | 2.44 | 2.68 | 2.80 | 0.225 | 2.37 | 2.48 | 2.46 | 2.39 | 2.51 | 2.31 | 2.42 | 0.0754 | 2.79 | 0.096 | 2.51 | 0.21 | 2.21 | 1.88 |
| **Ni** | 4.68 | 5.29 | 4.91 | 4.37 | 3.90 | 4.59 | 4.62 | 0.473 | 3.35 | 3.92 | 3.61 | 3.51 | 3.90 | 3.32 | 3.60 | 0.260 | 4.99 | 0.533 | 3.77 | 0.16 | 2.04 | 3.63 |
| **Cu** | 1.49 | 1.27 | 0.939 | 0.394 | 1.50 | 1.12 | 1.12 | 0.417 | 1.66 | 1.45 | 2.07 | 1.68 | 1.50 | 1.62 | 1.66 | 0.218 | 0.930 | 0.190 | 1.07 | 0.32 | – | 2.27 |
| **Zn** | 1.69 | 1.73 | 1.64 | 1.73 | 1.57 | 1.72 | 1.68 | 0.0659 | 1.87 | 1.78 | 2.02 | 1.86 | 1.77 | 1.77 | 1.84 | 0.096 | 1.38 | 0.151 | 1.81 | 0.2 | 1.53 | 1.64 |
| **Ga** | 0.0156 | 0.00781 | 0.0193 | 0.0385 | 0.0339 | 0.0160 | 0.0218 | 0.0118 | 0.0676 | 0.0417 | 0.112 | 0.0538 | 0.0377 | 0.0659 | 0.0631 | 0.0268 | 0.00578 | 0.00374 | 0.13 | 0.23 | – | – |
| **Ge** | 0.353 | 0.408 | 0.368 | 0.365 | 0.388 | 0.404 | 0.381 | 0.0224 | 0.555 | 0.531 | 0.471 | 0.552 | 0.463 | 0.500 | 0.512 | 0.0401 | 0.468 | 0.0340 | – | – | – | – |
| **As** | 1.14 | 1.12 | 0.985 | 0.772 | 0.429 | 1.23 | 0.946 | 0.300 | 1.06 | 0.763 | 0.964 | 1.07 | 0.905 | 0.973 | 0.956 | 0.114 | 1.07 | 0.117 | – | – | – | – |
| **Rb** | 0.202 | 0.0128 | 0.0480 | 0.0519 | 1.54 | – | 0.370 | 0.656 | 0.0485 | 0.178 | 0.650 | 0.0203 | 0.623 | 0.0892 | 0.268 | 0.290 | 0.771 | 0.392 | – | – | – | – |
| **Sr** | 0.0100 | 0.000324 | 0.0492 | 0.199 | 0.00151 | 0.0139 | 0.0456 | 0.0771 | 0.00328 | 0.0265 | 0.449 | 0.00119 | 0.0118 | 0.00893 | 0.083 | 0.179 | 0.281 | 0.588 | 0.36 | 0.83 | – | – |
| **Y** | 0.0356 | 0.0349 | 0.210 | 0.187 | 0.0405 | 0.0291 | 0.0895 | 0.0848 | 0.0616 | 0.262 | 0.200 | 0.0447 | 0.0440 | 0.185 | 0.133 | 0.0944 | 0.0132 | 0.0134 | 0.18 | 0.78 | – | – |
| **Zr** | 1.21 | 0.0905 | 0.253 | 0.441 | 0.493 | 0.496 | 0.497 | 0.382 | 0.523 | 1.06 | 0.509 | 0.662 | 0.742 | 0.525 | 0.670 | 0.212 | 0.227 | 0.497 | 0.06 | 0.83 | – | – |
| **Nb** | 7.36 | 2.40 | 0.815 | 1.21 | 1.47 | 5.60 | 3.14 | 2.70 | 1.12 | 2.41 | 0.381 | 1.55 | 2.70 | 0.313 | 1.41 | 1.00 | 0.589 | 0.621 | 0.57 | 0.88 | – | – |
| **Mo** | 0.902 | 0.360 | 0.703 | 0.715 | 0.0533 | 1.24 | 0.661 | 0.413 | 2.27 | 1.07 | 1.29 | 0.790 | 2.01 | 0.977 | 1.40 | 0.600 | 1.21 | 0.356 | – | – | – | – |
| **Ag** | 0.667 | 0.762 | 0.662 | 0.357 | 0.0893 | 0.824 | 0.560 | 0.281 | 0.876 | 0.393 | 0.496 | 0.906 | 0.536 | 1.37 | 0.762 | 0.363 | 0.651 | 0.262 | – | – | – | – |
| **Cd** | 0.692 | 0.451 | 0.704 | 0.817 | 0.847 | 0.209 | 0.620 | 0.245 | 0.810 | 1.00 | 0.570 | 0.671 | 0.494 | 0.369 | 0.652 | 0.226 | 0.542 | 0.103 | – | – | – | – |
| **In** | 0.882 | 0.980 | 0.765 | 0.694 | 0.0349 | 0.853 | 0.701 | 0.341 | 1.18 | 0.904 | 1.01 | 0.939 | 1.02 | 1.38 | 1.07 | 0.177 | 0.483 | 0.275 | – | – | – | – |
| **Cs** | – | – | 0.0356 | 0.0121 | 0.328 | – | 0.125 | 0.176 | 0.532 | 0.164 | 0.359 | 0.973 | 0.363 | 0.937 | 0.555 | 0.331 | 0.762 | 0.376 | – | – | – | – |
| **Ba** | 0.319 | 0.0132 | 0.111 | 0.225 | 0.00076 | 0.403 | 0.179 | 0.165 | 2.46 | 0.103 | 0.626 | 0.0464 | 0.160 | 0.0702 | 0.578 | 0.947 | 3.03 | 3.11 | – | – | – | – |
| **La** | 0.0199 | 0.00266 | 0.163 | 0.217 | 0.0783 | 0.0582 | 0.0898 | 0.0838 | 0.289 | 0.0431 | 0.328 | 0.0520 | 0.0843 | 0.112 | 0.151 | 0.125 | 0.716 | 0.802 | – | – | – | – |
| **Ce** | 0.00934 | 0.000369 | 0.168 | 0.223 | 0.00439 | 0.401 | 0.134 | 0.162 | 0.155 | 0.0145 | 0.318 | 0.0228 | 0.0418 | 0.0115 | 0.0940 | 0.122 | 0.0809 | 0.0791 | 1.07 | 0.64 | – | – |
| **Pr** | 0.00581 | 0.00717 | 0.0687 | 0.183 | 0.0105 | 0.0335 | 0.0514 | 0.0686 | 0.292 | 0.0654 | 0.273 | 0.0508 | 0.0347 | 0.0205 | 0.123 | 0.125 | 0.513 | 0.303 | – | – | – | – |
| **Nd** | 0.00721 | 0.00345 | 0.0648 | 0.174 | 0.0227 | 0.0300 | 0.0503 | 0.0644 | 0.115 | 0.0121 | 0.171 | 0.0223 | 0.0179 | 0.0199 | 0.0597 | 0.0670 | 0.433 | 0.597 | – | – | – | – |
| **Sm** | 0.0201 | 0.0184 | 0.0644 | 0.168 | 0.0236 | 0.202 | 0.0828 | 0.0817 | 0.0887 | 0.128 | 0.100 | 0.0637 | 0.0406 | 0.0286 | 0.0749 | 0.0375 | 0.581 | 0.174 | – | – | – | – |
| **Eu** | 0.0502 | 0.0279 | 0.162 | 0.141 | 0.0175 | 0.411 | 0.135 | 0.148 | 0.0725 | 0.357 | 0.120 | 0.0761 | 0.0699 | 0.0386 | 0.122 | 0.118 | 0.252 | 0.211 | – | – | – | – |
| **Gd** | 0.0173 | 0.0665 | 0.0662 | 0.166 | 0.0231 | 0.158 | 0.0828 | 0.0647 | 0.0533 | 0.0160 | 0.0729 | 0.0617 | 0.0195 | 0.0651 | 0.0481 | 0.0243 | 0.339 | 0.0712 | – | – | – | – |
| **Tb** | 0.0206 | 0.0780 | 0.0785 | 0.168 | 0.0238 | 0.163 | 0.0887 | 0.0646 | 0.0644 | 0.143 | 0.0565 | 0.108 | 0.0383 | 0.140 | 0.0918 | 0.0450 | 0.186 | 0.0883 | – | – | – | – |
| **Dy** | 0.0242 | 0.220 | 0.0761 | 0.166 | 0.0266 | 0.080 | 0.0988 | 0.0785 | 0.0762 | 0.123 | 0.126 | 0.0605 | 0.0345 | 0.132 | 0.0921 | 0.0407 | 0.0919 | 0.145 | – | – | – | – |
| **Ho** | 0.0356 | 0.0945 | 0.0840 | 0.175 | 0.0541 | 0.297 | 0.123 | 0.0977 | 0.0799 | 0.186 | 0.295 | 0.0729 | 0.0444 | 0.273 | 0.159 | 0.109 | 0.0680 | 0.117 | – | – | – | – |
| **Er** | 0.0490 | 0.559 | 0.186 | 0.170 | 0.0480 | 0.247 | 0.210 | 0.188 | 0.142 | 0.359 | 0.199 | 0.123 | 0.136 | 0.249 | 0.201 | 0.0905 | 0.0136 | 0.00550 | – | – | – | – |
| **Tm** | 0.0706 | – | 0.216 | 0.438 | 0.126 | 0.208 | 0.212 | 0.140 | 0.429 | 0.810 | 0.253 | 0.392 | 0.167 | 0.851 | 0.484 | 0.285 | 0.0367 | 0.0460 | – | – | – | – |
| **Yb** | 0.099 | 0.812 | 0.196 | 0.166 | 0.168 | 0.337 | 0.296 | 0.265 | 0.454 | 0.319 | 0.498 | 0.168 | 0.149 | 0.731 | 0.386 | 0.221 | 0.0176 | 0.0116 | – | – | – | – |
| **Lu** | – | 0.459 | 0.160 | 0.153 | 0.198 | 0.908 | 0.376 | 0.323 | 1.13 | 2.82 | 0.777 | 0.451 | 0.344 | 0.679 | 1.03 | 0.917 | 0.0517 | 0.0133 | – | – | – | – |
| **Hf** | 0.515 | 0.107 | 0.211 | 0.207 | 0.264 | 0.338 | 0.274 | 0.140 | 0.194 | 0.559 | 0.373 | 0.312 | 0.380 | 0.388 | 0.368 | 0.119 | 0.0900 | 0.139 | – | – | – | – |
| **Ta** | – | 0.869 | 0.492 | 1.06 | 0.566 | 1.62 | 0.921 | 0.453 | 0.630 | 1.21 | 0.151 | 0.694 | 1.19 | 0.238 | 0.686 | 0.452 | 2.18 | 2.62 | 1.11 | 0.92 | – | – |
| **W** | 1.79 | 0.114 | 0.366 | 0.198 | 0.00342 | 1.83 | 0.717 | 0.856 | 0.521 | 0.290 | 0.0585 | 0.435 | 0.731 | 1.60 | 0.606 | 0.535 | 0.588 | 0.178 | – | – | – | – |
| **Re** | 1.41 | 0.467 | 2.25 | 0.967 | 0.153 | 0.646 | 0.983 | 0.757 | 2.09 | 0.558 | 1.26 | 1.07 | 0.874 | 0.531 | 1.06 | 0.579 | 0.565 | 0.255 | – | – | – | – |
| **Tl** | – | 0.527 | 0.0622 | 0.329 | 0.0651 | – | 0.246 | 0.226 | 1.08 | 0.550 | 0.911 | 1.33 | 1.37 | 0.878 | 1.02 | 0.308 | 0.857 | 0.338 | – | – | – | – |
| **Pb** | 0.942 | 0.695 | 0.266 | 1.04 | 0.145 | 2.68 | 0.960 | 0.914 | 6.33 | 0.593 | 1.09 | 0.649 | 0.718 | 1.13 | 1.75 | 2.26 | 0.549 | 0.137 | – | – | – | – |
| **Bi** | 0.603 | 0.559 | 1.15 | 1.44 | 0.158 | 1.61 | 0.920 | 0.567 | 1.80 | 0.658 | 0.628 | 0.603 | 0.313 | 0.868 | 0.813 | 0.518 | 0.966 | 0.557 | – | – | – | – |
| **Th** | 0.0485 | 0.00150 | 0.200 | 0.150 | 0.276 | 1.25 | 0.321 | 0.466 | 1.19 | 0.201 | 0.521 | 0.644 | 0.613 | 0.644 | 0.635 | 0.319 | 0.293 | 0.133 | – | – | – | – |
| **U** | 0.158 | 0.0106 | 0.228 | 0.184 | 0.0495 | 1.19 | 0.304 | 0.443 | 0.808 | 0.393 | 0.629 | 0.560 | 0.484 | 0.473 | 0.558 | 0.147 | 0.504 | 0.242 | – | – | – | – |

Avrg = average; SD = standard deviation; – = not available; Experimental reference values: A = Le Roux et al., 2011; B = Foley et al., 2013.

### 4.5.4 Secondary orthopyroxene crystallization

Comparing the distribution coefficients of Ni ($D_{Ni}$) between olivine and opx in the different cratonic settings it is observed that Kaapvaal peridotites have systematically higher $D_{Ni}^{ol/opx}$ values in contrast to West Greenland peridotites, which speaks for higher Ni concentrations in olivines. Sobolev *et al.* (2007) showed that high Ni contents in olivine indicate lower olivine abundance in the source region. Thus, on a space of modal olivine/opx vs. NiO wt% in olivine (Figure 23) the higher opx content in xenoliths is accompanied by higher Ni abundances in olivines. Figure 23 demonstrates that the higher Ni concentrations in Kaapvaal olivines are a function of lower olivine/opx, which indicates higher modal opx abundances in the source region. West Greenland olivines demonstrate no clear correlation but rather plot at constant olivine/opx and a confined NiO wt% range, which may be interpreted as a signal of more depleted, olivine-rich composition.

Modal opx contents are 25 ±10 % in Kaapvaal peridotites compared to only 11 ±12 % in West Greenland peridotites (Wittig *et al.*, 2008). Orthopyroxene enrichment in Kaapvaal peridotites is characterized by (i) textural evidence for amoeboid opx replacing olivine (Bell *et al.*, 2005a; Rehfeldt *et al.*, 2008a), (ii) higher whole-rock $SiO_2$ contents compared to West Greenland peridotites (46±2 wt% vs. 44±2 wt%; Carswell and Dawson, 1970; Chen, 1971; Nixon and Boyd, 1973; Carswell *et al.*, 1979; Erlank, 1987; Kelemen *et al.*, 1998; Hanghøj *et al.*, 2001b; Grégoire *et al.*, 2003; Bernstein *et al.*, 2006b; Wittig *et al.*, 2008), (iii) trace element disequilibrium between opx and cpx or grt, and (iv) oxygen isotope fractionation between opx and olivine (Zhang *et al.*, 2001; Rehfeldt *et al.*, 2008a). The latter two of these features indicate that the opx enrichment event is distinct from later metasomatic introduction of cpx and grt.

The increase of Ni in olivine with increasing modal opx in Kaapvaal craton peridotites can be interpreted to reflect opx addition at the expense of olivine (Kelemen *et al.*, 1998). Orthopyroxene has a more limited capacity to accommodate Ni, so that Ni becomes enriched in the remaining olivine (Milke *et al.*, 2011). In agreement with this interpretation, no trend of increasing Ni in olivine with decreasing modal olivine/opx is present in West Greenland peridotites (Figure 23), whereas Kaapvaal demonstrates a slight increase in Ni abundances with increasing opx/olivine.

Sm-Nd and Lu-Hf age determination on grts in Kaapvaal peridotites, diamond inclusions and mineral concentrates have revealed at least two grt generations (Richardson *et al.*, 1984; Pearson *et al.*, 1995; Simon *et al.*, 2007a; Lazarov *et al.*, 2009). The older grts have been related to the introduction of opx during the late Archaean (Bell *et al.*, 2005a; Simon *et al.*, 2007a). Rhenium depletion ages (2.97 ±0.04 Ga) of Kaapvaal peridotites coincide with these first-generation grt ages, reflecting approximately coeval melt depletion and silica-enrichment (Bell *et al.*, 2005a) supporting the interpretation of a subduction-related environment for partial melting and silica-enrichment. Textural relationships clearly indicate crystallization of opx prior to cpx, so that cpx is probably related to the second episode of grt introduction (Rehfeldt *et al.*, 2008a).

Secondary opx crystallizing at the expense of olivine can be expected to have anomalously low trace element compositions inherited from the olivine for all elements other than Co, Ni, Cu and Zn, which have high $D^{ol/opx}$ and so will remain preferentially in olivine. Additionally, since several studies have shown that opx enrichment may be due to subduction-related silica-rich melt or fluid (Bell *et al.*, 2005a; Lee, 2006; Pearson and Wittig, 2008; Rehfeldt *et al.*, 2008a), the resulting opx compositions may be more enriched in large ion lithophile elements than in HFSE (Stalder *et al.*, 1998; Kessel *et al.*, 2005), and may be more enriched than olivines.

The lower $D^{ol/opx}$ for Al in Kaapvaal compared to West Greenland peridotites indicate incomplete re-equilibration of secondary opx with olivine, since it results from the higher Al introduced during the enrichment event that was accompanied by grt crystallization, thus buffering the opx at high $Al_2O_3$ contents. This may be explained by high $Al_2O_3$ contents in subduction fluids or melts, which are strongly feldspar-normative (Schneider and Eggler, 1986; Moyen and Martin, 2012). This opens the possibility that olivine may retain a geochemical signal from before the enrichment in opx.

Similarly, slightly lower $D^{ol/opx}$ for Cr, V and Cu in Kaapvaal compared to West Greenland peridotites (Table 20) may reflect inheritance from olivine during the replacement reaction. Partition coefficients for other chalcophile elements (Mo, Ag, Cd and In) are higher in West Greenland peridotites relative to Kaapvaal.

### 4.5.5 Modification by Phanerozoic melt infiltration

Both West Greenland and Kaapvaal peridotites have experienced Phanerozoic crystallization of cpx and grt (Carswell and Dawson, 1970; Simon *et al.*, 2003; Wittig *et al.*, 2010a) that may have also influenced the compositions of earlier olivine and opx. The addition of the majority of these Phanerozoic phases was relatively recent, close to the time of kimberlite sampling, thus equilibrium trace element partitioning relations with olivine and opx are less likely to have been attained, preserving substantial isotopic and trace element disequilibrium (Simon *et al.*, 2003; Simon *et al.*, 2007a). This process may be seen in disequilibrium values for $D^{ol/opx}$, enriched REE in opx, and in zonation of trace elements between cores and rims. An almost constant, but low modal amount of cpx in West Greenland peridotites is the result of a small but thorough metasomatic overprint; most of these rocks originally contained no cpx. In contrast, Kaapvaal peridotites have a large range of modal cpx, from zero to 28 vol% (Rehfeldt *et al.*, 2008a). The effect of this metasomatism on opx crystals is to increase their Ca contents towards levels buffered by the presence of cpx. A stronger metasomatic overprinting of Kaapvaal in comparison to West Greenland peridotites is also evident from higher whole-rock CaO and $Na_2O$ contents (stealth meatsomatism; O'Reilly and Griffin, 2013), enrichment in mildly compatible elements (Menzies *et al.*, 1987), low oxygen isotope ratios and mineral/mineral disequilibria (Zhang *et al.*, 2000; Rehfeldt *et al.*, 2008a), as well as disturbance of Sm-Nd and Rb/Sr isotope systematics (Richardson *et al.*, 1985; Simon *et al.*, 2007a).

The timing of secondary crystallization of cpx and grt in the West Greenland peridotite xenoliths has been suggested to be related to widespread kimberlite and ultramafic lamprophyre magmatism at ca. 570 ±20 Ma (Wittig *et al.*, 2008), although older ages of Gardar magmatism and a 2 Ga event probably related to craton assembly may have affected the lower lithosphere. In Kaapvaal peridotites, metasomatism may be related to Karoo magmatism (~180 Ma ago; Jourdan *et al.*, 2004) and/or to metasomatic events that also resulted in MARID suite assemblages at 80–140 Ma (Konzett *et al.*, 1998a; Konzett *et al.*, 2000).

The lower Ca and Al contents in Kaapvaal olivines relative to West Greenland peridotites (Figure 19) may reflect inheritance from cpx-free protoliths and indicate that full equilibrium with relatively recent secondary cpx was not achieved. This is also evident in textures, in which the recently introduced cpx and grt are spatially associated in patches that arose from closed and disrupted veins (Rehfeldt *et al.*, 2008a). In contrast, West Greenland peridotites with higher and more variable Ca and Al contents, cpx crystallization may have occurred a longer time before kimberlite eruption, so that equilibration of olivine with cpx was completed. The conditions of preservation of zoned olivines are not well understood: distinct trace element signatures in mineral cores characteristic of depleted Archaean cratonic mantle are preserved in Antarctic peridotites (Foley *et al.*, 2006), whereas spinel-grt peridotites from Vitim, Siberia, which contain textures in which cpx clearly mimics the form of melts from which they were introduced, show no trace element zonation (Glaser *et al.*, 1999). Most Kaapvaal and West Greenland olivines and opxs are unzoned.

The generally higher $D^{ol/opx}$ for Zr, Nb and Hf in the West Greenland and Kaapvaal suites compared to the Mt Gambier (Veter et al., Chapter 3) and Vitim samples (Glaser *et al.*, 1999) (Table 20) reflect lower HFSE contents in opx, possibly related to enrichment of HFSE in West Greenland and Kaapvaal during the Phanerozoic cpx infiltration event, which is related to a Fe- and Ti-enriched silicate melt. Flat to slightly negative sloping opx REE patterns in West Greenland and Kaapvaal peridotites reflect enrichment in REE (Figure 21) and are associated with this late introduction of cpx, which itself has a convex upward REE pattern, enriched in light and middle REE (Grégoire *et al.*, 2003; Rehfeldt *et al.*, 2008a). Disequilibrium cpx/opx and grt/opx partitioning in Kaapvaal peridotites reflects overprinting during this event, but there is no evidence for renewed formation of opx from the same infiltrating melt or fluid (Rehfeldt *et al.*, 2008a).

The sample DJ2104 from Kaapvaal craton has low modal opx of <2 vol%: this may be considered to contain primary opx. This primary opx has trace element compositions relatively enriched in Ca, Ti, Cu, Ga, Zr, Y and Hf. It differs from opx in arc-related peridotites from the Avacha volcano in Kamchatka that have primary opx enriched in Sc, V, Ti, Cr and Nb, but slightly depleted in Co and Ni compared to secondary opx (Ishimaru *et al.*, 2007; Ionov *et al.*, 2011). Overall, the melt responsible for cpx and grt crystallization was more enriched in Fe, Ti, Ca, V, Zr and LREE compared to the silica-richer agent that introduced opx. Similarly, in West Greenland peridotites an increase in Fe, Ca, LREE in opx and olivine may be related to small amounts of secondary cpx and grt.

## 4.6 Conclusions

Olivine and opx trace element compositions in peridotite xenoliths from West Greenland and Kaapvaal offer a unique opportunity to distinguish between primary and secondary opx and between different generations of lithospheric root formation and modification. High degree, low pressure, subduction-related melt depletion occurred in both cratons during the Archaean, and is seen in highly magnesian olivine and opx, negative correlation of Mn, Co, Zn and Li with Mg# in both olivine and opx, and in opx with $(La/Yb)_N$ >1.

The major differences between West Greenland and Kaapvaal peridotites are high modal olivine and high modal opx contents, respectively, positive correlation of Ni in olivine with modal abundance olivine/opx in Kaapvaal but not in West Greenland peridotites, and a large range of Ni contents in opx in Kaapvaal peridotites which does not correlate with Mg#. These can be related to silicate melt or fluid metasomatism that caused opx enrichment in the Kaapvaal craton only. The composition of this component can be assumed to be high in Si and Al, but low in HREE and HFSE. The enriching agent was most likely derived in the Archaean from subduction process. Low HREE contents opx reflecting earlier depletion were not overprinted.

Crystallization of secondary cpx occurred in both West Greenland and Kaapvaal peridotites and is mostly reflected in elevated Ca, Al and Ti contents in olivine and opx, and in middle and light REE enrichment in opx. Low Ca and Al contents in Kaapvaal olivines indicate cpx-free protoliths to which cpx was added late in the history of the cratonic root. Similarly, Ti anomalies in Kaapvaal craton peridotites reflect variable equilibration with secondary cpx.

Although it is currently not possible to establish a unique tool for deciphering between primary and secondary opx in cratonic mantle peridotites, a few features of Kaapvaal olivine and opx may help to identify metasomatic opx: (1) correlation of Ni in olivine with modal ol/opx, (2) high opx Al contents reflecting equilibrium with secondary grt, and (3) high Zr/Hf ratio in opx as seen in websterites. Additionally, partition coefficients for olivine/opx ($D^{ol/opx}$) are slightly lower in Kaapvaal relative to West Greenland peridotite xenoliths for the elements V, Cr, Cu, Ga and Sr and slightly higher in Nb and Ta (Table 20). These elements may prove to have potential for distinguishing between primary and secondary opx.


### ACKNOWLEDGMENTS

This work was carried out as part of a PhD study of MV at Macquarie University and was supported by the Australian Government International Research Training Program (iRTP) Scholarship (No. 2017056). This research was funded by the ARC Centre of Excellence for Core to Crust Fluid Systems (CCFS). This is contribution 615 from the CCFS (http://www.ccfs.mq.edu.au). Stephan Buhre and Nora

Groschopf (Johannes Gutenberg-University, Mainz) are thanked for assistance with EPMA analyses acquisition.

# CHAPTER 5

## SUMMARY AND CONCLUSION

In this thesis, the geochemical composition of the subcontinental lithospheric mantle is investigated by acquiring new precise trace and ultra-trace element compositions in the mantle minerals olivine, opx, cpx ±grt. The analysed samples are from three different locations, (1) spinel-peridotite xenoliths sampling the off-cratonic continental lithosphere at Mt Gambier (southeastern Australia), (2) cratonic mantle xenoliths entrained in kimberlites from the North Atlantic craton in West Greenland and (3) cratonic mantle xenoliths in kimberlites from the Kaapvaal craton (South Africa).

Achievement of thesis aims:

*1) Overcome the analytical limitations by refining in-situ LA-ICP-MS measurement for analysis of low-level concentration elements, e.g., incompatible REE in olivines and orthopyroxenes, and VCSE in silicates, (Chapter 2)*

The motivation for the first part was to acquire precise trace element concentrations in the mantle minerals olivine and orthopyroxene, which have abundances for many trace elements close to detection limits. To overcome the analytical limitations an improvement in the conventional method had to be developed. For this purpose, the widely used *in situ* LA-ICP-MS method was modified with the aim of sensitivity enhancement and improvement of detection limits. The method improvement included the analysis of reference material glasses with certified concentrations as well as a natural olivine sample, to test the applicability of the method.

The acquisition of trace elements was done in different modes, (1) 'normal mode' LA-ICP-MS ablation, which included no further changes to the standard acquisition and (2) 'hydrogen mode' where 5 mL $min^{-1}$ molecular hydrogen gas was admixed to the He-ablated sample mixture.

The improved method resulted in improved sensitivity on certified reference glasses, which is linked to higher first ionisation energy in Zn, As and Cd, which reported the most improvement. Furthermore, the addition of hydrogen gas improves the precision of data acquisition from 3–6 down to 2–6 %RSD. Measurements on the natural olivine demonstrate improvements in precision and the limit of detection (ranges), e.g., for Cu from 6–10 to 4–6 ng g-1, Nd from 1–2 to 0.6–1.0 ng $g^{-1}$. Moreover, the hydrogen mode method facilitates the acquisition of low-level concentration trace- and ultra-trace elements in olivine, which allow acquisition of a complete REE pattern as well as quantification of volatile chalcophile and siderophile elements (VCSE).

*2) Apply the improved method on natural mantle peridotite xenoliths and determine the distribution and behaviour of VSCE in mantle silicate phases. For this purpose, mantle spinel-peridotite xenoliths from Mt Gambier, southeastern Australia were chosen, which represent unusually fresh and mantle relatively unaffected by enriching metasomatic processes, (Chapter 3)*

With the analytical advances in the first part of the thesis, the improved method was applied on natural rock samples with the aim to acquire a complete set of elements, including the REE and VCSE, and thus to define the composition of the continental lithospheric mantle. For this purpose, samples from Mt Gambier from Cenozoic volcanic activity in the Newer Volcanic Province (NVP; south Australia) were analysed. The samples are spinel-peridotite xenoliths entrained in alkali basalts and sample the continental lithosphere at depths 60-80 km. Petrographic observations verified the freshness of the samples with limited melt infiltration observed along grain boundaries or in small glass pockets. The measured trace element abundances of the minerals with their modal abundances were used to recalculate the bulk composition and compare it with measured whole rock analyses. The results clearly demonstrate the involvement of an infiltrating agent in the measured bulk rock analyses, which corresponds to glass along grain boundaries seen in thin sections. The infiltrated melt was identified to be enriched in highly incompatible elements and to a lesser degree in LREE elements.

The volatile chalcophile and siderophile element concentrations in olivine and orthopyroxene are underrepresented in literature, since these phases are not the major hosts for this group of elements. However, to understand the magmatic and metasomatic processes in the mantle, and estimate its composition, the VCSE abundances were investigated in silicate phases. The results show that out of the three silicate phases (ol, opx and cpx) olivine is the major host for Mo, Ag and Cd, whereas In is distributed evenly.

*3) Apply the method to samples of the cratonic lithosphere mantle and compare previous observations with more "complex" samples that experienced several different depletion and re-enrichment events. For this part, kimberlite-hosted xenoliths from two different cratons, the Kaapvaal craton, South Africa and the North Atlantic craton, West Greenland were chosen for investigation and comparison with one another, (Chapter 4)*

The improved and tested LA-ICP-MS method was further applied on samples from two cratonic settings, Kaapvaal and North Atlantic, which both experienced high degrees of partial melting but later experienced different metasomatic overprinting events. The motivation was to acquire new and especially extended palette of trace element composition in these well-studied settings, and to determine differences and/or similarities between the two cratons preserved in the geochemical composition. The acquired trace element composition in olivine and orthopyroxene are investigated for geochemical fingerprinting, which may provide insights on the processes involved in the early stages of depletion and re-enrichment, which are not recorded in cpx and grt, since these minerals are introduced at a later stage of metasomatic enrichment. The establishment of a unique tool for deciphering between primary and secondary opx in

cratonic mantle peridotites is currently not identified. However, the plethora of new trace and ultra-trace element data may help to identify some key features between Kaapvaal and West Greenland which help unravel the history of primary and secondary orthopyroxene.

# REFERENCES


Alard, O., 2000. Chalcophile and siderophile elements in the mantle: geochemical characteristics and distributions. Macquarie University.

Alard, O., Griffin, W.L., Lorand, J.P., Jackson, S.E. and O'Reilly, S.Y., 2000. Non-chondritic distribution of the highly siderophile elements in mantle sulphides. *Nature* **407**, 891-894.

Allsopp, H., Bristow, J., Smith, C., Brown, R., Gleadow, A., Kramers, J. and Garvie, O., 1989. A summary of radiometric dating methods applicable to kimberlites and related rocks. *Kimberlites and related rocks* **1**, 343-357.

Ammannati, E., Jacob, D.E., Avanzinelli, R., Foley, S.F. and Conticelli, S., 2016. Low Ni olivine in silica-undersaturated ultrapotassic igneous rocks as evidence for carbonate metasomatism in the mantle. *Earth and Planetary Science Letters* **444**, 64-74.

Anhaeusser, C.R. and Walraven, F., 1999. Episodic granitoid emplacement in the western Kaapvaal Craton: evidence from the Archaean Kraaipan granite-greenstone terrane, South Africa. *Journal of African Earth Sciences* **28**, 289-309.

Armstrong, J.T., 1995. Citzaf-a package of correction programs for the quantitative Electron Microbeam X-Ray-Analysis of thick polished materials, thin-films, and particles. *Microbeam Analysis* **4**, 177-200.

Aulbach, S., Lin, A., Weiss, Y. and Yaxley, G., 2020a. Using wehrlites to monitor the passage of CO2-bearing melts in the shallow lithosphere, EGU General Assembly Conference Abstracts. Online, 4-8 May 2020, p. 8485.

Aulbach, S., Lin, A.-B., Weiss, Y. and Yaxley, G.M., 2020b. Wehrlites from continental mantle monitor the passage and degassing of carbonated melts. *Geochemical Perspectives Letters* **15**, 30–34.

Barth, M.G., Rudnick, R.L., Horn, I., McDonough, W.F., Spicuzza, M.J., Valley, J.W. and Haggerty, S.E., 2001. Geochemistry of xenolithic eclogites from West Africa, Part I: A link between low MgO eclogites and Archean crust formation. *Geochimica et Cosmochimica Acta* **65**, 1499-1527.

Bell, D.R., Gregoire, M., Grove, T., Chatterjee, N., Carlson, R. and Buseck, P., 2005a. Silica and volatile-element metasomatism of Archean mantle: a xenolith-scale example from the Kaapvaal Craton. *Contributions to Mineralogy and Petrology* **150**, 251.

Bell, D.R., Grégoire, M., Grove, T.L., Chatterjee, N., Carlson, R.W. and Buseck, P.R., 2005b. Silica and volatile-element metasomatism of Archean mantle: a xenolith-scale example from the Kaapvaal Craton. *Contributions to Mineralogy and Petrology* **150**, 251-267.

Bernstein, S., Hanghøj, K., Kelemen, P.B. and Brooks, C.K., 2006a. Ultra-depleted, shallow cratonic mantle beneath West Greenland: dunitic xenoliths from Ubekendt Ejland. *Contributions to Mineralogy and Petrology* **152**, 335-347.

Bernstein, S., Hanghøj, K., Kelemen, P.B. and Brooks, C.K., 2006b. Ultra-depleted, shallow cratonic mantle beneath West Greenland: dunitic xenoliths from Ubekendt Ejland. *Contributions to Mineralogy and Petrology* **152**, 335.

Bernstein, S., Kelemen, P.B. and Brooks, C.K., 1998. Depleted spinel harzburgite xenoliths in Tertiary dykes from East Greenland: restites from high degree melting. *Earth and Planetary Science Letters* **154**, 221-235.

Bizzarro, M. and Stevenson, R.K., 2003. Major element composition of the lithospheric mantle under the North Atlantic craton: evidence from peridotite xenoliths of the Sarfartoq area, southwestern Greenland. *Contributions to Mineralogy and Petrology* **146**, 223-240.

Black, L., Gale, N., Moorbath, S., Pankhurst, R. and McGregor, V., 1971. Isotopic dating of very early Precambrian amphibolite facies gneisses from the Godthaab district, West Greenland. *Earth and Planetary Science Letters* **12**, 245-259.

Bodinier, J.L., Merlet, C., Bedini, R.M., Simien, F., Remaidi, M. and Garrido, C.J., 1996. Distribution of niobium, tantalum, and other highly incompatible trace elements in the lithospheric mantle: The spinel paradox. *Geochimica et Cosmochimica Acta* **60**, 545-550.

Boyd, F. and Gurney, J.J., 1986. Diamonds and the African lithosphere. *Science* **232**, 472-477.

Boyd, F. and Mertzman, S., 1987. Composition and structure of the Kaapvaal lithosphere, southern Africa, *Magmatic processes: physicochemical principles*. The Geochemical Society. 13-24.

Boyd, F., Pokhilenko, N., Pearson, D., Mertzman, S., Sobolev, N. and Finger, L., 1997. Composition of the Siberian cratonic mantle: evidence from Udachnaya peridotite xenoliths. *Contributions to Mineralogy and Petrology* **128**, 228-246.

Boyd, F.R., 1989. Compositional distinction between oceanic and cratonic lithosphere. *Earth and Planetary Science Letters* **96**, 15-26.

Brey, G.P. and Köhler, T., 1990. Geothermobarometry in four-phase lherzolites II. new thermobarometers, and practical assessment of existing thermobarometers. *Journal of Petrology* **31**, 1353-1378.

Bridgwater, D., Watson, J. and Windley, B.F., 1973. The Archaean Craton of the North Atlantic Region. *Philosophical Transactions of the Royal Society of London* **273**, 493-512.

Buchanan, P., Reimold, W., Koeberl, C. and Kruger, F., 2004. Rb–Sr and Sm–Nd isotopic compositions of the Rooiberg Group, South Africa: early Bushveld-related volcanism. *Lithos* **75**, 373-388.

Canil, D., 1992. Orthopyroxene stability along the peridotite solidus and the origin of cratonic lithosphere beneath southern Africa. *Earth and Planetary Science Letters* **111**, 83-95.

Canil, D., 2004. Mildly incompatible elements in peridotites and the origins of mantle lithosphere. *Lithos* **77**, 375-393.

Carlson, R., Pearson, D., Boyd, F., Shirey, S., Irvine, G., Menzies, A. and Gurney, J., 1999a. Re–Os systematics of lithospheric peridotites: implications for lithosphere formation and preservation, Proceedings of the 7th International Kimberlite Conference. Red Roof Design Cape Town, pp. 99-108.

Carlson, R.W. and Moore, R.O., 2004. Age of the Eastern Kaapvaal mantle: Re-Os isotope data for peridotite xenoliths from the Monastery kimberlite. *South African Journal of Geology* **107**, 81-90.

Carlson, R.W., Pearson, D.G., Boyd, F.R., Shirey, S.B., Irvine, G., Menzies, A.H. and Gurney, J.J., 1999b. Re-Os systematics of lithospheric peridotites: Implications for lithosphere formation and preservation, In: Gurney, J.J., Gurney, J.L., Pascoe, M.D. and Richardson, S.H. (Eds.), Proceedings of the 7th International Kimberlite Conference. Red Roof, Cape Town, pp. 99-108.

Carswell, D., Clarke, D. and Mitchell, R., 1979. The petrology and geochemistry of ultramafic nodules from Pipe 200, northern Lesotho. *The Mantle Sample: Inclusion in Kimberlites and Other Volcanics* **16**, 127-144.

Carswell, D. and Dawson, J., 1970. Garnet peridotite xenoliths in South African kimberlite pipes and their petrogenesis. *Contributions to Mineralogy and Petrology* **25**, 163-184.

Chen, J.-C., 1971. Petrology and chemistry of garnet lherzolite nodules in kimberlite from South Africa. *American Mineralogist: Journal of Earth and Planetary Materials* **56**, 2098-2110.

Chenery, S. and Cook, J.M., 1993. Determination of Rare-Earth Elements in Single Mineral Grains by Laser Ablation Microprobe Inductively Coupled Plasma-Mass Spectrometry - Preliminary-Study. *Journal of Analytical Atomic Spectrometry* **8**, 299-303.

Chesley, J.T., Rudnick, R.L. and Lee, C.-T., 1999. Re-Os systematics of mantle xenoliths from the East African Rift: Age, structure, and history of the Tanzanian craton. *Geochimica et Cosmochimica Acta* **63**, 1203-1217.

Condie, K.C., O'Neill, C. and Aster, R.C., 2009. Evidence and implications for a widespread magmatic shutdown for 250 My on Earth. *Earth and Planetary Science Letters* **282**, 294-298.

Coney, P.J., Edwards, A., Hine, R., Morrison, F. and Windrim, D., 1990. The Regional Tectonics of the Tasman Orogenic System, Eastern Australia. *Journal of Structural Geology* **12**, 519-543.

Dalziel, I.W.D., 1991. Pacific Margins of Laurentia and East Antarctica — Australia as a Conjugate Rift Pair: Evidence and Implications for an Eocambrian Supercontinent. *Geology* **19**, 598-601.

Dasch, E.J. and Green, D.H., 1975. Strontium isotope geochemistry of lherzolite inclusions and host basaltic rocks, Victoria, Australia. *American Journal of Science* **275**, 461-469.

Dawson, J., 2004. A fertile harzburgite–garnet lherzolite transition: possible inferences for the roles of strain and metasomatism in upper mantle peridotites. *Lithos* **77**, 553-569.

Dawson, J.B., 1980. *Kimberlites and their xenoliths*. Springer-Verlag, Berlin Heidelberg. 250 p.

De Hoog, J.C.M., Gall, L. and Cornell, D.H., 2010. Trace-element geochemistry of mantle olivine and application to mantle petrogenesis and geothermobarometry. *Chemical Geology* **270**, 196-215.

De Wit, M.J., de Ronde, C.E., Tredoux, M., Roering, C., Hart, R.J., Armstrong, R.A., Green, R.W., Peberdy, E. and Hart, R.A., 1992. Formation of an Archaean continent. *Nature* **357**, 553-562.

Doin, M.P., Fleitout, L. and Christensen, U., 1997. Mantle convection and stability of depleted and undepleted continental lithosphere. *Journal of Geophysical Research-Solid Earth* **102**, 2771-2787.

Doin, M.P., Fleitout, L. and McKenzie, D., 1996. Geoid anomalies and the structure of continental and oceanic lithospheres. *Journal of Geophysical Research-Solid Earth* **101**, 16119-16135.

Duncan, R.A. and McDougall, I., 1989. Plate tectonic setting, *In*: Johnson, R.W. (Ed.), *Intraplate Volcanism in Eastern Australia and New Zealand*. Cambridge University Press, Cambridge. 13-18.

Durrant, S.F., 1993. Alternatives to All-Argon Plasmas in Inductively-Coupled Plasma-Mass Spectrometry (Icp-Ms) - an Overview. *Fresenius Journal of Analytical Chemistry* **347**, 389-392.

Eggins, S.M., Grün, R., McCulloch, M.T., Pike, A.W., Chappell, J., Kinsley, L., Mortimer, G., Shelley, M., Murray-Wallace, C.V. and Spötl, C., 2005. In situ U-series dating by laser-ablation multi-collector ICPMS: new prospects for Quaternary geochronology. *Quaternary Science Reviews* **24**, 2523-2538.

Eggins, S.M., Kinsley, L.P.J. and Shelley, J.M.G., 1998a. Deposition and element fractionation processes during atmospheric pressure laser sampling for analysis by ICP-MS. *Applied Surface Science* **127-129**, 278-286.

Eggins, S.M., Rudnick, R.L. and McDonough, W.F., 1998b. The composition of peridotites and their minerals: A laser-ablation ICP-MS study. *Earth and Planetary Science Letters* **154**, 53-71.

Emeleus, C. and Andrews, J.R., 1975. Mineralogy and petrology of kimberlite dyke and sheet intrusions and included peridotite xenoliths from south-west Greenland, *Physics and Chemistry of the Earth*. Elsevier. 179-197.

Erlank, A., 1987. Evidence for mantle metasomatism in peridotite nodules from the Kimberley pipes, South Africa. In. *Mantle metasomatism*, 221-311.

Foley, S.F., 2008. Rejuvenation and erosion of the cratonic lithosphere. *Nature Geoscience* **1**, 503-510.

Foley, S.F., Andronikov, A.V., Jacob, D.E. and Melzer, S., 2006. Evidence from Antarctic mantle peridotite xenoliths for changes in mineralogy, geochemistry and geothermal gradients beneath a developing rift. *Geochimica et Cosmochimica Acta* **70**, 3096-3120.

Foley, S.F. and Fischer, T.P., 2017. An essential role for continental rifts and lithosphere in the deep carbon cycle. *Nature Geoscience* **10**, 897-902.

Foley, S.F., Jacob, D.E. and O'Neill, H.S.C., 2011. Trace element variations in olivine phenocrysts from Ugandan potassic rocks as clues to the chemical characteristics of parental magmas. *Contributions to Mineralogy and Petrology* **162**, 1-20.

Foley, S.F., Link, K., Tiberindwa, J.V. and Barifaijo, E., 2012. Patterns and origin of igneous activity around the Tanzanian craton. *Journal of African Earth Sciences* **62**, 1-18.

Foley, S.F., Prelevic, D., Rehfeldt, T. and Jacob, D.E., 2013. Minor and trace elements in olivines as probes into early igneous and mantle melting processes. *Earth and Planetary Science Letters* **363**, 181-191.

Forte, A.M. and Perry, H.K.C., 2000. Geodynamic evidence for a chemically depleted continental tectosphere. *Science* **290**, 1940-1944.

Frey, F.A. and Green, D.H., 1974. The mineralogy, geochemistry and origin of Iherzolite inclusions in Victorian basanites. *Geochimica et Cosmochimica Acta* **38**, 1023-1059.

Frey, F.A., John Suen, C. and Stockman, H.W., 1985. The Ronda high temperature peridotite: Geochemistry and petrogenesis. *Geochimica et Cosmochimica Acta* **49**, 2469-2491.

Frey, F.A. and Prinz, M., 1978. Ultramafic inclusions from San Carlos, Arizona: petrologic and geochemical data bearing on their petrogenesis. *Earth and Planetary Science Letters* **38**, 129-176.

Friend, C., Nutman, A. and McGregor, V., 1988. Late Archaean terrane accretion in the Godthåb region, southern West Greenland. *Nature* **335**, 535-538.

Fryer, B.J., Jackson, S.E. and Longerich, H.P., 1995. Design, Operation and Role of the Laser-Ablation Microprobe Coupled with an Inductively-Coupled Plasma - Mass-Spectrometer (Lam-Icp-Ms) in the Earth-Sciences. *Canadian Mineralogist* **33**, 303-312.

Glaser, S.M., Foley, S.F. and Günther, D., 1999. Trace element compositions of minerals in garnet and spinel peridotite xenoliths from the Vitim volcanic field, Transbaikalia, Eastern Siberia. *Developments in Geotectonics* **24**, 263-285.

Green, D.H. and Wallace, M.E., 1988. Mantle Metasomatism by Ephemeral Carbonatite Melts. *Nature* **336**, 459-462.

Grégoire, M., Bell, D. and Le Roex, A., 2002. Trace element geochemistry of phlogopite-rich mafic mantle xenoliths: Their classification and their relationship to phlogopite-bearing peridotites and kimberlites revisited. *Contributions to Mineralogy and Petrology* **142**, 603-625.

Grégoire, M., Bell, D. and Le Roex, A., 2003. Garnet lherzolites from the Kaapvaal Craton (South Africa): trace element evidence for a metasomatic history. *Journal of Petrology* **44**, 629-657.

Griffin, W., O'Reilly, S. and Ryan, C., 1999a. The composition and origin of sub-continental lithospheric mantle, *In*: Fei, Y., Bertka, C.M. and Mysen, B.O. (Eds.), *Mantle Petrology: Field Observations and High Pressure Experimentation: A Tribute to Francis R. (Joe) Boyd*. Geochem. Soc. Spec. Publ., Geochemical Society, Houston. 13-45.

Griffin, W., O'Reilly, S.Y. and Stabel, A., 1988. Mantle metasomatism beneath western Victoria, Australia: II. Isotopic geochemistry of Cr-diopside lherzolites and Al-augite pyroxenites. *Geochimica et Cosmochimica Acta* **52**, 449-459.

Griffin, W.L. and O'Reilly, S.Y., 2019. Chapter 5 - The Earliest Subcontinental Lithospheric Mantle, *In*: Van Kranendonk, M.J., Bennett, V.C. and Hoffmann, J.E. (Eds.), *Earth's Oldest Rocks (Second Edition)*. Elsevier. 81-102.

Griffin, W.L., O'Reilly, S.Y., Natapov, L.M. and Ryan, C.G., 2003. The evolution of lithospheric mantle beneath the Kalahari Craton and its margins. *Lithos* **71**, 215-241.

Griffin, W.L., Shee, S.R., Ryan, C.G., Win, T.T. and Wyatt, B.A., 1999b. Harzburgite to Iherzolite and back again: Metasomatic processes in ultramafic xenoliths from the Wesselton kimberlite, Kimberley, South Africa. *Contributions to Mineralogy and Petrology* **134**, 232-250.

Guillong, M. and Günther, D., 2002. Effect of particle size distribution on ICP-induced elemental fractionation in laser ablation-inductively coupled plasma-mass spectrometry. *Journal of Analytical Atomic Spectrometry* **17**, 831-837.

Guillong, M. and Heinrich, C.A., 2007. Sensitivity enhancement in laser ablation ICP-MS using small amounts of hydrogen in the carrier gas. *Journal of Analytical Atomic Spectrometry* **22**, 1488-1494.

Günther, D., Frischknecht, R., Heinrich, C.A. and Kahlert, H.J., 1997. Capabilities of an Argon Fluoride 193 nm excimer laser for laser ablation inductively coupled plasma mass spectrometry microanalysis of geological materials. *Journal of Analytical Atomic Spectrometry* **12**, 939-944.

Günther, D. and Hattendorf, B., 2005. Solid sample analysis using laser ablation inductively coupled plasma mass spectrometry. *TrAC - Trends in Analytical Chemistry* **24**, 255-265.

Gurney, J. and Harte, B., 1980. Chemical variations in upper mantle nodules from southern African kimberlites. *Philosophical Transactions of the Royal Society of London. Series A, Mathematical and Physical Sciences* **297**, 273-293.

Gurney, J., Harte, B. and Cox, K., 1975. Mantle xenoliths in the Matsoku kimberlite pipe, *Physics and Chemistry of the Earth*. Elsevier. 507-523.

Handler, M.R., 1998. Platinum-group elements and osmium isotopic systematics in continental lithospheric mantle, Eastern Australia.

Handler, M.R., Bennett, V.C. and Esat, T.M., 1997. The persistence of off-cratonic lithospheric mantle: Os isotopic systematics of variably metasomatised southeast Australian xenoliths. *Earth and Planetary Science Letters* **151**, 61-75.

Hanghøj, K., Kelemen, P., Bernstein, S., Blusztajn, J. and Frei, R., 2001a. Osmium isotopes in the Wiedemann Fjord mantle xenoliths: A unique record of cratonic mantle formation by melt depletion in the Archaean. *Geochemistry, Geophysics, Geosystems* **2**.

Hanghøj, K., Kelemen, P., Bernstein, S., Blusztajn, J. and Frei, R., 2001b. Osmium isotopes in the Wiedemann Fjord mantle xenoliths: a unique record of cratonic mantle formation by melt depletion in the Archaean. *Geochemistry, Geophysics, Geosystems* **2**.

Harte, B., Cox, K. and Gurney, J., 1975. Petrography and geological history of upper mantle xenoliths from the Matsoku kimberlite pipe, *Physics and Chemistry of the Earth*. Elsevier. 477-506.

Hawkesworth, C., Erlank, A., Kempton, P. and Waters, F., 1990. Mantle metasomatism: isotope and trace-element trends in xenoliths from Kimberley, South Africa. *Chemical Geology* **85**, 19-34.

Herzberg, C., 2004. Geodynamic information in peridotite petrology. *Journal of Petrology* **45**, 2507-2530.

Herzberg, C.T., 1993. Lithosphere peridotites of the Kaapvaal craton. *Earth and Planetary Science Letters* **120**, 13-29.

Hoal, K.O., 2003. Samples of Proterozoic iron-enriched mantle from the Premier kimberlite. *Lithos* **71**, 259-272.

Holm, P.M. and Prægel, N.-O., 2006. Cumulates from primitive rift-related East Greenland Paleogene magmas: Petrological and isotopic evidence from the ultramafic complexes at Kælvegletscher near Kærven. *Lithos* **92**, 251-275.

Horn, I., Günther, D. and Guillong, M., 2003. Evaluation and design of a solid-state 193 nm OPO-Nd: YAG laser ablation system. *Spectrochimica Acta Part B: Atomic Spectroscopy* **58**, 1837-1846.

Ionov, D.A., Bénard, A. and Plechov, P.Y., 2011. Melt evolution in subarc mantle: evidence from heating experiments on spinel-hosted melt inclusions in peridotite xenoliths from the andesitic Avacha volcano (Kamchatka, Russia). *Contributions to Mineralogy and Petrology* **162**, 1159-1174.

Irvine, G.J., Pearson, D.G. and Carlson, R.W., 2001. Lithospheric mantle evolution of the Kaapvaal Craton: A Re-Os isotope study of peridotite xenoliths from Lesotho kimberlites. *Geophysical Research Letters* **28**, 2505-2508.

Irving, A., 1974. Geochemical and high pressure experimental studies of garnet pyroxenite and pyroxene granulite xenoliths from the Delegate basaltic pipes, Australia. *Journal of Petrology* **15**, 1-40.

Ishimaru, S., Arai, S., Ishida, Y., Shirasaka, M. and Okrugin, V.M., 2007. Melting and multi-stage metasomatism in the mantle wedge beneath a frontal arc inferred from highly depleted peridotite xenoliths from the Avacha volcano, southern Kamchatka. *Journal of Petrology* **48**, 395-433.

Jacob, D.E., 2006. High sensitivity analysis of trace element-poor geological reference glasses by laser ablation-inductively coupled plasma-mass spectrometry (LA-ICP-MS). *Geostandards and Geoanalytical Research* **30**, 221-235.

Jagoutz, E., Dawson, J., Hoernes, S., Spettel, B. and Wänke, H., 1984. Anorthositic oceanic crust in Archean Earth, 15th Lunar Planet. Sci. Conf., Houston, pp. 395-396.

Jagoutz, E., Palme, H., Baddenhausen, H., Blum, K., Cendales, M., Dreibus, G., Spettel, B., Lorenz, V. and Wänke, H., 1979. The abundances of major, minor and trace elements in the earth's mantle as derived from primitive ultramafic nodules, Lunar and Planetary Science Conference Proceedings, pp. 2031-2050.

Jaupart, C. and Mareschal, J.C., 1999. The thermal structure and thickness of continental roots. *Lithos* **48**, 93-114.

Jeffries, T.E., Pearce, N.J.G., Perkins, W.T. and Raith, A., 1996. Chemical fractionation during infrared and ultraviolet laser ablation inductively coupled plasma mass spectrometry - Implications for mineral microanalysis. *Analytical Communications* **33**, 35-39.

Jeffries, T.E., Perkins, W.T. and Pearce, N.J.G., 1995. Comparisons of Infrared and Ultraviolet-Laser Probe Microanalysis Inductively-Coupled Plasma-Mass Spectrometry in Mineral Analysis. *Analyst* **120**, 1365-1371.

Jochum, K., Hofmann, A. and Seufert, H., 1993. Tin in mantle-derived rocks: constraints on Earth evolution. *Geochimica et Cosmochimica Acta* **57**, 3585-3595.

Jochum, K.P., Mcdonough, W.F., Palme, H. and Spettel, B., 1989. Compositional Constraints on the Continental Lithospheric Mantle from Trace-Elements in Spinel Peridotite Xenoliths. *Nature* **340**, 548-550.

Jochum, K.P., Nohl, U., Herwig, K., Lammel, E., Stoll, B. and Hofmann, A.W., 2005. GeoReM: a new geochemical database for reference materials and isotopic standards. *Geostandards and Geoanalytical Research* **29**, 333-338.

Jochum, K.P., Stoll, B., Herwig, K., Willbold, M., Hofmann, A.W., Amini, M., Aarburg, S., Abouchami, W., Hellebrand, E. and Mocek, B., 2006. MPI-DING reference glasses for in situ microanalysis: New reference values for element concentrations and isotope ratios. *Geochemistry, Geophysics, Geosystems* **7**.

Jochum, K.P., Weis, U., Stoll, B., Kuzmin, D., Yang, Q., Raczek, I., Jacob, D.E., Stracke, A., Birbaum, K., Frick, D.A., Günther, D. and Enzweiler, J., 2011. Determination of reference values for NIST SRM 610-617 glasses following ISO guidelines. *Geostandards and Geoanalytical Research* **35**, 397-429.

Johnson, D., 2009. *The geology of Australia*. Cambridge University Press.

Johnson, R.W., Knutson, J. and Taylor, S.R., 1989. Johnson, R.W. (Ed.) *Intraplate Volcanism in Eastern Australia and New Zealand*. Cambridge University Press, Cambridge. 408 p.

Jordan, T.H., 1975. The continental tectosphere. *Reviews of Geophysics* **13**, 1-12.

Jourdan, F., Féraud, G., Bertrand, H., Kampunzu, A., Tshoso, G., Le Gall, B., Tiercelin, J. and Capiez, P., 2004. The Karoo triple junction questioned: evidence from Jurassic and Proterozoic 40Ar/39Ar ages and geochemistry of the giant Okavango dyke swarm (Botswana). *Earth and Planetary Science Letters* **222**, 989-1006.

Joyce, E. and Day, R., 1989. Victoria and South Australia, *In*: Johnson, R.W. (Ed.), *Intraplate Volcanism in Eastern Australia and New Zealand*. Cambridge University Press, Cambridge. 132-133.

Kaeser, B., Kalt, A. and Pettke, T., 2006. Evolution of the lithospheric mantle beneath the Marsabit volcanic field (northern Kenya): constraints from textural, P–T and geochemical studies on xenoliths. *Journal of Petrology* **47**, 2149-2184.

Kelemen, P.B., Hart, S.R. and Bernstein, S., 1998. Silica enrichment in the continental upper mantle via melt/rock reaction. *Earth and Planetary Science Letters* **164**, 387-406.

Kessel, R., Schmidt, M.W., Ulmer, P. and Pettke, T., 2005. Trace element signature of subduction-zone fluids, melts and supercritical liquids at 120–180 km depth. *Nature* **437**, 724-727.

King, S.D., 2005. Archean cratons and mantle dynamics. *Earth and Planetary Science Letters* **234**, 1-14.

Komiya, T., Yamamoto, S., Aoki, S., Sawaki, Y., Ishikawa, A., Tashiro, T., Koshida, K., Shimojo, M., Aoki, K. and Collerson, K.D., 2015. Geology of the Eoarchean,> 3.95 Ga, Nulliak supracrustal rocks in the Saglek Block, northern Labrador, Canada: The oldest geological evidence for plate tectonics. *Tectonophysics* **662**, 40-66.

König, S., Münker, C., Hohl, S., Paulick, H., Barth, A.R., Lagos, M., Pfänder, J. and Buchl, A., 2011. The Earth's tungsten budget during mantle melting and crust formation. *Geochimica et Cosmochimica Acta* **75**, 2119-2136.

Konzett, J., Armstrong, R.A. and Günther, D., 2000. Modal metasomatism in the Kaapvaal craton lithosphere: constraints on timing and genesis from U–Pb zircon dating of metasomatized peridotites and MARID-type xenoliths. *Contributions to Mineralogy and Petrology* **139**, 704-719.

Konzett, J., Armstrong, R.A., Sweeney, R.J. and Compston, W., 1998a. The timing of MARID metasomatism in the Kaapvaal mantle: an ion probe study of zircons from MARID xenoliths. *Earth and Planetary Science Letters* **160**, 133-145.

Konzett, J., Armstrong, R.A., Sweeney, R.J. and Compston, W., 1998b. The timing of MARID metasomatism in the Kaapvaal mantle: an ion probe study of zircons from MARID xenoliths. *Earth and Planetary Science Letters* **160**, 133-145.

Kopylova, M., Tso, E., Ma, F., Liu, J. and Pearson, D., 2019. The metasomatized mantle beneath the North Atlantic Craton: Insights from peridotite xenoliths of the Chidliak kimberlite province (NE Canada). *Journal of Petrology* **60**, 1991-2024.

Kramers, J., 1977. Lead and strontium isotopes in Cretaceous kimberlites and mantle-derived xenoliths from southern Africa. *Earth and Planetary Science Letters* **34**, 419-431.

Kröner, A., Hegner, E., Wendt, J. and Byerly, G., 1996. The oldest part of the Barberton granitoid-greenstone terrain, South Africa: evidence for crust formation between 3.5 and 3.7 Ga. *Precambrian Research* **78**, 105-124.

Larsen, L.M. and Rex, D.C., 1992. A review of the 2500 Ma span of alkaline-ultramafic, potassic and carbonatitic magmatism in West Greenland. *Lithos* **28**, 367-402.

Lazarov, M., Brey, G.P. and Weyer, S., 2009. Time steps of depletion and enrichment in the Kaapvaal craton as recorded by subcalcic garnets from Finsch (SA). *Earth and Planetary Science Letters* **279**, 1-10.

Le Roux, V., Dasgupta, R. and Lee, C.T.A., 2011. Mineralogical heterogeneities in the Earth's mantle: Constraints from Mn, Co, Ni and Zn partitioning during partial melting. *Earth and Planetary Science Letters* **307**, 395-408.

Lee, C.T.A., 2006. Geochemical/petrologic constraints on the origin of cratonic mantle. *Geophysical Monograph Series* **164**, 89-114.

Lee, C.T.A., Leeman, W.P., Canil, D. and Li, Z.X.A., 2005. Similar V/Sc systematics in MORB and arc basalts: Implications for the oxygen fugacities of their mantle source regions. *Journal of Petrology* **46**, 2313-2336.

Li, Z.X., Zhang, L. and Powell, C.M., 1996. Positions of the East Asian cratons in the Neoproterozoic supercontinent Rodinia. *Australian Journal of Earth Sciences* **43**, 593-604.

Li, Z.X., Zhang, L.H. and Powell, C.M., 1995. South China in Rodinia - Part of the Missing Link between Australia East Antarctica and Laurentia. *Geology* **23**, 407-410.

Liu, X.C., Xiong, X.L., Audetat, A., Li, Y., Song, M.S., Li, L., Sun, W.D. and Ding, X., 2014. Partitioning of copper between olivine, orthopyroxene, clinopyroxene, spinel, garnet and silicate melts at upper mantle conditions. *Geochimica et Cosmochimica Acta* **125**, 1-22.

Longerich, H.P., Jackson, S.E. and Günther, D., 1996. Laser ablation inductively coupled plasma mass spectrometric transient signal data acquisition and analyte concentration calculation. *Journal of Analytical Atomic Spectrometry* **11**, 899-904.

Lorand, J., 1990. Are spinel Iherzolite xenoliths representative of the abundance of sulfur in the upper mantle? *Geochimica et Cosmochimica Acta* **54**, 1487-1492.

Lorand, J.P. and Alard, O., 2001. Platinum-group element abundances in the upper mantle: New constraints from in situ and whole-rock analyses of massif central xenoliths (France). *Geochimica et Cosmochimica Acta* **65**, 2789-2806.

Lorand, J.P. and Luguet, A., 2016. Chalcophile and Siderophile Elements in Mantle Rocks: Trace Elements Controlled By Trace Minerals. *Highly Siderophile and Strongly Chalcophile Elements in High-Temperature Geochemistry and Cosmochemistry* **81**, 441-488.

Louie, H. and Soo, S.Y.P., 1992. Use of Nitrogen and Hydrogen in Inductively Coupled Plasma Mass-Spectrometry. *Journal of Analytical Atomic Spectrometry* **7**, 557-564.

Luguet, A., Lorand, J.-P., Alard, O. and Cottin, J.-Y., 2004. A multi-technique study of platinum group element systematic in some Ligurian ophiolitic peridotites, Italy. *Chemical Geology* **208**, 175-194.

Maaløe, S. and Aoki, K.-i., 1977. The major element composition of the upper mantle estimated from the composition of lherzolites. *Contributions to Mineralogy and Petrology* **63**, 161-173.

McDonough, W.F., 1990. Constraints on the Composition of the Continental Lithospheric Mantle. *Earth and Planetary Science Letters* **101**, 1-18.

McDonough, W.F. and Sun, S.s., 1995. The composition of the Earth. *Chemical Geology* **120**, 223-253.

Meija, J., Coplen, T.B., Berglund, M., Brand, W.A., De Bièvre, P., Gröning, M., Holden, N.E., Irrgeher, J., Loss, R.D. and Walczyk, T., 2016. Isotopic compositions of the elements 2013 (IUPAC technical Report). *Pure and Applied Chemistry* **88**, 293-306.

Menzies, A., Carlson, R., Shirey, S. and Gurney, J., 1999. Re–Os systematics of Newlands peridotite xenoliths: implications for diamond and lithosphere formation, Proceedings of the 7th International Kimberlite Conference. Red Roof Design, Cape Town, p. 583.

Menzies, M., 1983. Mantle ultramafic xenoliths in alkaline magmas: evidence for mantle heterogeneity modified by magmatic activity, UK volcanic studies group meeting, pp. 92-110.

Menzies, M. and Murthy, V.R., 1980. Enriched mantle: Nd and Sr isotopes in diopsides from kimberlite nodules. *Nature* **283**, 634-636.

Menzies, M., Rogers, N.W., Tindle, A. and Hawkesworth, C.J., 1987. Metasomatic and enrichment processes in lithospheric peridotites, an effect of asthenosphere-lithosphere interaction. *Mantle metasomatism*, 313-361.

Milke, R., Abart, R., Keller, L. and Rhede, D., 2011. The behavior of Mg, Fe, and Ni during the replacement of olivine by orthopyroxene: experiments relevant to mantle metasomatism. *Mineralogy and Petrology* **103**, 1-8.

Moores, E.M., 1991. Southwest United-States-East Antarctic (SWEAT) Connection: A hypothesis. *Geology* **19**, 425-428.

Moyen, J.-F. and Martin, H., 2012. Forty years of TTG research. *Lithos* **148**, 312-336.

Murillo, M. and Mermet, J., 1989. Improvement of the energy transfer with added-hydrogen in inductively coupled plasma atomic emission spectrometry. *Spectrochimica Acta Part B: Atomic Spectroscopy* **44**, 359-366.

Neumann, E.-R., Griffin, W.L., Pearson, N.J. and O'REILLY, S.Y., 2004. The evolution of the upper mantle beneath the Canary Islands: information from trace elements and Sr isotope ratios in minerals in mantle xenoliths. *Journal of Petrology* **45**, 2573-2612.

Neumann, E.-R., Wulff-Pedersen, E., Pearson, N. and Spencer, E., 2002. Mantle xenoliths from Tenerife (Canary Islands): evidence for reactions between mantle peridotites and silicic carbonatite melts inducing Ca metasomatism. *Journal of Petrology* **43**, 825-857.

Newsom, H.E., Sims, K.W., Noll Jr, P.D., Jaeger, W.L., Maehr, S.A. and Beserra, T.B., 1996. The depletion of tungsten in the bulk silicate earth: constraints on core formation. *Geochimica et Cosmochimica Acta* **60**, 1155-1169.

Nicholls, I.A. and Joyce, E.B., 1989. Newer Volcanics, *In*: Johnson, R.W. (Ed.), *Intraplate Volcanism in Eastern Australia and New Zealand*. Cambridge University Press, Cambridge. 137-143.

Nickel, K. and Green, D., 1984. The Nature of the Upper-Most Mantle Beneath Victoria, Australia as Deduced from Ultramafic Xenoliths, *In*: Kornprobst, J. (Ed.), *Kimberlites*. Elsevier, Amsterdam. 161-178.

Nixon, P. and Boyd, F., 1973. Petrogenesis of the granular and sheared ultrabasic nodule suite in kimberlites, Lesotho Kimberlites, *In*: Nixon, P. (Ed.), *Lesotho kimberlites*. Lesotho National Development Corporation. 48-56.

Nutman, A.P., Friend, C.R.L., Barker, S.L.L. and McGregor, V.R., 2004. Inventory and assessment of Palaeoarchaean gneiss terrains and detrital zircons in southern West Greenland. *Precambrian Research* **135**, 281-314.

Nutman, A.P., Kalsbeek, F., Marker, M., van Gool, J.A. and Bridgwater, D., 1999. U–Pb zircon ages of Kangamiut dykes and detrital zircons in metasediments in the Palaeoproterozoic Nagssugtoqidian Orogen (West Greenland): clues to the pre-collisional history of the orogen. *Precambrian Research* **93**, 87-104.

O'Neill, H.S.C. and Palme, H., 1998. Composition of the silicate Earth: implications for accretion and core formation, *In*: Jackson, I. (Ed.), *The Earth's mantle: Composition, structure, and evolution*. Cambridge University Press, Cambridge. 3-126.

O'Neill, H.S.C. and Wood, B.J., 1979. An experimental study of Fe-Mg partitioning between garnet and olivine and its calibration as a geothermometer. *Contributions to Mineralogy and Petrology* **70**, 59-70.

O'Reilly, S.Y., Chen, D., Griffin, W. and Ryan, C., 1997. Minor elements in olivine from spinel lherzolite xenoliths: implications for thermobarometry. *Mineralogical Magazine* **61**, 257-269.

O'Reilly, S.Y. and Griffin, W., 1985. A xenolith-derived geotherm for southeastern Australia and its geophysical implications. *Tectonophysics* **111**, 41-63.

O'Reilly, S.Y. and Griffin, W., 1988. Mantle metasomatism beneath western Victoria, Australia: I. Metasomatic processes in Cr-diopside lherzolites. *Geochimica et Cosmochimica Acta* **52**, 433-447.

O'Reilly, S.Y. and Griffin, W.L., 2013. Mantle metasomatism, *In*: Harlov, D.E. and Austrheim, H. (Eds.), *Metasomatism and the Chemical Transformation of Rock*. Lecture Notes in Earth System Sciences, Springer, Berlin Heidelberg. 471-533.

O'Reilly, S.Y., Nicholls, I.A. and Griffin, W.L., 1989. Xenoliths and megacrysts of Eastern Australia, *In*: Johnson, R.W. (Ed.), *Intraplate Volcanism in Eastern Australia and New Zealand*. Cambridge University Press, Cambridge. 249-288.

Oxford-Isotope-Geology-Laboratory and McGregor, V.R., 1971. Isotopic dating of very early Precambrian amphibolite facies gneisses from the Godthaab district, West Greenland. *Earth and Planetary Science Letters* **12**, 245-259.

Pearson, D., 1999a. The age of continental roots. *Developments in Geotectonics* **24**, 171-194.

Pearson, D., 1999b. Evolution of cratonic lithospheric mantle: an isotopic perspective, *In*: Fei, Y., Bertka, C.M. and Mysen, B.O. (Eds.), *Mantle Petrology: Field Observations and High Pressure Experimentation: A Tribute to Francis R. (Joe) Boyd*. Geochem. Soc. Spec. Publ., Geochemical Society, Houston. 57-78.

Pearson, D., Carlson, R., Shirey, S., Boyd, F. and Nixon, P., 1995. Stabilisation of Archaean lithospheric mantle: A ReOs isotope study of peridotite xenoliths from the Kaapvaal craton. *Earth and Planetary Science Letters* **134**, 341-357.

Pearson, D.G., Canil, D. and Shirey, S.B., 2003. 2.05 - Mantle Samples Included in Volcanic Rocks: Xenoliths and Diamonds, *In*: Holland, H.D. and Turekian, K.K. (Eds.), *Treatise on Geochemistry*. Pergamon, Oxford. 171-275.

Pearson, D.G., Irvine, G.J., Carlson, R.W., Kopylova, M.G. and Ionov, D.A., 2002. The development of lithospheric keels beneath the earliest continents: Time constraints using PGE and Re-Os isotope systematics. *Geological Society Special Publication* **199**, 65-90.

Pearson, D.G. and Nowell, G.M., 2002. The continental lithospheric mantle: characteristics and significance as a mantle reservoir. *Philosophical Transactions of the Royal Society A* **360**, 2383-2410.

Pearson, D.G. and Wittig, N., 2008. Formation of Archaean continental lithosphere and its diamonds: The root of the problem. *Journal of the Geological Society* **165**, 895-914.

Perkins, W.T. and Pearce, N.J.G., 1995. Mineral microanalysis by laserprobe inductively coupled plasma mass spectrometry, *In*: Potts, P.J., Bowles, J.F.W., Reed, S.J.B. and Cave, M.R. (Eds.), *Microprobe Techniques in the Earth Sciences*. Springer US, Boston, MA. 291-325.

Poujol, M., Robb, L., Anhaeusser, C. and Gericke, B., 2003. A review of the geochronological constraints on the evolution of the Kaapvaal Craton, South Africa. *Precambrian Research* **127**, 181-213.

Powell, C.M., Preiss, W.V., Gatehouse, C.G., Krapez, B. and Li, Z.X., 1994. South Australian Record of a Rodinian Epicontinental Basin and Its Mid-Neoproterozoic Breakup (Similar-to-700 Ma) to Form the Palaeo-Pacific Ocean. *Tectonophysics* **237**, 113-140.

Prelević, D., Jacob, D.E. and Foley, S.F., 2013. Recycling plus: a new recipe for the formation of Alpine–Himalayan orogenic mantle lithosphere. *Earth and Planetary Science Letters* **362**, 187-197.

Rampone, E., Bottazzi, P. and Ottolini, L., 1991a. Complementary Ti and Zr Anomalies in Ortho-Pyroxene and Clinopyroxene from Mantle Peridotites. *Nature* **354**, 518-520.

Rampone, E., Bottazzi, P. and Ottolini, L., 1991b. Complementary Ti and Zr anomalies in orthopyroxene and clinopyroxene from mantle peridotites. *Nature* **354**, 518-520.

Rehfeldt, T., Foley, S.F., Jacob, D.E., Carlson, R.W. and Lowry, D., 2008a. Contrasting types of metasomatism in dunite, wehrlite and websterite xenoliths from Kimberley, South Africa. *Geochimica et Cosmochimica Acta* **72**, 5722-5756.

Rehfeldt, T., Foley, S.F., Jacob, D.E., Carlson, R.W. and Lowry, D., 2008b. Contrasting types of metasomatism in dunite, wehrlite and websterite xenoliths from Kimberley, South Africa. *Geochimica et Cosmochimica Acta* **72**, 5722-5756.

Rehfeldt, T., Jacob, D.E., Carlson, R.W. and Foley, S.F., 2007. Fe-rich dunite xenoliths from South African kimberlites: Cumulates from Karoo flood basalts. *Journal of Petrology* **48**, 1387-1409.

Richardson, S., Gurney, J., Erlank, A. and Harris, J., 1984. Origin of diamonds in old enriched mantle. *Nature* **310**, 198.

Richardson, S.H., Erlank, A.J. and Hart, S.R., 1985. Kimberlite-borne garnet peridotite xenoliths from old enriched subcontinental lithosphere. *Earth and Planetary Science Letters* **75**, 116-128.

Richardson, S.H., Harris, J.W. and Gurney, J.J., 1993. Three generations of diamonds from old continental mantle *Nature* **366**, 256-258.

Rudnick, R.L. and Nyblade, A.A., 1999. The thickness and heat production of Archean lithosphere: constraints from xenolith thermobarometry and surface heat flow. *Mantle petrology: field observations and high pressure experimentation: a tribute to Francis R.(Joe) Boyd* **6**, 3-12.

Salters, V.J.M. and Shimizu, N., 1988. World-Wide Occurrence of HFSE-Depleted Mantle. *Geochimica et Cosmochimica Acta* **52**, 2177-2182.

Salters, V.J.M. and Stracke, A., 2004. Composition of the depleted mantle. *Geochemistry Geophysics Geosystems* **5**.

Schmitz, M.D., Bowring, S.A., de Wit, M.J. and Gartz, V., 2004a. Subduction and terrane collision stabilize the western Kaapvaal craton tectosphere 2.9 billion years ago. *Earth and Planetary Science Letters* **222**, 363-376.

Schmitz, M.D., Bowring, S.A., de Wit, M.J. and Gartz, V., 2004b. Subduction and terrane collision stabilize the western Kaapvaal craton tectosphere 2.9 billion years ago. *Earth and Planetary Science Letters* **222**, 363-376.

Schneider, M.E. and Eggler, D.H., 1986. Fluids in equilibrium with peridotite minerals: implications for mantle metasomatism. *Geochimica et Cosmochimica Acta* **50**, 711-724.

Secher, K., Heaman, L., Nielsen, T., Jensen, S., Schjøth, F. and Creaser, R., 2009. Timing of kimberlite, carbonatite, and ultramafic lamprophyre emplacement in the alkaline province located 64–67 N in southern West Greenland. *Lithos* **112**, 400-406.

Sheard, M.J. and Nicholls, I.A., 1989. Mount Gambier sub-province, *In*: Johnson, R.W. (Ed.), *Intraplate Volcanism in Eastern Australia and New Zealand*. Cambridge University Press, Cambridge. p142.

Shimizu, N., 1975. Rare earth elements in garnets and clinopyroxenes from garnet lherzolite nodules in kimberlites. *Earth and Planetary Science Letters* **25**, 26-32.

Shimizu, N., 1999. Young geochemical features in cratonic peridotites from southern Africa and Siberia, *In*: Fei, Y., Bertka, C.M. and Mysen, B. (Eds.), *Mantle Petrology: Field Observations and High Pressure Experimentation*. The Geochemical Society, Houston. 47-55.

Shirey, S.B., Harris, J.W., Richardson, S.H., Fouch, M., James, D.E., Cartigny, P., Deines, P. and Viljoen, F., 2003. Regional patterns in the paragenesis and age of inclusions in diamond, dianomd composition, and the lithosphereic seismic structure of Southern Africa. *Lithos* **71**, 243-258.

Simon, N.S.C., Carlson, R.W., Pearson, D.G. and Davies, G.R., 2007a. The origin and evolution of the Kaapvaal Cratonic Lithospheric Mantle. *Journal of Petrology* **48**, 589-625.

Simon, N.S.C., Carlson, R.W., Pearson, D.G. and Davies, G.R., 2007b. The origin and evolution of the Kaapvaal cratonic lithospheric mantle. *Journal of Petrology* **48**, 589-625.

Simon, N.S.C., Irvine, G.J., Davies, G.R., Pearson, D.G. and Carlson, R.W., 2003. The origin of garnet and clinopyroxene in "depleted" Kaapvaal peridotites. *Lithos* **71**, 289-322.

Sobolev, A.V., Hofmann, A.W., Kuzmin, D.V., Yaxley, G.M., Arndt, N.T., Chung, S.L., Danyushevsky, L.V., Elliott, T., Frey, F.A., Garcia, M.O., Gurenko, A.A., Kamenetsky, V.S., Kerr, A.C., Krivolutskaya, N.A., Matvienkov, V.V., Nikogosian, I.K., Rocholl, A., Sigurdsson, I.A., Sushchevskaya, N.M. and Teklay, M., 2007. The amount of recycled crust in sources of mantle-derived melts. *Science* **316**, 412-417.

Stalder, R., Foley, S., Brey, G. and Horn, I., 1998. Mineral-aqueous fluid partitioning of trace elements at 900–1200 C and 3.0–5.7 GPa: new experimental data for garnet, clinopyroxene, and rutile, and implications for mantle metasomatism. *Geochimica et Cosmochimica Acta* **62**, 1781-1801.

Steenfelt, A., Garde, A.A. and Moyen, J.-F., 2005. Mantle wedge involvement in the petrogenesis of Archaean grey gneisses in West Greenland. *Lithos* **79**, 207-228.

Stosch, H.-G. and Seck, H., 1980. Geochemistry and mineralogy of two spinel peridotite suites from Dreiser Weiher, West Germany. *Geochimica et Cosmochimica Acta* **44**, 457-470.

Takazawa, E., Okayasu, T. and Satoh, K., 2003. Geochemistry and origin of the basal lherzolites from the northern Oman ophiolite (northern Fizh block). *Geochemistry, Geophysics, Geosystems* **4**.

Tappe, S., Foley, S.F., Stracke, A., Romer, R.L., Kjarsgaard, B.A., Heaman, L.M. and Joyce, N., 2007. Craton reactivation on the Labrador Sea margins: 40Ar/39Ar age and Sr–Nd–Hf–Pb isotope constraints from alkaline and carbonatite intrusives. *Earth and Planetary Science Letters* **256**, 433-454.

Van Achterbergh, E., 2004. Geochemical fingerprints of mantle metasomatism. Macquarie University (Division of Environmental & Life Sciences, Department ….

Van Otterloo, J., Raveggi, M., Cas, R.A.F. and Maas, R., 2014. Polymagmatic activity at the monogenetic Mt Gambier volcanic complex in the Newer Volcanics Province, SE Australia: New insights into the occurrence of intraplate volcanic activity in Australia. *Journal of Petrology* **55**, 1317-1351.

Walker, R., Carlson, R., Shirey, S. and Boyd, F., 1989. Os, Sr, Nd, and Pb isotope systematics of southern African peridotite xenoliths: implications for the chemical evolution of subcontinental mantle. *Geochimica et Cosmochimica Acta* **53**, 1583-1595.

Walter, M.J., 1999. Melting residues of fertile peridotite and the origin of cratonic lithosphere. *Mantle petrology: field observations and high-pressure experimentation. Spec Publ Geochem Soc* **6**, 225-239.

Walter, M.J., 2003. Melt extraction and compositional variability in mantle lithosphere. *TrGeo* **2**, 568.

Wang, Z.C. and Becker, H., 2015. Abundances of Ag and Cu in mantle peridotites and the implications for the behavior of chalcophile elements in the mantle. *Geochimica et Cosmochimica Acta* **160**, 209-226.

Wang, Z.C., Becker, H. and Wombacher, F., 2015. Mass Fractions of S, Cu, Se, Mo, Ag, Cd, In, Te, Ba, Sm, W, Tl and Bi in Geological Reference Materials and Selected Carbonaceous Chondrites Determined by Isotope Dilution ICP-MS. *Geostandards and Geoanalytical Research* **39**, 185-208.

Wänke, H., Dreibus, G. and Jagoutz, E., 1984. Mantle chemistry and accretion history of the Earth, *Archaean geochemistry*. Springer. 1-24.

Wasch, L.J., van der Zwan, F.M., Nebel, O., Morel, M.L.A., Hellebrand, E.W.G., Pearson, D.G. and Davies, G.R., 2009. An alternative model for silica enrichment in the Kaapvaal subcontinental lithospheric mantle. *Geochimica et Cosmochimica Acta* **73**, 6894-6917.

Wells, P.R., 1977. Pyroxene thermometry in simple and complex systems. *Contributions to Mineralogy and Petrology* **62**, 129-139.

Wingate, M.T.D., Campbell, I.H., Compston, W. and Gibson, G.M., 1998. Ion microprobe U-Pb ages for Neoproterozoic basaltic magmatism in south-central Australia and implications for the breakup of Rodinia. *Precambrian Research* **87**, 135-159.

Witt-Eickschen, G., Palme, H., O'neill, H.S.C. and Allen, C.M., 2009. The geochemistry of the volatile trace elements As, Cd, Ga, In and Sn in the Earth's mantle: New evidence from in situ analyses of mantle xenoliths. *Geochimica et Cosmochimica Acta* **73**, 1755-1778.

Wittig, N., Pearson, D.G., Webb, M., Ottley, C.J., Irvine, G.J., Kopylova, M., Jensen, S.M. and Nowell, G.M., 2008. Origin of cratonic lithospheric mantle roots: A geochemical study of peridotites from the North Atlantic Craton, West Greenland. *Earth and Planetary Science Letters* **274**, 24-33.

Wittig, N., Webb, M., Pearson, D., Dale, C., Ottley, C., Hutchison, M., Jensen, S. and Luguet, A., 2010a. Formation of the North Atlantic Craton: timing and mechanisms constrained from Re–Os isotope and PGE data of peridotite xenoliths from SW Greenland. *Chemical Geology* **276**, 166-187.

Wittig, N., Webb, M., Pearson, D.G., Dale, C.W., Ottley, C.J., Hutchison, M.T., Jensen, S.M. and Luguet, A., 2010b. Formation of the North Atlantic Craton: Timing and mechanisms constrained from Re-Os isotope and PGE data of peridotite xenoliths from S.W. Greenland. *Chemical Geology* **176**, 166-187.

Wyborn, D., 1989. Geology of Eastern Australia, *In*: Johnson, R.W. (Ed.), *Intraplate Volcanism in Eastern Australia and New Zealand* Cambridge University Press, Cambridge. 18-21.

Yaxley, G.M., 1993. Carbonatite metasomatism in the mantle: sources and roles of carbonate in metasomatic enrichment processes in the lithosphere. University of Tasmania.

Yaxley, G.M., Crawford, A.J. and Green, D.H., 1991. Evidence for carbonatite metasomatism in spinel peridotite xenoliths from western Victoria, Australia. *Earth and Planetary Science Letters* **107**, 305-317.

Yaxley, G.M., Green, D.H. and Kamenetsky, V., 1998. Carbonatite metasomatism in the southeastern Australian lithosphere. *Journal of Petrology* **39**, 1917-1930.

Yaxley, G.M., Kamenetsky, V., Green, D.H. and Falloon, T.J., 1997. Glasses in mantle xenoliths from western Victoria, Australia, and their relevance to mantle processes. *Earth and Planetary Science Letters* **148**, 433-446.

Zanetti, A., Tiepolo, M., Oberti, R. and Vannucci, R., 2004. Trace-element partitioning in olivine: modelling of a complete data set from a synthetic hydrous basanite melt. *Lithos* **75**, 39-54.

Zhang, H., Menzies, M.A., Gurney, J.J. and Zhou, X., 2001. Cratonic peridotites and silica-rich melts: diopside-enstatite relationships in polymict xenoliths, Kaapvaal, South Africa. *Geochimica et Cosmochimica Acta* **65**, 3365-3377.

Zhang, H.-F., Mattey, D., Grassineau, N., Lowry, D., Brownless, M., Gurney, J. and Menzies, M., 2000. Recent fluid processes in the Kaapvaal Craton, South Africa: coupled oxygen isotope and trace element disequilibrium in polymict peridotites. *Earth and Planetary Science Letters* **176**, 57-72.

Zhang, L., Liu, Y., Wang, L., Wang, C. and Zhang, G., 2020. Multiple metasomatism of the lithospheric mantle beneath the northeastern North China Craton. *Lithos* **374-375**, 105719.

# APPENDICES

## SUPPLEMENTARY DATA FOR CHAPTER THREE

Appendix A-1: Operating parameters for EPMA analyses, Johannes Gutenberg-University Mainz, Germany

Appendix A-2: Petrographic description of Mt Gambier samples.

Appendix A-3: Whole rock REE data normalised to C1 chondrite (McDonough & Sun, 1995).

## SUPPLEMENTARY DATA FOR CHAPTER FOUR

Appendix B-1: Summarising table of LA-ICP-MS operating parameters.

Appendix B-2: LA-ICP-MS trace element composition on BCR-2G, GSA-1G, GSC-1G, GSD-1G and GSE-1G.

## ELECTRONIC SUPPLEMENTARY DATA FOR CHAPTER FOUR

B-1: Kaapvaal and West Greenland whole rock major and trace elements calculated from mineral modal abundances and measured major and trace element compositions (normal mode LA-ICP-MS).

B2: Representative major and trace element compositions for clinopyroxene and garnet. The trace element data presented here is acquired with LA-ICP-MS in hydrogen mode.

B3: Partition coefficients for Opx/Cpx and Cpx/Grt

# Appendix A-1

Johannes Gutenberg – Universität Mainz, Institut f. Geowissenschaften

## Elektronenstrahl - Mikrosonde (EMS)

JEOL JXA 8200

| Beschreibung: | Silikate Universalprogramm – Zeit 1' 45" |
|---|---|

**Quantitative Analysis** ***Analysenprogramm*** **= SAMPLE** (Meas. + Std. + Stg. Conditions)

| jx1 | Silikatroutine | **Silikate** |
|---|---|---|
| **USER** | **Standard GROUP** | **SAMPLE** |

| | | | | | | | |
|---|---|---|---|---|---|---|---|
| ACC. Voltage | **15** | **kV** | Probe Dia. | 2 | µm | calc. Elements | **O** |
| Beam | **12** | **nA** | Aperturblende | 2 | | fix. Elements | **-** |

**Standard Analysis** ***Standard*** **= SAMPLE** (Meas. + Stg. Conditions)

| Nr | Element Linie | Val | Mem | Block | **Standardname** | **.cond** | Net.-Int. / DL cps / ppm |
|---|---|---|---|---|---|---|---|
| 1 | **Na Ka** | 1 | 1 | a | **aALBIT** | **15** | 608 / 200 |
| 2 | **Al Ka** | 3 | 1 | a | **aAl2O3** | **15** | 11553 / 170 |
| 3 | **Cr Ka** | 3 | 1 | a | **aCr2O3** | **15** | 7115 / 180 |
| 4 | **Fe Ka** | 2 | 1 | a | **aFe2O3** | **15** | 6596 / 140 |
| 5 | **Mg Ka** | 2 | 1 | a | **aMgO** | **15** | 10145 / 140 |
| 6 | **Mn Ka** | 2 | 1 | a | **aMnTiO3** | **15** | 3145 / 140 |
| 7 | **Ti Ka** | 4 | 1 | a | **aMnTiO3** | **15** | 3153 / 160 |
| 8 | **K Ka** | 1 | 1 | a | **aORTHO** | **15** | 1257 / 140 |
| 9 | **Ca Ka** | 2 | 1 | a | **aWOLLA** | **15** | 3586 / 140 |
| 10 | **Si Ka** | 4 | 1 | a | **aWOLLA** | **15** | 5694 / 150 |
| | | | | | | | |
| falls gewünscht ergänzen mit | | | | | | | |
| 11 | **Ni Ka** | 2 | 1 | a | **aNiO** | **15** | 7419 / 250 |
| 12 | | | | | | | |
| 13 | | | | | | | |
| 14 | | | | | | | |
| 15 | | | | | | | |
| 16 | | | | | | | |
| 17 | | | | | | | |
| 28 | | | | | | | |

**WDS Channel**

(Spektrometer)

| **1** | **2** | **3** | **4** | **5** |
|---|---|---|---|---|
| WDS Kristalle | | | | |
| **T** | **T** | **P** | **P** | **LH** |
| WDS Elemente | | | | |
| **Na** **Al** | **Si** **Mg** | **K** **Ca** | **Ti** **Cr** | **Fe** **Mn** **(Ni)** |

Korrektur: Oxide, PRZ

Überlappungsfaktoren:

Kommentar

Bei Nacheichung, Na Probe_Dia. 5µ

Check Stand., 1. Na-Mess. evtl. löschen

Nacheichzeit: 35'

Gesamtmesszeit:1' 45"

Datum Bearbeiter

06.01.2014

Empfohlene Messzeiten **PEAK**: **UNK**sec (**STD**sec * n **points**)

Al 20(10*4) – Na 20(20*6) – Cr 20(10*4) – Fe 20(15*4) - Mg 20(10*4) –Mn 20(15*4) – Ti 20(20*4) – K 20(20*5) – Ca 20(15*4) – Si 20(15*5) – [Ni 20(10*4)]

# Appendix A-2

### Table with petrographic observations

| Sample | Phases | Texture | Special features |
|---|---|---|---|
| **GamTR1** | Ol, opx, cpx, sp | Intergranular, equigranular, coarse grain size, anhedral; cpx anhedral and some cpx crystallised along grain boundaries or in triple junctions | Melt infiltration; melt pockets with euhedral tiny ol, cpx, sp; cpx triple junction |
| **GamTR3** | Ol, opx, cpx, sp | Intergranular texture, with anhedral equigranular ol, opx, and cpx; cpx and sp crystallised in a preferred plane | |
| **GamTR4** | Ol, opx, cpx, sp | Intergranular, equigranular ol and opx, cpx smaller grain size; all grains anhedral, smaller sized grains look rounded, especially cpx | Sp describe a preferred orientation, looks like they crystallised subparallel |
| **MGam1** | Ol, opx, cpx, sp | Intergranular, equigranular, coarse grain size, anhedral; cpx rounded and anhedral and some cpx crystallised along grain boundaries or in triple junctions | Cpx triple junction; melt pocket with tiny cpx, ol, sp and remnant amp |
| **MGam2** | Ol, opx, cpx, sp | Intergranular texture with equigranular rounded ol, some grains of opx equigranular as well but less rounded and more anhedral and interstitial? Cpx looks interstitial as well, crystallised in a preferred orientation looks like foliation | Least modal abundance of cpx; |

# Appendix A-3

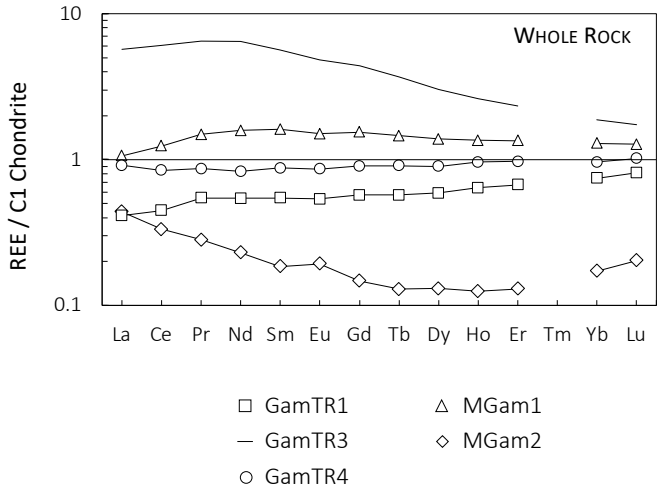


□ GamTR1 △ MGam1
— GamTR3 ◇ MGam2
○ GamTR4

**Appendix B-1 Summary of LA-ICP-MS equipment and operating parameters.**

| | Macquarie - normal mode | Macquarie - hydrogen mode | Mainz | Nuremberg-Erlangen |
|---|---|---|---|---|
| *equipment* | | | | |
| **mass spectrometer** | Agilent 7700series ICP quadrupole | Agilent 8900 Triple Quadrupole | Agilent 7500i ICP quadrupole | Agilent 7500i ICP quadrupole |
| **laser ablation system** | Photon Analyte G2 ArF Excimer | Photon Analyte G2 ArF Excimer | New Wave Research UP-213 | New Wave Research UP193FX |
| **laser wavelength** | 193 nm | 193 nm | 213 nm | 193 nm |
| **sample chamber** | HelEx II Volume Cell | HelEx II Volume Cell | large format cell | standard Agilent cell |
| **Laser energy** | ~5 J $cm^{-2}$ | 5.2-7.6 J $cm^{-2}$ | ~3.55 J $cm^{-2}$ | 3.4-4.4 J $cm^{-2}$ |
| **repetition rate** | 10 Hz | 5 Hz | 10 Hz | 15 Hz |
| **spot size** | 110-85µm ol; 85-65µm px, grt | 110-85µm ol; 85-65µm px, grt | 100-55µm diameter | 100 and 50µm diameter |
| **Carrier gas** | He | He; $H_2$ gas @5mL $min^{-1}$ | He | He |
| **Measurement time** | 60 s after 60 s gas blank | 60 s after 150 s gas blank | 60 s after 60 s gas blank | 40 s after 30 s gas blank |
| **Phases** | Ol, Opx, Cpx, Grt | Ol, Opx, Cpx, Grt | Ol, Opx | O, Opx |
| **Analysis programs** | | Standard | Transitional | Transition metal | REE | Transition metal | REE |
| | $^{7}Li$ $^{11}B$ $^{25}Mg$ $^{27}Al$ $^{29}Si$ $^{31}P$ $^{39}K$ $^{43}Ca$ $^{44}Ca$ $^{45}Sc$ $^{47}Ti$ $^{51}V$ 52Cr $^{53}Cr$ $^{55}Mn$ $^{57}Fe$ $^{59}Co$ $^{60}Ni$ $^{62}Ni$ $^{63}Cu$ $^{66}Zn$ $^{69}Ga$ $^{71}Ga$ 75As $^{85}Rb$ $^{86}Sr$ $^{88}Sr$ $^{89}Y$ $^{90}Zr$ $^{93}Nb$ $^{95}Mo$ $^{133}Cs$ $^{137}Ba$ $^{138}Ba$ $^{139}La$ $^{140}Ce$ $^{141}Pr$ $^{146}Nd$ $^{147}Sm$ $^{153}Eu$ $^{157}Gd$ $^{159}Tb$ $^{163}Dy$ $^{165}Ho$ $^{166}Er$ $^{169}Tm$ $^{172}Yb$ $^{175}Lu$ $^{178}Hf$ $^{181}Ta$ $^{208}Pb$ $^{209}Bi$ $^{232}Th$ $^{238}U$ | $^{7}Li$ $^{25}Mg$ $^{27}Al$ $^{29}Si$ $^{43}Ca$ $^{44}Ca$ $^{45}Sc$ $^{47}Ti$ $^{51}V$ $^{53}Cr$ $^{55}Mn$ $^{57}Fe$ $^{59}Co$ $^{60}Ni$ $^{62}Ni$ $^{63}Cu$ $^{66}Zn$ $^{69}Ga$ $^{71}Ga$ $^{85}Rb$ $^{86}Sr$ $^{88}Sr$ $^{89}Y$ $^{90}Zr$ $^{93}Nb$ $^{95}Mo$ $^{98}Mo$ $^{133}Cs$ $^{137}Ba$ $^{138}Ba$ $^{139}La$ $^{140}Ce$ $^{141}Pr$ $^{146}Nd$ $^{147}Sm$ $^{153}Eu$ $^{157}Gd$ $^{159}Tb$ $^{163}Dy$ $^{165}Ho$ $^{166}Er$ $^{169}Tm$ $^{172}Yb$ $^{175}Lu$ $^{178}Hf$ $^{181}Ta$ $^{208}Pb$ $^{209}Bi$ $^{232}Th$ $^{238}U$ | $^{25}Mg$ $^{29}Si$ $^{43}Ca$ $^{44}Ca$ $^{45}Sc$ $^{51}V$ $^{63}Cu$ $^{66}Zn$ $^{69}Ga$ $^{71}Ga$ $^{72}Ge$ $^{73}Ge$ $^{74}Ge$ $^{75}As$ $^{86}Sr$ $^{88}Sr$ $^{89}Y$ $^{90}Zr$ $^{93}Nb$ $^{95}Mo$ $^{97}Mo$ $^{98}Mo$ $^{100}Mo$ $^{107}Ag$ $^{109}Ag$ $^{111}Cd$ $^{112}Cd$ $^{114}Cd$ $^{115}In$ $^{118}Sn$ $^{120}Sn$ $^{121}Sb$ $^{123}Sb$ $^{139}La$ $^{140}Ce$ $^{153}Eu$ $^{166}Er$ $^{172}Yb$ $^{178}Hf$ $^{182}W$ $^{183}W$ $^{184}W$ $^{185}Re$ $^{187}Re$ $^{205}Tl$ $^{208}Pb$ $^{209}Bi$ $^{232}Th$ $^{238}U$ | $^{24}Mg$ $^{29}Si$ $^{42}Ca$ $^{43}Ca$ $^{44}Ca$ $^{45}Sc$ $^{47}Ti$ $^{51}V$ $^{53}Cr$ $^{55}Mn$ $^{59}Co$ $^{60}Ni$ $^{63}Cu$ $^{66}Zn$ $^{69}Ga$ $^{85}Rb$ $^{88}Sr$ $^{89}Y$ $^{90}Zr$ $^{93}Nb$ $^{137}Ba$ $^{178}Hf$ $^{181}Ta$ $^{232}Th$ $^{238}U$ | $^{7}Li$ $^{11}B$ $^{27}Al$ $^{29}Si$ $^{31}P$ $^{44}Ca$ $^{85}Rb$ $^{88}Sr$ $^{137}Ba$ $^{139}La$ $^{140}Ce$ $^{141}Pr$ $^{146}Nd$ $^{147}Sm$ $^{153}Eu$ $^{157}Gd$ $^{163}Dy$ $^{166}Er$ $^{172}Yb$ $^{175}Lu$ | $^{7}Li$ $^{27}Al$ $^{29}Si$ $^{43}Ca$ $^{45}Sc$ $^{47}Ti$ $^{51}V$ $^{52}Cr$ $^{53}Cr$ $^{55}Mn$ $^{59}Co$ $^{60}Ni$ $^{63}Cu$ $^{67}Zn$ $^{69}Ga$ $^{85}Rb$ $^{88}Sr$ $^{89}Y$ $^{90}Zr$ $^{93}Nb$ $^{137}Ba$ $^{140}Ce$ $^{178}Hf$ $^{181}Ta$ $^{232}Th$ $^{238}U$ | $^{7}Li$ $^{11}B$ $^{29}Si$ $^{31}P$ 43Ca 44Ca $^{88}Sr$ $^{89}Y$ $^{137}Ba$ $^{139}La$ $^{140}Ce$ $^{141}Pr$ $^{146}Nd$ $^{147}Sm$ $^{153}Eu$ $^{157}Gd$ $^{163}Dy$ $^{166}Er$ $^{172}Yb$ $^{175}Lu$ $^{178}Hf$ |
| **Internal standard** | $^{29}Si$ ol and opx; $^{43}Ca$ cpx and grt | $^{29}Si$ | $^{29}Si$ | $^{29}Si$ |
| **External standard** | NIST 612 | NIST 612 | NIST 612 | NIST 612 |
| **Accuracy control on** | BCR-2G | BCR-2G | BCR-2G GSA-1G GSC-1G GSD-1G GSE-1G | GSA-1G GSC-1G GSD-1G GSE-1G |

**Appendix B-2: LA-ICP-MS trace element composition of BCR2G, GSA-1G, GSc-1G, GSD-1G, GSE-1G**

Measured values compared with GeoReM database preferred values (http://georem.mpch-mainz.gwdg.de/) and USGS preliminary data

Elements that differ significantly are shown in italic

| sample | BCR-2G | | GSA-1G | | GSC-1G | | GSD-1G | | GSE-1G | |
|---|---|---|---|---|---|---|---|---|---|---|
| n | 52 | GeoReM | 21 | USGS | 21 | USGS | 21 | USGS | 20 | USGS |
| **Li** | 8.98±0.43 | 9±1 | *1.70±0.09* | <1 | 5.97±0.27 | 4.89-6.4 | 44.5±1.9 | 30-50 | 427±18 | 350-550 |
| **B** | 4.82±3.00 | 6±1 | 16.2±5.7 | - | 17.5±6.9 | 20-35 | 32.9±16.2 | - | 185±113 | - |
| **P** | 1884±402 | 1615±44 | 40.4±11.9 | - | 1381±382 | 960-1218 | 1151±300 | - | 40.5±6.2 | - |
| **V** | 415±18 | 425±18 | 1.01±0.05 | <2 | 5.29±0.24 | 5.2-5.6 | 42.6±1.8 | 30-60 | 412±20 | 300-500 |
| **Cr** | 15.4±1.3 | 17±2 | *5.63±0.43* | 5.9-6.7 | *9.20±0.59* | 13-17 | 42.8±2.4 | 25-55 | 371±21 | 300-500 |
| **Mn** | 1519±78 | 1550±70 | 155±6 | 120-160 | 177±6 | 155-180 | 211±6 | 150-250 | 568±39 | 400-600 |
| **Co** | 37.0±1.3 | 38±2 | 1.64±0.08 | 1.4-1.8 | 5.96±0.19 | 5.6-6.1 | 39.2±1.2 | 30-40 | 365±12 | 300-400 |
| **Ni** | 12.3±0.5 | 13±2 | 14.8±0.6 | 14.2-16.0 | *20.6±0.8* | 22-25 | 57.2±1.8 | 40-60 | 418±11 | 300-1000 |
| **Cu** | 16.5±0.7 | 21±5 | *2.85±0.20* | <2 | 15.5±0.9 | 12.5-20 | 38.3±1.5 | 30-50 | 342±15 | 300-400 |
| **Zn** | 153±14 | 125±5 | 10.7±1.1 | 9.1-10 | *14.7±1.0* | 12.4-13 | 61.3±4.5 | 30-80 | 518±35 | 400-800 |
| **Ga** | 38.6±4.6 | 23±1 | 7.86±1.00 | 5.4-7.8 | 10.7±0.7 | 8.4-11.8 | 54.6±2.2 | 50-70 | 486±21 | 300-600 |
| **Rb** | 45.1±2.2 | 47±0.5 | 0.888±0.045 | <2 | 4.96±0.18 | 4.86-5.6 | 37.8±1.4 | 30-50 | 350±17 | 200-400 |
| **Sr** | 340±16 | 342±4 | 28.4±1.9 | 25-35 | 32.5±2.2 | 26-34 | 70.5±4.0 | 50-70 | 447±33 | 300-600 |
| **Y** | 36.5±2.5 | 35±3 | 0.280±0.028 | <2 | 4.59±0.36 | 4.4-5.59 | 41.9±2.7 | 30-60 | 417±33 | 300-600 |
| **Zr** | 194±9 | 184±15 | *5.63±0.56* | <2 | 6.35±0.66 | 6-7.72 | 42.5±3.7 | 30-60 | 395±30 | 350-500 |
| **Nb** | 13.0±0.4 | 12.5±1 | 29.9±2.6 | 15-30 | 4.90±0.44 | 4.2-4.9 | 45.6±3.7 | 30-50 | 451±35 | 300-600 |
| **Ba** | 676±29 | 683±7 | 59.0±4.8 | 40-60 | 35.6±2.8 | 20-60 | 70.8±4.4 | 40-70 | 419±23 | 300-500 |
| **La** | 26.8±1.5 | 24.7±0.3 | 0.891±0.082 | 0.5-3 | 4.41±0.38 | 4.358-4.63 | 39.4±2.4 | 30-50 | 387±35 | 300-500 |
| **Ce** | 52.3±2.4 | 53.3±0.5 | 0.430±0.031 | <2 | 4.63±0.25 | 4.59-4.82 | 41.1±1.7 | 25-40 | 409±45 | 300-500 |
| **Pr** | 6.84±0.33 | 6.7±0.4 | 0.052±0.007 | <0.1 | 4.73±0.36 | 4.6-4.93 | 45.0±2.3 | 30-50 | 474±53 | 300-500 |
| **Nd** | 30.8±1.5 | 28.9±0.3 | 0.200±0.017 | <2 | 4.79±0.48 | 4.6-5.01 | 45.1±2.9 | 20-50 | 441±18 | 350-550 |
| **Sm** | 7.15±0.41 | 6.59±0.07 | 0.042±0.012 | <0.1 | 5.07±0.51 | 4.8-5.35 | 48.2±3.6 | 30-60 | 475±26 | 300-600 |
| **Eu** | 2.03±0.10 | 1.97±0.02 | 0.009±0.003 | <0.1 | 4.32±0.38 | 4.25-4.6 | 40.0±2.5 | 30-40 | 385±23 | 300-600 |
| **Gd** | 7.06±0.47 | 6.71±0.07 | 0.037±0.013 | <0.1 | 5.11±0.45 | 4.9-5.96 | 48.7±3.2 | 40-60 | 486±23 | 400-600 |
| **Dy** | 7.06±0.47 | 6.44±0.06 | 0.027±0.008 | <0.1 | 5.51±0.54 | 3.3-6.21 | 52.8±3.5 | 40-55 | 518±25 | 400-600 |
| **Er** | 3.99±0.27 | 3.7±0.04 | 0.017±0.004 | <0.1 | 3.72±0.40 | 3.3-4.17 | 40.3±2.9 | 30-40 | 563±36 | 400-600 |
| **Yb** | 3.77±0.28 | 3.39±0.03 | 0.026±0.012 | <0.1 | 5.45±0.51 | 4.8-6.21 | 52.9±3.1 | 40-60 | 521±22 | 400-600 |
| **Lu** | 0.556±0.044 | 0.503±0.005 | 0.003±0.001 | <0.1 | 5.45±0.51 | 5.1-6.28 | 53.2±3.3 | 40-60 | 575±76 | 400-600 |
| **Hf** | 5.18±0.33 | 4.84±0.28 | *0.170±0.019* | <0.1 | 4.22±0.36 | 4-5 | 39.8±2.7 | 25-45 | 385±23 | 350-450 |
| **Ta** | 0.861±0.042 | 0.78±0.06 | 1.74±0.15 | <2 | 4.95±0.44 | 3.6-5.21 | 46.4±3.3 | 30-60 | 482±59 | 300-600 |
| **Th** | 6.53±0.35 | 5.9±0.3 | 0.115±0.016 | <0.1 | 4.01±0.48 | 3.55-5.06 | ***43.7±3.1*** | 50-100 | 386±45 | 400-1500 |
| **U** | 1.66±0.08 | 1.69±0.12 | 0.171±0.011 | 0.1-0.6 | 4.55±0.26 | 4.1-5.19 | 41.3±2.0 | 30-60 | 408±51 | 300-600 |

**Electronic Supplement B-1 Kaapvaal (KC) and North Atlantic Craton (NAC) whole rock major and trace elements calculated from mineral modal abundances and measured major and trace element compositions (normal mode LA-ICP-MS).**

| Sample | AJE407 | AJE439 | AJE464 | DJ0203 | DJ0205 | DJ0224 | DJ0250 | DJ0254 | DJ0261 | DJ0262 | DJ0264 | DJ0277 | DJ0278 | DJ0298 | DJ2104 | DJ02152 | JJG6356 | KDJ5 | KDJ6 | KIM4 | KIM5 | KIM.FLOOR | YC2 | 474527 | 474538 | 474544 | 474545 | 474551 | 474555 | 474557 | 474570 | 474573 | 474575 | 474577 | 477421 | 488802 | 488836 |
|---|---|---|---|---|---|---|---|---|---|---|---|---|---|---|---|---|---|---|---|---|---|---|---|---|---|---|---|---|---|---|---|---|---|---|---|---|---|
| **Locality** | **KC** | **KC** | **KC** | **KC** | **KC** | **KC** | **KC** | **KC** | **KC** | **KC** | **KC** | **KC** | **KC** | **KC** | **KC** | **KC** | **KC** | **KC** | **KC** | **KC** | **KC** | **KC** | **KC** | **NAC** | **NAC** | **NAC** | **NAC** | **NAC** | **NAC** | **NAC** | **NAC** | **NAC** | **NAC** | **NAC** | **NAC** | **NAC** | **NAC** |
| ***Major element (wt%), calculated*** | | | | | | | | | | | | | | | | | | | | | | | | | | | | | | | | | | | | | |
| **SiO2** | 42.67 | 44.01 | 44.00 | 45.53 | 47.60 | 46.30 | 44.80 | 46.70 | 42.86 | 46.51 | 42.99 | 46.05 | 45.82 | 44.23 | 40.09 | 44.38 | 42.27 | 46.84 | 44.62 | 45.88 | 45.00 | 44.58 | 45.21 | 42.46 | 44.60 | 40.32 | 43.99 | 44.43 | 44.07 | 38.91 | 40.46 | 40.16 | 44.58 | 45.80 | 23.93 | 39.94 | 36.08 |
| **TiO2** | 0.011 | 0.031 | 0.075 | 0.008 | 0.012 | 0.007 | 0.034 | 0.007 | 0.013 | 0.060 | 0.005 | 0.029 | 0.005 | 0.018 | 0.032 | 0.004 | 0.030 | 0.016 | 0.027 | 0.006 | 0.017 | 0.008 | 0.042 | 0.07 | 0.08 | 0.01 | 0.03 | 0.05 | 0.09 | 0.01 | 0.03 | 0.03 | 0.07 | 0.02 | 0.02 | 0.01 | 0.02 |
| **Al2O3** | 0.07 | 0.12 | 0.29 | 1.15 | 2.22 | 1.01 | 0.09 | 2.06 | 2.02 | 1.26 | 0.39 | 0.93 | 0.22 | 0.77 | 0.02 | 0.18 | 0.53 | 1.41 | 0.30 | 0.34 | 0.63 | 2.36 | 0.02 | 0.11 | 1.05 | 0.01 | 0.40 | 0.54 | 0.45 | 0.02 | 0.03 | 0.42 | 1.24 | 0.25 | 0.01 | 0.01 | 0.02 |
| **Cr2O3** | 0.13 | 0.13 | 0.51 | 0.39 | 0.34 | 0.32 | 0.17 | 0.68 | 0.46 | 0.63 | 0.08 | 0.29 | 0.10 | 0.26 | 0.04 | 0.09 | 0.43 | 0.36 | 0.18 | 0.18 | 0.32 | 0.41 | 0.09 | 0.13 | 0.27 | 0.05 | 0.28 | 0.50 | 0.29 | 0.09 | 0.06 | 0.25 | 0.29 | 0.22 | 0.03 | 0.03 | 0.04 |
| **FeO** | 4.87 | 9.21 | 7.24 | 5.07 | 6.75 | 5.75 | 4.40 | 5.27 | 6.39 | 6.02 | 6.24 | 5.78 | 6.03 | 7.14 | 10.55 | 5.90 | 5.24 | 6.29 | 6.42 | 5.75 | 5.74 | 5.77 | 6.74 | 7.53 | 8.72 | 7.92 | 6.66 | 6.63 | 7.80 | 7.15 | 11.08 | 9.80 | 7.81 | 7.23 | 6.40 | 7.16 | 7.87 |
| **MnO** | 0.09 | 0.14 | 0.10 | 0.09 | 0.14 | 0.10 | 0.08 | 0.11 | 0.15 | 0.11 | 0.10 | 0.11 | 0.10 | 0.11 | 0.14 | 0.09 | 0.09 | 0.12 | 0.10 | 0.11 | 0.11 | 0.10 | 0.13 | 0.12 | 0.15 | 0.12 | 0.11 | 0.11 | 0.13 | 0.12 | 0.14 | 0.15 | 0.13 | 0.12 | 0.09 | 0.12 | 0.12 |
| **MgO** | 49.88 | 44.26 | 43.90 | 46.87 | 41.47 | 45.27 | 49.28 | 42.23 | 40.30 | 35.64 | 48.95 | 44.62 | 45.21 | 45.73 | 48.30 | 46.11 | 49.58 | 43.79 | 45.31 | 44.86 | 41.65 | 46.52 | 41.79 | 47.60 | 44.43 | 51.22 | 47.48 | 46.81 | 46.23 | 48.10 | 47.67 | 48.14 | 45.28 | 44.46 | 28.64 | 50.03 | 44.32 |
| **CaO** | 0.09 | 0.89 | 2.99 | 0.17 | 0.81 | 0.30 | 0.13 | 0.52 | 1.19 | 5.88 | 0.10 | 0.30 | 0.13 | 0.34 | 0.05 | 0.18 | 0.38 | 0.98 | 0.77 | 0.08 | 0.67 | 0.39 | 0.58 | 0.26 | 0.38 | 0.03 | 0.25 | 0.38 | 0.37 | 0.55 | 0.04 | 0.38 | 0.39 | 0.48 | 0.04 | 0.03 | 0.04 |
| **Na2O** | 0.03 | 0.11 | 0.35 | 0.05 | 0.05 | 0.01 | 0.06 | 0.04 | 0.12 | 0.60 | 0.01 | 0.05 | 0.02 | 0.03 | 0.01 | 0.03 | 0.06 | 0.12 | 0.13 | 0.02 | 0.12 | 0.04 | 0.05 | 0.06 | 0.05 | 0.01 | 0.06 | 0.06 | 0.07 | 0.05 | 0.02 | 0.01 | 0.05 | 0.08 | 0.01 | 0.01 | 0.01 |
| **K2O** | 0.004 | 0.006 | 0.008 | 0.003 | 0.004 | 0.004 | 0.004 | 0.005 | 0.006 | 0.005 | 0.005 | 0.006 | 0.005 | 0.005 | 0.003 | 0.005 | 0.004 | 0.005 | 0.005 | 0.021 | 0.005 | 0.003 | 0.012 | 0.007 | 0.004 | 0.004 | 0.002 | 0.006 | 0.004 | 0.004 | 0.005 | 0.005 | 0.006 | 0.004 | 0.002 | 0.006 | 0.004 |
| **NiO** | 0.28 | 0.29 | 0.37 | 0.28 | 0.27 | 0.27 | 0.30 | 0.24 | 0.23 | 0.20 | 0.38 | 0.26 | 0.30 | 0.33 | 0.26 | 0.31 | 0.32 | 0.28 | 0.27 | 0.27 | 0.24 | 0.28 | 0.25 | 0.33 | 0.27 | 0.32 | 0.27 | 0.28 | 0.30 | 0.32 | 0.34 | 0.33 | 0.27 | 0.28 | 0.17 | 0.37 | 0.32 |
| **Total** | 98.1 | 99.2 | 99.8 | 99.6 | 99.7 | 99.3 | 99.4 | 97.9 | 93.7 | 96.9 | 99.2 | 98.4 | 97.9 | 99.0 | 99.5 | 97.3 | 98.9 | 100.2 | 98.1 | 97.5 | 94.5 | 100.5 | 94.9 | 98.7 | 100.0 | 100.0 | 99.5 | 99.8 | 99.8 | 95.3 | 99.9 | 99.7 | 100.1 | 98.9 | 59.3 | 97.7 | 88.8 |
| **Mg#** | **94.8** | **89.5** | **91.5** | **94.3** | **91.6** | **93.4** | **95.2** | **93.5** | **91.8** | **91.3** | **93.3** | **93.2** | **93.0** | **91.9** | **89.1** | **93.3** | **94.4** | **92.5** | **92.6** | **93.3** | **92.8** | **93.5** | **91.7** | **91.8** | **90.1** | **92.0** | **92.7** | **92.6** | **91.4** | **92.3** | **88.5** | **89.7** | **91.2** | **91.6** | **88.9** | **92.6** | **90.9** |
| ***Trace elements (µg g$^{-1}$), calculated for normal mode data*** | | | | | | | | | | | | | | | | | | | | | | | | | | | | | | | | | | | | | |
| **Li** | 0.74 | 1.79 | 1.76 | 1.05 | 1.19 | 1.25 | 0.64 | 0.80 | 1.29 | 1.32 | 0.92 | 1.23 | 0.97 | 1.17 | 3.14 | 0.97 | 1.28 | 1.22 | 1.62 | 0.90 | 1.72 | 0.84 | 1.64 | 1.86 | 1.62 | 1.35 | 1.35 | 1.61 | 2.44 | 2.35 | 2.10 | 1.46 | 1.64 | 1.21 | 1.25 | 1.44 | 1.87 |
| **B** | 5.30 | 5.85 | 10.26 | 4.96 | 4.63 | 3.85 | 3.59 | 3.85 | 8.21 | 5.85 | 11.39 | 7.56 | 3.67 | 5.09 | 10.31 | 0.98 | 1.08 | 2.43 | 2.01 | 0.73 | 3.16 | 3.96 | 5.19 | 16.81 | 11.18 | 6.32 | 7.73 | 12.09 | 9.69 | 1.38 | 0.73 | 13.46 | 18.10 | 10.45 | 10.56 | 12.05 | 11.65 |
| **P** | 53.5 | 81.7 | 33.2 | 82.4 | 56.0 | 34.2 | 49.3 | 94.7 | 69.1 | 69.0 | 37.0 | 81.3 | 17.1 | 60.4 | 96.9 | 15.5 | 37.9 | 53.0 | 59.7 | 10.8 | 53.0 | 56.0 | 17.2 | 31.2 | 32.3 | 26.0 | 24.2 | 35.4 | 34.6 | 47.7 | 36.3 | 23.6 | 35.9 | 25.0 | 29.7 | 23.1 | 30.9 |
| **Sc** | 3.09 | 5.73 | 8.58 | 5.86 | 10.07 | 7.25 | 2.62 | 11.22 | 15.97 | 14.53 | 5.35 | 8.73 | 2.97 | 7.14 | 6.33 | 0.81 | 6.93 | 7.09 | 2.27 | 2.89 | 7.66 | 9.98 | 13.44 | 5.56 | 8.22 | 3.73 | 5.02 | 12.38 | 5.72 | 2.10 | 1.31 | 5.47 | 9.23 | 5.13 | 1.91 | 3.17 | 3.06 |
| **Ti** | 14 | 253 | 403 | 49 | 124 | 3 | 233 | 20 | 111 | 400 | 10 | 177 | 8 | 83 | 124 | 4 | 212 | 106 | 208 | 15 | 96 | 20 | 635 | 409 | 557 | 155 | 143 | 280 | 567 | 89 | 217 | 173 | 517 | 108 | 112 | 77 | 83 |
| **V** | 7.8 | 23.6 | 25.6 | 22.5 | 29.9 | 22.8 | 6.2 | 30.8 | 32.4 | 104.8 | 11.0 | 20.1 | 19.0 | 22.4 | 4.0 | 12.1 | 11.9 | 30.5 | 24.3 | 15.0 | 23.9 | 30.1 | 28.1 | 16.1 | 34.7 | 6.7 | 19.5 | 22.3 | 25.8 | 6.0 | 8.3 | 17.5 | 29.5 | 21.3 | 5.7 | 2.8 | 3.0 |
| **Cr** | 1163 | 821 | 3666 | 2473 | 2516 | 1994 | 989 | 4518 | 3178 | 4323 | 643 | 1945 | 1704 | 1586 | 140 | 409 | 2969 | 2269 | 977 | 2194 | 2056 | 2739 | 1256 | 742 | 1906 | 304 | 1820 | 3437 | 1898 | 515 | 211 | 1523 | 1861 | 1411 | 169 | 69 | 72 |
| **Mn** | 609 | 1030 | 843 | 634 | 1063 | 702 | 522 | 826 | 969 | 800 | 658 | 777 | 671 | 830 | 990 | 730 | 680 | 986 | 819 | 901 | 801 | 735 | 680 | 828 | 1040 | 1130 | 789 | 898 | 1003 | 929 | 1050 | 1158 | 1069 | 941 | 623 | 930 | 1011 |
| **Co** | 102 | 133 | 123 | 98 | 109 | 100 | 96 | 92 | 102 | 86 | 132 | 101 | 110 | 122 | 140 | 107 | 100 | 103 | 111 | 100 | 97 | 106 | 94 | 126 | 124 | 153 | 119 | 115 | 129 | 125 | 165 | 160 | 133 | 120 | 97 | 132 | 128 |
| **Ni** | 2286 | 2429 | 2746 | 2246 | 2117 | 2022 | 2343 | 2002 | 1935 | 1759 | 2970 | 2300 | 2515 | 2789 | 2609 | 2809 | 2726 | 2556 | 2455 | 2414 | 2092 | 2404 | 2183 | 2620 | 2583 | 3178 | 2795 | 2493 | 2786 | 2829 | 2819 | 3287 | 2747 | 2537 | 1706 | 3149 | 3081 |
| **Cu** | 1.03 | 0.20 | 1.97 | 0.68 | 0.24 | | 0.83 | 0.20 | 0.32 | 0.64 | 0.28 | 0.53 | 0.35 | 1.98 | 0.91 | 0.24 | 1.55 | 0.01 | 0.37 | | 0.39 | 1.10 | 0.13 | 6.88 | 3.58 | 4.79 | 1.88 | 6.05 | 5.20 | 0.46 | 3.97 | 8.68 | 3.64 | 4.50 | 6.23 | 0.54 | 0.42 |
| **Zn** | 38.0 | 76.4 | 56.2 | 39.5 | 48.0 | 43.3 | 30.8 | 37.0 | 47.1 | 45.8 | 46.0 | 44.6 | 46.8 | 53.4 | 92.1 | 33.3 | 41.2 | 39.0 | 45.1 | 35.1 | 42.0 | 43.6 | 51.1 | 59.4 | 71.1 | 88.2 | 57.8 | 52.4 | 66.4 | 45.1 | 73.5 | 80.8 | 69.6 | 55.9 | 54.9 | 63.3 | 70.5 |
| **Ga** | 0.242 | 0.533 | 0.926 | 0.339 | 1.187 | 0.324 | 0.078 | 0.440 | 0.725 | 1.845 | 0.109 | 0.448 | 0.373 | 0.445 | 0.145 | 0.235 | 0.324 | 0.595 | 0.694 | 0.581 | 0.294 | 0.563 | 0.367 | 0.449 | 1.204 | 0.182 | 0.350 | 0.645 | 1.195 | 0.103 | 0.269 | 0.593 | 1.031 | 0.572 | 0.138 | 0.053 | 0.155 |
| **As** | | 0.016 | 0.025 | 0.007 | 0.029 | | | 0.012 | 0.039 | 0.214 | 0.005 | 0.142 | 0.103 | 0.147 | 0.202 | 0.001 | 0.007 | 0.031 | 0.016 | | 0.092 | 0.157 | 0.205 | 0.001 | 0.008 | | 0.003 | 0.005 | 0.003 | 0.007 | | | 0.007 | 0.000 | | | | |
| **Rb** | 0.260 | 0.005 | 0.036 | 0.002 | 0.014 | 0.008 | | 0.113 | 0.021 | 0.856 | 0.001 | 0.286 | 0.022 | 0.125 | 0.059 | 0.001 | 0.002 | 0.004 | 0.006 | 0.641 | 0.101 | 0.073 | 7.969 | 0.008 | 0.053 | | 0.001 | 0.143 | 0.051 | 0.034 | | 0.017 | 0.030 | 0.006 | 0.005 | | | |
| **Sr** | 1.089 | 23.736 | 21.626 | 0.121 | 9.015 | 0.032 | 0.078 | 0.189 | 22.070 | 149.979 | 0.042 | 5.824 | 2.582 | 1.415 | 0.422 | 4.986 | 0.994 | 31.219 | 30.220 | 2.672 | 4.709 | 0.363 | 170.1 | 1.002 | 0.191 | 0.103 | 0.887 | 0.677 | 0.985 | 10.059 | 0.014 | 0.115 | 0.317 | 1.001 | 0.149 | 0.021 | 0.110 |
| **Y** | 0.034 | 0.480 | 0.284 | 0.060 | 1.050 | 0.011 | 0.020 | 0.382 | 2.220 | 1.285 | 0.036 | 0.584 | 0.004 | 0.197 | 0.020 | 0.002 | 1.535 | 0.777 | 0.069 | 0.062 | 0.445 | 0.166 | 0.334 | 0.038 | 0.261 | | 0.197 | 0.216 | 0.449 | 0.232 | 0.004 | 0.280 | 0.489 | 0.021 | 0.008 | 0.012 | 0.033 |
| **Zr** | 0.177 | 2.737 | 2.033 | 1.376 | 0.787 | 0.005 | 0.288 | 8.523 | 4.546 | 17.252 | 0.576 | 4.524 | 0.046 | 2.039 | 0.581 | 0.067 | 5.863 | 3.342 | 2.815 | 0.175 | 4.020 | 1.819 | 3.737 | 0.296 | 2.173 | 0.148 | 2.115 | 2.653 | 2.267 | 3.684 | 0.264 | 1.174 | 3.305 | 0.129 | 0.161 | 0.607 | 0.785 |
| **Nb** | 0.515 | 0.384 | 0.116 | 0.186 | 0.794 | 0.002 | 0.112 | 0.635 | 0.354 | 1.082 | 0.828 | 0.999 | 0.532 | 0.098 | 0.497 | 1.074 | 0.125 | 0.439 | 0.550 | 0.939 | 0.245 | 0.265 | 0.267 | 0.061 | 0.085 | 0.032 | 0.146 | 0.072 | 0.091 | 0.945 | 0.170 | 0.057 | 0.075 | 0.045 | 0.057 | 1.809 | 1.842 |
| **Mo** | | 0.003 | 0.020 | 0.001 | 0.004 | | | 0.003 | 0.004 | 0.059 | 0.001 | 0.400 | 0.022 | 0.022 | 0.023 | 0.000 | 0.001 | 0.003 | 0.002 | | 0.017 | 0.010 | 0.101 | 0.000 | 0.001 | | 0.001 | 0.004 | 0.000 | 0.001 | | 0.001 | 0.001 | 0.000 | | | | |
| **Cs** | | 0.001 | 0.002 | 0.001 | 0.003 | | | 0.017 | 0.005 | 0.035 | | 0.136 | 0.010 | 0.030 | 0.001 | | | 0.003 | 0.001 | | 0.041 | 0.029 | 0.049 | | 0.002 | | 0.001 | 0.004 | 0.005 | 0.002 | | 0.003 | 0.002 | 0.000 | | | | |
| **Ba** | 11.146 | 0.136 | 0.427 | 0.015 | 0.059 | 0.001 | 0.017 | 0.056 | 0.513 | 6.008 | 0.036 | 4.260 | 0.576 | 2.235 | 0.551 | 0.003 | 0.019 | 0.139 | 7.093 | 27.466 | 0.304 | 0.081 | 4.899 | 0.028 | 0.204 | | 0.007 | 0.565 | 0.115 | 1.571 | 0.011 | 0.044 | 0.227 | 0.009 | 0.474 | | 0.542 |
| **La** | 0.015 | 0.745 | 0.234 | 0.020 | 0.452 | 0.001 | 0.001 | 0.016 | 0.603 | 4.776 | 0.007 | 0.611 | 0.151 | 0.069 | 0.067 | 0.150 | 0.018 | 0.554 | 0.633 | 0.030 | 0.137 | 0.014 | 0.403 | 0.029 | 0.037 | | 0.015 | 0.035 | 0.020 | 0.159 | 0.001 | 0.009 | 0.026 | 0.012 | 0.009 | 0.015 | 0.064 |
| **Ce** | 0.039 | 2.396 | 0.999 | 0.021 | 1.545 | 0.004 | 0.009 | 0.064 | 2.724 | 16.076 | 0.024 | 1.493 | 0.330 | 0.167 | 0.119 | 0.502 | 0.080 | 1.994 | 2.579 | 0.083 | 0.393 | 0.103 | 1.753 | 0.089 | 0.084 | | 0.064 | 0.100 | 0.066 | 0.662 | 0.003 | 0.064 | 0.049 | 0.062 | 0.007 | 0.018 | 0.062 |
| **Pr** | 0.004 | 0.348 | 0.175 | 0.007 | 0.162 | 0.001 | 0.001 | 0.021 | 0.434 | 2.158 | 0.006 | 0.170 | 0.034 | 0.031 | 0.021 | 0.074 | 0.019 | 0.319 | 0.405 | 0.011 | 0.078 | 0.044 | 0.331 | 0.014 | 0.016 | | 0.014 | 0.018 | 0.014 | 0.123 | 0.000 | 0.017 | 0.011 | 0.011 | 0.002 | | 0.018 |
| **Nd** | 0.019 | 1.489 | 0.857 | 0.074 | 0.611 | | 0.009 | 0.284 | 1.969 | 8.351 | 0.062 | 0.729 | 0.125 | 0.291 | 0.080 | 0.276 | 0.147 | 1.453 | 1.666 | 0.047 | 0.427 | 0.440 | 1.581 | 0.048 | 0.063 | | 0.092 | 0.139 | 0.078 | 0.635 | 0.001 | 0.127 | 0.065 | 0.044 | | | 0.308 |
| **Sm** | 0.006 | 0.264 | 0.220 | 0.078 | 0.145 | 0.002 | 0.006 | 0.267 | 0.446 | 1.183 | 0.035 | 0.181 | 0.023 | 0.135 | 0.023 | 0.028 | 0.097 | 0.290 | 0.230 | 0.014 | 0.153 | 0.131 | 0.336 | 0.017 | 0.026 | | 0.050 | 0.063 | 0.037 | 0.156 | | 0.044 | 0.047 | 0.005 | | | 0.074 |
| **Eu** | 0.002 | 0.074 | 0.062 | 0.026 | 0.055 | | 0.001 | 0.106 | 0.145 | 0.293 | 0.010 | 0.067 | 0.004 | 0.042 | 0.008 | 0.005 | 0.046 | 0.089 | 0.050 | 0.006 | 0.048 | 0.034 | 0.093 | 0.005 | 0.016 | | 0.021 | 0.027 | 0.019 | 0.048 | 0.000 | 0.016 | 0.022 | 0.008 | | | 0.012 |
| **Gd** | 0.007 | 0.186 | 0.150 | 0.063 | 0.133 | | 0.005 | 0.284 | 0.394 | 0.666 | 0.020 | 0.194 | 0.016 | 0.117 | 0.012 | 0.007 | 0.188 | 0.224 | 0.100 | 0.017 | 0.137 | 0.074 | 0.203 | 0.015 | 0.041 | | 0.061 | 0.103 | 0.062 | 0.124 | 0.000 | 0.049 | 0.086 | 0.031 | | 0.062 | |
| **Tb** | | 0.022 | 0.018 | 0.005 | 0.023 | | | 0.028 | 0.062 | 0.070 | 0.001 | 0.026 | 0.002 | 0.014 | 0.003 | 0.000 | 0.039 | 0.032 | 0.008 | | 0.020 | 0.008 | 0.023 | 0.005 | 0.014 | | 0.009 | 0.021 | 0.031 | 0.016 | 0.000 | 0.008 | 0.013 | 0.009 | | | |
| **Dy** | 0.006 | 0.118 | 0.081 | 0.020 | 0.166 | | 0.005 | 0.118 | 0.388 | 0.326 | 0.008 | 0.140 | 0.011 | 0.051 | 0.011 | 0.001 | 0.280 | 0.176 | 0.027 | 0.015 | 0.108 | 0.024 | 0.102 | 0.005 | 0.044 | | 0.047 | 0.056 | 0.089 | 0.072 | | 0.050 | 0.084 | 0.001 | | | |
| **Ho** | | 0.019 | 0.012 | 0.002 | 0.040 | | | 0.016 | 0.080 | 0.055 | 0.001 | 0.024 | 0.003 | 0.008 | 0.003 | 0.000 | 0.061 | 0.028 | 0.003 | | 0.018 | 0.007 | 0.017 | 0.001 | 0.019 | | 0.008 | 0.008 | 0.017 | 0.013 | | 0.011 | 0.019 | 0.000 | 0.007 | | 0.047 |
| **Er** | 0.003 | 0.050 | 0.026 | 0.006 | 0.132 | 0.004 | | 0.033 | 0.225 | 0.132 | 0.002 | 0.053 | 0.000 | 0.017 | 0.006 | 0.005 | 0.180 | 0.063 | 0.005 | 0.008 | 0.046 | 0.026 | 0.034 | 0.001 | 0.028 | | 0.018 | 0.018 | 0.048 | 0.021 | | 0.032 | 0.061 | 0.002 | | | |
| **Tm** | | 0.005 | 0.003 | 0.000 | 0.021 | | | 0.004 | 0.032 | 0.017 | 0.000 | 0.008 | 0.000 | 0.002 | 0.003 | 0.000 | 0.026 | 0.008 | 0.000 | | 0.006 | 0.008 | 0.005 | 0.002 | 0.009 | | 0.007 | 0.007 | 0.013 | 0.008 | 0.007 | 0.005 | 0.010 | 0.000 | | 0.026 | 0.039 |
| **Yb** | 0.003 | 0.036 | 0.016 | 0.009 | 0.165 | 0.007 | 0.004 | 0.025 | 0.229 | 0.111 | 0.003 | 0.046 | 0.000 | 0.020 | 0.006 | 0.000 | 0.174 | 0.052 | 0.002 | 0.009 | 0.044 | 0.061 | 0.020 | 0.006 | 0.047 | | 0.016 | 0.021 | 0.047 | 0.060 | 0.009 | 0.037 | 0.099 | 0.003 | 0.011 | 0.106 | 0.093 |
| **Lu** | 0.001 | 0.007 | 0.002 | 0.001 | 0.027 | 0.002 | | 0.004 | 0.035 | 0.019 | 0.001 | 0.009 | 0.001 | 0.005 | 0.002 | 0.000 | 0.026 | 0.008 | 0.000 | 0.001 | 0.008 | 0.013 | 0.005 | 0.000 | 0.009 | | 0.002 | 0.006 | 0.008 | 0.001 | | 0.006 | 0.015 | 0.000 | | | 0.021 |
| **Hf** | 0.010 | 0.131 | 0.160 | 0.040 | 0.012 | | 0.003 | 0.144 | 0.108 | 0.761 | 0.005 | 0.081 | 0.011 | 0.050 | 0.032 | 0.001 | 0.119 | 0.094 | 0.132 | 0.005 | 0.180 | 0.042 | 0.216 | 0.008 | 0.044 | | 0.048 | 0.070 | 0.052 | 0.170 | | 0.029 | 0.080 | 0.001 | | | 0.015 |
| **Ta** | 0.022 | 0.010 | 0.008 | 0.020 | 0.010 | | 0.009 | 0.043 | 0.019 | 0.052 | 0.031 | 0.037 | 0.014 | 0.006 | 0.025 | 0.010 | 0.010 | 0.022 | 0.031 | 0.026 | 0.011 | 0.021 | 0.011 | 0.000 | 0.001 | | 0.000 | 0.002 | 0.001 | 0.001 | | 0.002 | 0.001 | 0.000 | | | |
| **Pb** | | 0.160 | 0.068 | 0.002 | 0.034 | | | 0.012 | 0.084 | 0.773 | 0.017 | 0.429 | 0.060 | 0.102 | 0.068 | 0.009 | 1.018 | 0.131 | 0.102 | | 0.099 | 0.042 | 1.512 | 0.002 | 0.005 | | 0.003 | 0.008 | 0.011 | 0.010 | | 0.004 | 0.070 | 0.001 | | | |
| **Bi** | | 0.001 | 0.001 | 0.000 | 0.001 | | | 0.001 | 0.002 | 0.012 | 0.000 | 0.187 | 0.000 | 0.005 | | 0.000 | 0.001 | 0.001 | 0.001 | | 0.002 | 0.001 | 0.010 | | 0.001 | | 0.000 | 0.000 | 0.000 | 0.000 | | | 0.001 | 0.000 | | | |
| **Th** | 0.015 | 0.020 | 0.004 | 0.000 | 0.024 | | | 0.004 | 0.027 | 0.227 | 0.003 | 0.068 | 0.030 | 0.011 | 0.012 | 0.006 | 0.001 | 0.019 | 0.029 | 0.036 | 0.010 | 0.007 | 0.045 | 0.000 | 0.000 | | 0.000 | 0.002 | 0.000 | 0.001 | | 0.002 | 0.001 | 0.000 | | | |
| **U** | 0.013 | 0.003 | 0.001 | 0.001 | 0.025 | | 0.002 | 0.010 | 0.005 | 0.033 | 0.003 | 0.020 | 0.019 | 0.003 | 0.004 | 0.007 | 0.001 | 0.003 | 0.003 | 0.031 | 0.002 | 0.006 | 0.004 | 0.000 | 0.000 | | 0.000 | 0.001 | 0.000 | 0.000 | | 0.001 | 0.001 | 0.000 | | | |

**Electronic Supplement B-2 Representative major and trace element compositions for clinopyroxene and garnet. The trace element data presented here is acquired with LA-ICP-MS in hydrogen mode.**

| Sample | AJE439 | DJ0205 | DJ0262 | DJ0277 | JJG6356 | KDJ5 | 474527 | 474545 | 474551 | 474555 | 474570 | 474577 | AJE439 | DJ0205 | DJ0262 | DJ0277 | JJG6356 | KDJ5 | 474527 | 474545 | 474551 | 474555 | 474570 | 474577 |
|---|---|---|---|---|---|---|---|---|---|---|---|---|---|---|---|---|---|---|---|---|---|---|---|---|
| Litholo | hzb | grt hzb | grt lhz | grt hzb | grt hzb | grt hzb | grt hzb | grt hzb | grt hzb | grt hzb | hzb | grt hzb | hzb | grt hzb | grt lhz | grt hzb | grt hzb | grt hzb | grt hzb | grt hzb | grt hzb | grt hzb | hzb | grt hzb |
| Locality | KC | KC | KC | KC | KC | KC | NAC | NAC | NAC | NAC | NAC | NAC | KC | KC | KC | KC | KC | KC | NAC | NAC | NAC | NAC | NAC | NAC |
| Phase | *cpx* | *cpx* | *cpx* | *cpx* | *cpx* | *cpx* | *cpx* | *cpx* | *cpx* | *cpx* | *cpx* | *cpx* | *grt* | *grt* | *grt* | *grt* | *grt* | *grt* | *grt* | *grt* | *grt* | *grt* | *grt* | *grt* |
| ***Major elements (wt%)*** | | | | | | | | | | | | | | | | | | | | | | | | |
| **SiO2** | 54.63 | 55.11 | 54.29 | 54.41 | 55.52 | 54.61 | 54.86 | 54.99 | 54.76 | 54.64 | 54.42 | 55.00 | – | 42.27 | 41.71 | 41.56 | 41.49 | 39.73 | – | 39.41 | 38.72 | 38.79 | – | – |
| **TiO2** | 0.16 | 0.07 | 0.15 | 0.11 | 0.19 | 0.08 | 0.46 | 0.11 | 0.33 | 0.36 | 0.28 | 0.08 | – | 0.03 | 0.06 | 0.12 | 0.42 | 0.03 | – | 0.29 | 0.29 | 1.11 | – | – |
| **Al2O3** | 1.34 | 2.37 | 2.25 | 2.56 | 2.21 | 2.75 | 1.85 | 2.07 | 1.41 | 1.96 | 1.95 | 1.24 | – | 21.76 | 21.65 | 20.49 | 15.86 | 22.52 | – | 18.16 | 15.93 | 17.13 | – | – |
| **Cr2O3** | 2.02 | 1.75 | 1.79 | 2.57 | 3.91 | 2.32 | 1.95 | 3.55 | 2.72 | 2.17 | 2.05 | 1.57 | – | 2.55 | 2.91 | 4.49 | 10.63 | 3.44 | – | 8.56 | 11.56 | 8.70 | – | – |
| **FeO** | 3.20 | 1.56 | 2.48 | 1.93 | 1.58 | 2.25 | 2.87 | 2.27 | 2.48 | 2.93 | 3.68 | 3.13 | – | 8.56 | 8.51 | 6.72 | 5.09 | 7.71 | – | 6.87 | 6.11 | 7.50 | – | – |
| **MnO** | 0.09 | 0.06 | 0.08 | 0.06 | 0.06 | 0.07 | 0.12 | 0.10 | 0.11 | 0.10 | 0.12 | 0.11 | – | 0.49 | 0.47 | 0.38 | 0.30 | 0.44 | – | 0.39 | 0.36 | 0.38 | – | – |
| **MgO** | 15.76 | 15.53 | 15.84 | 15.70 | 16.39 | 15.58 | 18.21 | 16.26 | 18.15 | 17.49 | 16.39 | 19.55 | – | 20.07 | 20.22 | 21.24 | 20.02 | 21.35 | – | 20.71 | 20.33 | 19.66 | – | – |
| **CaO** | 20.41 | 21.38 | 20.39 | 19.40 | 18.28 | 19.90 | 17.31 | 17.93 | 18.20 | 17.93 | 19.19 | 17.74 | – | 4.86 | 4.82 | 4.94 | 6.72 | 4.87 | – | 5.55 | 6.42 | 6.31 | – | – |
| **Na2O** | 2.09 | 1.85 | 2.08 | 2.42 | 2.72 | 2.58 | 1.98 | 2.63 | 1.78 | 2.10 | 2.19 | 1.29 | – | 0.020 | 0.032 | 0.033 | 0.089 | 0.029 | – | 0.056 | 0.045 | 0.107 | – | – |
| **K2O** | 0.007 | 0.007 | 0.005 | 0.005 | 0.050 | 0.003 | 0.024 | 0.022 | 0.035 | 0.025 | 0.049 | 0.033 | – | 0.005 | 0.007 | 0.006 | 0.015 | 0.004 | – | 0.004 | 0.004 | 0.004 | – | – |
| **NiO** | 0.041 | 0.038 | 0.041 | 0.033 | 0.050 | 0.041 | 0.056 | 0.026 | 0.051 | 0.034 | 0.048 | 0.024 | – | 0.011 | 0.009 | 0.012 | 0.004 | 0.010 | – | 0.012 | 0.018 | 0.010 | – | – |
| **Total** | 99.7 | 99.7 | 99.4 | 99.2 | 101.0 | 100.2 | 99.7 | 100.0 | 100.0 | 99.7 | 100.4 | 99.8 | – | 100.6 | 100.4 | 100.0 | 100.6 | 100.1 | – | 100.0 | 99.8 | 99.7 | – | – |
| ***Mg#*** | ***89.8*** | ***94.7*** | ***91.9*** | ***93.6*** | ***94.9*** | ***92.5*** | ***91.9*** | ***92.7*** | ***92.9*** | ***91.4*** | ***88.8*** | ***91.8*** | – | ***80.7*** | ***80.9*** | ***84.9*** | ***87.5*** | ***83.2*** | – | ***84.3*** | ***85.6*** | ***82.4*** | – | – |
| ***Cr#*** | *0.50* | *0.33* | *0.36* | *0.40* | *0.54* | *0.37* | *0.41* | *0.53* | *0.56* | *0.43* | *0.41* | *0.46* | – | *0.07* | *0.08* | *0.13* | *0.31* | *0.09* | – | *0.24* | *0.33* | *0.25* | – | – |
| ***Trace elements hydrogen mode (µg g$^{-1}$)*** | | | | | | | | | | | | | | | | | | | | | | | | |
| **Li** | 0.62 | 0.77 | 0.82 | 1.16 | 0.65 | 0.77 | 0.96 | 1.07 | 1.71 | 1.38 | – | 0.81 | – | 0.09 | 0.11 | 0.57 | 0.09 | 0.07 | – | 0.13 | 0.23 | 0.36 | – | – |
| **Na** | 14725 | n.a. | 15089 | 17093 | 19407 | n.a. | n.a. | 19211 | 13644 | n.a. | – | 9010 | – | 129 | 189 | 376 | 484 | 151 | – | 346 | 336 | 1105 | – | – |
| **Al** | 7384 | 12860 | 12311 | 14236 | 11631 | 16374 | 10456 | 11263 | 8037 | 10513 | – | 7055 | – | 115577 | 106522 | 101465 | 80927 | 101605 | – | 82960 | 71933 | 77348 | – | – |
| **P** | 54.76 | n.a. | 90.97 | 136.73 | 50.38 | n.a. | n.a. | 32.52 | 66.71 | n.a. | – | 26.96 | – | 90.4 | 112 | 266 | 155 | 75.7 | – | 132 | 121 | 91.1 | – | – |
| **K** | 54.45 | n.a. | 318.20 | 239.50 | 349.80 | n.a. | n.a. | 15.41 | n.a. | n.a. | – | 563.15 | – | 57.9 | 2801.00 | 121 | 202 | 110 | – | | 615 | 780 | – | – |
| **Ca** | 146293 | 149081 | 146792 | 141973 | 129765 | 134223 | 117045 | 132536 | 137376 | 118751 | – | 125615 | – | 33152 | 30909 | 32599 | 43801 | 30309 | – | 36256 | 40895 | 42765 | – | – |
| **Sc** | 87.41 | 26.45 | 36.72 | 36.74 | 32.49 | 29.65 | 19.89 | 27.42 | 24.94 | 22.41 | – | 14.78 | – | 88.0 | 96.2 | 111 | 167 | 95.2 | – | 138 | 326 | 129 | – | – |
| **Ti** | 906 | 424 | 1057 | 882 | 1194 | 466 | 2482 | 730 | 2320 | 2092 | – | 387 | – | 212 | 429 | 759 | 2510 | 233 | – | 1571 | 1582 | 6279 | – | – |
| **V** | 380 | 366 | 324 | 324 | 197 | 353 | 245 | 385 | 284 | 297 | – | 170 | – | 106 | 96.6 | 146 | 190 | 106 | – | 275 | 276 | 346 | – | – |
| **Cr** | 12898 | 11181 | 11791 | 17171 | 25538 | 15418 | 12281 | 24109 | 18255 | 14489 | – | 10603 | – | 17685 | 18708 | 29965 | 70766 | 20956 | – | 52985 | 73058 | 60931 | – | – |
| **Mn** | 676 | 409 | 558 | 542 | 531 | 458 | 768 | 759 | 874 | 861 | – | 1031 | – | 3698 | 3485 | 2793 | 2230 | 3002 | – | 2717 | 2500 | 2798 | – | – |
| **Co** | 19.11 | 15.44 | 18.04 | 17.72 | 16.78 | 15.69 | 23.59 | 19.82 | 24.59 | 23.99 | – | 32.39 | – | 41.65 | 42.48 | 40.33 | 33.91 | 39.24 | – | 37.29 | 36.83 | 39.70 | – | – |
| **Ni** | 327 | 296 | 313 | 343 | 350 | 310 | 421 | 377 | 438 | 438 | – | 554 | – | 17.11 | 23.88 | 39.64 | 56.38 | 23.79 | – | 51.87 | 66.28 | 77.79 | – | – |
| **Cu** | 0.32 | 0.43 | 0.81 | 0.60 | 1.66 | 0.35 | 4.43 | 1.97 | 2.89 | 3.33 | – | 3.08 | – | 0.04 | 0.07 | 0.12 | 0.14 | 0.02 | – | 0.16 | 0.33 | 0.86 | – | – |
| **Zn** | 12.03 | 7.05 | 11.10 | 7.97 | 6.90 | 6.60 | 12.13 | 10.54 | 16.87 | 14.27 | – | 15.94 | – | 8.23 | 10.25 | 9.13 | 8.22 | 8.09 | – | 9.42 | 9.15 | 12.76 | – | – |
| **Ga** | 4.88 | 4.94 | 4.73 | 2.82 | 2.62 | 2.86 | 4.08 | 3.05 | 5.40 | 7.51 | – | 2.23 | – | 3.34 | 3.74 | 2.11 | 3.47 | 1.95 | – | 4.39 | 3.04 | 11.13 | – | – |
| **Ge** | 2.63 | 2.06 | 2.40 | 2.85 | 1.29 | 2.05 | 1.29 | 1.52 | 1.53 | 1.39 | – | 1.44 | – | 1.85 | 2.09 | 1.56 | 1.89 | 1.01 | – | 1.98 | 2.56 | 3.09 | – | – |
| **As** | 0.29 | 0.20 | 0.27 | 0.26 | 0.13 | 0.30 | 0.09 | 0.14 | 0.17 | 0.09 | – | 0.15 | – | 0.08 | 0.28 | 0.11 | 0.12 | 0.41 | – | 0.10 | 0.11 | 0.11 | – | – |
| **Rb** | 0.03 | 0.01 | 0.83 | 0.47 | 0.15 | 0.02 | 0.02 | 0.12 | 0.37 | 0.31 | – | 0.03 | – | 0.01 | 0.01 | 0.32 | 0.01 | 0.02 | – | 0.04 | 0.39 | 0.10 | – | – |
| **Sr** | 592 | 636 | 532 | 576 | 144 | 844 | 121 | 251 | 190 | 133 | – | 146 | – | 0.18 | 0.18 | 24.00 | 0.60 | 0.47 | – | 0.75 | 1.82 | 0.96 | – | – |
| **Y** | 11.77 | 1.03 | 3.27 | 2.31 | 3.76 | 3.42 | 2.44 | 1.09 | 2.42 | 2.94 | – | 0.51 | – | 11.22 | 14.57 | 14.48 | 44.21 | 10.43 | – | 9.37 | 5.38 | 20.53 | – | – |
| **Zr** | 52.58 | 13.81 | 64.37 | 92.13 | 51.03 | 63.11 | 10.89 | 29.81 | 15.96 | 17.39 | – | 2.54 | – | 6.51 | 19.03 | 82.27 | 158.48 | 14.53 | – | 91.07 | 75.89 | 97.67 | – | – |
| **Nb** | 0.48 | 0.89 | 2.64 | 2.56 | 0.56 | 0.66 | 0.17 | 0.31 | 1.46 | 0.20 | – | 0.21 | – | 0.13 | 0.23 | 0.58 | 0.33 | 0.12 | – | 0.26 | 0.46 | 0.33 | – | – |
| **Mo** | 0.05 | 0.01 | 0.09 | 0.07 | 0.05 | 0.01 | 0.01 | 0.02 | 0.05 | 0.02 | – | 0.08 | – | 0.07 | 0.08 | 0.07 | 0.04 | 0.05 | – | 0.04 | 0.04 | 0.08 | – | – |
| **Ag** | 0.017 | 0.008 | 0.020 | 0.021 | 0.019 | 0.024 | 0.008 | 0.019 | 0.013 | 0.015 | – | 0.0057 | – | 0.0026 | 0.0030 | 0.0030 | 0.0033 | 0.0016 | – | 0.0116 | 0.0051 | 0.0142 | – | – |
| **Cd** | 0.127 | 0.060 | 0.107 | 0.093 | 0.108 | 0.093 | 0.093 | 0.073 | 0.126 | 0.134 | – | 0.0695 | – | 0.0667 | 0.0966 | 0.0635 | 0.1308 | 0.0919 | – | 0.0717 | 0.0689 | 0.1406 | – | – |
| **In** | 0.093 | 0.031 | 0.045 | 0.031 | 0.027 | 0.048 | 0.021 | 0.115 | 0.120 | 0.037 | – | 0.1022 | – | 0.0766 | 0.0864 | 0.0867 | 0.1329 | 0.0938 | – | 0.0888 | 0.0811 | 0.1616 | – | – |
| **Sb** | 0.022 | 0.019 | 0.024 | 0.032 | 0.015 | 0.034 | bdl | 0.038 | 0.028 | 0.027 | – | 0.0287 | – | 0.0841 | 0.0637 | 0.0425 | 0.0394 | 0.0401 | – | 0.0298 | 0.0327 | 0.5235 | – | – |
| **Cs** | 0.005 | bdl | 0.015 | 0.153 | 0.005 | 0.006 | 0.006 | 0.014 | 0.017 | 0.007 | – | 0.0122 | – | 0.0017 | 0.0066 | 0.2058 | 0.0074 | 0.0098 | – | 0.0042 | 0.0146 | 0.0144 | – | – |
| **Ba** | 2.52 | 0.46 | 20.93 | 24.43 | 2.38 | 0.42 | 0.17 | 0.74 | 9.57 | 0.56 | – | 1.83 | – | 0.008 | 0.016 | 11.17 | 0.02 | 0.07 | – | 0.08 | 0.56 | 0.14 | – | – |
| **La** | 19.54 | 31.49 | 16.89 | 14.34 | 1.95 | 14.88 | 1.45 | 3.46 | 2.77 | 1.56 | – | 1.60 | – | 0.033 | 0.026 | 0.86 | 0.04 | 0.04 | – | 0.04 | 0.08 | 0.05 | – | – |
| **Ce** | 58.33 | 91.10 | 53.38 | 56.11 | 8.29 | 53.73 | 5.70 | 13.05 | 8.50 | 6.46 | – | 5.74 | – | 0.41 | 0.58 | 2.76 | 0.47 | 0.44 | – | 0.50 | 0.84 | 0.46 | – | – |
| **Pr** | 8.59 | 10.35 | 7.54 | 9.55 | 1.64 | 8.58 | 1.07 | 2.22 | 1.90 | 1.24 | – | 1.00 | – | 0.13 | 0.13 | 0.55 | 0.20 | 0.18 | – | 0.20 | 0.33 | 0.17 | – | – |
| **Nd** | 37.43 | 36.97 | 29.61 | 45.46 | 8.92 | 37.92 | 5.69 | 11.39 | 8.18 | 6.51 | – | 4.95 | – | 1.20 | 1.15 | 4.49 | 2.37 | 1.70 | – | 2.24 | 3.25 | 1.75 | – | – |
| **Sm** | 6.44 | 4.87 | 4.18 | 7.21 | 2.50 | 6.17 | 1.58 | 2.76 | 1.60 | 1.67 | – | 1.20 | – | 0.91 | 0.62 | 2.80 | 2.37 | 1.11 | – | 2.06 | 2.02 | 1.53 | – | – |
| **Eu** | 1.60 | 0.93 | 1.00 | 1.70 | 0.76 | 1.46 | 0.48 | 0.76 | 0.45 | 0.52 | – | 0.31 | – | 0.39 | 0.35 | 1.22 | 1.23 | 0.52 | – | 0.93 | 0.79 | 0.77 | – | – |
| **Gd** | 4.19 | 1.78 | 2.20 | 3.36 | 2.06 | 3.55 | 1.34 | 1.57 | 1.22 | 1.46 | – | 0.62 | – | 1.20 | 1.10 | 3.89 | 5.08 | 1.56 | – | 2.77 | 2.28 | 2.90 | – | – |
| **Tb** | 0.53 | 0.13 | 0.22 | 0.27 | 0.25 | 0.36 | 0.16 | 0.14 | 0.14 | 0.19 | – | 0.05 | – | 0.23 | 0.26 | 0.58 | 1.10 | 0.30 | – | 0.43 | 0.31 | 0.57 | – | – |
| **Dy** | 2.71 | 0.42 | 0.92 | 0.88 | 1.15 | 1.40 | 0.77 | 0.50 | 0.69 | 0.88 | – | 0.16 | – | 1.70 | 1.70 | 3.19 | 8.05 | 1.81 | – | 2.27 | 1.50 | 3.73 | – | – |
| **Ho** | 0.47 | 0.049 | 0.13 | 0.10 | 0.16 | 0.16 | 0.12 | 0.05 | 0.11 | 0.13 | – | 0.02 | – | 0.42 | 0.42 | 0.56 | 1.79 | 0.33 | – | 0.38 | 0.23 | 0.72 | – | – |
| **Er** | 1.15 | 0.075 | 0.27 | 0.16 | 0.32 | 0.25 | 0.20 | 0.08 | 0.22 | 0.26 | – | 0.04 | – | 1.39 | 1.56 | 1.36 | 5.31 | 0.87 | – | 0.87 | 0.48 | 1.87 | – | – |
| **Tm** | 0.14 | 0.007 | 0.03 | 0.014 | 0.03 | 0.021 | 0.021 | 0.006 | 0.019 | 0.03 | – | 0.00 | – | 0.23 | 0.23 | 0.18 | 0.77 | 0.11 | – | 0.10 | 0.06 | 0.12 | – | – |
| **Yb** | 0.82 | 0.026 | 0.15 | 0.060 | 0.15 | 0.077 | 0.089 | 0.024 | 0.110 | 0.14 | – | 0.03 | – | 1.75 | 1.89 | 1.16 | 5.43 | 0.78 | – | 0.64 | 0.43 | 0.85 | – | – |
| **Lu** | 0.11 | 0.003 | 0.02 | 0.007 | 0.02 | 0.009 | 0.010 | 0.003 | 0.014 | 0.02 | – | 0.00 | – | 0.28 | 0.28 | 0.18 | 0.82 | 0.13 | – | 0.10 | 0.09 | 0.09 | – | – |
| **Hf** | 2.98 | 0.39 | 2.93 | 4.05 | 2.58 | 2.42 | 0.75 | 2.15 | 0.85 | 1.16 | – | 0.15 | – | 0.07 | 0.18 | 1.02 | 2.95 | 0.12 | – | 2.02 | 2.17 | 2.44 | – | – |
| **Ta** | 0.0131 | 0.0259 | 0.1336 | 0.0910 | 0.0424 | 0.0676 | 0.0092 | 0.0179 | 0.0694 | 0.0123 | – | 0.0104 | – | 0.0015 | 0.0040 | 0.0286 | 0.0284 | 0.0044 | – | 0.0159 | 0.0321 | 0.0262 | – | – |
| **W** | 0.0060 | 0.0037 | 0.0574 | 0.0314 | 0.0116 | 0.0073 | 0.0008 | 0.0018 | 0.0132 | 0.0017 | – | 0.0270 | – | 0.0012 | 0.0724 | 0.0157 | 0.0015 | 0.0009 | – | 0.0015 | 0.0009 | 0.0079 | – | – |
| **Re** | 0.0003 | 0.0003 | 0.0003 | 0.0003 | 0.0004 | 0.0014 | bdl | 0.0013 | 0.0012 | 0.0012 | – | 0.0019 | – | 0.0009 | 0.0016 | 0.0011 | 0.0016 | 0.0007 | – | 0.0024 | 0.0007 | 0.0054 | – | – |
| **Tl** | 0.0006 | 0.0008 | 0.0079 | 0.0031 | 0.0015 | 0.0064 | bdl | 0.0019 | 0.0005 | bdl | – | 0.0025 | – | 0.0011 | 0.0017 | 0.0009 | 0.0007 | 0.0012 | – | 0.0008 | 0.0009 | 0.0019 | – | – |
| **Pb** | 4.1120 | 1.0587 | 2.3936 | 1.4723 | 0.5416 | 3.5310 | 0.2389 | 0.4561 | 0.6410 | 0.2528 | – | 0.2686 | – | 0.1645 | 0.0558 | 0.9924 | 0.1792 | 0.1440 | – | 0.2405 | 0.1745 | 0.1021 | – | – |
| **Bi** | 0.0201 | 0.0110 | 0.0206 | 0.0101 | 0.0043 | 0.0293 | 0.0034 | 0.0048 | 0.0045 | 0.0041 | – | 0.0017 | – | 0.0019 | 0.0026 | 0.0023 | 0.0030 | 0.0020 | – | 0.0016 | 0.0036 | 0.0069 | – | – |
| **Th** | 0.3298 | 1.0955 | 0.7399 | 0.3473 | 0.0707 | 0.5223 | 0.0122 | 0.0338 | 0.1648 | 0.0178 | – | 0.0198 | – | 0.0098 | 0.0497 | 0.0743 | 0.0069 | 0.0134 | – | 0.0068 | 0.0162 | 0.0141 | – | – |
| **U** | 0.0503 | 0.3522 | 0.0794 | 0.0765 | 0.0214 | 0.0473 | 0.0030 | 0.0093 | 0.0340 | 0.0032 | – | 0.0051 | – | 0.1252 | 0.0259 | 0.0470 | 0.0217 | 0.0279 | – | 0.0198 | 0.0363 | 0.0207 | – | – |

n.a. = not acquired; bdl = below detection limit

**Electronic Supplement B-3 Partition coefficients for Opx/Cpx and Cpx/Grt**

| | Opx/Cpx - Kaapval | | | | | | | | | Opx/Cpx - West Greenland | | | | | | | | | Mt. Gambier Opx/Cpx | | | Cpx/Grt - Kaapvaal | | | | | | | | | Cpx/Grt - West Greenland | | | | | | | | |
|---|---|---|---|---|---|---|---|---|---|---|---|---|---|---|---|---|---|---|---|---|---|---|---|---|---|---|---|---|---|---|---|---|---|---|---|---|---|---|
| | AJE439 | DJ0205 | DJ0262 | DJ0277 | JJG6356 | KDJ5 | AVRG | *SD* | MED | 474527 | 474545 | 474551 | 474555 | 474570 | 474577 | AVRG | *SD* | MED | AVRG | *SD* | MED | AJE439 | DJ0205 | DJ0262 | DJ0277 | JJG6356 | KDJ5 | AVRG | *SD* | MED | 474527 | 474545 | 474551 | 474555 | 474570 | 474577 | AVRG | *SD* | MED |
| **Li** | 1.28 | 0.95 | 1.42 | 0.98 | 1.12 | 1.07 | **1.14** | *0.18* | 1.09 | 1.15 | 0.84 | 0.65 | 1.04 | – | 0.89 | **0.91** | *0.19* | 0.89 | 1.45 | 0.54 | 1.35 | | 9.02 | 7.67 | 2.03 | 7.21 | 11.57 | **7.50** | *3.50* | 7.67 | – | 8.03 | 7.37 | 3.79 | – | – | **6.40** | *2.28* | 7.37 |
| **Na** | 0.03 | – | 0.06 | 0.06 | 0.07 | – | **0.054** | *0.015* | 0.060 | – | 0.07 | 0.15 | – | – | 0.15 | **0.12** | *0.05* | 0.15 | – | – | – | | – | 79.8 | 45.5 | 40.1 | – | **55.1** | *21.5* | 45.5 | – | 55.6 | 40.6 | – | – | – | **48.1** | *10.6* | 48.1 |
| **Al** | 0.21 | 0.26 | 0.29 | 0.29 | 0.32 | 0.23 | **0.27** | *0.04* | 0.28 | 0.30 | 0.25 | 0.31 | 0.30 | – | 0.50 | **0.33** | *0.10* | 0.30 | – | – | – | | 0.11 | 0.12 | 0.14 | 0.14 | 0.16 | **0.13** | *0.02* | 0.14 | – | 0.14 | 0.11 | 0.14 | – | – | **0.13** | *0.01* | 0.14 |
| **P** | 0.49 | – | 0.64 | 0.42 | 0.47 | – | **0.50** | *0.09* | 0.48 | – | 0.53 | 0.26 | – | – | 0.62 | **0.47** | *0.19* | 0.53 | – | – | – | | – | 0.81 | 0.51 | 0.32 | – | **0.55** | *0.25* | 0.51 | – | 0.25 | 0.55 | – | – | – | **0.40** | *0.22* | 0.40 |
| **K** | 0.29 | – | 1.70 | 0.56 | 0.29 | – | **0.71** | *0.67* | 0.42 | – | 10.00 | – | – | – | 0.03 | **5.02** | *7.04* | 5.02 | – | – | – | | – | 0.11 | 1.98 | 1.73 | – | **1.27** | *1.01* | 1.73 | – | – | – | – | – | – | – | – | – |
| **Ca** | 0.01 | 0.02 | 0.02 | 0.02 | 0.02 | 0.01 | **0.018** | *0.005* | 0.019 | 0.04 | 0.02 | 0.03 | 0.04 | – | 0.06 | **0.038** | *0.013* | 0.037 | – | – | – | | 4.50 | 4.75 | 4.36 | 2.96 | 4.43 | **4.20** | *0.71* | 4.43 | – | 3.66 | 3.36 | 2.78 | – | – | **3.26** | *0.45* | 3.36 |
| **Sc** | 0.05 | 0.14 | 0.10 | 0.11 | 0.11 | 0.13 | **0.11** | *0.03* | 0.11 | 0.27 | 0.11 | 0.15 | 0.21 | – | 0.27 | **0.20** | *0.07* | 0.21 | 0.26 | 0.02 | 0.26 | | 0.30 | 0.38 | 0.33 | 0.19 | 0.31 | **0.30** | *0.07* | 0.31 | – | 0.20 | 0.08 | 0.17 | – | – | **0.15** | *0.06* | 0.17 |
| **Ti** | 0.47 | 0.37 | 0.36 | 0.39 | 0.42 | 0.30 | **0.39** | *0.06* | 0.38 | 0.45 | 0.37 | 0.22 | 0.48 | – | 0.56 | **0.42** | *0.13* | 0.45 | 0.24 | 0.02 | 0.25 | | 2.00 | 2.46 | 1.16 | 0.48 | 2.00 | **1.62** | *0.79* | 2.00 | – | 0.46 | 1.47 | 0.33 | – | – | **0.75** | *0.62* | 0.46 |
| **V** | 0.06 | 0.11 | 0.10 | 0.11 | 0.13 | 0.09 | **0.10** | *0.02* | 0.10 | 0.19 | 0.10 | 0.12 | 0.16 | – | 0.26 | **0.17** | *0.06* | 0.16 | 0.37 | 0.03 | 0.37 | | 3.44 | 3.35 | 2.22 | 1.04 | 3.34 | **2.68** | *1.05* | 3.34 | – | 1.40 | 1.03 | 0.86 | – | – | **1.10** | *0.28* | 1.03 |
| **Cr** | 0.08 | 0.15 | 0.13 | 0.14 | 0.16 | 0.12 | **0.13** | *0.03* | 0.13 | 0.21 | 0.12 | 0.21 | 0.17 | – | 0.29 | **0.20** | *0.06* | 0.21 | 0.47 | 0.06 | 0.49 | | 0.63 | 0.63 | 0.57 | 0.36 | 0.74 | **0.59** | *0.14* | 0.63 | – | 0.46 | 0.25 | 0.24 | – | – | **0.31** | *0.12* | 0.25 |
| **Mn** | 1.76 | 1.99 | 1.65 | 1.50 | 1.32 | 1.79 | **1.67** | *0.23* | 1.71 | 1.13 | 1.18 | 1.00 | 1.20 | – | 0.95 | **1.09** | *0.11* | 1.13 | 1.88 | 0.05 | 1.89 | | 0.11 | 0.16 | 0.19 | 0.24 | 0.15 | **0.17** | *0.05* | 0.16 | – | 0.28 | 0.35 | 0.31 | – | – | **0.31** | *0.04* | 0.31 |
| **Co** | 3.07 | 3.29 | 3.07 | 3.00 | 2.95 | 3.38 | **3.13** | *0.17* | 3.07 | 2.23 | 2.73 | 2.20 | 2.45 | – | 1.91 | **2.30** | *0.30* | 2.23 | 3.08 | 0.14 | 3.11 | | 0.37 | 0.42 | 0.44 | 0.49 | 0.40 | **0.43** | *0.05* | 0.42 | – | 0.53 | 0.67 | 0.60 | – | – | **0.60** | *0.07* | 0.60 |
| **Ni** | 2.27 | 2.25 | 2.30 | 2.44 | 2.38 | 2.45 | **2.35** | *0.09* | 2.34 | 1.96 | 2.23 | 1.98 | 2.09 | – | 1.80 | **2.01** | *0.16* | 1.98 | 2.30 | 0.19 | 2.39 | | 17.3 | 13.1 | 8.7 | 6.2 | 13.0 | **11.7** | *4.3* | 13.0 | – | 7.27 | 6.61 | 5.63 | – | – | **6.50** | *0.83* | 6.61 |
| **Cu** | 0.50 | 0.54 | 0.76 | 1.45 | 0.81 | 0.32 | **0.73** | *0.40* | 0.65 | 0.99 | 0.74 | 1.07 | 1.08 | – | 1.05 | **0.99** | *0.14* | 1.05 | 0.48 | 0.16 | 0.50 | | 11.0 | 11.6 | 4.9 | 11.6 | 16.0 | **11.0** | *4.0* | 11.6 | – | 12.59 | 8.78 | 3.86 | – | – | **8.41** | *4.37* | 8.78 |
| **Zn** | 4.27 | 5.02 | 3.68 | 3.89 | 3.92 | 5.03 | **4.30** | *0.59* | 4.10 | 2.78 | 2.90 | 1.68 | 2.80 | – | 2.10 | **2.45** | *0.54* | 2.78 | 4.69 | 0.72 | 4.98 | | 0.86 | 1.08 | 0.87 | 0.84 | 0.82 | **0.89** | *0.11* | 0.86 | – | 1.12 | 1.84 | 1.12 | – | – | **1.36** | *0.42* | 1.12 |
| **Ga** | 0.30 | 0.40 | 0.42 | 0.34 | 0.48 | 0.37 | **0.38** | *0.06* | 0.38 | 0.52 | 0.41 | 0.29 | 0.49 | – | 0.68 | **0.48** | *0.14* | 0.49 | 0.89 | 0.08 | 0.87 | | 1.48 | 1.26 | 1.34 | 0.75 | 1.47 | **1.26** | *0.30* | 1.34 | – | 0.69 | 1.78 | 0.67 | – | – | **1.05** | *0.63* | 0.69 |
| **Ge** | 0.54 | 0.64 | 0.70 | 0.40 | 0.94 | 0.59 | **0.63** | *0.18* | 0.61 | 1.06 | 1.09 | 1.08 | 1.10 | – | 0.97 | **1.06** | *0.05* | 1.08 | 1.03 | 0.06 | 1.05 | | 1.11 | 1.15 | 1.83 | 0.68 | 2.04 | **1.36** | *0.56* | 1.15 | – | 0.77 | 0.60 | 0.45 | – | – | **0.60** | *0.16* | 0.60 |
| **As** | 0.33 | 0.31 | 0.47 | 0.42 | 1.30 | 0.28 | **0.52** | *0.39* | 0.37 | 0.64 | 0.59 | 0.41 | 0.66 | – | 0.54 | **0.57** | *0.10* | 0.59 | 0.67 | 0.08 | 0.63 | | 2.53 | 0.95 | 2.40 | 1.07 | 0.74 | **1.54** | *0.86* | 1.07 | – | 1.35 | 1.62 | 0.82 | – | – | **1.26** | *0.41* | 1.35 |
| **Rb** | 0.47 | 38.01 | 1.60 | 1.08 | 0.04 | 0.32 | **6.92** | *15.24* | 0.78 | 17.23 | 0.09 | 0.31 | 0.82 | – | 0.98 | **3.88** | *7.47* | 0.82 | 0.63 | 0.19 | 0.61 | | 1.17 | 59.8 | 1.46 | 22.9 | 0.99 | **17.3** | *25.6* | 1.46 | – | 2.93 | 0.93 | 2.94 | – | – | **2.27** | *1.16* | 2.93 |
| **Sr** | 0.00 | 0.01 | 0.03 | 0.02 | 0.00 | 0.00 | **0.010** | *0.011* | 0.009 | 0.01 | 0.00 | 0.01 | 0.01 | – | 0.01 | **0.0067** | *0.0037* | 0.0062 | 0.0042 | 0.0019 | 0.0045 | | 3493 | 2904 | 24 | 239 | 1805 | **1693** | *1551* | 1805 | – | 334 | 105 | 139 | – | – | **192** | *124* | 139 |
| **Y** | 0.01 | 0.02 | 0.06 | 0.07 | 0.02 | 0.01 | **0.033** | *0.024* | 0.024 | 0.04 | 0.02 | 0.03 | 0.03 | – | 0.05 | **0.032** | *0.010* | 0.029 | 0.041 | 0.004 | 0.039 | | 0.09 | 0.22 | 0.16 | 0.09 | 0.33 | **0.18** | *0.10* | 0.16 | – | 0.12 | 0.45 | 0.14 | – | – | **0.24** | *0.19* | 0.14 |
| **Zr** | 0.00 | 0.02 | 0.05 | 0.03 | 0.01 | 0.00 | **0.019** | *0.016* | 0.016 | 0.03 | 0.01 | 0.03 | 0.02 | – | 0.06 | **0.030** | *0.020* | 0.026 | 0.052 | 0.032 | 0.044 | | 2.12 | 3.38 | 1.12 | 0.32 | 4.34 | **2.26** | *1.63* | 2.12 | – | 0.33 | 0.21 | 0.18 | – | – | **0.24** | *0.08* | 0.21 |
| **Nb** | 0.10 | 0.50 | 0.48 | 0.38 | 0.14 | 0.15 | **0.29** | *0.18* | 0.26 | 0.25 | 0.26 | 0.06 | 0.27 | – | 0.32 | **0.23** | *0.10* | 0.26 | 0.024 | 0.014 | 0.021 | | 6.97 | 11.62 | 4.41 | 1.68 | 5.71 | **6.08** | *3.67* | 5.71 | – | 1.18 | 3.21 | 0.59 | – | – | **1.66** | *1.38* | 1.18 |
| **Mo** | 0.59 | 1.35 | 0.77 | 0.65 | 7.30 | 0.59 | **1.87** | *2.67* | 0.71 | 0.83 | 0.48 | 0.23 | 0.91 | – | 0.16 | **0.52** | *0.34* | 0.48 | 2.64 | 1.92 | 1.95 | | 0.16 | 1.10 | 1.00 | 1.09 | 0.27 | **0.72** | *0.47* | 1.00 | – | 0.56 | 1.23 | 0.23 | – | – | **0.67** | *0.51* | 0.56 |
| **Ag** | 0.05 | 0.37 | 0.09 | 0.11 | 0.39 | 0.15 | **0.19** | *0.15* | 0.13 | 0.38 | 0.60 | 0.10 | 0.22 | – | 0.27 | **0.31** | *0.19* | 0.27 | 1.30 | 0.85 | 0.98 | | 3.06 | 6.66 | 7.04 | 5.71 | 14.99 | **7.49** | *4.47* | 6.66 | – | 1.63 | 2.58 | 1.08 | – | – | **1.77** | *0.76* | 1.63 |
| **Cd** | 0.33 | 0.25 | 0.33 | 0.32 | 0.29 | 0.34 | **0.31** | *0.03* | 0.32 | 0.28 | 0.32 | 0.24 | 0.24 | – | 0.40 | **0.30** | *0.07* | 0.28 | 0.23 | 0.08 | 0.26 | | 0.90 | 1.11 | 1.47 | 0.83 | 1.01 | **1.06** | *0.25* | 1.01 | – | 1.01 | 1.83 | 0.95 | – | – | **1.26** | *0.49* | 1.01 |
| **In** | 0.07 | 0.16 | 0.11 | 0.15 | 4.51 | 0.14 | **0.86** | *1.79* | 0.15 | 0.35 | 0.81 | 0.84 | 0.26 | – | 0.92 | **0.63** | *0.31* | 0.81 | 0.45 | 0.13 | 0.41 | | 0.41 | 0.52 | 0.36 | 0.21 | 0.51 | **0.40** | *0.13* | 0.41 | – | 1.30 | 1.47 | 0.23 | – | – | **1.00** | *0.67* | 1.30 |
| **Cs** | 5.79 | – | 7.28 | 2.17 | 1.61 | – | **4.21** | *2.76* | 3.98 | 0.48 | 0.46 | 0.22 | 0.54 | – | 0.12 | **0.36** | *0.18* | 0.46 | 0.87 | 0.26 | 0.80 | | – | 2.31 | 0.74 | 0.64 | 0.64 | **1.08** | *0.82* | 0.69 | – | 3.29 | 1.16 | 0.48 | – | – | **1.64** | *1.47* | 1.16 |
| **Ba** | 0.00 | 0.08 | 0.39 | 0.31 | 0.15 | 0.01 | **0.16** | *0.16* | 0.12 | 0.08 | 0.06 | 0.06 | 0.02 | – | 0.00 | **0.044** | *0.030* | 0.056 | 0.20 | 0.35 | 0.04 | | 56.6 | 1316 | 2.2 | 133 | 6.3 | **303** | *569* | 56.6 | – | 9.6 | 17.1 | 4.1 | – | – | **10.2** | *6.5* | 9.6 |
| **La** | 0.00 | 0.02 | 0.08 | 0.07 | 0.00 | 0.00 | **0.028** | *0.035* | 0.010 | 0.00 | 0.01 | 0.01 | 0.00 | – | 0.01 | **0.0068** | *0.0022* | 0.0077 | 0.0074 | 0.0065 | 0.0055 | | 967 | 644 | 16.7 | 45.9 | 335 | **402** | *405* | 335 | – | 92.6 | 36.0 | 31.0 | – | – | **53.2** | *34.2* | 36.0 |
| **Ce** | 0.00 | 0.02 | 0.05 | 0.04 | 0.00 | 0.00 | **0.020** | *0.023* | 0.010 | 0.01 | 0.01 | 0.01 | 0.01 | – | 0.01 | **0.0079** | *0.0028* | 0.0076 | 0.0085 | 0.0074 | 0.0054 | | 224 | 93 | 20.3 | 17.5 | 121 | **95.1** | *84.9* | 92.6 | – | 26.1 | 10.1 | 13.9 | – | – | **16.7** | *8.4* | 13.9 |
| **Pr** | 0.00 | 0.01 | 0.04 | 0.03 | 0.00 | 0.00 | **0.013** | *0.015* | 0.006 | 0.00 | 0.00 | 0.01 | 0.00 | – | 0.01 | **0.0063** | *0.0029* | 0.0050 | 0.0067 | 0.0061 | 0.0048 | | 77.6 | 58.0 | 17.4 | 8.3 | 48.8 | **42.0** | *28.8* | 48.8 | – | 11.0 | 5.7 | 7.2 | – | – | **7.94** | *2.75* | 7.16 |
| **Nd** | 0.00 | 0.01 | 0.03 | 0.02 | 0.00 | 0.00 | **0.012** | *0.013* | 0.007 | 0.01 | 0.00 | 0.01 | 0.01 | – | 0.01 | **0.0079** | *0.0032* | 0.0073 | 0.0061 | 0.0045 | 0.0043 | | 30.7 | 25.7 | 10.1 | 3.8 | 22.3 | **18.5** | *11.2* | 22.3 | – | 5.1 | 2.5 | 3.7 | – | – | **3.77** | *1.28* | 3.72 |
| **Sm** | 0.00 | 0.01 | 0.03 | 0.02 | 0.01 | 0.00 | **0.013** | *0.012* | 0.009 | 0.01 | 0.01 | 0.01 | 0.01 | – | 0.02 | **0.010** | *0.005* | 0.008 | 0.0077 | 0.0032 | 0.0069 | | 5.32 | 6.71 | 2.58 | 1.05 | 5.55 | **4.24** | *2.34* | 5.32 | – | 1.34 | 0.79 | 1.09 | – | – | **1.07** | *0.27* | 1.09 |
| **Eu** | 0.00 | 0.02 | 0.04 | 0.02 | 0.01 | 0.00 | **0.015** | *0.014* | 0.013 | 0.02 | 0.01 | 0.01 | 0.01 | – | 0.02 | **0.014** | *0.004* | 0.014 | 0.0083 | 0.0028 | 0.0092 | | 2.38 | 2.81 | 1.40 | 0.62 | 2.79 | **2.00** | *0.96* | 2.38 | – | 0.82 | 0.57 | 0.67 | – | – | **0.69** | *0.13* | 0.67 |
| **Gd** | 0.00 | 0.01 | 0.04 | 0.03 | 0.01 | 0.00 | **0.017** | *0.016* | 0.011 | 0.02 | 0.01 | 0.02 | 0.01 | – | 0.02 | **0.016** | *0.005* | 0.015 | 0.012 | 0.002 | 0.012 | | 1.48 | 2.01 | 0.86 | 0.41 | 2.27 | **1.41** | *0.78* | 1.48 | – | 0.57 | 0.54 | 0.50 | – | – | **0.54** | *0.03* | 0.54 |
| **Tb** | 0.01 | 0.02 | 0.05 | 0.04 | 0.01 | 0.00 | **0.021** | *0.018* | 0.015 | 0.02 | 0.01 | 0.02 | 0.02 | – | 0.03 | **0.020** | *0.006* | 0.019 | 0.020 | 0.002 | 0.020 | | 0.57 | 0.86 | 0.46 | 0.23 | 1.20 | **0.67** | *0.38* | 0.57 | – | 0.34 | 0.47 | 0.32 | – | – | **0.38** | *0.08* | 0.34 |
| **Dy** | 0.01 | 0.01 | 0.06 | 0.04 | 0.02 | 0.01 | **0.025** | *0.020* | 0.016 | 0.03 | 0.01 | 0.02 | 0.02 | – | 0.03 | **0.022** | *0.007* | 0.022 | 0.028 | 0.003 | 0.027 | | 0.25 | 0.54 | 0.28 | 0.14 | 0.77 | **0.40** | *0.26* | 0.28 | – | 0.22 | 0.46 | 0.24 | – | – | **0.31** | *0.13* | 0.24 |
| **Ho** | 0.01 | 0.03 | 0.07 | 0.06 | 0.02 | 0.01 | **0.032** | *0.024* | 0.026 | 0.03 | 0.02 | 0.02 | 0.02 | – | 0.03 | **0.025** | *0.004* | 0.025 | 0.038 | 0.005 | 0.037 | | 0.12 | 0.31 | 0.17 | 0.09 | 0.50 | **0.24** | *0.17* | 0.17 | – | 0.14 | 0.46 | 0.18 | – | – | **0.26** | *0.18* | 0.18 |
| **Er** | 0.02 | 0.02 | 0.07 | 0.07 | 0.03 | 0.01 | **0.037** | *0.028* | 0.026 | 0.04 | 0.03 | 0.03 | 0.03 | – | 0.04 | **0.035** | *0.008* | 0.033 | 0.055 | 0.004 | 0.054 | | 0.05 | 0.17 | 0.12 | 0.06 | 0.29 | **0.14** | *0.10* | 0.12 | – | 0.09 | 0.46 | 0.14 | – | – | **0.23** | *0.20* | 0.14 |
| **Tm** | 0.02 | 0.06 | 0.07 | 0.08 | 0.03 | 0.02 | **0.048** | *0.025* | 0.047 | 0.05 | 0.05 | 0.03 | 0.03 | – | 0.04 | **0.040** | *0.012* | 0.044 | 0.082 | 0.008 | 0.081 | | 0.03 | 0.12 | 0.08 | 0.04 | 0.20 | **0.094** | *0.069* | 0.079 | – | 0.06 | 0.32 | 0.23 | – | – | **0.20** | *0.13* | 0.23 |
| **Yb** | 0.03 | 0.07 | 0.09 | 0.13 | 0.03 | 0.05 | **0.066** | *0.038* | 0.059 | 0.03 | 0.09 | 0.03 | 0.04 | – | 0.04 | **0.045** | *0.023* | 0.037 | 0.12 | 0.01 | 0.11 | | 0.01 | 0.08 | 0.05 | 0.03 | 0.10 | **0.054** | *0.035* | 0.052 | – | 0.04 | 0.25 | 0.16 | – | – | **0.15** | *0.11* | 0.16 |
| **Lu** | – | 0.15 | 0.11 | 0.13 | 0.04 | 0.06 | **0.10** | *0.05* | 0.11 | 0.05 | 0.06 | 0.03 | 0.04 | – | 0.03 | **0.043** | *0.014* | 0.042 | 0.16 | 0.02 | 0.16 | | 0.01 | 0.06 | 0.04 | 0.02 | 0.07 | **0.039** | *0.024* | 0.040 | – | 0.03 | 0.16 | 0.18 | – | – | **0.12** | *0.08* | 0.16 |
| **Hf** | 0.00 | 0.02 | 0.02 | 0.02 | 0.01 | 0.00 | **0.013** | *0.009* | 0.014 | 0.02 | 0.01 | 0.02 | 0.02 | – | 0.04 | **0.020** | *0.012* | 0.017 | 0.050 | 0.014 | 0.049 | | 5.45 | 16.08 | 3.98 | 0.87 | 20.72 | **9.42** | *8.52* | 5.45 | – | 1.06 | 0.39 | 0.48 | – | – | **0.64** | *0.37* | 0.48 |
| **Ta** | – | 0.27 | 0.52 | 0.42 | 0.33 | 0.17 | **0.34** | *0.13* | 0.33 | 0.47 | 0.51 | 0.16 | 0.55 | – | 0.68 | **0.47** | *0.19* | 0.51 | 0.028 | 0.029 | 0.016 | | 17.2 | 33.5 | 3.18 | 1.49 | 15.33 | **14.1** | *12.9* | 15.3 | – | 1.13 | 2.16 | 0.47 | – | – | **1.26** | *0.85* | 1.13 |
| **W** | 0.32 | 2.34 | 0.86 | 0.64 | 7.37 | 0.09 | **1.94** | *2.78* | 0.75 | 3.54 | 2.19 | 0.31 | 0.93 | – | 0.04 | **1.40** | *1.46* | 0.93 | 0.66 | 0.46 | 0.57 | | 3.15 | 0.79 | 2.00 | 7.84 | 8.10 | **4.38** | *3.39* | 3.15 | – | 1.19 | 15.35 | 0.21 | – | – | **5.59** | *8.47* | 1.19 |
| **Re** | 0.84 | 1.04 | 0.75 | 1.33 | 5.06 | 0.39 | **1.57** | *1.74* | 0.94 | – | 0.74 | 0.75 | 0.24 | – | 0.56 | **0.57** | *0.24* | 0.65 | 0.65 | 0.26 | 0.68 | | 0.33 | 0.16 | 0.24 | 0.26 | 1.88 | **0.57** | *0.73* | 0.26 | – | 0.54 | 1.68 | 0.21 | – | – | **0.81** | *0.77* | 0.54 |
| **Tl** | 0.65 | 1.08 | 12.36 | 0.65 | 2.58 | – | **3.46** | *5.04* | 1.08 | – | 0.31 | 0.79 | – | – | 0.24 | **0.45** | *0.30* | 0.31 | 0.65 | 0.39 | 0.64 | | 0.79 | 4.77 | 3.56 | 2.08 | 5.57 | **3.35** | *1.95* | 3.56 | – | 2.39 | 0.50 | – | – | – | **1.45** | *1.33* | 1.45 |
| **Pb** | 0.00 | 0.07 | 0.09 | 0.34 | 1.48 | 0.02 | **0.33** | *0.57* | 0.08 | 0.41 | 0.17 | 0.18 | 0.17 | – | 0.18 | **0.22** | *0.11* | 0.18 | 0.15 | 0.09 | 0.15 | | 6.44 | 42.89 | 1.48 | 3.02 | 24.5 | **15.7** | *17.8* | 6.4 | – | 1.90 | 3.67 | 2.48 | – | – | **2.68** | *0.91* | 2.48 |
| **Bi** | 0.05 | 0.18 | 0.05 | 0.12 | 1.12 | 0.04 | **0.26** | *0.42* | 0.09 | 0.42 | 0.59 | 0.76 | 0.61 | – | 1.06 | **0.69** | *0.24* | 0.61 | 0.67 | 0.31 | 0.70 | | 5.79 | 7.96 | 4.44 | 1.45 | 14.8 | **6.88** | *5.00* | 5.79 | – | 3.07 | 1.26 | 0.59 | – | – | **1.64** | *1.28* | 1.26 |
| **Th** | 0.01 | 0.19 | 0.26 | 0.44 | 0.02 | 0.00 | **0.15** | *0.18* | 0.10 | 0.04 | 0.11 | 0.05 | 0.03 | – | 0.02 | **0.054** | *0.033* | 0.045 | 0.075 | 0.013 | 0.069 | | 112 | 14.9 | 4.7 | 10.3 | 39.1 | **36.2** | *44.5* | 14.9 | – | 4.99 | 10.17 | 1.26 | – | – | **5.47** | *4.47* | 4.99 |
| **U** | 0.03 | 0.15 | 0.59 | 0.50 | 0.16 | 0.02 | **0.24** | *0.25* | 0.15 | 0.12 | 0.17 | 0.17 | 0.16 | – | 0.05 | **0.13** | *0.05* | 0.16 | 0.14 | 0.11 | 0.08 | | 2.81 | 3.06 | 1.63 | 0.98 | 1.70 | **2.04** | *0.87* | 1.70 | – | 0.47 | 0.94 | 0.16 | – | – | **0.52** | *0.39* | 0.47 |